Doctoral Dissertation
Doctoral Program in Material Science and Technology (36th Cycle)

Towards a more sustainable world: UV-curing & 3D printing of bio-based monomers

Synthesis and characterization of bio-derived monomers for cationic and radical UV-curing

Lorenzo Pezzana

Supervisor(s):

Prof. Marco Sangermano, Supervisor, Politecnico di Torino, Department of Applied Science and Technology, Torino, Italy
Prof. Eva Malmström, Co-Supervisor, KTH Royal Institute of Technology, Division of Coating technology, Stockholm, Sweden

Doctoral Examination Committee:

- Prof. Jean Pierre Habas, University of Montpellier, ICGM, Equipe Ingénierie et Architectures Macromoléculaires, Montpellier, France (Referee)
- Prof. Minna Hakkarainen, KTH Royal Institute of Technology, Department of Fibre and Polymer Technology, Stockholm, Sweden (Referee)
- Prof. Galder Kortaberria, University of the Basque Country, Chemical and Environmental Engineering Department, San Sebastian, Spain
- Dr. Sandra Schlögl, Polymer Competence Center Leoben, Chemistry of Functional Polymer, Leoben, Austria
- Prof. Massimo Messori, Politecnico di Torino, Department of Applied Science and Technology, Torino, Italy

Politecnico di Torino
2024

Declaration

I hereby declare that, the contents and organization of this dissertation constitute my own original work and does not compromise in any way the rights of third parties, including those relating to the security of personal data.

Lorenzo Pezzana

Torino, 2024

* This dissertation is presented in partial fulfillment of the requirements for **Ph.D. degree** in the Graduate School of Politecnico di Torino (ScuDo).

I would like to dedicate this thesis to my sweetest grandmother, my loving parents and brother

Acknowledgement

First, I would like to express my profound gratitude to Marco Sangermano, my PhD supervisor for the past years. His unwavering support, invaluable guidance, and expertise have been crucial in shaping my research and academic journey. I am truly fortunate to have had the privilege of working under his mentorship allowing me to make the PhD a journey across Europe. Thank you for the trust in me during the time spent abroad in other research groups and thank to all the suggestions, discussions, and truly interaction during these years.

A special thanks to Eva Malmström, my co-supervisor, and Mats Johansson, who kindly host me in their lab from my master thesis to a great period during the PhD. You both make me feel part of the group already from the first day. Thanks for your wise scientific inputs that have expanded my knowledge in polymer chemistry.

I also would like to express my deepest gratitude to all professors, Robert Liska, Nathanael Guigo, and Nicolas Sbirrazzuoli that give me the opportunity to work in their lab during my PhD. Their generosity in hosting me and the knowledge I gained during these periods have been invaluable to my research and academic growth. I am truly grateful for their support and mentorship.

A special gratitude to my friend and colleagues in Torino. We not only share three years, but also our success, our bad monuments, and most important our friendship. Thank to: Micheal, Daniele, Andrea, Rossella, Matilde, Matteo, Dumitru, Camilla, Andrea, Giacomo, Sofia, Angelo, Cristian.

Now is the time for my second family, my Austrian friends. Thank you FBMC group to make me feel at home, thank you to welcome me in your group without any hesitations, thank for all the great time spent in the lab and also for all the time of the life that we shared. It was AMAZING. A special thanks to Ralle, who guide and support me through time in Vienna. Oskar, Anna, Lala, Lisa, Fitzi, Klaus, Flo, Floky, Toni, Tina, Michy, Ricky, David, Philips, Jo, Carola, Danijela, Miriam, Pontus, Marcus and all the fantastic people that I have met.

I thank all the groups that host me and all the people that I met during this time. Thank to Giuseppe, who introduce me into the MAPEC group in Nice, and thank to all the fantastic group. Emelie, Pierre, Mona, Lucie, Ocean and Marie. Thank to Maryam who introduce me in the Division of coating Technology in Stockholm and guide me in my chemical synthesis with important tips and suggestions. Thanks to all friends there, Iuliana, Alessio, Martina, Rosella, Alexandros, Tijana, Åsa, Adrian, and all the great people that I have met.

A special thanks to my flat mates of Stockholm, who start to host me from my Erasmus, and then multiple times. Elida, Saif and Kenny, you are my Swedish family. Thank you for all the moments spent together.

Going back to Italy, a special thanks to my crazy and wild friends from Cuneo, who share with me my free time exploring mountains. Colin, Fiore, Nick, Bande, Rena, Mena, and all the others. Thank to my lifelong friends, Veronica, Giulia, Pietro, Stefano, Luca, Simone, Amos, Erica, Jessica and all the others.

I want to take a moment to express my deepest gratitude to my entire family: Mamma, Pa, Fabri, Mimi, Pim, Parin, Zia Stefi and Vittoria. You always encouraged and supported me to go further, your presence has been my greatest source of strength and comfort. I am truly fortunate to have such an incredible family with a really special and huge thank to my grandmother, “Grazie Nonna, per essere sempre stata la mia guida nel mio percorso di scuola e di vita”.

Last but not least, my Auri. Thank you to be on my side, thank you to support me, thank you to be patient with me all time, thank you to share with me all the moments, thank you to be amazing with me.

Abstract

Sustainable development is one of the main challenges of our time, underlined by the United Nations which embraced the 2030 Agenda for Sustainable Development by adopting 17 Sustainable Development Goals. Economic, social, environmental, and governance dimensions are crucial factors to international agreements to face these challenges. The limitation of climate change needs to handle multiple challenges such the use of fossil-based resources, the reduction of greenhouse emission, and the minimization of the carbon foot print. To meet these challenges, important innovations have to be done in material science to create and develop new materials aiming to a circular economy. Bio-based polymers can represent a promising avenue towards a more sustainable future, being the natural substitute of fossil-based plastic. Indeed, speaking of plastics, the impressive achievable properties make these materials exploitable in a wide spread of applications making the global market one of the most profiting over the world. However, the plastic production is causing, apart from the depletion of fossil resources, an increasing environmental concern due to the high greenhouse emissions and toxic products released into the environment giving rise to potential threats to human health and climate change. Thus, the industrial processes become crucial to reach sustainability. Progress has to be reached in all the different steps of the material production processed aiming for a sustainable future.

In this view, this thesis aims to show possible innovations in the world of bio-based polymers and UV-curing. The Introduction to the world of green materials and sustainability (**Chapter 1**) points out the potential benefits in the exploitation of natural resources to create new materials. Lignocellulosic biomass is one of the main platforms that can generate a wide palette of several monomers suitable for material production. Industrial and food side streams are under deep investigation, being valuable source of monomers which, after suitable treatment, can be reused to produce further value chemicals. Moreover, environmentally green and efficient processes are required to make a further step toward a more sustainable development. The synergy between natural monomer and UV-curing (**Chapter 2**) can move toward this scope showing interesting benefits in term of energy, cost and time production.

After this brief introduction about general principles and fundamentals, the first part of the scientific contribution is devoted to UV-cationic curing of bio-based monomers. The multiple works presented in **Chapter 3** aim to highlight the great potential of different classes of biopolymer in distinct areas, from coatings to 3D printing. The first part is focused on furan-based monomers and three possible uses of this class of monomers. Specifically, hybrid coatings were accomplished to illustrate the benefits of a dual network, then an innovative cross-linking of monofunctional furan-based monomer was investigated by two-step curing approach. Lastly, a breakthrough in 3D printing is presented, where bio-based epoxy resins are successfully 3D printed, exploiting the Hot-lithography technology.

Moreover, the second part of the chapter is dedicated to different bio-based epoxy-functional monomers employed in different applications covering adhesives, coatings, and 3D printings. The ferulic-based epoxy shows remarkable adhesive properties and a versatility in the possible curing mechanisms which can be used to achieve the formation of green thermosets. This open the possibility to obtain a wide spectrum of different thermo-chemical properties. Then, the great potential of isosorbide-based epoxy in coating application is presented, highlighting the possible reinforcement given by the addition of bio-derived macadamia fillers. Lastly, the 3D printing field is once more area of focus exploiting this time epoxy vegetable oils (EVOs). The innovation using Hot-lithography is presented in the successfully 3D printing of fully bio-based composites generating by bio-based polymer matrix and bio-derived filler based on wall-nut shell powders.

After this excursus on cationic UV-curing, the focus changes to radical mechanism with a particular attention to thiol-ene chemistry (**Chapter 4**). In this case several works present the innovation in coating applications using ferulic acid, isosorbide and furan-based monomers as platform to synthetize several allyl derivatives. Remarkably, a deep investigation of the influence of the chemical structure is carried out to find the main important features responsible for the thermo-mechanical properties of the resulted thiol-ene networks. The new horizons open by 3D printing are investigated adopting levoglucosenone-based monomers to develop bio-based photocurable green resins. Lastly, a different application of the thiol-ene chemistry is shown, the surface functionalization of a green coating is investigated highlighting a further use of UV-light in the field of post-functionalization.

In general, the presented works aim to show the efficacy in the use of bio-based polymers in different applications spacing from coatings to 3D printing. Furthermore, the different syntheses performed were evaluated aiming to understand possible benefit of using green reagents or criticism caused by less green reagents. Chemical and kinetic aspects of the UV-curing were carefully analyzed aiming to better understand the process. A thermo-mechanical characterization of the different thermosets was performed all through the studies aiming to increase the knowledge of structure-properties relationship and to verify the possibility to use this bio-based monomer instead of fossil-based ones. Overall, these works present significant steps toward the realization of the SDGs contributing in a more sustainable, and circular economy.

Table of contents

1. Brief overview about green and sustainability

In September 2015, the United Nations embraced the 2030 Agenda for Sustainable Development by adopting 17 Sustainable Development Goals (SDGs). These purposes and principles, interconnected and comprehensive (**Figure 1.1**), aspire to face global challenges across social, economic, and environmental spheres. Sustainable development, as the underlying principle, seeks to meet present needs without compromising the ability of future generations to meet their own [1]. Economic, social, environmental, and governance dimensions are crucial factor to achieve a successful sustainable development. The road map is designed by the 2030 Agenda, in conjunction with the Paris Agreement on Climate Change, which supports international agreements to face these challenges [2].

Figure 1.1. The 17 Sustainable Development Goals (SDGs) [1].

The serious threat of climate change, which is one of the main problems of our era, needs to deal with several issues, among the others, the use of fossil-based resources, the limitation of greenhouse emission, the minimization of carbon footprint (the ratio of CO2 emissions to material production mass) and embodied energy (the energy input per kilogram of usable material) [3,4]. Furthermore, equally important are the circularity principles in material design, emphasizing reusability, repurposing, upcycling, and recycling [5].

To meet these issues, bio-based polymers have emerged as a promising avenue towards a more sustainable future. Indeed, speaking of plastic in general terms, the global market was valued at 593 billion U.S. dollars in 2021 [6]. The plastics market is projected to grow in the coming years to reach a value of more than 810 billion U.S. dollars by 2030; during the period from 2022 to 2030, a forecast compound annual growth rate (CAGR) of 3.7 % is estimated [7]. Thus, acting on the plastic materials with the use of bio-based polymers can help to achieve a higher level of sustainability. Indeed, the bio-based polymer market is expected to grow from 1.2 million tons in 2023 to 3.6 million tons by 2028, at a CAGR of 24.3% during the forecast period (2023-2028) [8]. Moving toward bio-based polymer means using renewable raw materials to develop new materials which can perform in the same manners or even better than the fossil-based ones [9]. However, the use of bio-based polymer cannot solve all the challenges, indeed the synergy with the development of green processes is tremendously required to act in an efficient way toward the decarbonization limiting the impact on Earth [10].

Natural resources such as forests, crops, algae as well as agricultural, industrial side stream, and food side streams play a crucial role in providing renewable raw materials [11]. Lignocellulosic biomass is a valuable feedstock for sustainable energy and bio-based material production [12]. This renewable, biodegradable, widely accessible, non-toxic, and cost-effective resource aligns with the goals of sustainable development. To achieve this, it is imperative to minimize energy and water consumption in production and processing, all while considering the life cycle assessment of end products [13].

1.1. Aims of the thesis

This thesis investigates the production of bio-based thermosetting materials, exploring the intricate relationships between structure and properties. This research agenda resonates strongly with several SDGs, notably SDGs 12, 13, 14, and 15. These goals aim to encourage the use of renewable resources in material design to mitigate the adverse effects of global warming. In this thesis, the synergy between environmentally green and efficient processes, and the use of renewable materials is examinate to achieve the formation of green thermosets which can fulfill different applications from coating to 3D printing. Starting from the chemical synthesis, the thesis aimed to analyze the criticisms of new paths pointing out benefits of the different functionalization performed to synthetized suitable reactive monomers for UV-curing. The efficacy in the use of bio-based polymers can significantly hold the potential to make worthy steps toward the realization of the SDGs contributing in a more sustainable, and circular economy. However, achieving this vision requires meticulous considerations which includes cost-effective processability of bio-based polymers, high-quality of derived materials and optimal life cycle analysis. Thus, the thesis aimed to perform a comprehensive characterization of the UV-curing process looking into different aspects of the curing, from chemicals to kinetics. A better knowledge of the process may allow to improve the final outcomes resulting in improved quality of the final products. Indeed, with the purpose to use the bio-based thermosets, a comparison of the performance with the ones achievable using traditional fossil-based monomers has been detailed. Several applications were covered aimed to increase the array of possible use of these bio-based monomers. Finally, the design of the material, from the raw material to the end of use, needs to face circularity principles aiming for a sustainable development to maintain our wellbeing thus end-of-life studies were carried out to aiming to investigate this crucial and important aspect.

2. Sustainability meets the power of the UV-curing

The synergy between bio-based monomers and UV-curing is the topic of this thesis aiming to empathize the benefits of using ultraviolet (UV) light to generate polymers for various applications [14]. The following paragraphs will point out the principles, the fundamentals of UV-curing, and its benefits in the fabrication of polymer-based thermoset. The UV-curable resin market is estimated to be 4. billion US dollars testifying the extend use across several applications of this technology. The projection are event better, with a prediction to reach 6.6 billion U.S. dollars by 2028, registering a CAGR of about 6.8 % during the forecast period. The major driving factors are the usage of environment-friendly industrial coatings, the rising demand for UV-curable resins in packaging applications, and the increasing applications in 3D printing which spread from biomedicine to automotive [15].

2.1. Fundamentals of photochemistry

UV-light is a powerful tool to initiate cross-linking reactions to produce thermosets starting from liquid resins [16]. The photo-chemical reaction is usually started by a compound, called photoinitiator (PI), which can generate vey reactive radicals or ionic species upon irradiation [17]. These can start the cross-linking reaction generating polymer networks. The basic principle of one-photon absorption (OPA) is universally valid for all the photochemical process relying on the absorption of a photon which then can activate subsequent reactions within a molecule, as illustrates in the typical Jablonsky diagram (**Figure 2.1**). The target molecule absorbs the photon promoting an electron from its ground state (S_0) to its short-life excited singlet state (S_1). At this point different paths can occur; firstly, the excited short-lived state (S1) can return to the ground state S0 through processes such as fluorescence emission or via internal conversion involving non-radiative transitions. On the other hand, S1 can transition to a lower-energy triplet state (T1) through intersystem crossing (ISC), which can revert to S0 through various photophysical processes (e.g., phosphorescence emission) or give rise to the initiation of primary photochemical reactions [16].

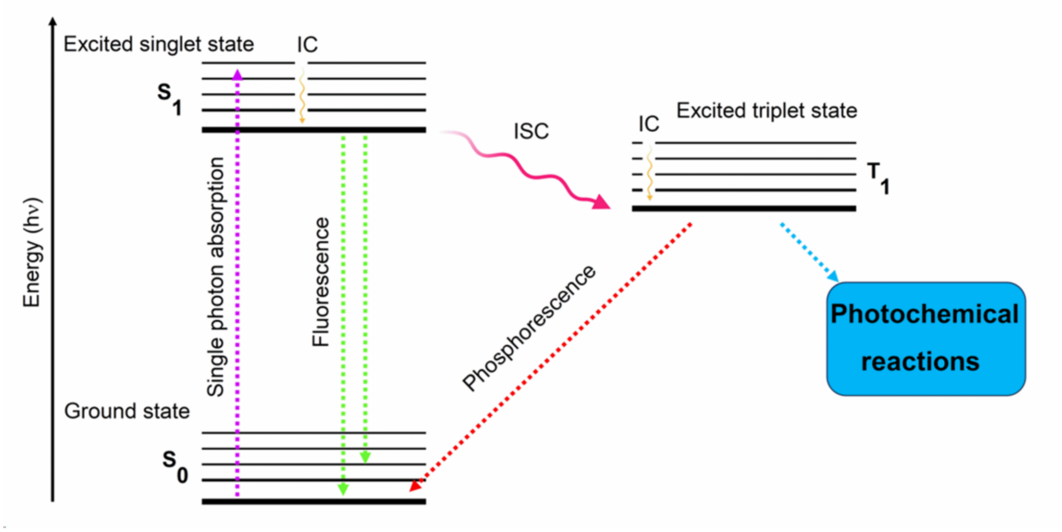

Figure 2.1. Jablosnki diagram illustrating electronic states and transitions activated upon one photon absorption (OPA): from the ground state (S_0) to the excited singlet state (S_1) which can then undergo intersystem crossing (ISC) to a triplet state (T_1), which leads to different photochemical reactions.

The main photochemical transformations involve isomerization [18,19], bond-forming, such as [2+2] photoaddition [20,21], and bond-breaking [22–24]. The generation of radicals and acid/cationic reactive intermediates implicates bond-breaking reaction which allowed the activation of photopolymerization processes. According to type of the activating centre of polymerization two main categories can be highlighted for the UV-curing, radical or cationic UV-activated polymerization.

2.2. Photoinitiators for UV-curing

Speaking of UV-induced photopolymerization by radical processes, two distinct reactive mechanisms may occur in the photochemical process depending on the type of PI used. Norrish type I reaction (NT1) is a homolytic cleavage of a chemical bond within the PI which generates two reactive radical intermediates [25,26]. The cleavage commonly involves the carbon-carbon (C-C) bond near to (α position) the carbonyl (C=O) chromophore groups, leading to formation of radicals, as presented as example for bis(2,4,6-trimethylbenzoyl) phenyl phosphine oxide (BAPO) in **Figure 2.2**. In presence of reactive monomers, such as acrylates or thiols, the generated radicals my initiate free-radical polymerization [27,28]. On the other hand, Norrish type II reaction (NT2) involves hydrogen abstraction to generate a radical specie. In this case the mechanism is bimolecular since the PI, usually belonging to benzophenones, camphorquinone, thioxanthones or diallkyl ketones, interacts with a hydrogen donor molecule (usually amines), used as co-initiator specie to generate radicals [27,29,30].

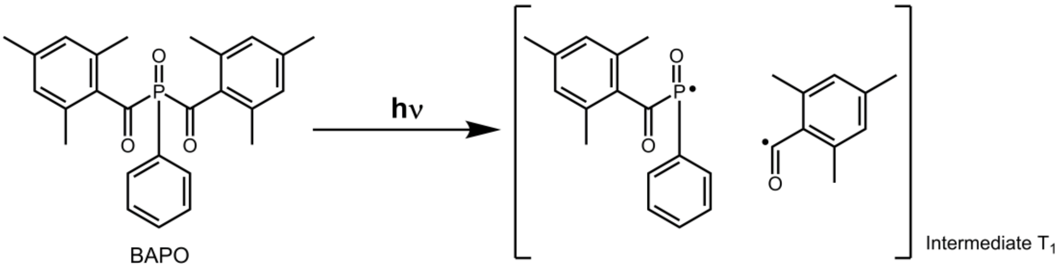

Figure 2.2. Generation of radicals from BAPO, a photoinitiator, upon UV-irradiation. The triplet state (T_1) is shown as result of UV triggered fragmentation of the PI.

Light-exposure can induce another typical bond-breaking of PhIs generating ah acid/cationic reactive intermediate. In this type of photochemical process, the decomposition of PI generate a strong acid species (PAG) which can activate further reactions [31]. Specifically, the photolysis of PAG can produce Brønsted acid which can initiate the cationic chain-growth polymerization. Onium salt, discovered by Crivello et al. [32], belongs to the famous category of PAG structured by an organic cation coupled with an inorganic anion [22]. The light-absorption properties, e.g., absorption wavelength, quantum yield, and thermal stability are governed by the former, while the latter determines the strength of the acid generated by photolysis. UV-light can induce complex both homolytic and heterolytic decomposition of diaryliodonium salt (Ar_2I) generating the so called "super acid", as presented in **Figure 2.3**. These super acids have values ranging from – 14 to – 30 of Hammet scale, which is a well-establish evaluation method [33]. The acidity increases with the increase of dimension of the counterion ($BF4^- < PF6^- < AsF6^- < SbF6^-$), due to a lower nucleophilic character of the latter. Sulfonium-based salts represent another class of onium PIs which shows high thermal stability and extremely high photosensitivity useful for activation of several UV-cationic curing mechanism [22,34].

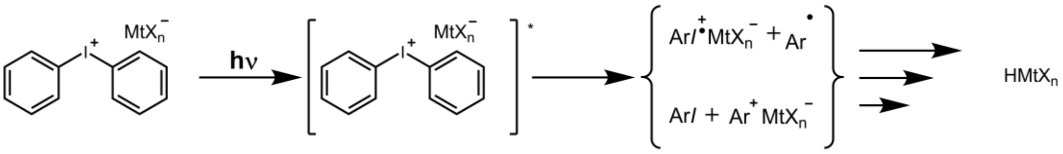

Figure 2.3. Schematically simplified mechanism of onium salt activation by UV-light.

2.3. Photopolymerization reaction

Photochemical curing is a well-established environmental-friendly technique to cure liquid resins to generate thermosets. The advantages in the UV-induced curing can be found in energy-, time- and thus cost savings with respect to the traditional thermal curing [35]. Indeed, mild conditions are adopted in UV-curing; usually room temperature (r.t.) curing is performed and the exposition time is in the order of minutes. These conditions create enormous advantages comparing to the harsh conditions of thermal curing, where high temperature, usually above 150 °C, prolonged time, hours of curing, and multiple steps are required to ensure complete cross-linking [23,36]. Furthermore, the lack of volatile organic compounds (VOCs) emission due to the absence of solvent is a brilliant innovation which lead to sustainability [31,37]. The two main mechanisms discussed in this thesis are related to UV-cationic curing and UV-induce thiol-ene curing. The former is a chain growth mechanism while the latter is a step-growth mechanism, reported in **Figure 2.4**.

Cationic photopolymerization, which emerged in the 1970s [22,34], was primarily developed to address certain limitations observed in radical systems. One of the key advantages of cationic systems is their immunity to oxygen inhibition leading to no need for a protective atmosphere during the photocuring process. In radical systems, free radicals have a short life resulting in rapid termination, which translates into relatively low monomer conversion rates [38]. In contrast, cationic systems have a more long-lived cation center, which enhances monomer conversion. Furthermore, when it comes to the photopolymerization of cationic species, particularly epoxides, it leads to reduced volumetric shrinkage, improved mechanical properties and thermal resistance compared to their radical system counterparts [39]. Notably, the "dark polymerization" phenomenon is present in cationic polymerization, allowing the continue through a chain-growth mechanism for extended time periods even after the light source has been turned off. This characteristic result in high monomer conversion contributing to improved final properties [31].

Instead, thiol-ene "click" reactions follow the step-growth mechanism [40]. The "click" features discovered by Sharpless *et al.* refer to quantitative yield, stereospecific and orthogonal which provide the 1:1 reaction between ene and thiol functional groups [41]. Furthermore, the orthogonality of thiol-ene chemistry makes a selective reaction of thiol and ene functional groups with no interferences with other functional groups. This selectivity allows for the sequential or simultaneous execution of multiple reactions, providing flexibility in designing complex chemical transformations, valuable tool in various applications, such as material science, bioconjugation, and polymer synthesis [42]. In this configuration, when a PI generates radicals upon exposure to UV-light, it can start the curing process. Indeed, a thiyl radical is formed by abstraction of a hydrogen atom from the thiol group via the radical intermediate. Subsequently, this thiyl radical can react with the C=C double bond, leading to the formation of a thioether bond and the generation of a carbon-centered radical. This carbon-centered radical is then capable of interacting with a second thiol-functional molecule through a chain transfer mechanism, providing a thiol-ene addition product and contemporary giving rise to a new thiyl radical [40,43,44].

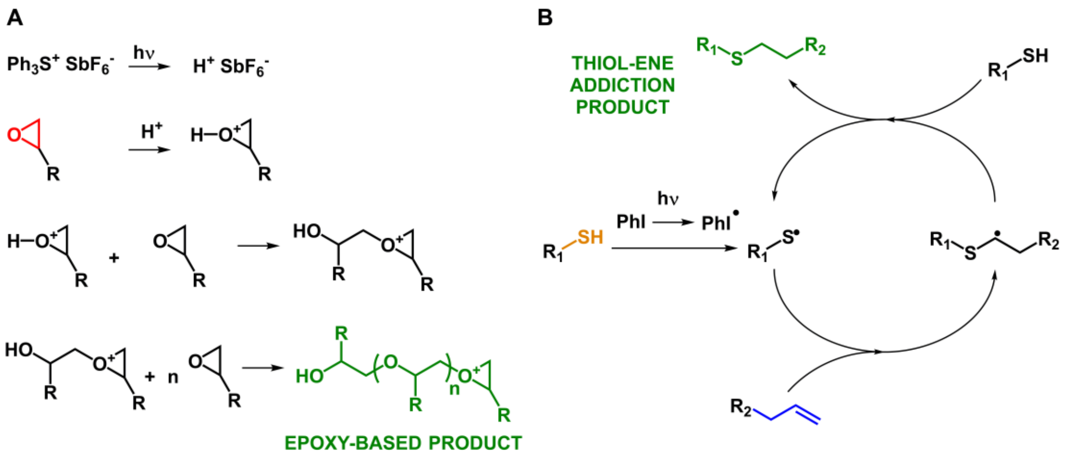

Figure 2.4. (A) UV-activated cationic curing of epoxy monomer with sulfonium-based cationic Phi; (B) UV-activated mechanism of thiol-ene "click" chemistry with a generic radical PI.

2.4. Monomers for UV-curing

Part of the work described in this chapter has been already published and it is available at the references:

[45] **Pezzana, L.**; Malmström, E.; Johansson, M.; Sangermano, M. UV-Curable Bio-Based Polymers Derived from Industrial Pulp and Paper Processes. *Polymers.* **2021**, 13 (9), 1530. DOI: https://doi.org/10.3390/polym13091530.

[46] **Pezzana, L.**; Melilli, G.; Guigo, N.; Sbirrazzuoli, N.; Sangermano, M. Photopolymerization of furan-based monomers: Exploiting UV-light for a new age of green polymers. *React. Funct. Polym.* **2023**, 185, 105540. DOI: https://doi.org/10.1016/j.reactfunctpolym.2023.105540.

Sustainability is a complex concept which also embraces several socio-economic aspects of the society. In the previous paragraphs, the efficiency and the benefits of UV-curing were highlighted, underling the energy- and cost-savings of this techniques. Here, the focus change toward the polymers which can be used for developing new materials or for substituting the existing materials. Remarkably, the choice of moving in different direction needs to create benefits for the industry and for the environment thus it is very important investigate where and when the advantages are present. The synergy between technologies and materials is tremendously important to be able to achieve valuable results.

Over the past decades, the majority of the commercial available polymeric resins for UV-curing was derived from petroleum-based resources, with a predominant role of acrylate- and epoxy-based ones due to the high reactivity and good performance retrieved from their usage [31,39,47,48]. However, due to the concern about climate change and depletion of fossil fuels, new bio-based polymer are becoming increasingly explored for UV-curing. Natural resources contribute to a vast array of monomer and polymer which can be used to substitute fossil-based one [11]. The interesting multiple, distinct and unique structures of natural polymers make them appeal for functionalization and modification to meet the requirements of several applications [49]. The large availability of biomass, either from forestry [50], agriculture or side stream of food chains or industries [51–53], is a crucial factor for the competitiveness with respect to the well-established fossil-based polymer resins. Recent works highlights the increasing exploitation of bio-based monomer in UV-curing field [54–58]. Vanillin [59–61], furan monomers [62], vegetable oils [56], isosorbide [63,64], starch [65], lignin [66] are only some of the potential actor in this interesting field.

Lignin has been used both as filler in UV-curable resins [67,68] and, after modification, as reactive acrylate- or methacrylate-monomer for 3D printing applications [66,69,70]. Vanillin has been also employed to developed UV-curable resin for 3D printing application in the field of stereolithography (SLA) [60,71] or digital light processing (DLP) [72]. Moreover, other tree-based polymer platforms can be exploited for UV-curable resins, such as rosins and terpenes [73]. Rosins, component of the conifer tree resin, has been exploited for coating applications [74], or adhesives [75,76]. Instead terpenes, molecules synthesized by plants and fungi [77], has been firstly studied by Crivello, which in-depth studies of their reactivity towards UV-light [78–80]. Then, some attractive structures has been used for UV-curing. Limonene is one example, investigated in thermosetting resin employing thiol-ene UV-curing [57,81]. This interesting molecule has been also used for 3D printing [82,83]. **Figure 2.5** reports the chemical structure of the monomer derived as side stream from pulp and paper industry (Paper I) which can be exploited for UV-curing increasing the add value of the by-products [45]. Another class of polymer under intensive examination are based on furans. Furan monomers, derivatives of cellulose [84], are an interesting class of molecules which can be functionalized and used for several purposes, from thermoplastic applications, substituting polyethylene terephthalate (PET) [85–87], being a versatile building block for polyester [88], to UV-curable resins as presented in latest reviews [46]. **Figure 2.5** highlights the different possibilities to use furan-based monomers in UV-curing (Paper II).

Driven by these fascinating results about the use of bio-based monomers for UV-curing, the work of this thesis has been focused on exploiting some of the available monomers to develop new UV-curable resins aiming to embrace the sustainability concept. The following chapter will be divided according to the UV-curing mechanism used to achieve the formation of the polymer materials. Specifically, the **Chapter 3** will be devoted to the cationic UV-curing and the progress done using several bio-based monomers spreading from coating applications to 3D printing. An Analogous debate can be applied to **Chapter 4**, where bio-based thiol-ene UV-curable resins are formulated and investigate for UV-curing. Also in this case, several applications has been covered pointing out the benefits and the performance of these new bio-based resins.

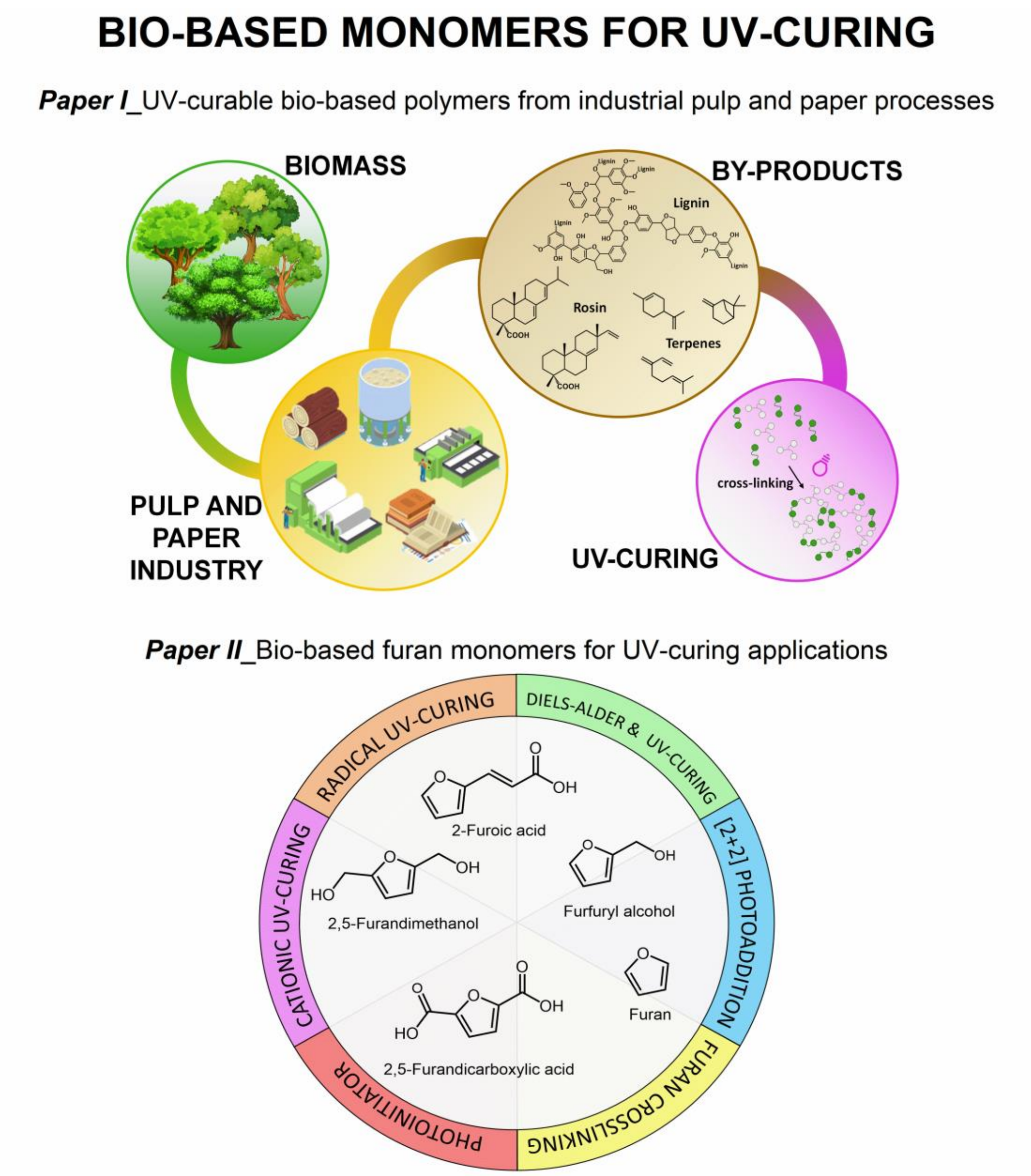

Figure 2.5. Chemical structure of the bio-based monomers derived from pulp and paper industry (Paper I) and furan-based monomers used in UV-curing (Paper II).

3. Cationic UV-curing of epoxy bio-based monomers

Cationic UV-curing is a significant technique employed to transform liquid resin into thermoset materials. Epoxy-based monomers represent the main class of chemical employed in the field. Indeed, the global market settled around 3.6 million tons in 2022 with a forecast of CARG growth of 3.4 % until 2028 [89]. Paints and coatings dominate the epoxy market ranging from automotive field to construction. Furthermore, the increasing demand of light weigh high performance materials for wind power, solar, and aerospace industry are driving demand for epoxy resins [89,90]. Utilizing diverse bio-resources allows for sustainable transition maintaining a broad spectrum of final properties, tailored to specific material requirements. This chapter showcases the outcomes obtained from employing various bio-based monomers in cationic UV-curing processes. By examining different aspects, we underscore the importance of each step in the process, as they collectively contribute to forging a new path towards sustainability.

The different studies in this thesis (**Figure 3.1**) aim to emphasize the importance and effectiveness of using bio-based monomers instead of fossil-based ones to achieve essential properties. This begins with the synthesis of appropriate monomers for curing, followed by an investigation into the optimization of the UV-curing process. Additionally, the final properties will be tailored to meet various requirements, which contribute to the successful substitution of fossil-based monomers with bio-based alternatives. This approach is helpful in achieving crucial properties while promoting sustainability. The first part of the chapter is related to the exploitation of the furan monomers in the context of cationic UV-curing exploring different prospectives (Paper I, Paper II, and Paper III). Then a brief section is dedicated to the investigation of other important bio derived compounds which has been exploited in cationic UV-curing (Paper IV, Paper V, and Paper VI). The research focused on ferulic acid, isosorbide, and epoxy vegetable oils highlighting different possible applications.

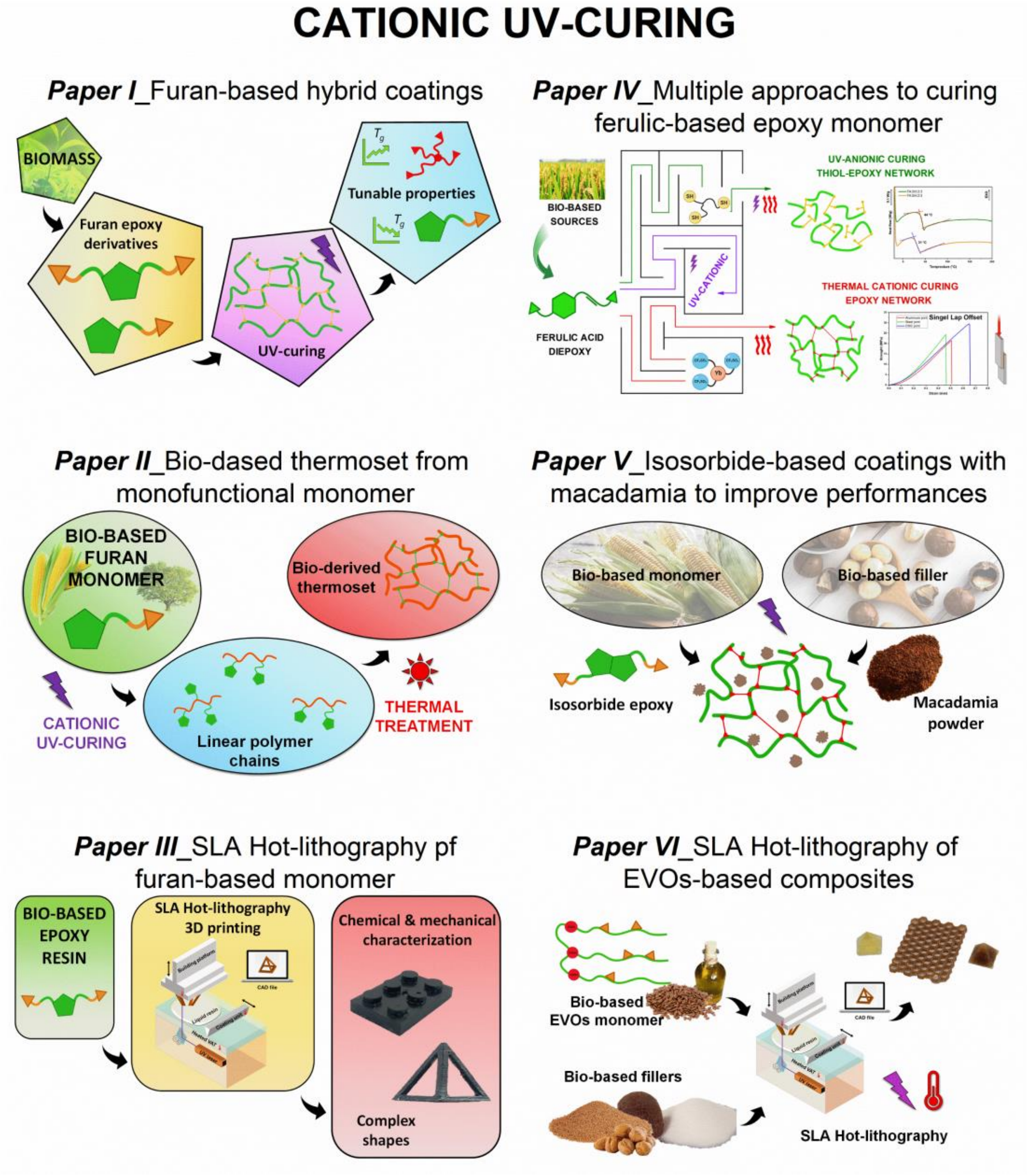

Figure 3.1. Schematic representation of the subjects addressed in the different paper about the UV-cationic curing discussed in the thesis.

3.1. Why furan-based monomers are used for UV-curing?

Furanic compounds are derived from carbohydrate biomass, specifically from hexose and pentose units [84,91,92]. They are originated from cellulose and hemicellulose which are the main components of the biomass along with lignin [45,50]. Furan represent a valid alternative to petroleum-based monomers due to the large availability of the raw materials [93,94]. Indeed, side streams of industry, such as forestry or agricultural, and food chain can be exploited to derive furan compounds. Thus, the interest in these products has been grown in the last decades due to the world-wide availability of the raw source and the low cost [10].

Furfural and hydroxymethyl furfural are the main platform to produce a wide range of monomers as presented in **Figure 3.2**. The process behind the synthesis of furfural and hydroxymethyl furfural is well known and it is based on the acid-catalyzed hydrolytic depolymerization of hemicellulose [95–97]. C5- and C6-glycosidic units are dehydrated creating the base platform for furan monomers [98]. The increasing demand for various furfural derivatives across multiple industries and the growing interest in environmentally friendly manufacturing processes are driving the furfural market. The market size for furfural is expected to reach 700 $ million by 2024, observing growth from 551 $ million in 2019. Globally, furfural production can range from 300 to 700 ktons annually. Notably, China stands out as the largest producer, accounting for 70% of the total production, with an annual output of approximately 200 ktons [99].

Furfuryl alcohol (FA) represent the mostly produced monomer and it has been used for fuel, fine chemicals and biobased polymers [100]. Interestingly, FA has been used for polyurethanes, polyesters, and it has been used to substitute phenolic resins [101–103] . Moreover, FA has been intensely investigated due to its intrinsic self-condensation reaction which generates polyfurfuryl alcohol (PFA) thermosetting resin leading to vast range of capabilities and fascinating properties [104,105].

Another deeply investigated monomer is 2,5-furandicarboxylic acid (FDCA) because of its interesting chemical structure which make it appreciable to substitute terephthalic acid for the synthesis of greener polyethylene terephthalate (PET) called poly(ethylene 2,5-furandicarboxylate) (PEF) [86,88,106]. This bio-based polymer can compete with traditional PET regarding price, performance as well as sustainability issues [107].

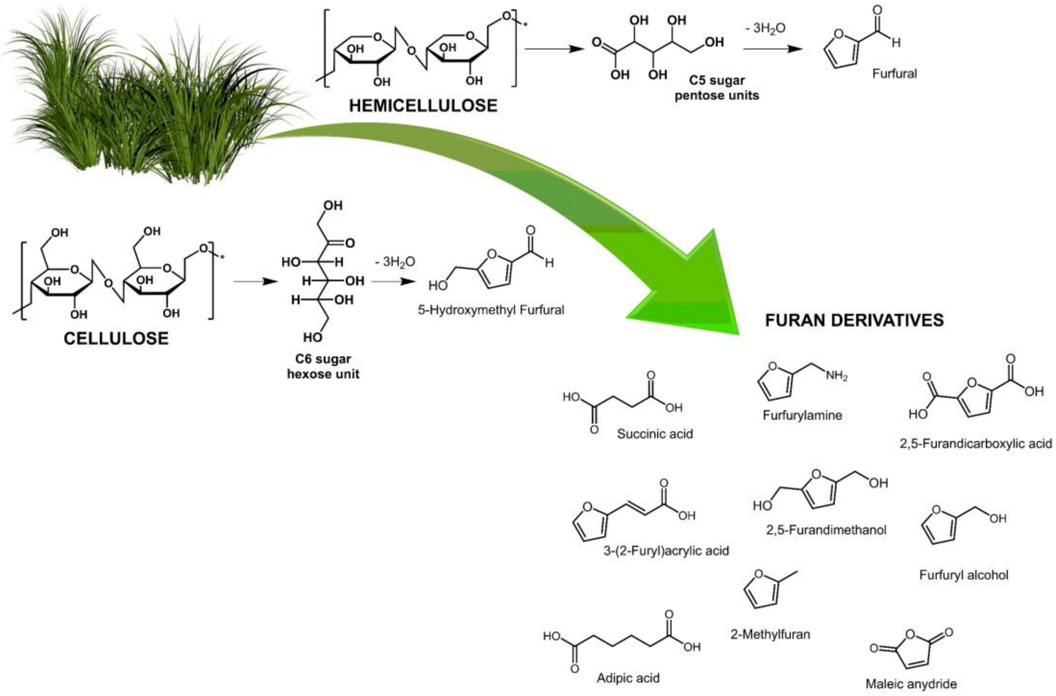

Figure 3.2. Furan derivatives from hemicellulose and cellulose: pentose- and hexose- sugar units as resources to produce furfural and 5-hydroxymethylfurfural as furan-based chemical platforms.

The bifunctional furan-based alcohol 2,5-furandimethanol (FDM) has been investigated to develop coatings by thermal curing with different properties [108]. Among several properties, the addition of titania as filler gave anticorrosive effect to the coatings [109].

Considering the actual level of concern about the implementation of green resources to substitute fossil-based material, the conducted study aims to cover this gap [10,13,110]. Few studies has been reported in literature for cationic photopolymerization of furan monomer for coating applications. Cho et al. [111] successfully synthesized three epoxy furan-based monomers, derived from furfuryl alcohol and 2,5-furandimethanol (two were bifunctional, containing one or two furan units, while the third was a monofunctional furan epoxy). The primary objective of their study was to assess the suitability of these epoxy furan resins as adhesives. Remarkably, the results indicated that the furan-based resins exhibited superior performance compared to a commercial phenyl glycidyl ether adhesive in terms of shear strength. An additional furan-based monomer, FDCA, was employed to create an epoxy thermoset [62]. The derived epoxy furan was combined with epoxy linseed oil to produce an eco-friendly thermoset material. Notably, the study highlighted the possibility of achieving structure-property control, leveraging the significantly different characteristics of the triglyceride monomers.

Due to the lack of in-depth investigation of furan-based monomer for UV-curing, the aim of this part of the thesis is to investigate the UV-cationic curing of these to increase the portfolio of possible exploitable bio-based monomer. Three different investigations exploiting epoxy furan-based monomers have been proposed in the UV-field. Firstly, the bifunctional epoxy furan monomer derived from 2,5-furandimethanol has been investigated in the UV-curing facing the customization of the final properties of the coating. Specifically, hybrid network was generated and characterized. Then an interesting cross-linking of monofunctional furan derivative was carried out highlighting the effect of chemical bonding and the final properties of the thermoset. Lastly, the 3D printing of a furan resin was carried out employing Hot-lithography SLA process. A deep investigation of the reactivity and final properties of 3D printed object was performed.

Parts of the work described in this chapter have already published and it is available in the following references:

[112] **Pezzana, L.**; Melilli, G.; Guigo, N.; Sbirrazzuoli, N.; Sangermano, M. Cationic UV Curing of Bioderived Epoxy Furan-Based Coatings: Tailoring the Final Properties by In Situ Formation of Hybrid Network and Addition of Monofunctional Monomer. *ACS Sustainable Chem. Eng.* **2021** 9 (51), 17403-17412 DOI: 10.1021/acssuschemeng.1c06939

[113] **Pezzana, L.**; Melilli, G.; Guigo, N.; Sbirrazzuoli, N.; Sangermano, M. Cross-Linking of Biobased Monofunctional Furan Epoxy Monomer by Two Steps Process, UV Irradiation and Thermal Treatment. *Macromol. Chem. Phys.* **2023**, 224, 2200012 DOI: https://doi.org/10.1002/macp.202200012

[114] **Pezzana, L.**; Wolff, R.; Melilli, G.; Guigo, N.; Sbirrazzuoli, N.; Stampfl J.; Liska, R.; Sangermano, M. Hot-lithography 3D printing of biobased epoxy resins. *Polymer* **2022**, 254, 12507. DOI: https://doi.org/10.1016/j.polymer.2022.125097

3.1.1. Experimental section

3.1.1.1. Material and Chemicals

2,5-Furandimethanol, FDM (purity 97 %), was supplied by Apollo Scientific; furfuryl alcohol, FA (purity 98 %), epichlorohydrin, ECH (purity >99 %), sodium hydroxide, NaOH, tetrabutylammoium hydrogenosulphate, TBHS (purity 97 %), magnesium sulphate, $MgSO_4$, were purchased from Sigma Aldrich. Tetrahydrofuran, THF, ethyl acetate, EtOAC, and acetonitrile were supplied by Carlo Erba. Resocinol diglycidyl ether, RDE, was supplied by Nagase ChemteX as DENACOL EX-201 while 1,4-cyclohexanendimethanol diglycidyl ether, CDE, was obtained by UPPC as Polyprox R11. m, was supplied by Sigma Aldrich. The photoinitiator used were triarylsulfonium hexafluoroantimoniate, S-SbF6, mixed in propylene carbonate 50 wt% supplied from Sigma Aldrich, and p-(octyloxyphenyl)phenyl iodonium hexafluoroantimoniate, I-SbF6, purchased from ABCR. NMR analysis was performed with deuterate chloroform, $CDCl_3$, provided by Sigma Aldrich.

3.1.1.2. Procedures

3.1.1.2.1. Epoxidation of 2,5-furandimethanol

The synthesis of the furandimethanol diglycidyl ether (FDE) was carried out following previous protocols reported in literature [108,111]. The etherification reaction is reported in **Figure 3.3**. Epichlorohydrin (55.6 g, 600 mmol) was poured into a three neck round bottom flask. Then a solution of NaOH 50 wt% (20.6 g, 520 mmol) was added with the TBHS (1.38 g, 4.06 mmol) which was used as transfer catalyst. The solution was stirred for 30 min at room temperature, meanwhile nitrogen atmosphere was provided to the system. FDM (5.5 g, 43 mmol) was dissolved in THF (40 mL) and then added dropwise to the reaction. The reaction was left for 2 h at 50 °C. The reaction was stopped by adding ice water into the mixture. The product was extracted with ethyl acetate and dried over MgSO4. The crude was purified by vacuum distillation and left in a vacuum oven (35 °C for 24 h) to give brownish viscous liquid (9.3 g, yield 90 %). The characterization was carried out by NMR:

^{1}H-NMR (400 MHz, $CDCl_3$) δ 6.29 (s, 1H), 4.57 – 4.42 (m, 2H), 3.76 (dd, J = 11.5, 3.1 Hz, 1H), 3.44 (dd, J = 11.5, 5.8 Hz, 1H), 3.16 (ddt, J = 5.8, 4.1, 2.9 Hz, 1H), 2.79 (dd, J = 5.0, 4.1 Hz, 1H), 2.61 (dd, J = 5.0, 2.7 Hz, 1H).

^{13}C-NMR (101 MHz, $CDCl_3$) δ 151.94, 110.45, 70.85, 65.32, 50.86, 44.45.

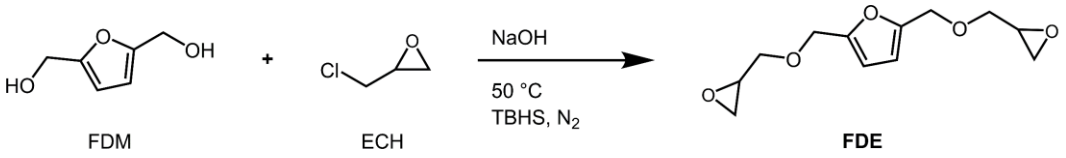

Figure 3.3. Epoxidation of 2,5-furandimethanol (FDM).

3.1.1.2.2. Epoxidation of furfuryl alcohol

The synthesis of glycidyl furfuryl alcohol (FGE) was performed on the basis of previous protocol reported in literature [111,115]. The etherification reaction is reported in **Figure 3.4**. Epichlorohydrin (56.6 g, 610 mmol) was poured into a three round bottom flask; a solution of NaOH 50 wt% (22.4 g, 560 mmol) was added with the TBHS (0.66 g, 2 mmol) was used as transfer catalyst. The solution was stirred for 30 min at room temperature, and nitrogen atmosphere was provided to the system. Furfuryl alcohol (20.0 g, 200 mmol) was slowly added, and the reaction was left for 24 h at 50 °C. The reaction was stopped by adding ice water into the mixture. The product was extracted with ethyl acetate and dried over MgSO4. The solvent was eliminated by vacuum distillation and the crude was left for 24 h in a vacuum oven (35 °C) to give yellowish liquid (25.0 g, yield 81 %). The ^{1}H-NMR and ^{13}C-NMR spectra give the following signals:

^{1}H-NMR (400 MHz, $CDCl_3$) δ 7.41 (t, J = 1.3 Hz, 1H), 6.34 (d, J = 1.6 Hz, 2H), 4.59 – 4.42 (m, 2H), 3.75 (dd, J = 11.5, 3.1 Hz, 1H), 3.44 (dd, J = 11.5, 5.8 Hz, 1H), 3.16 (ddt, J = 5.8, 4.2, 2.9 Hz, 1H), 2.79 (dd, J = 5.0, 4.1 Hz, 1H), 2.61 (dd, J = 5.0, 2.7 Hz, 1H).

^{13}C-NMR (101 MHz, $CDCl_3$) δ 151.39, 142.95, 110.31, 109.60, 70.59, 65.07, 50.74, 44.34.

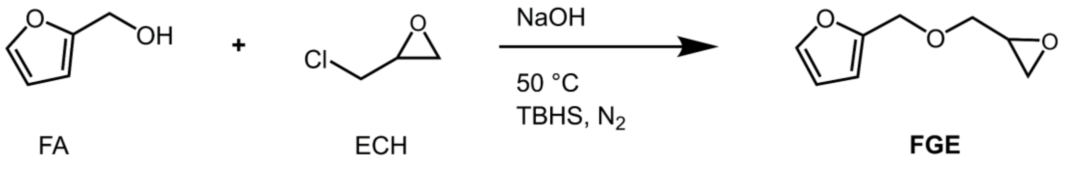

Figure 3.4. Etherification reaction of furfuryl alcohol (FA) by reaction with epichlorohydrin.

3.1.1.2.3. Photopolymerization of FDE

Firstly, the reactivity of FDE as bifunctional epoxy resin for cationic UV-curing was investigated. The bifunctional monomer (usually ~ 0.4 g) was poured into a brown vial to avoid light contact and then the photoinitiator was added as 2 parts per hundred resin (phr). The formulation was mixed by magnetic stirring for 5 min then the different studied were carried out by UV-curing the formulation on glass substrate or into silicon mold. The photocuring was conducted by exposing the formulation to UV-light for two minutes. DYMAX Flood lamp was used as UV-light source with light intensity set around 130 mW/cm^2 (total dose of 15.6 J/cm^2).

The tailoring of the properties aiming to a different mechanical response was performed modifying the pristine formulation in two distinct ways; firstly, by addition of monofunctional epoxy monomer (FGE) and then by addition of tetraethyl orthosilicate (TEOS). The weight ratio between bifunctional and monofunctional monomer was varied from 0:100 to 30:70 while TEOS was added in 30 and 50 phr with respect to the FDE as listed in **Table 3.1**. The S-SbF6 was added in 2 phr with respect to the total amount of the resin in case of FDE/FGE formulations. On the other way, for the formulation containing TEOS, the S-SbF6 was added with respect to the reactive bi-functional monomer to keep the same molar ratio as the pristine formulation. The formulations were mixed by magnetic stirring and UV-cured as previously described by DYMAX exposure. Considering the formulation containing TEOS, the films were further annealed at 150 °C for 4 hours under humid condition (by means of water bath inside the oven).

Table 3.1. Different formulations produced to tailor the properties of FDE. The photoinitiator (PI) used was S-SbF6.

FORMULATION	FDE/FGE	TEOS	PI
	(weight ratio)	(phr)	(phr)
FDE	100/0	-	2
90/10 FDE/FGE	90/10	-	2
80/20 FDE/FGE	80/20	-	2
70/30 FDE/FGE	70/30	-	2
FDE + 30 TEOS	100/0	30	2
FDE + 50 TEOS	100/0	50	2

3.1.1.2.4. Photopolymerization and thermal cross-linking of FGE

The monofunctional monomer FGE was poured into a brown vial and then the photoinitiator, S-SbF6, was added (2 phr). The formulation was mixed mechanically for 5 min. The irradiation step was carried out by exposing the formulation to UV-light for two minutes by DYMAX Flood lamp with total energy dose around 15.6 J/cm^2. After the thermal treatment of the photocured films was conducted in an oven at 160 °C for 1 hour.

3.1.1.2.6. Formulations and 3D printing Hot-lithography SLA

The Hot-lithography was carried out for three different epoxy resins, FDE, RDE and CDE. The epoxy resins were added with 3 wt% of the photoinitiator I-SbF6. Then the formulations were mixed and left in ultrasound bath until the complete dissolution of the photoinitiator. The formulations were handled in brownish vials in order to avoid light contact and the photoinitiator was weighted in an orange room. The formulations were tested and used for the 3D printing. The SLA 3D printer used in this work was a Caligma 200 UV prototype developed by Cubicure (Vienna, Austria) with a bottom exposure SLA setup. The different components of the printer, specifically the vat, the building platform, and the coating unit were heated up to 80 °C. The laser emitted at a wavelength of 375 nm with power of 70 mW/mm^2, while the laser spot diameter was set at 25 μm during printing. The laser beam is scanned over a 2-dimensional plane using a galvanometer scanning system; the laser speed was set at 100 mm/s and the layer thickness of the resins was 100 μm. The different specimens (for DMTA and tensile tests) of each formulation were printed in the same conditions to be able to compare the results. The CAD file of the different object was transferred in the .cli extension to be read by the 3D printer software.

3.1.1.3. Characterization

Nuclear magnetic resonance (NMR)

NMR analysis was conducted on a Bruker AM 400 MHz. $CDCl_3$ was used as solvent and internal reference for the chemical shift given in ppm. ^{1}H-NMR was recorded at 400 MHz while ^{13}C-NMR was at 101 MHz.

Fourier transform infrared spectroscopy (FTIR)

The epoxy ring opening was followed by means of real-time FTIR analysis. A Nicolet iS 50 spectrometer was used in transmittance mode to record the data. The sample was spread on Si wafer by film bar guaranteeing a thickness of 32 μm. The conversion curves were collected by spectral resolution of 4 cm^{-1}. The epoxy band of FDE and FGE was monitored at 897 cm^{-1} and 854 cm^{-1} and the spectra were normalized by the peak at 1550 cm^{-1} which was considered unaffected by UV-curing. Equation 3.1 was used to evaluate the conversion.

$$Conversion = \frac{\left(\frac{A_{897}}{A_{1550}}\right)_{t=0} - \left(\frac{A_{897}}{A_{1550}}\right)_{t}}{\left(\frac{A_{897}}{A_{1550}}\right)_{t=0}} \qquad \text{Equation 3.1}$$

Regarding the thermal treated sample of FGE, some FTIR analysis were carried out in non-isothermal condition. In this case, a Thermo Fischer IS-20 spectrometer equipped with a hot-plate GladiATR device (Pike Technologies) with a monolithic diamond in ATR configuration. The spectra were recorder each 10 °C from 30 to 180 °C with a resolution of 4 cm^{-1}. 64 scans were recorded for each temperature. All the FTIR data were handled with the software Omnic from Thermo Fisher Scientific.

Real time near infrared (NIR)/photorheology

The kinetics of the ring opening reaction for 3D printing was evaluated by means of a real time NIR/photorheometer instrument. This prototype is able to in situ monitored chemical and mechanical features during the curing reaction [116]. A Bruker Vertex 80 FTIR spectrometer, equipped with interchangeable NIR optics, a rapid scan module was coupled with an Anton Paar MCR302 WESP rheometer. The bottom plate of the photorheometer was a borosilicate disk to ensure the irradiation of the UV-light on the sample. The source for initiating photopolymerization reactions was UV-light projected via a waveguide on the surface of the sample through the bottom window using an Exfo OmniCure 2000 light source with a broadband Hg-lamp (320-500 nm). The intensity was set around 60 mW/cm^2 at the contact with the sample. The calibration was done by means of Ocean Optics USB 2000+spectrometer. The rheometer was set as plate-plate geometry with a steel accessory with diameter of 25 mm (PP25). The thickness of the layer was set as 200 μm corresponding about 150 μL of resin. The tests were performed at different temperature: 25, 50 and 80 °C. The temperature can be controlled by Peltier elements located around the window holder in the temperature control system (Anton Paar P-PTD200/GL). Additional heating from above by an external Peltier-controlled hood was employed for experiments at elevated temperatures (H-PTD 200 from Anton Paar). The measurements were performed in triplicate to have reproducible data. The epoxy conversion was evaluated by integrating the band peak at 4530 cm^{-1}; the rubber band correction and interactions to normalize the peak were used to evaluate the final conversion. OPUS 7.0 and RheoCompass 1.24 respectively for NIR data and rheological data were used to analyze the results.

Differential scanning calorimetry (DSC)

The UV-curing process was followed by means of photo-DSC measurement conducted on a Netzsch DSC 204 F1 with autosampler. The tests were performed in isothermal condition at different temperatures, at 25, 50 and 80 °C under a constant flow of N_2 atmosphere (20 mL/min). The resins (10-15 mg) were irradiated twice with filtered UV-light (320−500 nm) via an Exfo OmniCureTM series 2000 broadband Hg lamp. The light intensity was set around to 20 mW/cm^2 on the surface of the sample. The heat flow of the polymerization reaction was recorded as a function of time. The correction of the measure was done by subtracting the first curve derived from the first irradiation to the one derived from the second cycle. The important parameters detected through this analysis were: the time of which the maximum of heat evolution was reached (t_{max}), the height of the exothermic peaks (h), and the total enthalpy (ΔH), evaluated as the integration of the curing peak. All measurements were performed in triplicate with satisfactory reproducibility.

The DSC analysis was performed to determine the T_g of the different thermoset and to characterize the thermal isocuring of FGE. The testes were done on a Mettler Toledo DSC-1 equipped with Gas Controller GC100. The data were analyzed with Mettler Toledo STARe software V9.2. Samples of about 5-10 mg were sealed in 40 µl aluminum pans and analyzed by DSC.

The T_g of the hybrid coating was analyzed with the following method: the first heating went from room temperature (r.t.) to 100 °C; then the temperature was maintained at 100 °C for 2 min in order to stabilize the sample, after that the chamber was cooled until -20 °C was reached and then this temperature was maintained for 10 min, finally was a second heating from -20 °C to 300 °C applied. The first heating was done in order to eliminate the thermal history of the polymers. The heating and the cooling rates were set at 10 °C/min and the analysis was performed in a N_2 atmosphere with a flow rate of 40 mL/min.

Instead considering the UV-irradiated FGE samples and the UV-irradiated + thermal treated samples, the DSC was performed in a different way. The samples were analyzed applying the following method: the first dynamic stage was set from room temperature to -60 °C, then 5 minutes of stabilization were set; the first heating was then performed from -60 °C to 240 °C; then the temperature was decreased again to -60 °C and a final heating step was performed until 300 °C. The heating and the cooling rates were the same for all dynamic stage and were set at

10 °C/min. The analysis was performed in a N_2 atmosphere with a flow rate of 40 mL/min.

The thermal curing step was studied by means of DSC analysis on UV-irradiated samples. An isocuring stage was performed to evaluate the heat released during the curing. The characteristics of the tests were the following: one hour at different temperatures, 100 °C, 120 °C, 140°C, 160 °C, 170 °C and 180 °C in a constant N_2 flow of 40 mL/min.

Simultaneous thermogravimetry–differential scanning calorimetry (STA)

The resins investigated in the 3D printing were tested by means of STA 449F1 Jupiter from Netzsch in order to evaluate the UV-curing stage and the start of the degradation. The samples around 15 mg were placed into aluminum pan and sealed. The test was performed in controlled atmosphere of N_2 with 20 mL/min flow. The temperature ramp was set with an increase of 10 °C/min from r.t. to 300 °C; after the samples were cooled down to r.t. with 20 °C/min. The data of weight loss and heat flow were analyzed by NETZSCH-Proteus-80.

Stability test

The stability test was done by means of viscosity measurements of the formulation for 3D printing. An Antoon Paar MCR300 was used to examine the viscosity of the epoxy resins through the time. A cone-plate geometry was chosen, and the diameter of the support was 25 mm. The distance between the cone and the plate was 0.048 mm and 15-20 μL of resin was used to perform the analysis. The test was run at 80 °C and the formulation were prepared using 3 wt% of photoinitiator and then kept in the oven at 80 °C for all time of the investigation. The viscosity was measured by applying an increase shear stress from 1 to 100 1/s and the final value was the average of 5 points at 100 1/s.

Elecrospray-Mass spectrometry (ESI/MS)

The molecular weight of the linear polymer chains derived from FGE was evaluated by means of mass spectrometry. The UV-irradiated samples were dissolved in $CHCl_3$ and then they were solubilized in acetonitrile, the solvent used for the test. The solution was introduced into a classic (LCQ) quadrupole ion trap (Thermo Scientific, San Jose, CA, USA) equipped with an electrospray source. The spectra were acquired in the range m/z 200-800 in the positive mode. The electrospray source and ion trap were operated under the following conditions: flow rate, 5 μLmin^{-1}, electrospray ionization voltage, 4.5–5 kV. The ESI-MS technique uses a soft ionization process that does not fragment compounds and provides molecular weight information with unit mass resolution.

Gel content

The gel content percentage (% gel) of the polymers was determined by measuring the weight loss after 24 h extraction with chloroform. The samples after the immersion were allowed to dry for 24 h in air. % gel was calculated according to Equation 3.2.

$$\% \, gel = \frac{W_{\mathrm{f}}}{W_{\mathrm{i}}} * 100 \qquad \text{Equation 3.2}$$

Where W_f is the weight of the dry film after the treatment with chloroform and W_i is the weight of the dry sample before the treatment.

Dynamic mechanical thermal analysis (DMTA)

The thermal mechanical analysis of the thermoset derived from FDE and FGE was carried out with a Triton Technology instrument. The instrument applied uniaxial tensile stress at frequency of 1 Hz with a heating rate of 3 °C/min. The initial temperature of – 40 °C was achieved by cooling down the test chamber with liquid nitrogen. The samples were UV-irradiated in rectangular silicon mold with dimensions of 12×4×0.3 mm^3.

The samples derived from 3D printing were tested by means of an Anton Paar MCR 301 device with a CTD 450 oven and an SRF 12 measuring system. The 3D printed DMTA samples at 80 °C were tested in torsion mode with a frequency of 1 Hz and a strain of 0.1 %. The dimensions were 40×4×2 mm^3. The temperature was increased from −25 to 300 °C with a heating rate of 2 °C/min.

The measurements were done to detect the T_g as maximum of *Tan δ* curve and were stopped after the rubbery plateau. *Tan δ* is the loss factor, thus the ratio between the loss modulus (E'') and storage modulus (E'). The DMTA analysis allowed the evaluation of the cross-link density (v_c) calculated by Equation 3.3 derived from the statistical theory of rubber elasticity [117,118].

$$v_c = \frac{E'}{3RT} \qquad \text{Equation 3.3}$$

Where E' is the storage modulus in the rubbery plateau (T_g + 50 °C), R is the gas constant and T is the T_g expressed in Kelvin.

Tensile test

The tensile test of the 3D printed dog bone samples was performed by means of Zwick Z050 equipped with a 1 kN load cell (Zwick Roell, Ulm, Germany) according to ISO 527 with a test speed of 5 mm/min. The shape of the specimens was a type 5B and five samples for each formulation were tested. The printing was done at 80 °C for all specimens. The stress-strain curves were recorded and analyzed via testXpert II testing software. The Young's modulus (E) was evaluated in the linear portion of the stress-strain curve from the start of the test. The toughness (U) was calculated as the area under the stress-strain curve. Moreover, strength at break (σ) and strain (ε) were retrieved from the curves.

Thermogravimetric analysis (TGA)

The thermal stability of the coatings was studied by means of a Mettler Toledo TGA1. The test was done imposing a heating ramp of 10 °C/min from r.t. to 700 °C under N_2 atmosphere with flow of 40 mL/min. The analysis was done considering different features: T_5, temperature at which the sample lost 5 wt%; T_{peak}, temperature at peak of degradation, evaluated as peak of the first derivative, and *Char*, analyzed as final char residue in wt%.

Contact angle and pencil hardness

The hybrid coating were characterized by means of contact angle and pencil hardness tests. The films were beforehand photocured on glass substrate with a thickness of 150 μm. The contact angle test was performed with Drop Shape Analyzer, DSA100, Krüss. The water droplets were placed on free surface films and the results were an average value of at least 5 different droplets. The pencil hardness was measured according to the standard ASTM D3363. For the hardness different pencils were used from 8 B to 8 H. The hardness value was defined as the last pencil (in order of hardness) which did not make a scratch on the film surface.

Morphology

The microstructure of the hybrid material was investigated by scanning electron microscopy (FESEM, Zeiss SUPRA 40). The cross-section of the coating was realized by cryofracture. The coating was deep in liquid nitrogen for at least 5 minutes to ensure the cool down of the sample far below the glass transition. The surface of the fracture was coated with a Pt layer at a thickness of 5 nm. This inhibited charging, reduced thermal damage and improved the secondary electron signal required for the topographic examination.

Instead, the overview to observe morphology of the 3D printed samples was recorded by a Leitz Laborlux 12 Me S. The imagines were taken with 5× and 10× magnification to visualize the 3D printed layer.

3.1.2. Result and discussion

3.1.2.1. Synthesis route and characterization of furan epoxies

The furan monomers, 2,5-furandimethanol and furfuryl alcohol, were used as platform chemicals to develop photocurable epoxies. The etherification reaction was carried out by reacting the alcohol functional group bearing on the furan monomers with epichlorohydrin (ECH) in a one-step reaction. The reaction is already known in literature [111] and it allows to reach high conversion and very high purity of the final product. Indeed, the synthesis of FGE reached 90 % yield in only four hours. Furthermore, the relatively low reaction temperature (50 °C) and the easy purification step, which did not involve large amount of solvent, are interesting advantages for industrial production in terms of energy and cost saving. However, the involving of ECH as epoxidation reagent could represent a limitation in green level of the entire process [119], nevertheless at this moment this reagent is crucial to achieve the epoxidation of several monomers [120–122]. Future studies could be performed to avoid the hazardous ECH, scouting for greener processes to increase the sustainability of this established class of monomers [123–125]. An example of green process could involve the use of H_2O_2 as epoxidation agent [126].

The characterization of the final products was performed by ^{1}H-NMR highlighting the presence of the epoxy peak in the region between 2 and 3 ppm for FDE and FGE as presented in **Figure 3.5**. ^{13}C-NMR was performed to corroborate the proton NMR data confirming the epoxy functionalization.

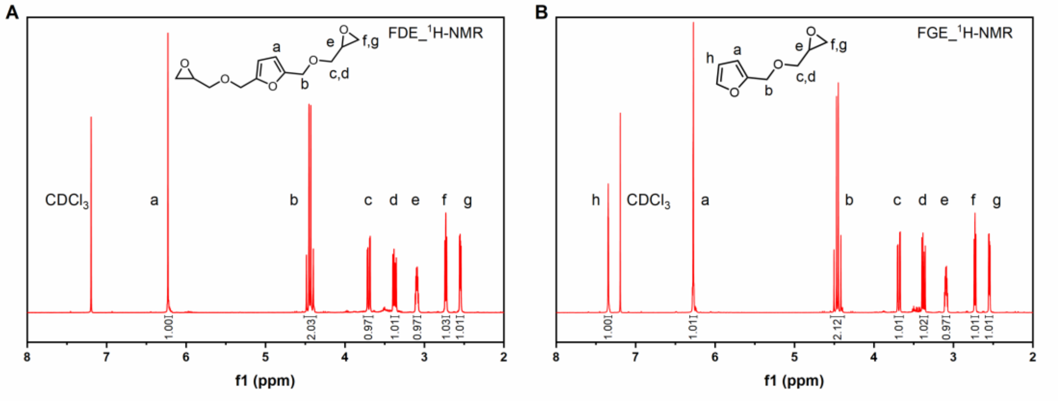

Figure 3.5. (A) ^{1}H-NMR of FDE and (B) ^{1}H-NMR of FGE in CDCl$_3$ as internal reference and solvent.

3.1.2.2. Furan-based hybrid coating

The bifunctional epoxy furan-based monomer (FDE) was investigated as the main component for an UV-curable formulation to verify the possibility of network formation achieving the prospect of coating application. The UV-curing process was studied by means of real-time FTIR. The technique allowed to follow the epoxy bands located at 897 and 854 cm^{-1} during the curing [127]. **Figure 3.6A** reports the spectra collected over irradiation time where the decrease of the epoxy peak is clear meaning that the ring-opening occurs creating the network (**Figure 3.6B**). A further confirmation of the cross-linking is the increase in the OH band (3600-3200 cm^{-1}) due to epoxy ring opening (**Figure 3.5C**).

The effect of the amount of photoinitiator (S-SbF6) on the kinetic of the process was further investigated. **Figure 3.6D** showed different formulation containing 1,2, and 4 phr of S-SbF6. The evident increase of the kinetic occurred when increasing from 1 to 2 phr testify by the steep increase in the conversion. Indeed, at 30 s the conversion was 30 % for 1 phr while it double with 2 phr. The advantage of 4 phr was limited in terms of enhancement of conversion and kinetics, thus the selection was 2 phr of S-SbF6. This amount provided faster kinetic and high conversion limiting the percentage of photoinitiator allowing the highest green content.

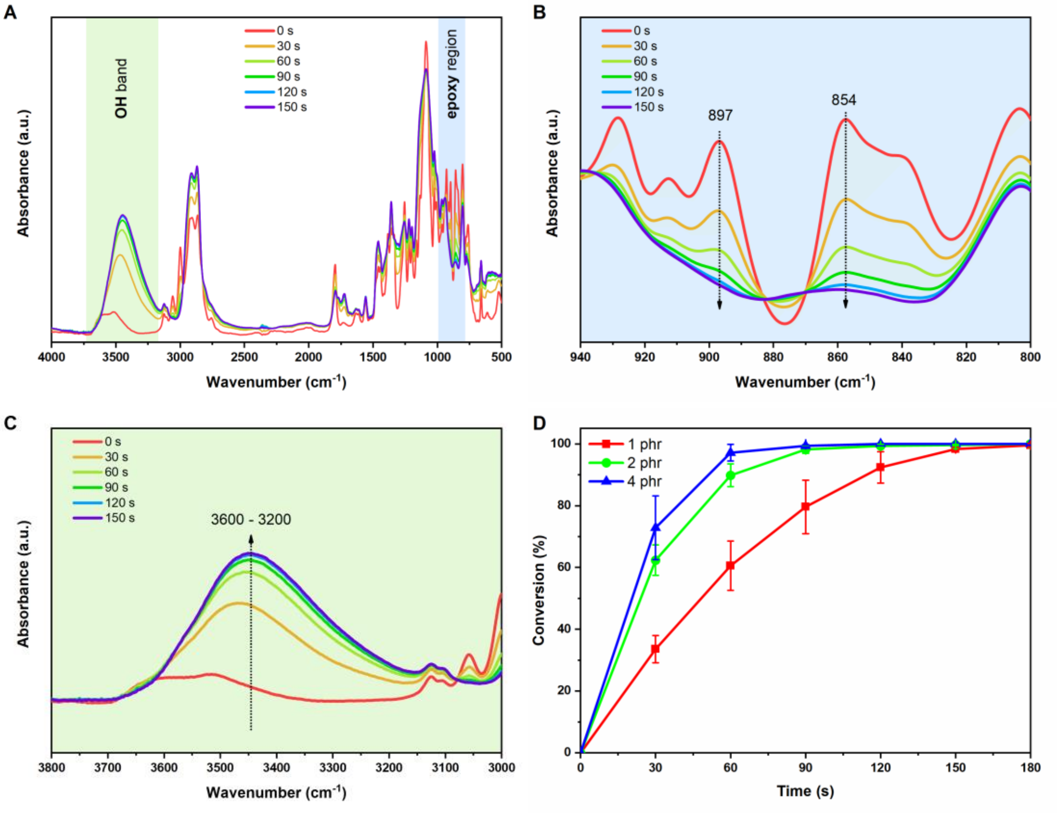

Figure 3.6. (A) FTIR spectra of FDE with 2 phr of PI recorded during the UV-curing; (B) decrease of epoxy peak located at 897 and 854 cm^{-1}; (C) increase of OH-band during the UV-curing and (D) conversion over time evaluated from FTIR analysis of the FDE epoxy peak with different concentrations of S-SbF6 (1, 2 and 4 phr).

Once the UV-curing process was investigate revealing interesting result, the aim of the study moved towards the tailoring of the thermo-mechanical properties of the coating. Two different approaches were selected to have a vast array of final properties covering a potential wide range of applications. Firstly, the monofunctional epoxy monomer, FGE, was added to the formulation in 10, 20, and 30 wt% with respect to the FDE. The introduction of the monofunctional monomer can reduce the cross-link density, thus tailoring the final T_g of the coatings. On the other hand, a hybrid network was generated to increase the rigidity of the coating improving the properties [128]. In this case the chain polymer mobility can be hindered by the presence of inorganic domain which can enhance the rigidity and the T_g of the coatings. The inorganic domain were created *in situ* through sol-gel process adding silica precursor as TEOS [129,130]. The alkoxysilane upon condensation and hydrolysis reaction can generate silica which is useful for surface hardness and barrier properties [131].

In our research, the hybrid coating was produced using a two-stage process. Initially, the liquid formulation composed by FDE as epoxy monomer, TEOS as silica precursor, and S-SbF6 as photoinitiator, was subjected to UV-curing in order to ensure the development of the organic network based on epoxy. Subsequently, the second phase involved heating the sample at 150°C for 4 hours within a humid environment. This step triggered the creation of silica, leading to the formation of the inorganic domains. The sequence of these steps is illustrated in **Figure 3.7** for clarity.

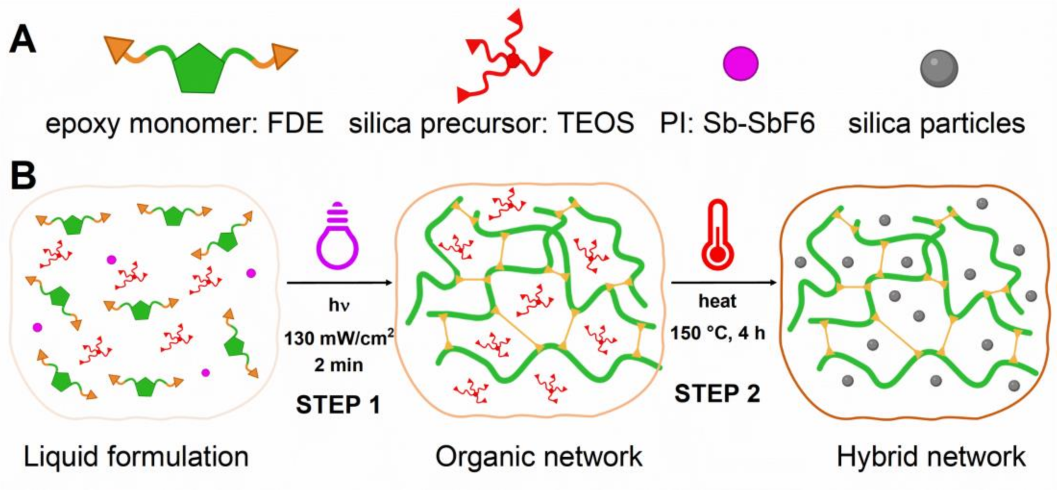

Figure 3.7. (A) main components involved in the formulation: epoxy bifunctional monomer (FDE); silica precursor (TEOS); cationic photoinitiator (S-SbF6); and silica generated particles (SiO_2); (B) schematic view of the two-steps reaction to generate the hybrid network.

Dynamic thermo-mechanical analysis (DMTA) was carried out to investigate T_g and the cross-link density of the UV-cured network by evaluating the trend the loss factor (*Tan δ*), storage modulus (G'), and loss modulus (G'') in function of the temperature as shown in **Figure 3.8**. The UV-cured FGE showed interesting T_g around 80 °C which is due to the chemical structure of the furan monomer which gives rigidity to the network. The addition of the monofunctional monomer decrease the cross-link density, as expected, due to the limitation in the chemical cross-linking. Indeed, the T_g decrease proportionally to the increased amount of the added monofunctional monomer (**Figure 3.8A**). The network containing the highest amount of FGE (30 wt%) reached a T_g of about 44 °C which represents an evident decrease with respect to the 80 °C demonstrated for the neat FDE. Moreover, it is possible to retrieve information about the homogeneity of the polymer network by looking the shape of the *Tan δ* curve. The studied UV-cured networks showed very broad curves indicating a heterogenous network with a wide distribution of chain segment mobility.

Higher stability and better performances are given by significant increment in the T_g due to the high rigidity of the polymer network. The idea of hybrid coatings formed *via* in-situ generation of silica could fulfill this important requirement. The formation of the silica was accomplished by two-steps curing process; firstly, a UV-stage allowed the formation of the organic coating by cationic epoxy ring opening. Secondly, the thermal-stage, at 150 °C for 4 hours in humid environment, enabled the formation of the inorganic network of silica. The presence of the photoinitiator which generate strong acid species upon UV-irradiation, and the humid environment were the two crucial prerequisites for the silica generation. The presence of the silica nanoparticles into the organic network can reduce the mobility of the polymer chains, having a beneficial effect in terms of rigidity and thermal stability. The validation was performed by DMTA which highlighted an increase of the T_g for the hybrid coatings with respect to the pristine organic coating. The maximum was reached with 50 phr of TEOS which corresponded to a T_g of 106 °C corresponding to 26 °C of increment with respect to UV-cured FDE (**Figure 3.8B**).

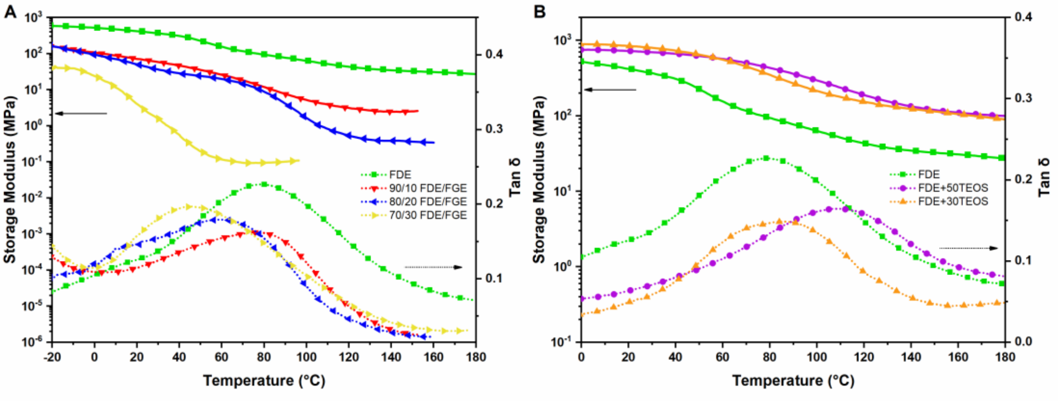

Figure 3.8. (A) Tan δ and Storage modulus trend in function of the temperature for the pristine FDE and for the thermoset derived by addition of FGE; (B) trend in function of the temperature for Tan δ and Storage modulus derived by pristine FDE and hybrid network containing 30 and 50 phr of TEOS.

The presence of the silica nanoparticles was validated by means of morphological analysis performed by SEM analysis. **Figure 3.9** reports the cross-section surfaces of the hybrid material obtained with 50 phr of TEOS in FDE matrix. It is clear that the thermal stage allowed the silica formation with a homogeneous distribution. Furthermore, no agglomeration were found, and the dimension of the particles was in the nanometer scale with average value of 230 ± 50 nm.

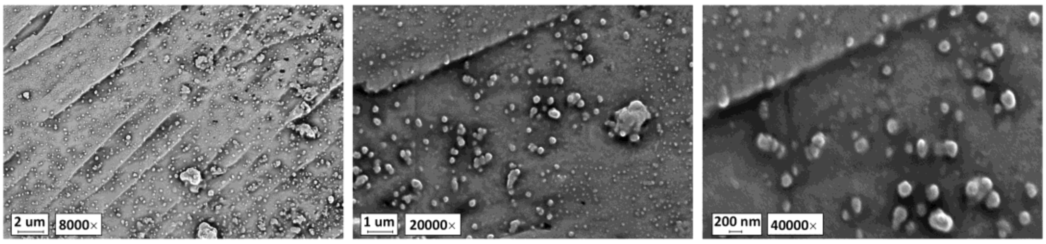

Figure 3.9. SEM images of coating of FDE + 50 TEOS. Different magnification at 8000×, 20000×, and 40000×. The silica nanoparticles are visible as white domains in the organic polymer matrix. The image at 8000× presents evidence of the fracture identified by the peculiar fracture line visible on the surface.

The presence of silica also influenced the thermal stability of the coating which was addressed by TGA analysis. The UV-cured coating were thermally degraded following the weight loss in function of the temperature as presented in **Figure 3.10**. The presence of FGE did not affect the thermal behave due to the similar chemical structure of the monomer involved into the resin, FDE and FGE. Both monomers contain furan cycle as back bone with glycidyl ether as main functional groups. Instead, the formation of the hybrid network had a beneficial effect on T_5, T_{peak} and *Char*. Almost 60 °C of increment were showed by the FDE_50TEOS on T_5 with respect to FDE which can be represent an increment of thermal stability due to the delay in the weight loss. Moreover, also the T_{peak} increased confirming the benefit of having silica nanoparticles enclosed into the polymer matrix. Finally, the increment in the residual char can be explained considering the residual silica left after the thermal degradation.

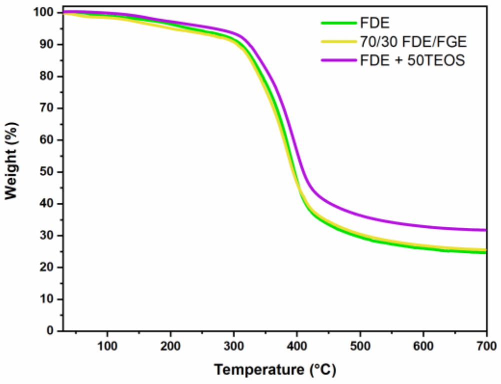

Figure 3.10. TGA thermograms of the pristine FDE (green), network with 30 wt% of FGE, 70/30 FDE/FGE (yellow), and thermoset with 50 phr of TEOS, FDE + 50 TEOS (violet).

The last characterization investigated the specific coating properties, such as pencil hardness and contact angle. The contact angle of the UV-cured and thermally treated films decreased by introduction of TEOS in the photocurable formulations. This can be explained by the possibility to have additional OH-group on the surface (formed from condensation reaction) which can reduce the hydrophobicity of the crosslinked network. The FDE-network had a contact angle of about 80° while the coating formed in the presence of 50 phr of TEOS showed a contact angle of 65°. The monofunctional monomer had no effect on the surface contact angle of the UV-cured coatings since the chemical structure of the FGE monomer was similar to the bifunctional FDE. Regarding the pencil hardness, the addition of TEOS increased the surface hardness of the coating as already reported in literature [131,132]. The *in-situ* formation of the inorganic domains homogeneously distributed within the polymeric matrix can importantly enhance the rigidity of the network, as observed by the increase of the T_g values, and therefore inducing an important increase on the surface hardness. On the other hand, the decrease of crosslinking density achieved in the presence of the monofunctional monomer did not affect the surface hardness of the crosslinked coatings.

3.1.2.3. Cross-linking of monofunctional furan monomer

As a following step, the investigation of the cross-linking reaction of the monofunctional monomer was carried out. It is known that FA can create cross-linking in the polyfurfuryl alcohol (PFA) network due to the opening of furan rings [133–135]. The furan ring-opening can occur through Diels-Alder reaction or other side reaction during the polycondensation. Furthermore, it has been demonstrate that it can start from FA monomers or oligomer chains [136]. Therefore, FGE was investigate as starting monomer to create a cross-linked network exploiting UV-light irradiation starting from a monofunctional monomer. A two-step reaction was performed where, in the first UV-step the formation of linear polymers was achieved which can then undergo cross-linking reactions in the second thermal stage.

The UV-irradiation of a monofunctional monomer, as FGE, generates the formation of linear polymer chains as previously reported [137]. The validation of the reaction was carried out by ATR-FTIR analysis showed in **Figure 3.11** where it is visible the disappearance of the epoxy band due to the ring opening reaction, and the consecutive OH-band increment. Furthermore, mass spectroscopy analysis was carried out to investigate the molecular weight of the linear polymer chains. The analysis provided a value of 437 g/mol. Considering that the monomer unit had a value of 154 g/mol, it is possible to affirm that the average number of units present in the chains are 2.8, meaning a predominant formation of chains with three monomeric units. This result is in agreement with previous studies done on the formation of linear polymer by UV-irradiation [138].

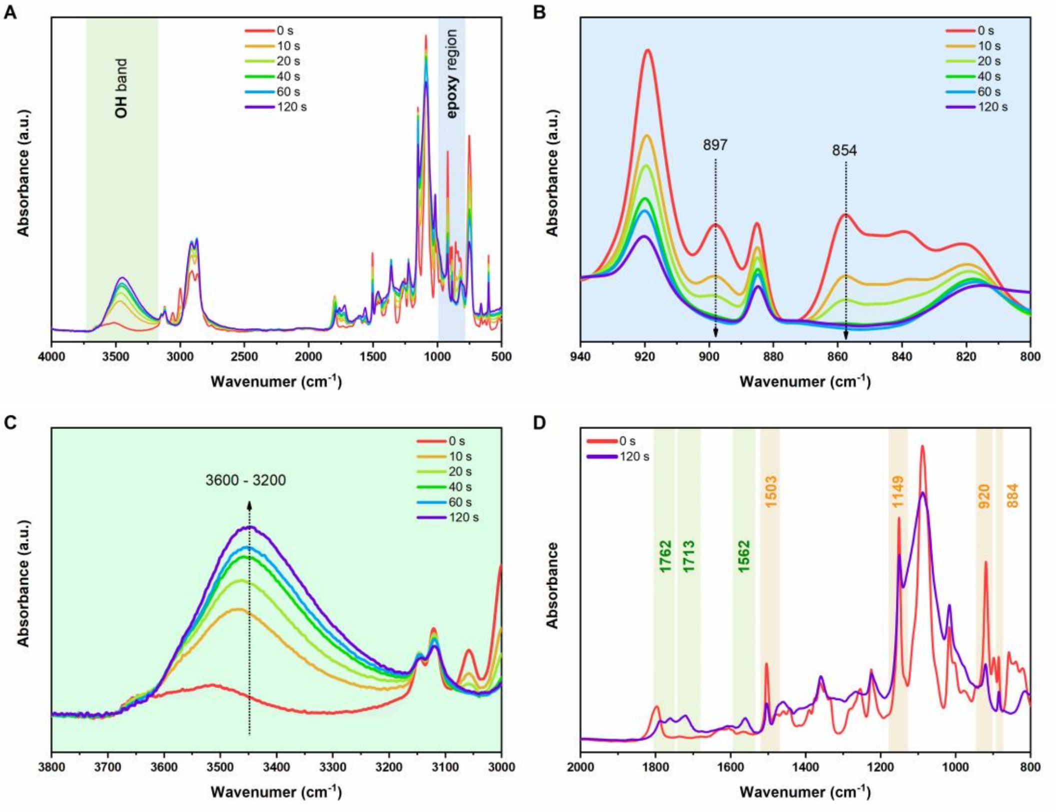

Figure 3. 11. (A) The real-time spectra for the cationic UV-curing of FGE in presence of 2 phr of photoinitiator. On the left side the increasing of the peak for the stretching of the OH group is reported while on the right there is the decrease through the time of the epoxy peaks situated at 897 cm^{-1} and 854 cm^{-1}; (B) FTIR spectra of the epoxy region; (C) Highlight on OH-band; (D) FTIR spectra of the FGE neat and UV-irradiated. As it can be notice, the changes are highlighted in correspondence of 1762 cm^{-1}, 1719 cm^{-1}, 1562 cm^{-1} considering the hypothesis of Mechanism 1. Instead, the orange bands show the decrease in the furan peaks at 1503, 1149, 920 and 884 cm^{-1}.

Furthermore, after the UV-irradiation it was possible to observe the appearance of three distinct peaks at 1762, 1713, 1562, and 1458 cm^{-1} (**Figure 3.11D**). The hypothesis behind these new peaks might be associated with a two-steps reaction mechanism towards the formation of alpha/beta-angelica lactone (**Figure 3.12**, Mechanism 1). As previously reported by Falco [136], the ring opening of furfuryl alcohol undergoes different chemical reactions which leads to the formation of levulinic acid (LevA). The super-acidic condition, created by the photoinitiator, could further catalyze the ring closure of LevA yielding to alpha-angelica lactone [139,140]. This result is confirmed by the presence of the bands 1762 cm^{-1} (C=O stretching of the ester lactone), 1562, 1458 cm^{-1} carboxylate (O−C−O) stretching mode [139]. The band at 1713 cm^{-1} is assigned to the carbonyl of saturated ketones probably caused by a residual LA in the system. The ring opening of the furan is also confirmed by the reduced intensity of the bands located at 1503, 1149, 920 and 884 cm^{-1} [133,134].

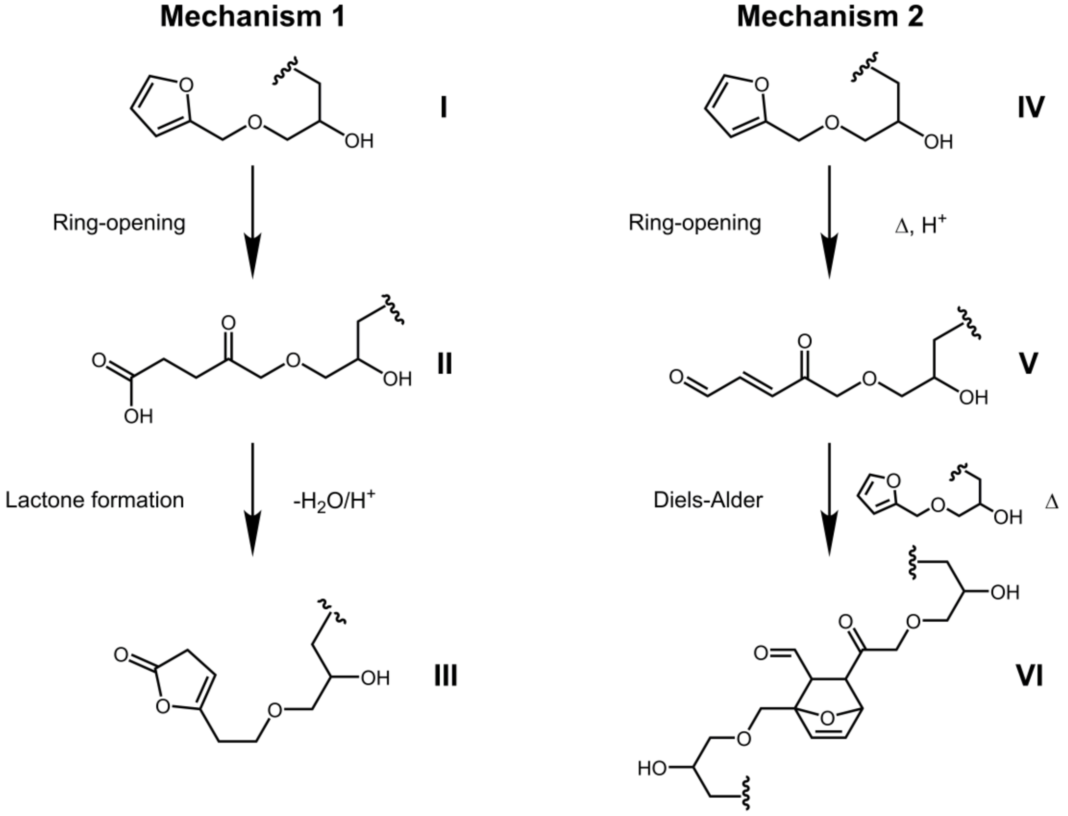

Figure 3.12. Proposed reactions which could happen in the two-steps process based on FT-IR investigations. Lactone formation (Mechanism 1) and Diels-alder reaction (Mechanism 2).

The thermal-step induced the cross-links between the linear polymer chains obtained by UV-irradiation as represented in **Figure 3.13**. In order to investigate this aspect, non-isothermal real-time FTIR were performed to demonstrate the structure variation upon heating. **Figure 3.14** reports the collected spectra from 30 to 180 °C. Shoulders and new bands appears between 1550 and 1750 cm^{-1} consequently to the ring opening reactions starting from 110 °C. In particular, the shoulder 3 is assigned to conjugated carbonyl also observed in ring opening of PFA [134,135]. The new band 5 is characteristic of C=C stretching vicinal to α, β unsaturated C=O [134]. These chemical bands confirmed the o formation of the structure V (**Figure 3.12**). The occurrence of Diels-Alder reaction is confirmed by the presence of two signals: the saturated C=O stretching vibration 2, and C=C stretching 4. The Diels-alder reaction could happen between the furan ring (IV, diene) and the double bond belonging to the structure (V) (dienophile). Nevertheless, the cycloaddition Diels-Alder could take place between the furan and lactone previously formed. Similar reactions have been reported in presence of cyclopentadiene [141]. In fact, by increasing the temperature the characteristic peaks of the lactone 1, 6 and 8 decrease. Because of the ring opening and Diels-alder reaction with the temperature all the main furan bands (7, 9, 10, 11, 12, 13, 14 and 15) are strongly reduced.

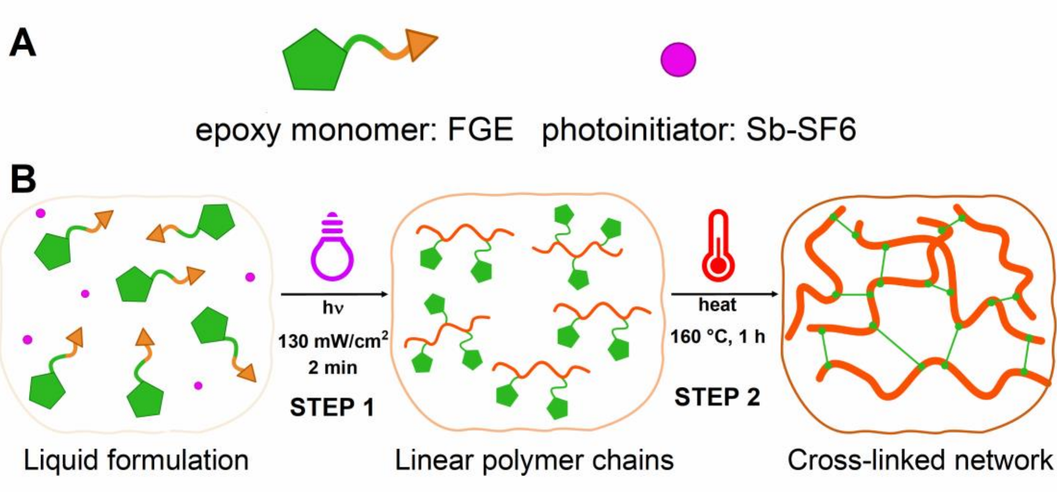

Figure 3.13. (A) two components of the coating formulation; the epoxy monofunctional monomer, FGE, and the cationic photoinitiator, S-SbF6; (B) two-steps reaction involved for the formation of the final epoxy furan-based coating.

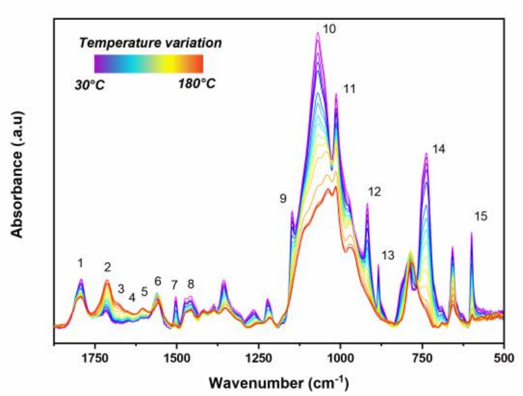

Figure 3.14. ART-FTIR spectra obtained under non-isothermal condition on UV-irradiated polymer. The temperature steps were 10 °C for each scan. The numbers (from 1 to 15) highlight the characteristic peaks that change during the thermal treatment.

To conclude, the FTIR analysis allowed to assess the chemical nature of the cross-links formed during the thermal-step. The proper conditions for the post-irradiation were established by DSC analysis. Isothermal tests were performed at different temperatures to evaluate the maximum of the exothermic peak which corresponds to the highest network cross-links. Different tests were done starting from 100 °C to 180 °C as reported in **Figure 3.15A**. It is clear that the reaction was initiated above 140 °C due to the absence of the exothermic peak at lower temperatures while the maximum was reached at 160 °C as highlighted in **Figure 3.15B**. Therefore 160 °C was chosen as temperature to perform the thermal-step.

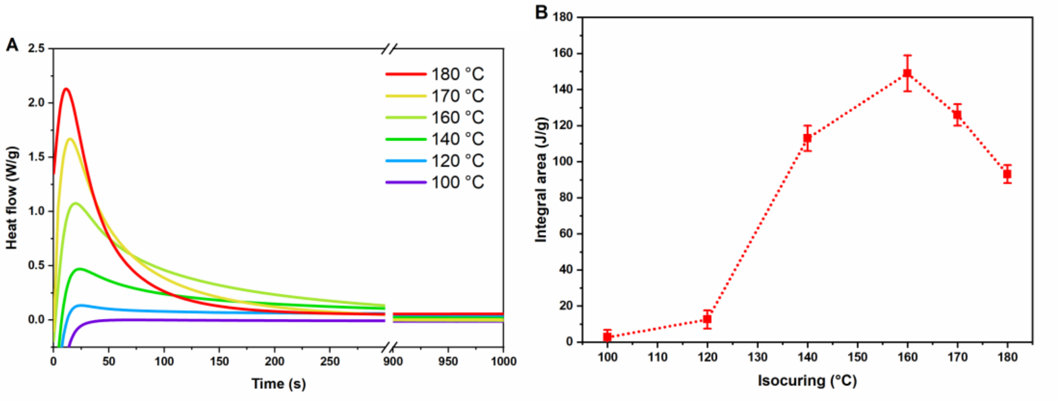

Figure 3.15. (A) photo-DSC thermogram of isothermal analysis of UV-irradiated FGE conducted at different temperatures; (B) integral area of the photo-DSC curves in function of the isothermal temperature adopted in the thermal step.

The DSC was employed to evaluate the T_g of the UV-irradiated sample (linear polymer) and for the dual treated (UV-thermal) samples (crosslinked material). The outcomes provided a further validation of the cross-linking reaction. Indeed, the UV-irradiated sample showed a T_g of −25 °C and an exothermic peak with a maximum located around 160 °C. On the other hand, the thermally treated FGE sample showed a T_g of 52 °C with no further exothermic peak. The increment of about 75 °C can be attributed to the cross-links between the linear polymer chains while the absence of the exothermic peak was a sign of complete curing process during the heating.

DMTA analysis validate the previous result as reported in Figure 3.15. The T_g evaluated as maximum of $Tan\ \delta$ was 5 °C for UV-irradiated FGE and 96 °C for UV-irradiated and thermally treated FGE. The increment was in agreement with DSC analysis confirmed the occurrence of cross-linking reaction. Furthermore, the E'had an important increase for the thermal treated FGE reaching 2×10^8 MPa due to high rigidity given by the cross-link between the linear chains. The UV-irradiated sample just reached 8×10^4 MPa. As can be notice in **Figure 3.16** after the rubbery plateau, the E' had a new increment around 160 °C. This could be explained by the starting of the cross-linking reaction during the test.

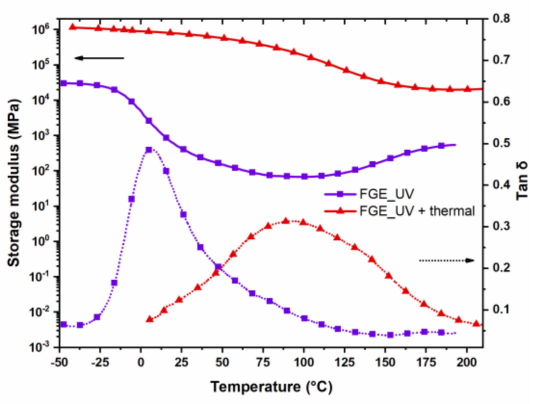

Figure 3.16. DMTA analysis of the UV-irradiated FGE (purple line) and UV-irradiated and thermally treated FGE (red line).

The gel content evaluation was finally in accordance with the proposed mechanism since the UV-irradiated sample had a 63 % of gel content, while the thermal treated sample reached 98 % of insoluble material corroborating the formation of a thermoset.

3.1.2.4. Hot-Lithography 3D printing of biobased epoxy resin

Bio-based monomers are attracting growing interest in different field, from coatings to 3D printing [142,143]. However, their utilization in practical applications has been more prominent only in recent years [144–146]. Among the bio-based formulations, acrylate or methacrylate-based monomers have gained significant attention due to their high reactivity [60,147–149]. This characteristic makes them particularly appealing for fast prototyping, which is a critical requirement in Additive Manufacturing (AM) processes.

A recent breakthrough in light-induced technology is the development of Hot-lithography, which involves 3D printing at high temperatures [47,150,151]. This innovation allows for the use of 3D printing at elevated temperatures, leading to a reduction in the viscosity of printable formulations. Moreover, it has been demonstrated that this approach can significantly enhance the curing kinetics of certain mechanisms, leading to a higher degree of conversion [47]. As a result, new types of resins, such as cationic curing of oxazolines [152] or epoxy resins [151], which may not be reactive enough at room temperature for UV-curing, can now be processed, expanding the possibilities for formulation design and selection to a new level. However, the use of bio-based epoxy resins in Hot-lithography is an area that has not been thoroughly explored yet.

To address this gap in knowledge, the printing properties of two bio-based epoxy resins, FDE (furan-based diglycidyl ether) and RDE (resorcinol-based diglycidyl ether), are being investigated using the Hot-lithography technique. The chemical structure is reported in **Figure 3.17**. This research aims to shed light on the feasibility and potential applications of these bio-based epoxy resins in 3D printing, providing valuable insights for future developments in sustainable additive manufacturing. The choice to study FDE and RDE in comparison with 1,4-cyclohexanedimethanol diglycidyl ether (CDE) is driven by the significant importance of aromatic building blocks which arise rigidity and mechanical performance. These aromatic compounds hold great potential in various industries and applications [10,153]. This comparative study will contribute to a better understanding of the properties and performance of FDE and RDE, providing valuable data for the advancement of sustainable and efficient materials in the field of additive manufacturing and beyond.

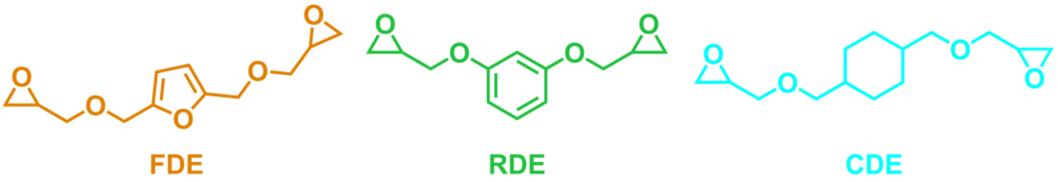

Figure 3.17. Chemical structures of the epoxy-based monomers used in the SLA Hot-lithography.

UV-curing process

In the first step of the study, the photoreactivity of the three resins (FDE, RDE, and CDE) was assessed using Near-Infrared (NIR) spectroscopy coupled with photorheology analysis and photo-Differential Scanning Calorimetry (photo-DSC) analysis. The real-time NIR/photorheology analysis allowed to monitor the epoxy group conversion during the curing process by tracking the decrease of the characteristic peak at 4530 cm^{-1}, which is associated to the epoxy ring [154]. The characteristic storage and loss moduli (G', and G'') were recorded throughout the irradiation process. Therefore, by monitoring the curing process at different temperatures it is possible to evaluate the effect of the temperature on gel point, photocuring kinetics, final conversion, and shrinkage. **Figure 3.18** displays the NIR spectra of the FDE formulation during photocuring at 80 °C. **Figure 3.18C/D** illustrates the trend over time of epoxy conversion and Storage modulus, respectively for FDE at three different temperatures (25 °C, 50 °C, and 80 °C). Notably, the epoxy conversion of FDE increased from 54 % to 92 % after 300 seconds of irradiation when the temperature was raised from 25 °C to 80 °C. Similarly to FDE, an increase of the photoreactivity was also observed for RDE as a function of the temperature. The cyclohexane-based CDE showed a sluggish reactivity at 25 °C but achieving an excellent conversion at 50 °C. All collected data are summarized in **Table 3.2** for the three resins investigated at 25 °C, 50 °C and 80 °C, respectively.

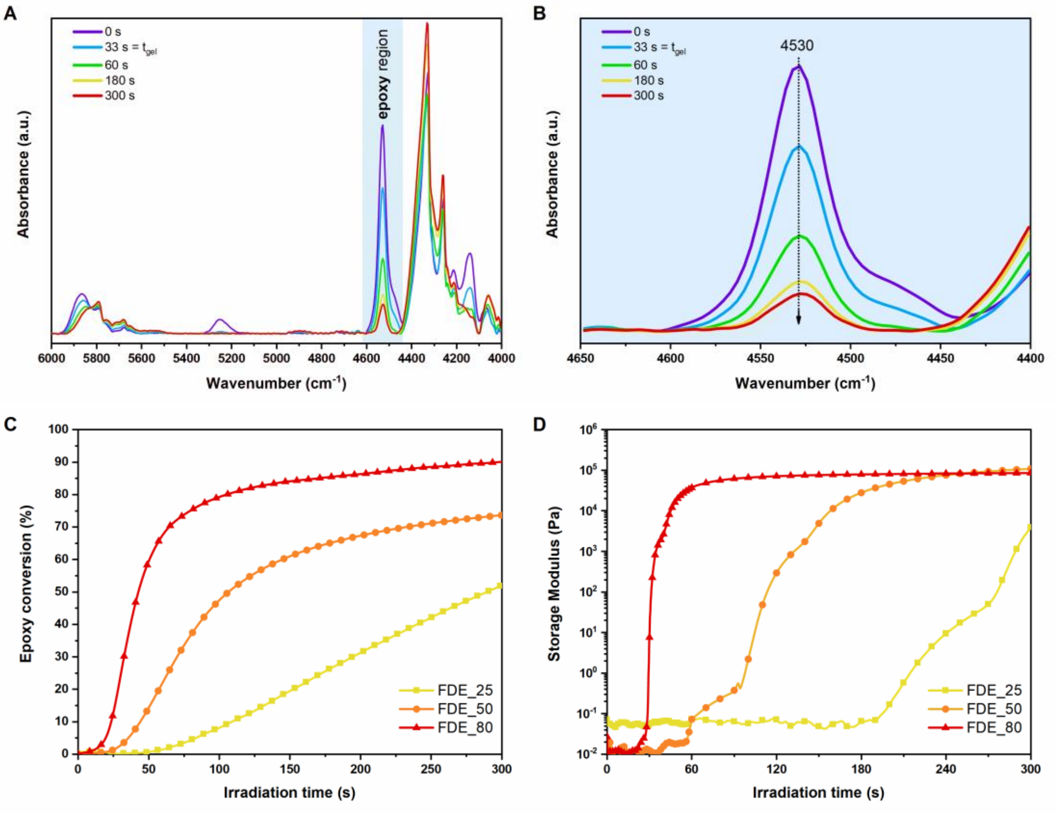

Figure 3.18. (A) NIR spectra of FDE formulation photocured at 80 °C with 3 wt% of I-SbF6. The UV-lamp intensity was set at 60 mW/cm^2; (B) epoxy peak centered at 4530 cm^{-1} during the UV-irradiation; (B) epoxy conversion evaluated by NIR analysis in function of the time in different isothermal condition; (D) trend of G' as a function of time at different temperatures registered by photorheology.

Table 3.2. Results obtained from NIR-photorheology study. Epoxy conversion (*EC*), time at gel point (t_{gel}), epoxy conversion at gel time (EC_{gel}) and normal force. Test performed at 25 °C (*); test performed at 50 °C (**); test performed at 80 °C (***).

SAMPLE	EC	t_{gel}	EC_{gel}	Normal Force
	(%)	(s)	(%)	(N)
FDE_25 *	54 ± 3	206 ± 14	35 ± 5	-2.0 ± 0.5
FDE_50 **	79 ± 2	100 ± 15	50 ± 7	-2.5 ± 0.5
FDE_80 ***	92 ± 2	33 ± 5	38 ± 4	-3.0 ± 0.5
RDE_25	52 ± 7	106 ± 1	27 ± 7	-7.5 ± 1.0
RDE_50	76 ± 3	27 ± 4	17 ± 1	-7.0 ± 1.0
RDE_80	89 ± 3	15 ± 3	15 ± 7	-7.0 ± 1.0
CDE_25	27 ± 1	-	-	-0.0 ± 0.5
CDE_50	96 ± 3	120 ± 5	57 ± 2	-3.5 ± 1.0
CDE_80	97 ± 3	44 ± 5	63 ± 2	-5.0 ± 2.0

The photoreactivity of the three resins was verified performing photo-DSC analysis in the same temperature curing conditions, e.g. 25 °C, 50 °C and 80 °C. In **Figure 3.19** the photo-DSC curves are collected for FDE, RDE and CDE at the different investigated temperatures. Consistent with the findings from photorheology and NIR data, the time to reach the maximum polymerization heat (t_{peak}) decreased as the temperature was increased, indicating an enhancement in photoreactivity at higher temperatures. This observation was supported by the increase in peak height (h_{peak}), meaning a faster reaction rate with rising temperature [155].

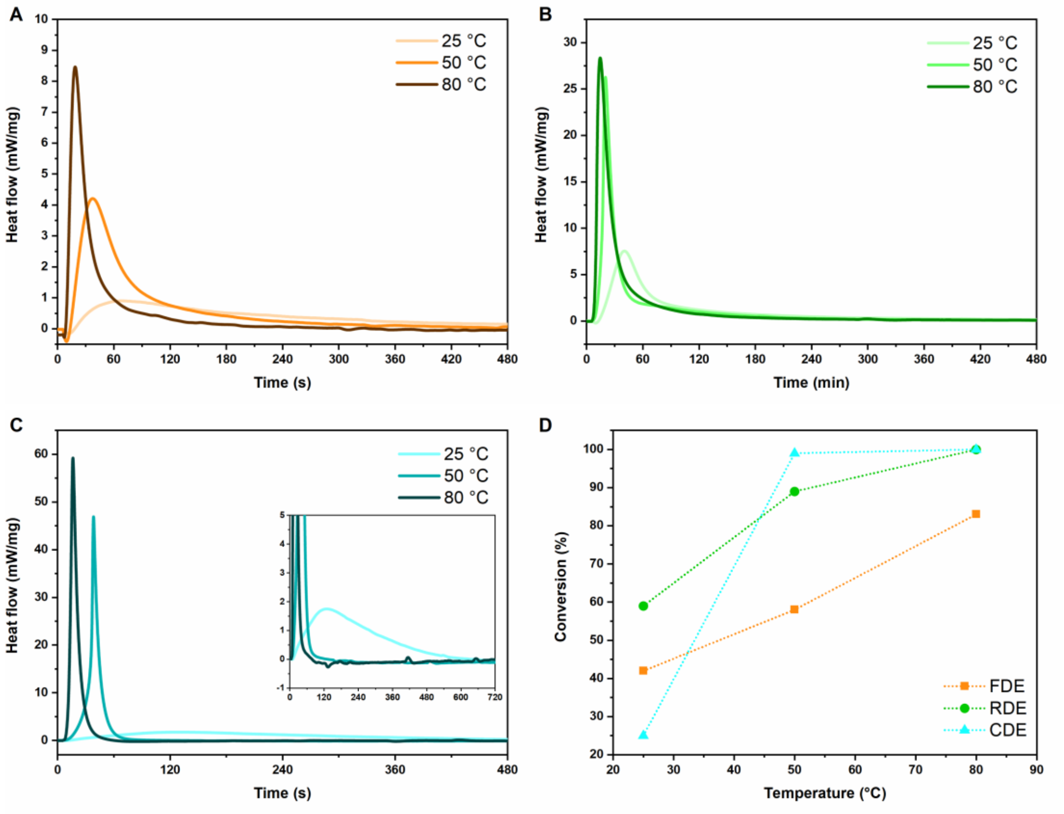

Figure 3.19. Photo-DSC thermograms of the formulations (A) FDE; (B) RDE; (C) CDE at different temperatures: 25 °C, 50 °C and 80 °C; (D) conversion in function of temperature calculated by enthalpy released.

The relatively slow reactivity at room temperature can be attributed to the monomer structure and the presence of glycidyl ether as functional group. Indeed, the glycidyl ether creates a stable intermediate structure during the ring opening leading to a slower curing speed [156,157]. All the data are summarized in **Table 3.3**. The heat recorded during irradiation, due to the epoxy ring-opening, correlates to the overall conversion of the resin. The larger the heat release, the higher is the achieved conversion. The three epoxy resins showed an increment of the heat flow with higher reaction temperature. An increase in conversion can be observed as the heat flow of the furan-based FDE raised from 172 J/g at 25 °C, up to 345 J/g when the temperature is raised to 80 °C. The same trend was observed for RDE and CDE. Indeed, by exploiting the *ΔH* values it is possible to calculate the epoxy conversion. The CDE and RDE formulations reached full conversion, as successively demonstrate by STA analysis, see **Figure 3.20**, while the FDE showed a residual peak. The peak has been taken into consideration (*ΔH* ≈ 69 J/g) to evaluate the final conversion. The three epoxy-based formulation achieved *EC* comparable with the results of the real-time NIR.

Table 3.3. Results obtained from DSC analysis. Time at peak (t_{peak}), height of the peak (h_{peak}), time to 95 % of heat evolution ($t_{95\%DSC}$), total heat flow (ΔH), epoxy conversion (EC_{DSC}) evaluated as ratio between heat flow at the set temperature (ΔH_{80}) and heat flow for theoretical total conversion (ΔH_{80}).

SAMPLE	t_{peak}	h_{peak}	$t_{95\%DSC}$	ΔH	$EC_{DSC}=\Delta H_{@T}/\Delta H_{80}$
	(s)	(W/g)	(s)	(J/g)	(%)
FDE_25	63 ± 2	0.8 ± 0.1	238 ± 1	172 ± 6	42
FDE_50	33 ± 1	2.9 ± 1.0	184 ± 8	242 ± 40	58
FDE_80	16 ± 1	7.0 ± 2.0	130 ± 5	345 ± 26	83
RDE_25	36 ± 1	7.5 ± 1.0	180 ± 1	354 ± 7	59
RDE_50	14 ± 1	27.0 ± 2.0	144 ± 8	533 ± 35	89
RDE_80	10 ± 1	33.0 ± 5.0	117 ± 11	596 ± 23	≈ 100
CDE_25	122 ± 1	2.0 ± 0.5	457 ± 45	130 ± 40	25
CDE_50	36 ± 3	47.0 ± 13.0	75 ± 13	527 ± 3	99
CDE_80	11 ± 3	57.0 ± 10.0	31 ± 4	528 ± 15	≈ 100

The overall conclusion is that the increasing temperature significantly enhance the photoreactivity of epoxy towards UV-induced ring-opening reaction [31,158]. 3D printing is possible by employing the Hot-lithography technique, which involves the 3D printing process at elevated temperatures, specifically at 80 °C. This approach ensures the attainment of feasible printing parameters, making the entire process more viable and practical. Utilizing elevated temperatures enhances the photoreactivity and curing kinetics of the materials, such as FDE and RDE, resulting in improved conversion rates and faster curing times. Consequently, this method enables the production of high-quality 3D printed objects with desirable properties, offering new opportunities for utilizing bio-based materials in additive manufacturing applications.

The thermal stability is a critical factor to consider in Hot-lithography. To assess this aspect thoroughly, both simultaneous thermal analysis (STA) and rheology studies were conducted. The cationic photoinitiator I-SbF6 can also be thermally triggered, (e.g. during the Hot lithography process) thus the thermal stability of the epoxy-based formulations was investigated to ensure a pure UV-activation curing process analysis (STA) [159]. A liquid formulation of FDE was tested and the STA curve is reported in **Figure 3.20**. It is clear the occurrence of the exothermic curing peak at 160 °C, indicating a good thermal stability of this formulation below this temperature, especially in the Hot-lithography process performed at 80 °C. The exothermal curing peak was at 200 °C for RDE and at 145 °C for CDE. Based on these results, it can be assumed that the cross-linking reaction during 3D printing at 80 °C is purely UV-triggered.

Additionally, the UV-cured materials at 80 °C were subjected to STA analysis to evaluate the completeness of the reaction. The curve for the cured FDE is reported in **Figure 3.20**. A residual exothermic peak around 160 °C was observed, constituting only 15 % of the total enthalpy of FDE. This demonstrated an almost quasi-complete achievement of the curing reaction through the UV-irradiation stage. The absence of a residual exothermic peak can be observed for resorcinol-based RDE and cyclohexane-based CDE. These results suggest the possibility to avoid a thermal post-treatment after the Hot-lithography, which is an usual step in traditional 3D printing process. The TGA data recorded by STA displayed a 5 % weight loss at 300 °C for both FDE and CDE UV-cured materials and a 3 % weight loss for RDE.

The last evaluation was rheological testing performed at the printing temperature to ensure the printability for long time which usually is required for complex geometries. The results, presented in **Figure 3.20**, indicate that the liquid formulation can remain in the heated VAT for at least 32 hours without exceeding the viscosity threshold of 20 Pa×s, which is considered a limit for performing printing [160]. Even after being stored at 80 °C for three days, the two bio-based resins showed a slight increase in viscosity but were still suitable for printing. However, the cyclohexane-based CDE formulation experienced a significant increase in viscosity after 32 hours of storage, rendering it unsuitable for printing. By the 48-hour mark, the resin failed to flow properly and cover the VAT with a uniform layer, leading to potential printing process failure.

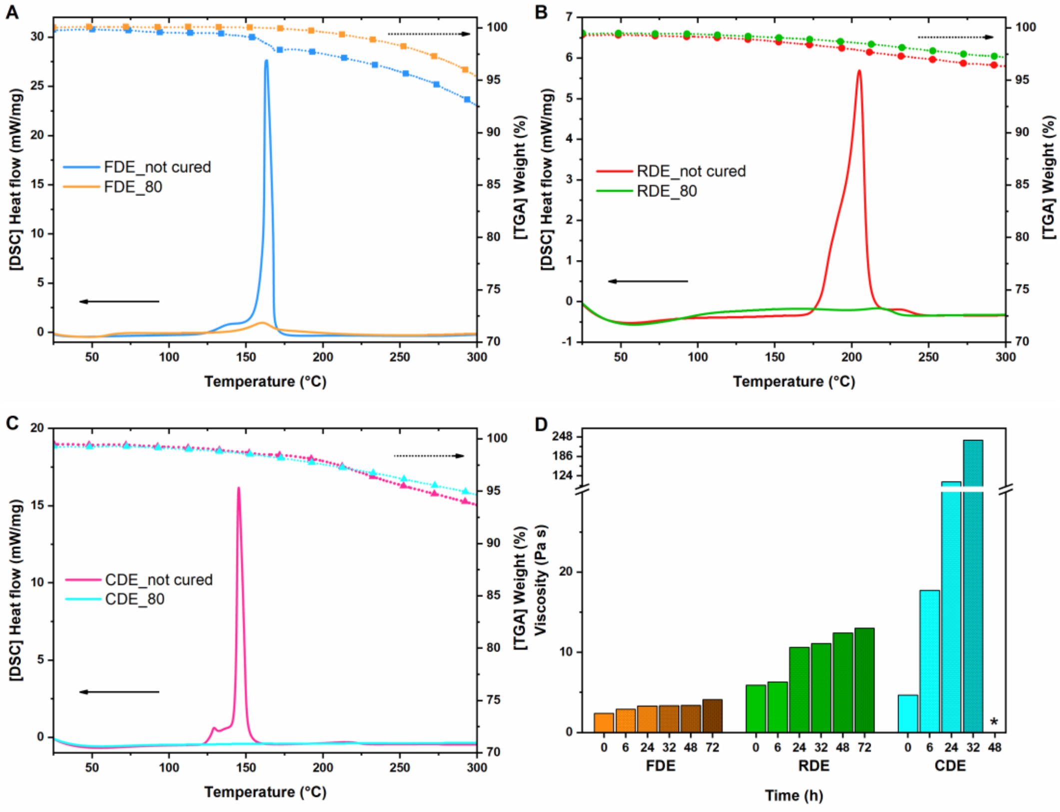

Figure 3.20. STA curves of the tested formulations. The DSC and TGA data for the thermoset UV-cured at 80 °C are reported as well as the data for the liquid formulation of each epoxy monomers. (A) FDE; (B) RDE; (C) CDE; (D) stability test performed at 80 °C for the epoxy-based formulations.

Mechanical characterization of 3D printed objects

The mechanical characterization was performed on 3D printed specimens processed at 80 °C to decrease viscosity and facilitate rapid photocuring kinetics, allowing for high laser speeds, leading to successful 3D printing of the test specimens. DMTA and tensile test were chosen to compare the properties of thermoset derived from FDE, RDE, and CDE.

Observations of *Tan δ* curves as a function of the temperature (**Figure 3.21**) indicate that the cyclohexane-based CDE formed a more flexible polymeric network, evident from its lower T_g of 35 °C. On the contrary, the two bio-based epoxy resins exhibit higher T_g values, with FDE around 70 °C and the crosslinked network derived from RDE having a T_g of 105 °C. Furthermore, the G' of FDE and RDE in the glassy state is approximately 1.5 GPa, significantly higher than that of CDE (~0.7 GPa). This difference can be attributed to the chemical structure of the monomers. The furan ring as well as the benzene ring in the bio-based precursors are aromatic and planar enhancing the rigidity of the repeating units, leading to higher T_g than the cyclohexane ring presents in CDE. Consistent with the T_g values, the storage modulus of the crosslinked RDE resin exhibits higher values in the rubbery plateau, indicating a higher degree of crosslinking and greater rigidity in the polymeric network. FDE also shows a higher modulus compared to the 3D printed CDE. Moreover, the shape of the *Tan δ* curves suggests that the network derived from resorcinol-based RDE was highly inhomogeneous due to the broadness of the curve. In contrast, the network structures of the UV-cured FDE and CDE were more homogeneous, characterized by narrow *Tan δ* peaks.

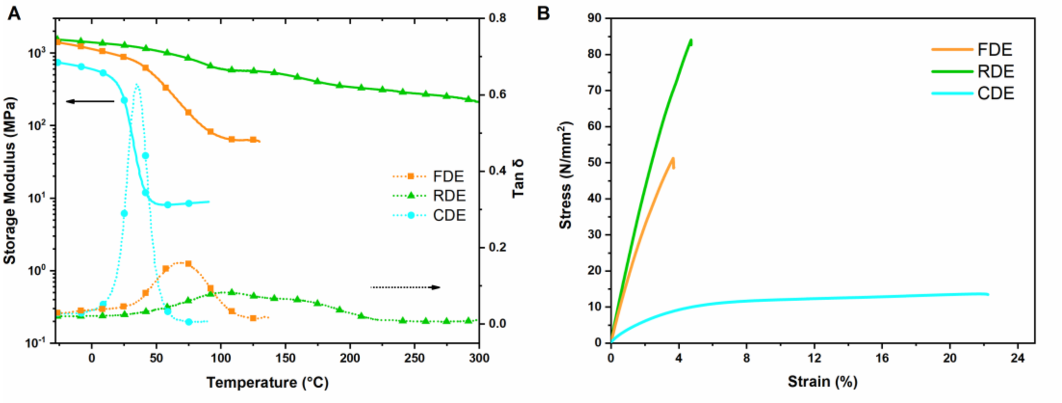

Figure 3.21. (A) DMTA curves for the 3D printed resin. Tan δ curves and Storage modulus curves as a function of the temperature are reported; (B) tensile test of 3D printed specimens of FDE, RDE and CDE. Representative curves are reported.

Tensile testing was conducted to assess the mechanical behavior of the 3D printed epoxy resins. As depicted in **Figure 3.21**, the three resin systems exhibited significantly different behaviors. Specifically, the CDE thermoset displayed the lowest strength at break demonstrating the highest elongation at break (18.5 %). This ductile behavior was expected since the tensile properties were recorded at 20 °C during the material's relaxation. In contrast, the FDE and RDE performances were comparable, with both polymer networks showing brittle behavior, offering respectively only 3 % and 4.5 % of elongation before rupture. Nevertheless, they exhibited higher strength compared to the fossil-based CDE resin. The highest strength results were achieved with the resorcinol-based RDE resin. The evaluation of the Young's modulus (*E*) as the tangent of the curve resulted in the highest value for RDE and the lowest for CDE. The furan-based FDE showed a behavior like the resorcinol-based RDE. These data (**Table 3.4**) align with the thermo-mechanical properties evaluated by DMTA analysis. Finally, the toughness was evaluated as the area under the stress-strain curves. This property is related to the energy required for crack propagation, and typically, toughness decreases as strength increases

[161]. CDE exhibited the highest toughness (257 $Jm^{-3}10^4$), while the two bio-based resins had lower values (123 $Jm^{-3}10^4$ for furan-based FDE and 203 $Jm^{-3}10^4$ for resorcinol-based RDE).

Table 3.4. Results obtained from DMTA test (T_g) and tensile test for the three printed resins. Strength at break (σ), elongation at break (ε), Young's modulus (E), deformation energy (U).

SAMPLE	T_g	σ	ε	E	U
	(°C)	(MPa)	(%)	(MPa)	(J $m^{-3}10^4$)
FDE	70	45 ± 9	3.0 ± 1.0	1924 ± 86	123 ± 23
RDE	105	79 ± 11	4.5 ± 1.0	2355 ± 45	203 ± 27
CDE	35	13 ± 1	18.5 ± 4.0	428 ± 39	257 ± 13

Lastly, the feasibility of utilizing bio-based epoxy resins for 3D printing was demonstrated by printing complex shapes with high precision. One of the key advantages of 3D printing is the ability to produce intricate structures with excellent final properties, and accuracy close to the original CAD design. The reproducibility achieved with the bio-based resins was precise and accurate, as evident in **Figure 3.22**. The morphology of the printed samples was further examined using optical microscopy confirming the accurate representation of thin parts in the furan-based FDE printed sample, showcasing the successful interaction between different printed layers of 100 um. Furthermore, self-standing shapes were successfully printed using both FDE and RDE, highlighting the potential of bio-based resins as alternatives to fossil-based ones. The efficient kinetics and reactivity of these resins allow for the printing of intricate features, without any over-polymerization effects. This successful outcome reinforces the suitability of bio-based resins for various 3D printing applications, showcasing their promise as eco-friendly and high-performance materials.

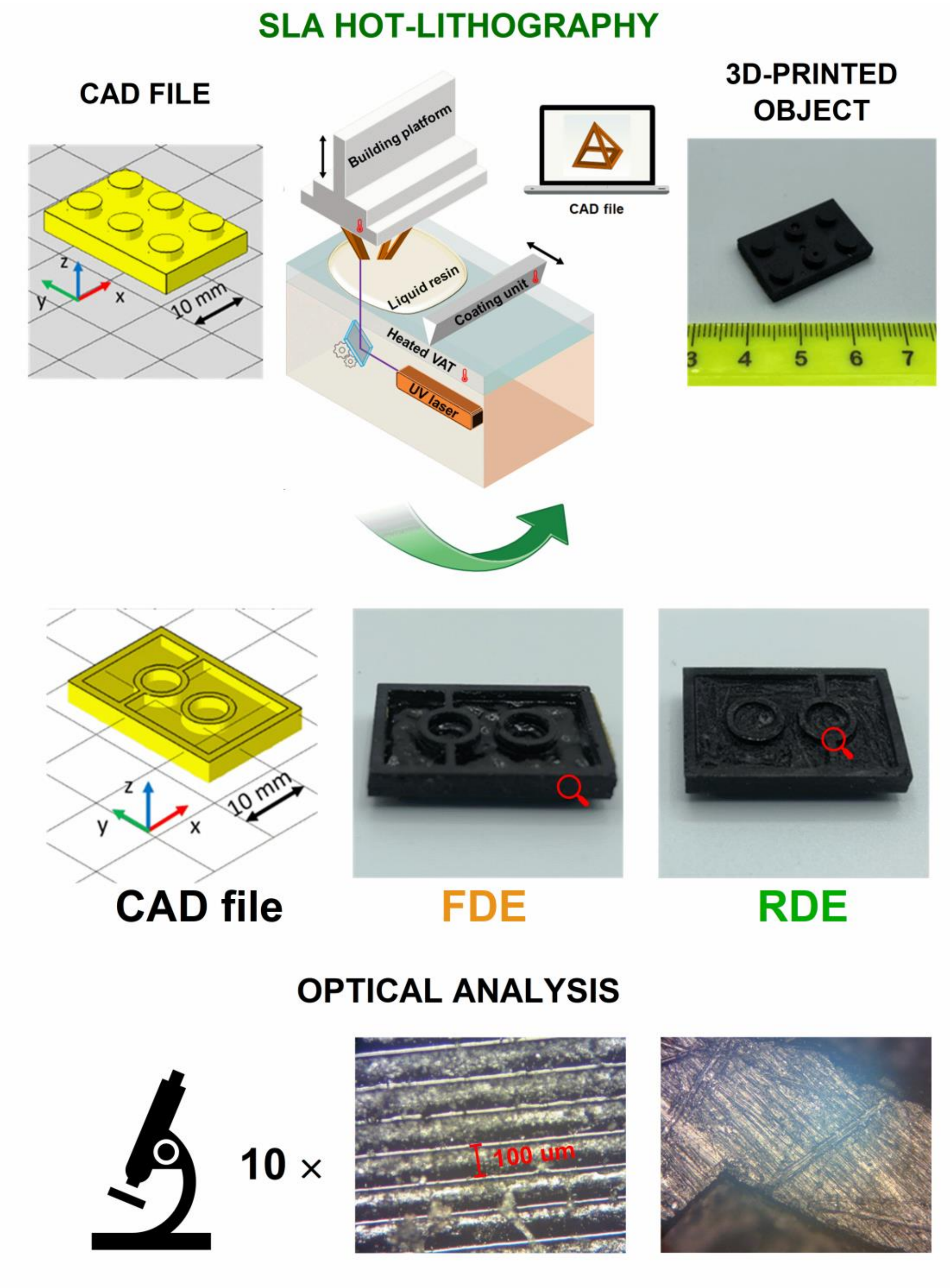

Figure 3.22. 3D printed bricks with the CAD file for both FDE and RDE. The biobased resins were 3D printed at 80 °C with a speed laser of 100 mm/s and intensity of 70 W/mm^2. Optical images obtained with 10× magnification for both printed resins.

3.1.3. Conclusions

Within the frameworks to exploit bio-based monomers for cationic UV-curing, the works presented here showed the possibility to achieve outstanding and interesting result employing furan-based monomers. The successful functionalization allowed the synthesis of epoxy derivatives which have been used in different ways from coating application to 3D printing. The first two parts of the work investigated the use of furans-derived monomers for coating applications, demonstrating the possibility of tailoring the final properties by two different approaches, addition of monofunctional monomer to decrease the network rigidity, or achievements of hybrid coating by *in situ* formation of silica particles to enhance the mechanical response of the thermoset. It was possible to achieve T_g around 100 °C which is comparable with the well-known commercially available epoxy resins. Interestingly, from the study of the monofunctional epoxy monomer, FGE, it was possible to investigate the cross-linking reaction of a monofunctional monomer introducing a two-step approach. Indeed, the UV-irradiation create the linear polymer which was then cross-linked by thermal treatment. This step allowed to increase the T_g of the polymer. Finally, the breakthrough in 3D printing was allowed by employing the Hot-lithography technique which permitted to exploit the less reactive epoxy resin for 3D printing. Indeed, the high temperature increase the kinetic of the cationic ring opening polymerization giving access to perform the 3D printing. FDE was successfully 3D printed showing comparable or even better properties with fossil-based epoxy resins as testify by the higher T_g (70 °C) compared to CDE-based network (35 °C). Furthermore, the mechanical response of FDE- and RDE-based polymeric material was comparable with the aromatic fossil-based monomers [151] confirming the remarkable potential of bio-derived monomer to substitute the petroleum-based ones.

3.2. Not only furan: other interesting bio-based monomers for cationic UV-curing

The investigation of the epoxy monomer for cationic UV-curing covered also other kind of important building blocks coming from different bio-resources. Cellulose, hemicellulose and lignin make up the lignocellulosic biomass. Lignin, the second most abundant worldwide polymer, with around 50 million tons of lignin generated by the pulp and paper industry, of which only a small fraction (less than 2 %) is utilized for chemical-value products, presents a significant opportunity to develop polymers [162,163]. Historically regarded as a low-value waste byproduct, lignin's potential as a valuable polymeric precursor has emerged due to its complex aromatic structure containing reactive groups like phenylpropanoid entities and carbon-carbon bonds, offering prospects for polymerizable reactive groups [164].

The lignin content varies between 15 to 30 % of the wood compositions, as reports in **Table 3.5**. Its structure changes according to the biomass family. Its composition undergoes alterations based on the specific biomass category, with softwoods generally containing a higher proportion of lignin, while hardwoods exhibit greater richness in hemicellulose [165].

Table 3.5. The different percentages of cellulose, hemicellulose, and lignin in the different plans and paper industry side stream [164].

Lignocellulosic materials	Cellulose	Hemicellulose	Lignin
	(%)	(%)	(%)
Hardwood stems	40-55	24-40	18-25
Softwood stems	45-50	25-35	25-35
Nut shells	25-30	25-30	30-40
Corn cobs	45	35	15
Wheat straw	30	50	15
Rice straw	32	24	18
Leaves	15-20	80-85	0
Grasses	25-40	25-50	10-30
Switch grass	31-32	35-50	20-25
Sugarcane bagasse	42	25	20
Sweet sorghum	45	27	21
Cotton seed hairs	80-95	5-20	0
Coconut husk	39	16	30
Sorted refuse	60	20	20
Paper	85-99	0	0-15
Newspaper	40-55	25-40	18-30
Waste paper from chemical pulps	60-70	10-20	5-10
Primary wastewater solids	8-15	NA	24-29

Lignin primarily consists of cinnamic alcohols, including p-coumaryl alcohol, coniferyl alcohol, and sinapyl alcohol [13]. Different wood families exhibit distinct proportions of these monolignols, as shown in **Table 3.6**, further contributing to lignin's complexity. Besides principal phenolic nuclei, lignin also includes other components like coniferaldehyde, sinapaldehyde, p-hydroxybenzoate, ferulate, p-coumarate, hydroxycinnamates, and by-products from incomplete monolignol biosynthesis [166].

Table 3.6. Percentages of the three alcohol moligon units in the main plant families [166].

Monolignol	Broadleaf wood	Conifer wood	Grass
	(%)	(%)	(%)
Sinapyl alcohol (S)	50-75	0-1	25-50
Coniferyl alcohol (G)	25-50	90-95	25-50
p-Coumaryl alcohol (H)	Trace	0.5-3.4	10-25

Commercially, only three products are extensively derived from lignin: vanillin, dimethyl sulfide and dimethyl sulfoxide. Among these, vanillin stands out as a notable phenolic compound produced from biomass on an industrial scale, holding potential as a renewable aromatic building block [59,167]. Aromatic compounds play a crucial role in the manufacturing of polymers, making the synthesis of these derivatives from lignin a prominent focus in the field. This interest stems from the fact that lignin serves as a primary source of aromatic biobased substrates. Phenolic compounds with various chemical structures can be obtained from lignin deconstruction, as depicted in **Table 3.7**; ferulic acid (FeA) is a key example [168]. Other products, such as sinapic acid and its derivatives, can be isolated from lignin depolymerization mixtures [162]. A Fenton modification improves the yield of phenolic monomers, especially for ethyl-*p*-coumarate and ethyl-ferulate [169].

Table 3. 7. Phenolic acids which can be derived from lignin [166].

Phenolic acid and aldhehydes	**Lignin fraction (% yeld, w/w)**				
	OPF lignin	Caligonum monogoliacum Lignin	Tamarix spp Lignin	Maize stem Lignin	Rice straw Lignin
p-Hydroxybenzoic acid	0.42	1.68	1.67	0.82	1.12
p-Hydroxybenzaldehyde	0.49	1.35	1.21	2.48	1.59
Vanillic acid	0.25	1.04	1.14	0.03	0.36
Syringic acid	0.84	2.16	1.77	1.28	1.82
Vanillin	1.02	17.96	18.12	10.49	15.49
Syringaldehyde	2.60	9.36	10.34	13.05	13.00
p-Coumaric acid	N/A	3.08	2.55	0.32	0.61
Ferulic acid	0.30	0.91	0.47	0.82	1.22
Molar ratio (S:G:H)	58:22:15	58:22:15	31:59:10	N/A	N/A

Ferulic acid is part of the hydroxycinnamic family alongside sinapic and caffeic acids [170,171] and it plays essential roles in the cell wall, boosting anti-oxidizing and free radical scavenger properties [172,173]. Diverse methods, including chemical and physical approaches as well as enzymatic synthesis, are being explored to isolate these components from different sources such as sugarcane bagasse, bark trees, and kraft lignin [174–177]. Additionally, synthetic biology holds promise for lignin valorization and biosynthesized coumarins [178]. Agro-industrial waste is another potential source of FeA, offering a large, cost-effective, and abundant pool of chemicals [173,179]. From a chemical perspective, the intriguing nature of FeA lies in its structural composition. It embodies a hydroxy cinnamic acid structure with three distinct functional groups: an acid group, a phenolic moiety, and a double bond, all of which offer potential avenues for extended functionalization [180,181]. Its aromatic ring contributes of rigidity to the structure, enhancing the properties of resulting networks [182]. FeA has gained interest of polymer chemists and has been explored as a promising bio-renewable monomer to potentially replace certain fossil-based counterpart, such as phthalic acid in PET [183,184]. In this prospective application, FeA undergoes conversion into a polyester; however, its versatility extends to serving as a valuable foundational unit for polyurethanes, epoxides, and phenolic resins [168,185,186]. Notably, FeA has recently found application in thermoset contexts, being combined with a furan-derivative to yield thermosets with elevated T_g achieved through the creation of a cross-linked structure via thermal curing [115]. Furthermore, it has contributed to the creation of polymeric networks with vitrimeric properties [187]. Given its significant potential and the prospect of yielding advantageous properties, FeA has been employed as a starting monomer in the synthesis of epoxy derivatives intended for utilization in cationic UV-curing processes.

Recent research efforts have especially focused on exploring cellulose as a versatile starting point, leading to the development of various different platforms, such as terpenes [125,188–190], furans [92], isosorbide [191], carboxylic acids and bio-derived multifunctional alcohols [9,49,192]. Isosorbide, a sugar-based monomer derived from cellulose has gained prominence as one of the top 15 molecules earmarked for sustainable development by the US Department of Energy [193]. Its chemical structure was first elucidated in 1946 [194], and it is alternatively recognized as 1,4:3,6-dianhydro-D-glucitol and 1,4:3,6-dianhydro-D-sorbitol presented in **Figure 3.23** [191]. Monomers derived from cellulose and starch have garnered extensive attention as precursors for a diverse array of novel polymers. These sugar-based monomers sourced from lignocellulosic biomass offer economic feasibility, widespread availability, and contribute enhanced degradability to the final polymer products [195]. The synthesis of isosorbide involves a multi-step reaction sequence, commencing with the enzymatic depolymerization of cellulose into D-glucose and D-mannose. Subsequent hydrogenation yields D-sorbitol, as illustrated in **Figure 3.23**, and a dehydration step culminates in the formation of isosorbide [196]. The overall yield, achievable through optimized reaction conditions, can exceed 75%, making it a favorable pathway for a versatile monomers platform. Various avenues for employing isosorbide and its derivatives has been proposed [163,195] highlighting the potential as promising platform for biobased monomers across several polymerization reactions [193]. Isosorbide has been utilized for several applications including the synthesis of functional materials [197], pharmaceutical compounds, development of surfactants [198], creation of novel organ catalysts [199], and as cross-linking agents [200]. The biocompatible properties of polymers derived from isosorbide have rendered them suitable for producing medical devices [201]. Isosorbide has also found use in coating technologies, spanning from powder coatings [202] to UV-curable coatings [55,203].

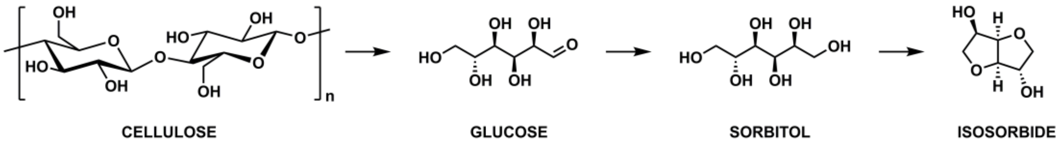

Figure 3.23. From cellulose to isosorbide, main reaction intermediates.

In this study the exploration of isosorbide's potential as an epoxy-based monomer for UV-curable resin was conducted with the aim to expand the range of potential applications for this intriguing compound. A comprehensive study was conducted to develop reinforced coatings with the addition of a bio-based filler to enhance the final properties. Indeed, a drawback associated with bio-based monomers is the limited mechanical properties observed in the cured films when compared to films derived from fossil-based epoxy coatings [204]. One potential way for enhancing the final properties involves the incorporation of fillers. Utilizing bio-based fillers offers a promising strategy for creating composite and reinforced polymeric materials while reducing reliance on inorganic fillers [205]. Various byproducts from the food and industrial sectors can serve as suitable fillers, including materials like nutshell and macadamia shell [206,207]. The macadamia nut (Macadamia integrifolia), is originated from the rainforests of Eastern Australia and also found in South Africa, which ranks as the third-largest global producer [208,209]. Comprising cellulose (40 %), hemicellulose (20%), and lignin (40 %) on average, the macadamia nutshell represents a lignocellulosic material [210]. Guaiacyl (G) and syringyl (S) are the main monolignol units presented in the macadamia structure. Interestingly, the macadamia nut shell is predominantly composed of 93% G-units [211]. It has been proved that macadamia nutshell powder can serve as reinforcement in a bio-based printable formulation centered on acrylated soybean oil, resulting in improved thermo-mechanical properties of 3D printed objects [149].

Leveraging on the advantage offered by bio-based fillers addition, a further study was conducted, focusing on epoxy vegetable oils and the formulation of corresponding bio-composites. Vegetable oils (VOs) stand out as the most widely utilized bio-based resources due to their abundant and cost-effective availability [212]. The primary components of plant oils consist of triglycerides, which result from the esterification process involving glycerol and three fatty acids. Fatty acids make up 95% of the overall weight of triglycerides, and their composition is distinctive for each type of plant oil [213]. Within these triglycerides, numerous reactive sites are present, including double bonds and ester groups. This presents a range of opportunities to customize novel structures for the creation of cross-linked polymers *via* two primary methodologies [214]. The initial approach takes advantages of functional groups within triglycerides, such as internal double bonds, alcohols, or epoxides, which can undergo polymerization through diverse techniques. The second strategy revolves around chemical functionalization prior to polymerization and addresses the challenge of the relatively modest reactivity of natural triglycerides (typically containing only double bonds) by introducing readily polymerizable functional groups, thereby expanding the scope of synthetic prospects. The unsaturated sites can be readily altered using various types of photocurable functional groups, such as methacrylate or epoxy groups [215]. Epoxy vegetable oils (EVOs) have already been employed by Crivello et al. to investigate the UV-reactivity of several triglycerides for the development of new green coatings [216,217]. More recently, multiple studies have demonstrated the viability of utilizing EVOs for producing a wide spectrum of eco-friendly coatings [56,218], some of which can possess specific attributes such as corrosion resistance [219]. However, thermosetting materials derived from EVOs typically exhibit modest mechanical properties. This is attributed to the presence of flexible aliphatic chains within their molecular structures, which restricts their application to non-structural contexts. To improve the properties of the final thermoset, sustainable EVOs matrices has been used in blends alongside other epoxy monomers such as furan [62] or aromatic based ones [127] aimed to arise the final properties.

In light of the necessity to improve final properties of bio-based thermosets, the field of bio-composites was investigated. The potential benefits of integrating bio-based fillers to reinforce matrices based on epoxy vegetable oils were explored and studied within the context of 3D printing. The purpose of this study was to demonstrate the advantages of incorporating fillers and the viability of producing structural materials with inherent self-staining properties.

Part of the work described in this chapter has been already submitted and it is available at the following references:

[220] **Pezzana, L.**; Malmström, E.; Johansson, M.; Casalegno, V.; Sangermano, M. Multiple approaches to exploit ferulic acid bio-based epoxy monomers for green thermosets. *Industrial products and crops,* SUBMITTED

[221] **Pezzana, L.**; Emanuele, A.; Sesana, R.; Delprete, C.; Malmström, E.; Johansson, M.; Sangermano, M. Cationic UV-curing of isosorbide-based epoxy

coating reinforced with macadamia nut shell powder. *Prog. Org. Coatings* **2023**, 185, 107949, DOI: https://doi.org/10.1016/j.porgcoat.2023.107949.

[222]**Pezzana, L.**; Wolff, R.; Stampfl J.; Liska, R.; Sangermano, M. Hot-lithography 3D printing of fully bio-based composites: green vegetable oil epoxy matrix & bio-derived filler powder. *Additive Manufacturing* **2024**, accepted paper.

3.2.1. Experimental section

3.2.1.1. Material and Chemicals

The ferulic acid (FeA 99 % purity), isosorbide (IS, 98 % purity), epichlorohydrin (ECH), tetrabutylammonium bromide (TBAB), sodium hydroxide (NaOH), hydrochloric acid (HCl, 37 %), trimethylolpropane tris(3-mercaptopropionate) (TMPMP), allyl bromide (97 % purity) and the 3-chloroperbenzoic acid (m-CPBA, 77 % purity) were purchased from Sigma-Aldrich. Commercially available resins of Bisphenol A diglycidyl ether (BADGE), 3,4-epoxycyclohexylmethyl-3,4-epoxycyclohexanecarboxylate (ECC), 1,4-cyclohexanedimethanol diglycidyl ether (CDE), and neopentyl glycol diglycidyl ether (NPGDGE) were purchased from Sigma-Aldrich. The epoxy linseed oil (ELO) and the epoxy soybean oil (ESO) were gently given from HOBUM Oleochemicals GmbH (Hamburg, Germany). The macadamia nut shell powder (MAC) was obtained from the 814 integrifolia variety of macadamia; the shells were received in powder particles after grinding and used without any further purification. The bio-based fillers were donated from Composition Materials Co., Inc. (Milford, USA). Wall-nut shell powder (WS) was provided in two different mesh, 200 and 325, labelled WS200 and WS325 respectively. Furthermore, tagua powder (T200) and hemp powder (H200) with a 200 mesh were provided. According to the standard sieve specification used by the company, the mesh 200 indicate a minimum of 88 % of particles below 75 um while the mesh 325 ensure that at least 88 % of particle have a diameter below 45 um.

The different initiator were used. The ytterbium(III) trifluoromethanesulfonate (YTT, 99 % purity) and triarylsulfonium hexafluoroantimonate salts (S-SbF6) mixed in propylene carbonate were purchased from Sigma Aldrich. The photolatent base 4-(hexahydro-pyrrolo[1,2-a]pyrimidin-1-ylmethyl)-benzoic acid methyl ester (PLB) was supplied from BASF. The photoinitiator, p-(Octyloxyphenyl)phenyl Iodonium Hexafluoroantimonate, (I-SbF6, 95 %), was purchased from ABCR. The sensitizer Isopropylthioxanthone (ITX) was supplied from Lambson. Tris(4-((4-acetylphenyl)thio)phenyl) sulfonium tetrakis(pentafluorophenyl) borate (Irgacure 290, S-BF5, 95%) was supplied by BASF.

Magnesium sulphate ($MgSO_4$) was acquired from Acros Organic. Ethyl acetate (EtOAC), heptane (Hept) and dichloromethane (DCM) were supplied by VWR Solvent. The Trimethylchlorosilane ($Si(CH_3)_3Cl$) was purchased from VWR Chemicals. Triethylamine (TEA) was purchased from Sigma Aldrich. Deuterated chloroform ($CDCl_3$), and dimethyl sulfoxide (DSMO-*d6*) were purchased from Sigma Aldrich and used as solvent and reference for NMR analyses.

3.2.1.2. Procedures

3.2.1.2.1. Epoxidation of ferulic acid

The epoxidation was performed combining previous protocols as presented in **Figure 3.24** [115,187]. Ferulic acid (FeA 15 g, 77 mmol) was mixed with ECH (10 equivalent, 71 g) and TBAB as catalyst (0.01 equivalent, 0.25 g) in a three-necked flask equipped with a magnetic stirrer. The mixture was heated at 105 °C under reflux for 2 h. Then the solution was cooled down to room temperature. The mixture was then further cooled down at 0 °C in an ice bath and a water solution of NaOH 40 wt% was added to the mixture employing an adding funnel (100 mL). The solution was kept under stirring for 3 hours. The organic phase was extracted three times with ethyl acetate (30 mL) then the collected phases were washed six times with water (30 mL). After removal of water by drying with $MgSO_4$, the solvent was evaporated to obtain a yellow liquid. The last traces of ECH were removed by precipitation of the liquid in heptane (50 mL). The precipitation was repeated two times. The ferulic acid based diepoxy (FeADE) was collected as a white solid and dried overnight in vacuum (16.5 g, yield: 70 %).

^{1}H-NMR (400 MHz, CDCl3) δ 7.67 (d, J = 16.0 Hz, 1H), 7.14 – 7.03 (m, 2H), 6.93 (d, J = 8.3 Hz, 1H), 6.35 (d, J = 15.9 Hz, 1H), 4.56 (dd, J = 12.3, 3.0 Hz, 1H), 4.31 (dd, J = 11.4, 3.3 Hz, 1H), 4.10 – 4.01 (m, 2H), 3.91 (s, 3H), 3.44 – 3.25 (m, 2H), 2.98 – 2.86 (m, 2H), 2.74 (ddd, J = 23.8, 4.9, 2.6 Hz, 2H).

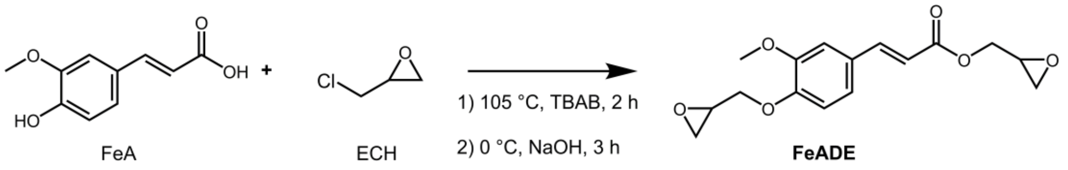

Figure 3.24. Reaction scheme of epoxidation of ferulic acid (FeA) to obtain the bifunctional epoxy.

3.2.1.2.2. Epoxidation of isosorbide

The epoxidation of isosorbide was conducted by two-step reactions (**Figure 3.25**) which generate the allyl intermediate as previously describe [223,224]. Isosorbide

(15.0 g, 100 mmol) was set in a round bottom flask and allyl bromide was added (3 eq, 26 mL, 300 mmol). The mixture was heated to 65 °C and a water solution of NaOH 50 wt% (12 g of NaOH) was added dropwise to the mixture. The solution was kept under stirring and heating for 6 hours. The reaction was stopped by decreasing the temperature and then was extraction with DCM performed. The reaction solution was extracted three times with a total amount of 150 mL of solvent. The organic phase was finally rinsed three time with HCl 1M (50 mL) and three times with water (50 mL) to remove impurities. Finally, $MgSO_4$ was used to remove traces of water. A final roto-evaporation of the solvent was performed to give the final product as a yellowish liquid (IDAE, 19.70 g, yield 85 %).

The synthetized allyl derivative (IDAE, 5.0 g, 22 mmol) was poured in a round bottom flask with a small addition of DCM (10 mL). m-CPBA (11.4 g, 66 mmol) was dissolved in DCM (40 mL) and drop wise added to the reagent solution meanwhile an ice bath ensured a temperature between 0 and 10 °C. The reaction started by the addition of m-CPBA at 0 °C and was run at room temperature under agitation over 24 hours. The excess of m-CPBA was precipitated in the reaction mixture by decreasing consequentially temperature and amount of solvent. The cycle was repeated three times to ensure the precipitation of the unreacted reagent. Finally, an extraction against water was performed to remove the last impurities to give the final product as a colored viscous oil (IDGE, 3.45 g, yield 61 %).

IDAE NMR analysis:

^{1}H NMR (400 MHz, $CDCl_3$) δ 6.01 – 5.81 (m, 2H), 5.35 – 5.15 (m, 4H), 4.63 (t, J = 4.4 Hz, 1H), 4.51 (d, J = 4.3 Hz, 1H), 4.23 – 4.11 (m, 1H), 4.08 – 3.84 (m, 8H), 3.56 (td, J = 8.4, 2.0 Hz, 1H).

^{13}C NMR (101 MHz, $CDCl_3$) δ 134.62, 134.29, 117.95, 117.62, 86.45, 83.90, 80.33, 79.58, 73.58, 71.78, 70.65, 69.93.

IDGE NMR analysis:

^{1}H NMR (400 MHz, CDCl3) δ 4.73 – 4.51 (m, 2H), 4.19 – 3.78 (m, 6H), 3.64 (m, 2H), 3.50 – 3.35 (m, 2H), 3.25 – 3.09 (m, 2H), 2.83 (m, 2H), 2.70 – 2.54 (m, 2H).

^{13}C NMR (101 MHz, CDCl3) δ 86.30, 84.85, 80.75, 80.42, 73.48, 71.82, 70.29, 69.86, 50.91, 50.63, 44.35, 44.15.

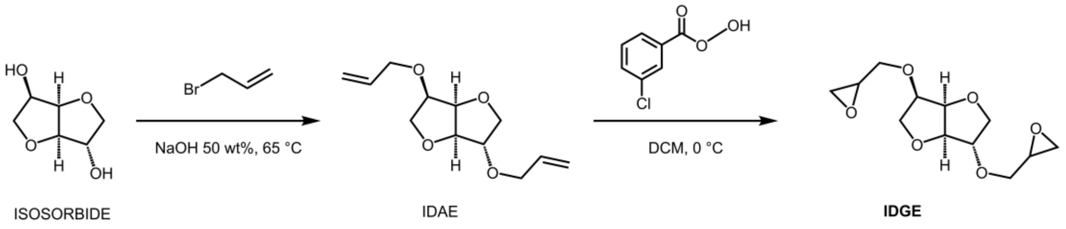

Figure 3.25. Two-steps reaction to obtain epoxy bifunctional based monomer (IDGE) from isosorbide by IDAE as allyl intermediate.

3.2.1.2.3. Silanization of wall-nut shell

The silanization reaction was performed according to similar protocol reported in literature [225,226]. The WS325 (5 g) was suspended in anhydrous DCM in a three-bottom round flask. Si(CH$_3$)$_3$Cl was added in ratio 1:10 (50 g) to ensure the excess of the silane reagent. TEA (1.2 equivalent of Si(CH$_3$)$_3$Cl) was mixed with 20 mL of DCM and was added drop wise through adding funnel. The reaction was kept under nitrogen atmosphere at room temperature with high mixing ensured by magnetic stirring. The reaction last for 24 hours then the reaction was stopped by neutralization adding saturated solution of NaHCO$_3$. This step was done in an ice bath to keep control over the temperature due to the exothermicity of the reaction step. The final suspension was filtered through a Buchner funnel (porosity 4) and rinsed with deionized water multiple times to eliminate the possible formation of salt. WS325_SIL was then recovered and dried in a vacuum oven over night at 50 °C. **Figure 3.26** reports the schematic view of the functionalization.

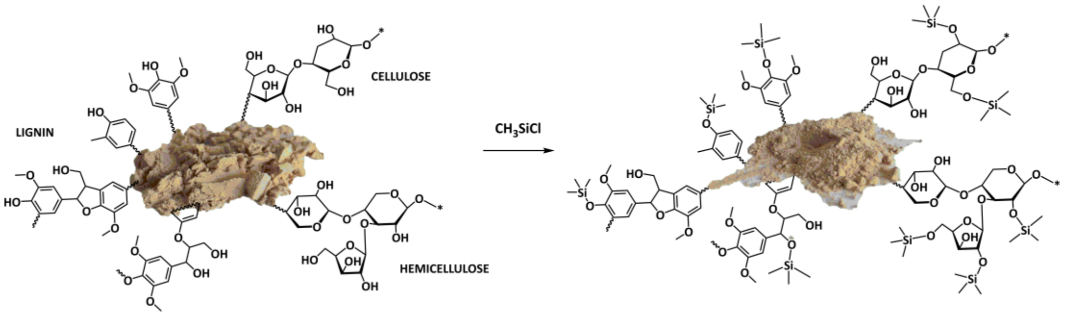

Figure 3.26. Schematic view of silanization of WS325.

3.2.1.2.4. Formulations and UV-curing of ferulic based diepoxy (FeADE)

The diepoxy ferulic acid was used as main epoxy monomer in three different formulations listed in **Table 3.8** allowed for three different types of curing.

The FeADE was melted (around 80 °C) and then the triarylsulfonium hexafluoroantimonate (S-SbF6, cationic photoinitiator) was added in 2 wt% and mixed with the resin. The formulation was UV-cured in a silicon mold ($12\times8\times0.2$ mm^3) by a UV-light guaranteed by a UV-DYMAX Flood lamp equipped with a static mercury lamp with an emission spectrum between 600 and 250 nm centered around 365 nm and a light intensity of about 100 mW/cm^2. This procedure allowed to generate sample *via* UV cationic curing for further analysis. The samples were irradiated for 2 minutes.

The second adopted route was a thiol-epoxy system which was obtained by mixing FeADE with TMPMP in a stochiometric ratio (epoxy:thiol functionality). For clarity the formulation is denoted as FeADE:SH,2:3, due to the reactive groups of FeADE (2 epoxies) and TMPMP (3 thiols), respectively. The photolatent base (PLB) was then added (2 wt%) and the formulation was cured under the UV-lamp (100 mW/cm^2) for 2 minutes in silicon molds, either with a rectangular shape (12×8 mm^2, with different thickness of 0.2, 0.4 and 1 mm) or dog-bone shape for tensile test. Moreover, a further formulation with equimolar amounts of epoxy and thiol groups, was produced and analyzed. In this case the formulation is denoted FeADE:SH,3:3 due to reactive groups considered for each monomer, FeADE (2 epoxy and 1 carbon-carbon double bond, 3 total) and TMPMP (3 thiols).

Finally, FeADE was mixed with YTT (2 wt%) as a thermal cationic initiator whereafter the samples were thermally cured in silicon molds at 150 °C and for two hours and 180 °C for another 2 hours to ensure complete curing. Different samples were produced according to the mechanical test requirement, rectangular shape for DMA-analysis ($12\times8\times0.4$ mm^3), and dog-bone shape (type 5B) for tensile tests. The cationic curing technique was used for the production of specimens for adhesive tests.

Table 3.8. Formulations containing FeADE tested in different curing methods.

ENTRY	Epoxy Monomer	Thiol monomer	Initiator	Curing
FeADE	FAE	-	S-SbF6 (2 wt%)	UV
FeADE:SH,2:3	FAE	TMPMP (ratio 2:3)	PLB (2 wt%)	UV + thermal
FeADE:SH,3:3	FAE	TMPMP (ratio 1:1)	PLB (2 wt%)	UV + thermal
FeADE_YTT	FAE	-	YTT (2 wt%)	Thermal

3.2.1.2.5. Formulations and photopolymerization of isosorbide diglycidyl ether based reinforced coating

The bio-based diepoxy isosorbide (IDGE) was used together with macadamia nut shell powder to obtain reinforced cationic UV-cured coatings. Different formulations were prepared to test the effect of the filler and are listed in **Table 3.9**. Firstly, an optimum photoinitiator loading of 3 wt% was determined, then the isosorbide-based resin was either used pristine or mixed with the macadamia nut shell powder (MAC) in different amount. The formulations were kept under magnetic stirring (1000 rpm) at room temperature for 10 minutes to ensure a homogenous dispersion of both initiator and filler. The storage was done in brown vials to minimize exposure to light. Different samples were prepared using a silicon mold with a rectangular shape 8 mm × 12 mm with a thickness of 0.4 mm. The UV-source was a UV-DYMAX Flood lamp equipped with a static mercury lamp with an emission spectrum between 600 and 250 nm centered around 365 nm and a light intensity of 100 mW/cm^2. The coatings were irradiated for two minutes guaranteeing a total dose of 12 kJ/cm^2.

Table 3. 9. IDGE based formulations produced to investigate the effect of the MAC.

FORMULATION	**Bio-based epoxy resin (IDGE)**	**Macadamia nut shell powder (MAC)**	**Photoinitiator (PhI)**
	(g)	(wt% / g)	(wt% / g)
IDGE	1.5	/	3 / 0.046
IDGE_10MAC	1.5	10 / 0.17	3 / 0.046
IDGE_20MAC	1.5	20 / 0.38	3 / 0.046
IDGE_30MAC	1.5	30 / 0.64	3 / 0.046

3.2.1.2.6. Formulations and Hot-lithography SLA of composites

The 3D printing was performed using the epoxy vegetable oils as main monomers for the resin. Epoxy linseed oil (ELO) or epoxy soybean oil (ESO) were added with 3 phr (per hundred resin) of the three different photoinitiators in order to test the reactivity and the thermal stability. Once established the best formulation, the best system was adopted for the further investigations. The photoinitiator was added in 3 phr with respect to the ELO resin and mixed in ultrasound bath until the complete dissolution of the photoinitiator (30 minutes). The filler was added with respect to the resin weight (i.e. 5, 10 or 20 phr) in a second step according to **Table 3.10**. The formulations were repeated for epoxy soybean oil (ESO) adding the same amount of filler as the formulations containing ELO. Mechanical mixing was provided to the formulations to homogenize and distribute the filler by Vortex Genie for 5 minutes at 300 rpm. The formulations were handled in brownish vials to avoid light contact and the components were weighted in an orange room.

The formulations were tested and used for the Hot-lithography SLA, thus 15 g batch were prepared each time to fulfill the printing. The SLA 3D printer used in this work was a Caligma 200 UV prototype developed by Cubicure (Vienna, Austria) with a bottom exposure SLA setup. The different components of the printer, specifically the vat, the building platform, and the coating unit were heated up to 100 °C. The laser emission was centered at the wavelength of 375 nm with power of 70 mW/mm^2, while the laser spot diameter was set at 25 μm during printing. The laser beam is scanned over a 2-dimensional plane using a galvanometer scanning system; the layer thickness of the resin was kept at 100 μm for all the printing job. The laser speed was adjusted according to the formulation used varying from 1000 to 500 mm/s for pristine formulations and filled one respectively. The different geometries were developed through a CAD file saved in extension.cli to be read by the printer software.

Table 3.10. Formulation used for 3D printing containing epoxy linseed oil (ELO) and soybean oi (ESO) with the different fillers, wall-nut shell (WS200 and WS325), tagua (T200), and hemp (H200). The photoinitiator was S-BF5 used in 3 phr with respect to the epoxy resin for all formulations.

ENTRY	Epoxy vegetable oil	Filler (phr)	ENTRY	Epoxy vegetable oil	Filler (phr)
ELO	ELO	/	**ESO**	ESO	/
ELO_WS325_10	ELO	WS325 (10)	**ESO_WS325_10**	ESO	WS325 (10)
ELO_WS325_20	ELO	WS325 (20)	**ESO_WS325_20**	ESO	WS325 (20)
ELO_WS200_10	ELO	WS200 (10)	**ESO_WS200_10**	ESO	WS200 (10)
ELO_WS200_20	ELO	WS200 (20)	**ESO_WS200_20**	ESO	WS200 (20)
ELO_T200_10	ELO	T200 (10)	**ESO_T200_10**	ESO	T200 (10)
ELO_T200_20	ELO	T200 (20)	**ESO_T200_20**	ESO	T200 (20)
ELO_H200_5	ELO	H200 (5)	**ESO_H200_5**	ESO	H200 (5)
ELO_H200_10	ELO	H200 (10)	**ESO_H200_10**	ESO	H200 (10)

3.2.1.3. Characterization

Nuclear magnetic resonance (NMR)

NMR analysis of the synthetized monomers was conducted on a Bruker AM 400 MHz. $CDCl_3$ and DMSO-d_6 were used as solvent and internal reference for the chemical shift given in ppm. ^{1}H-NMR was recorded at 400 MHz while ^{13}C-NMR was at 101 MHz.

Fourier transform infrared spectroscopy (FTIR)

The FTIR analysis was used over the different studies to follow the UV-curing process by characterization of the epoxy ring opening. A Nicolet iS 50 spectrometer was used to record the data. For the first work, the FTIR analysis was conducted in ATR mode and the spectra were obtained with 32 scans with a spectral resolution of 4.0 cm^{-1}. The epoxy band of FeADE was monitored at 905 cm^{-1} and 855 cm^{-1}. Furthermore, the thiol peak (-SH) was followed at 2750 cm^{-1} and the carbon-carbon double bond (C=C) by the peak at 1640 cm^{-1}.

Regarding the second work having the IDGE as main monomer, FTIR analysis was conducted in transmission mode by spreading the UV-curable resin over Si wafer with a thickness of 32 μm. The spectra were collected in a real-time mode, with 1 scan per second with a spectral resolution of 4 cm^{-1}. The epoxy peak was followed at 855 cm^{-1}. The ether peak at 1270 cm^{-1} was assumed to be unaffected by the UV-curing and used as reference to use Equation 3.1 for the determination of the conversion. All the FTIR data were handled with the software Omnic from Thermo Fisher Scientific.

Considering the 3D-printing, the ATR-FTIR spectra of the ESO and ELO based resins were recorded on a Perkin Elmer Spectrum 65 equipped with diamond crystal. 32 scans with resolution of 4 cm^{-1} were performed for each sample and the spectra were collected in a range between 4000-500 cm^{-1}. The handling of the data was done by means of the software Spectrum from Perkin Elmer in version 10.03.07.0112. Liquid formulations before UV-irradiation, cross-linked network after UV-irradiation, filler powders, functionalized filler and degraded product were tested. The epoxy peak taken in consideration was located at 825 cm^{-1}. The spectra were normalized by the ester peak at 1738 cm^{-1} which was assumed to be unaffected by the cationic UV-curing. The epoxy conversion (EC_{FTIR}) was evaluated according to Equation 3.4.

$$EC_{FTIR} = \left(1 - \frac{A_{@T}}{A_i}\right) \times 100 \qquad \text{(Equation 3.4)}$$

Where $A_{@T}$ is the epoxy area after the UV-curing at certain temperature; A_i is the initial epoxy area before the UV-irradiation.

Photorheology

The instrument Anton Paar MC 302 was used to investigate the UV-process for FeADE and IDGE based thermoset. The light source was guarantee from a Hamamatsu LIGHTINGCURE LC8 lamp that was equipped with an optic fiber. The intensity of the UV-light was 40 mW/cm^2. The tests were performed with a plate-plate geometry; the upper metal accessory had a diameter of 2.5 cm while the bottom plate was a quartz disk to ensure the irradiation on the sample. The distance between the crystal and the plate was varied from 100 to 600 μm according to the test, however a constant thickness of 200 μm which corresponds approximately to 150 μL of coating resin was used to compare the different results. The frequency test was 1 Hz, with a strain of 1 % and the lamp was switched on after 60 seconds which were used to ensure initial stability to the system.

A different Anton Paar MCR302 WESP rheometer was instead used for photo-rheology studies related to 3D printing. In this case, the bottom plate of the rheometer was a borosilicate disk to guarantee the irradiation of the sample. The source for initiating photopolymerization reactions, was UV-light projected via a waveguide on the surface of the sample through the bottom window using an Exfo OmniCure 2000 light source with a broadband Hg-lamp (320-500 nm). The intensity was set around 60 mW/cm^2 at the contact with the sample. The calibration was done by means of Ocean Optics USB 2000+spectrometer. The rheometer was set as plate-plate geometry with a steel accessory with diameter of 25 mm (PP25). The thickness of the layer was set as 200 μm. The tests were performed at different temperature: 25, 50, 75 and 100 °C. The temperature can be controlled by Peltier elements located around the window holder in the temperature control system (Anton Paar P-PTD200/GL). Additional heating from above by an external Peltier-controlled hood was employed for experiments at elevated temperatures (H-PTD 200 from Anton Paar). The measurements were performed in triplicate to have reproducible data. RheoCompass 1.24 was used to analyze the results.

Epoxy number

Epoxy number was evaluated with titration to corroborate the NMR data of the pristine epoxy oils, ELO and ESO. The standard procedure was used [227]. Briefly, 1 g of resin was reacted with 50 mL of pyridinium hydrochloride solution for 20 minutes under reflux. After cooling down to room temperature, the residual HCl was titrated against NaOH 0.1 N using an automated titration device Methrom 848 titrino plus. Triplicates of resin and blind resins were done. The epoxy value (mol/kg) was calculated according to Equation 3.5.

$$Epoxy\ value\ = f \times N \times \frac{B-A}{m} \qquad \text{(Equation 3.5)}$$

Where f is the correction factor of aqueous NaOH; N is normality of NaOH (mmol/mL); B is volume of NaOH used for blind solution (mL); A is the volume of NaOH used for sample titration (mL); m is the mass of resin sample (g).

Photo-Differential scanning calorimetry (photo-DSC) and Differential scanning calorimetry (DSC)

The photo-DSC analysis of ferulic-based resins was performed on a Mettler Toledo DSC-1 equipped with Gas Controller GC100. A Hamamatsu LIGHTINGCURE LC8 equipped with a mercury lamp and an optic fiber was used to ensure the UV-irradiation on the formulation. The irradiation was directed on the open aluminum pan with the formulation and an open empty pan used as references. The samples were irradiated two time to investigate the completeness of the UV-curing process. Indeed, the second step allows the generation of the base line of the method since no exothermic peak are visible in case of complete UV-curing. The final curve is the result of the subtraction between the two UV steps. Regarding the thiol-epoxy system different temperatures (25, 50, 75 and 100 °C) were selected to investigate the benefit of the UV-irradiation. Moreover, isothermal analysis of one hour at the selected temperature without UV-irradiation was performed to reveal the influence of temperature during cure. The thiol-epoxy conversion for the FeADE_SH formulations and the epoxy conversion of FeADE_YTT system achieved by thermal curing were calculated by Equation 3.6.

$$Conversion = \frac{\Delta H_{exp}}{\Delta H_{dynamic}} \qquad \text{(Equation 3.6)}$$

Where ΔH_{exp} is the enthalpy registered in the isocuring condition and $\Delta H_{dynamic}$ is the enthalpy evaluated in the dynamic run performed from 25 to 300 °C which can theoretically guarantee complete curing. Thus, it can be taken as references to evaluate the conversion.

Finally, the dynamic curing was performed on epoxy formulation containing YTT. Heating rates of 2, 5, 10 or 20 K/min, respectively, were applied from 25 to 300 °C. The isothermal runs were conducted at 150, 160, 170 and 180 °C and

Equation 3.7 was used to describe the curing process [228] and Equation 3.7 was used to derive the activation energy of the curing process [229,230].

$$\frac{d\alpha}{dt} = Ae^{-\frac{E_a}{RT}}f(\alpha) \qquad \text{(Equation 3.7)}$$

Where α is the fraction of the conversion, t is the curing time, $d\alpha/dt$ is the conversion rate, A is the preexponential factor, E_a is the activation energy, R is the gas constant, T is the absolute temperature. Equation 3.7 represents the kinetic model for the evaluation of the thermal curing.

$$\frac{d\left[\frac{\ln(\phi)}{T_p^2}\right]}{d\left(\frac{1}{T_p}\right)} = -\frac{E_a}{R} \qquad \text{(Equation 3.8)}$$

Where ϕ is the heating rate (°C/min) and T_p is the maximum in the dynamic DSC curve. From the slope of the Arrhenius plot the E_a can be determined.

The DSC was also performed on UV-cured thermoset and thermally cured ones to investigate the thermal behavior of the different thermosets. The first heating went from 25 to 100 °C to eliminate the thermal history; then the chamber was cooled until – 40 °C, finally a second heating to detect the T_g was applied until 250 °C. The dynamic stage were set at 10 °C/min and the analysis was performed in a nitrogen atmosphere with a flow rate 40 mL/min. In this study 40 μL aluminum pans were used. The data were analyzed with Mettler Toledo STARe software V9.2.

Considering the isosorbide-based epoxy monomer, photo-DSC analysis was performed to investigate the UV-curing process. The Equation 3.9 was used to evaluate the epoxy conversion (EC_{DSC}) taking as reference the theoretical value of reaction enthalpy equal to 70 KJ/mol as reported in literature [231–234]. For the formulations bearing the filler (MAC) a correction factor (*f*) was applied considering that only the epoxy monomer participate to the cross-linking reaction. A *f* factor of 0.9 was used for IDGE_10MAC, 0.8 for IDGE_20MAC and 0.7 for IDGE_30MAC to ensure a right evaluation of the conversion (*f=1* was used for pristine IDGE).

$$\textit{Epoxy Conversion } (EC_{DSC}) = \frac{\Delta H_{exp}}{\Delta H_{teo}} \times \frac{1}{f} \qquad \text{(Equation 3.9)}$$

DSC measurements were also performed on UV-cured thermosets to investigate the thermal behavior of the coatings. Heating from 25 to 100 °C to eliminate the thermal history; then the chamber was cooled until – 20 °C, finally a second heating to detect the T_g was applied up to 250 °C. The heating and the cooling rates were set at 10 °C/min and the analysis was performed in a nitrogen atmosphere with a flow rate 40 mL/min. In this study 40 μL aluminum pans were used. The data were analyzed with Mettler Toledo STARe software V9.2.

Lasty, considering the 3D printing study, photo-DSC measurements were conducted on a Netzsch DSC 204 F1 with autosampler to determine the epoxy reactivity of the bio-based oils. All tests were performed in isothermal condition at different temperatures, at 25, 50, 75, and 100 °C under a N_2 atmosphere. The resins (10-15 mg) were irradiated twice with filtered UV-light (320-500 nm) via an Exfo OmniCureTM series 2000 broadband Hg-lamp under constant N_2 flow (20 mL/min). The light intensity was set around to 60 mW/cm^2 on the surface of the sample. The heat flow of the polymerization reaction was recorded as a function of time. Different parameters were analyzed: the time of which the maximum of heat evolution was reached (t_{max}), the height of the exothermic peaks (h_{peak}), and the total enthalpy (ΔH), evaluated as the integration of the curing peak. All measurements were performed in triplicate with satisfactory reproducibility. The epoxy conversion (EC_{DSC}) was evaluated according to Equation 3.10.

$$EC_{DSC} = \left(\frac{\Delta H \times f_f}{Epoxy\ value}\right) \times \Delta H_0^{-1} \qquad \text{(Equation 3.10)}$$

Where ΔH is the total enthalpy generated from the cross-linking reaction (J/g); f_f is the correction factor used for the formulation containing the filler; *Epoxy value* is the epoxy value of the resin used for the different formulations (mol/kg); ΔH_0 is the theoretical enthalpy which was between 66 and 75 kJ/mol [234,235].

The photo-DSC also allowed the evaluation of the Rate of Polymerization (R_P) by Equation 3.11.

$$R_P = \frac{h_{peak} \times \rho \times 1000}{\Delta H_0} \qquad \text{(Equation 3.11)}$$

Where h_{peak} is the height of the photo-DSC exothermic reaction peak (W/g); ρ is the density (g/mL) of the resin evaluated by pycnometer (triplicates were measured to determine the value); ΔH_0 is the theoretical enthalpy (kJ/mol).

UV-vis spectroscopy

The monomer light absorption was evaluated with a Jenway 6850 UV/Vis Spectrophotometer. The spectra were recorded from 600 nm to 200 nm. Quartz cuvettes were used for the bio-based monomers. Acetonitrile was used as solvent and different concentrations of FeADE and IDGE were tested.

Simultaneous thermogravimetry–differential scanning calorimetry (STA)

The resins investigate for the Hot-lithography were tested by means of STA 449F1 Jupiter from Netzsch in order to evaluate the curing stage and the start of the degradation. Uncured formulations of ELO and ESO were tested to investigate the thermal stability and the thermal activation of the photoinitiators employed. Moreover UV-cured samples were analyzed to investigate the possibility of post curing. The samples around 15 mg were placed into aluminum pan and sealed. The test was performed in controlled atmosphere of N_2 with 20 mL/min flow. The dynamic temperature ramp was set with an increase of 10 °C/min from room temperature (r.t.) to 300 °C. The data of weight loss and heat flow were analyzed by NETZSCH-Proteus-80. T_{95} was evaluated as the temperature which the sample had 5 % of weight loss.

Viscosity and Stability test

The Anton Paar MC 302 was used to evaluate the steady shear viscosity of the IDGE-based formulation. A plate-plate geometry was used with both metal plate. The upper disk was 2.5 cm diameter and the distance was kept to 400 μm. The test was done with a shear rate varying from 0.1 to 1000 s^{-1}.

Instead, the stability test for the formulations used in Hot-lithography was performed by means of viscosity measurements at printing temperature. An Anton Paar MCR300 was used to examine the viscosity of the epoxy resins through the time. A plate-plate geometry was chosen, and the diameter of the support was 25 mm. The distance between the disks was 400 μm. The formulations were kept at printing temperature for all the time in an oven. The viscosity was measured by applying an increase shear stress from 1 to 100 1/s after 60 seconds of stabilization.

Gel content

The gel content percentage (% gel) of the IDGE coatings was determined by measuring the weight loss after 24 h extraction with chloroform at room temperature. The samples after the immersion were allowed to dry for 24 h in air. % gel was calculated according to Equation 3.2.

Dynamic mechanical thermal analysis (DMTA)

The thermal mechanical analysis of the thermoset derived from FeADE and IDGE was carried out with a Triton Technology instrument. The instrument applied uniaxial tensile stress at frequency of 1 Hz with a heating rate of 3 °C/min. The initial temperature of – 40 °C was achieved by cooling down the test chamber with liquid nitrogen. The samples were UV-irradiated in rectangular silicon mold with dimensions of $12\times4\times0.3$ mm^3.

The samples derived from 3D printing were tested by means of an Anton Paar MCR 301 device with a CTD 450 oven and an SRF 12 measuring system. The 3D printed DMTA samples at 100 °C were tested in torsion mode with a frequency of 1 Hz and a strain of 0.1 %. The dimensions were $40\times4\times2$ mm^3. The temperature was increased from −50 to 150 °C with a heating rate of 2 °C/min.

The measurements were done to detect the T_g as maximum of $Tan\ \delta$ curve and were stopped after the rubbery plateau. Moreover, it was possible to evaluate the cross-link density (v_c) calculated by Equation 3.3 derived from the statistical theory of rubber elasticity [117,118].

Tensile test

The tensile test (ASTM D638) of FeADE and IDGE based thermoset was performed on a 5B type dog-bone samples (with l_0 = 12 mm, $A_0 \approx 3$ mm^2). The stress-strain curve was registered using an electromechanical universal machine (MTS QTestTM/10 Elite, MTS System Corporation) controlled with a measurement software (TestWorks® 4, MTS System Corporation). A 500 KN load cell was used, and the crosshead speed of the machine was set as 5 mm/min. Another tensile test for IDGE-based polymers was run in the SEM to detect crack initiation and to investigate crack propagation. To this aim a DEBEN MT5000 MICROTEST 5KN system was used to tensile test the specimen (5B type dog-bone).

The tensile test of the epoxy oil-based 3D printed dog bone samples was performed by means of Zwick Z050 equipped with a 1 kN load cell (Zwick Roell, Ulm, Germany) according to ISO 527 with a test speed of 5 mm/min. The shape of the specimens was a type 5B and five samples for each formulation were tested.

The printing was done at 100 °C for all specimens. The stress-strain curves were recorded and analyzed via testXpert II testing software.

The tensile test allowed to determine different parameters, the Young's modulus (E) was evaluated in the linear portion of the stress-strain curve from the start of the test, the toughness (U) was calculated as the area under the stress-strain curve, and moreover, strength at break (σ) and strain (ε) were retrieved from the curves.

Mechanical joint characterization

The thermally cured FeADE in the presence of YTT was tested for adhesive applications. The adhesive epoxy glue was tested on different substrates of aluminum, CMC composite and steel. Aluminum was a precipitation-hardened EN AW-6082 T6 alloy; CMC was a carbon short-fiber reinforced core material. This core material undergoes a liquid silicon infiltration process after the manufacturing of the green body and pyrolysis. During this infiltration, an *in-situ* reaction takes place between silicon and carbon, leading to the formation of silicon carbide. As a result of this process, the silicon infiltration leaves behind a porosity ranging from 0.5 % to 3.0 %. Upon completion of the manufacturing process, the CMCs consist of a mixture of free silicon, silicon carbide, and carbon, as both carbon fiber and residual pyrolytic carbon, in a 15-50-35 % ratio respectively. The steel was an AISI 441. The substrates were cut into a rectangular shape (~ 25×25 mm^2) and they were joined in a single shear-lap test. The surfaces of the substrate were polished to guarantee uniformity in the contact between surface and adhesive. A polishing machine, equipped with sandpaper (400 grit), was used and after the polishing treatment, substrates were sequentially rinsed in a sonic bath with ethanol. A spatula was used to apply the adhesive on the facing surfaces, ensuring a sufficient amount of mixed adhesive was used to achieve an appropriate thickness for the final adhesive bond area. The adhesive thickness was range between 0.2 and 0.3 μm and the area of the joint was about half of the length of the substrate (~ 12×25 mm^2). The thickness of the joint was derived measuring the thickness of the total piece subtracting the thickness of the two substrates. The shear strength was evaluated by applying Equation 3.12 where *Load* was the maximum force applied on the joint while the *Adhesive area* was the area of the glue joint.

$$\tau = \frac{Load}{Adhesive\ area} \qquad \text{(Equation 3.12)}$$

The mechanical strength (apparent shear strength) of the joined samples was assessed through a single lap offset (SLO) test conducted under compression at room temperature. The testing method employed was adapted from the ASTM D1002-05 standard, utilizing the universal testing machine SINTEC D/10 with a cross-head speed of 0.5 mm/min. At least five samples were tested for each similar joint (i.e steel-to -steel, CMC to CMC, aluminum-to-aluminum). The results of the mechanical tests were expressed as mean ± standard deviation.

Thermogravimetric analysis (TGA)

The thermal stability of the IDGE coatings was studied by means of a Mettler Toledo TGA1. The test was done imposing a heating ramp of 10 °C/min from r.t. to 700 °C under N_2 atmosphere with flow of 40 mL/min. The analysis was done considering different features: T_5, temperature at which the sample lost 5 wt%; T_{peak}, temperature at peak of degradation, evaluated as peak of the first derivative, and *Char*, analyzed as final char residue in wt%.

Chemical degradation

The 3D printed samples derived from tensile test (100-150 mg) were immersed into an alkaline solution of NaOH 10 M (20 mL) and magnetically stirred (300 rpm) on a thermoregulate mixer at 80 °C. The degradation was evaluated by mass loss weighting the samples after a determined amount of time. The samples were recovered from the alkaline solution, washed with acidic solution to avoid salt formation and deionized water, then they were dried overnight in a vacuum oven at 60 °C. The loss evaluation over time was performed according to the Equation 3.13 was used for the evaluation.

$$Mass\ fraction = \frac{W_\mathrm{r}}{W_\mathrm{i}} * 100 \qquad \text{(Equation 3.13)}$$

where Wr is the weight of the residual sample after the treatment in NaOH and Wi is the initial weight of the sample before the treatment.

The mixtures derived from ELO and ELO_T200_20 after the alkaline treatment were centrifugate by means of Centrifuge 5804 R, Eppendorf. The yellow solution was acidified with HCl, and the final precipitate was centrifugate. ATR-FTIR analysis and ^{1}H-NMR analysis were carried out on the final product.

Contact angle, hardness, roughness and adhesion

The main coating properties, such as contact angle, hardness, roughness and adhesion, were tested for IDGE-based coating. The contact angle test was performed on the free surface using water. The instrument used was a Drop Shape Analyzer, DSA100, Kruss. The hardness was measured by means of Shore D indentation instrument according to the ASTM2240. The roughness was investigated employing a RTP80 Alpa roughness tester, the analysis was performed with a length of 1.5 mm and a cut off of 0.25 mm. Considering that the curing was performed in a silicon mold the rugosity measurements were performed in both side of the samples: free side surface and side in contact with the silicon. The sample were cured with UV-DYMAX Flood lamp as previously described. The adhesion test was performed according to the ISO 2409 (ASTM D3359). Eclometer 107, as cross hatch cutter, was used for determining the adhesion of the photocured coating on glass substates. The insert number 3 was used as cutter to perform the test. The samples were spread on the glas and UV-cured with UV-DYMAX Flood lamp for 2 min with a light intensity of 100 mW/cm^2.

Morphology

The morphology of the different polymer materials was investigated by FESEM, Zeiss SUPRA 40. Firstly, the fillers were seen to investigate the morphology and the effective dimension. Then, the cross-sections of the broken tensile samples were analyzed to investigate the interaction between filler and polymer matrix. The different samples were glue on SEM stubs by carbon tape and metal clamps, then a coating of 5 nm of Pt was sputtered on top of the sample to ensure conductivity on the surface.

3.2.2. Result and discussion

3.2.2.1. Synthesis route and characterization of ferulic-, isosorbide-based epoxy monomers and epoxy vegetable oils

The epoxy monomers were used to develop photocurable resin aiming to produce green thermosets. Two distinct approaches were used to achieve the formation of the epoxy rings. Regarding the ferulic acid, the etherification reaction was conducted by reacting phenol group (-OH) and the OH-group of the cinnamic acid with epichlorohydrin (ECH) in a one-step reaction. This procedure adhered to establish protocols outlined in the literature [115,187] ensuring excellent conversion, straightforward purification step, and very high purity of the final product, as confirmed by NMR analysis (**Figure 3.27A**). Moreover, the high scalability of the reaction made it possible to obtain the required amount of product for the further characterization. However, it's important to note that the involvement of ECH as the epoxidation reagent may pose limitations from an environmental perspective [119], as previously describe in the Paragraph 3.3.1. Nevertheless, currently this reagent remains indispensable to achieve the epoxidation of several bio-based monomers [120–122].

The epoxidation of the isosorbide involved a two-steps reaction. This allowed the avoidance of ECH, and thereby increasing the safety of the entire process. The epoxidation reaction involved the allylation of the OH-groups of the isosorbide and the subsequent oxidation of the double bond by reaction with m-CPBA. This method has been verified to yield a formation of pure bifunctional monomer [223,224]. The first step reached final yield of 85 % and high purity confirmed by NMR analysis (**Figure 3.27B**). The subsequent oxidation step reached 60 % yield generating the pure bifunctional epoxy monomer, IDGE, as confirmed by NMR analysis (**Figure 3.27C**).

In the last work conducted on EVOs, NMR analysis was used to validate the experimental epoxy value obtained for ESO and ELO, which were commercially supplied. The epoxy number of the resins calculated by titration, 5.55 ± 0.10 and 4.36 ± 0.7 for ELO and ESO respectively, was verified through ^{1}H-NMR (**Figure 3.27D**, epoxy value derived by NMR analysis for ELO: 5.29).

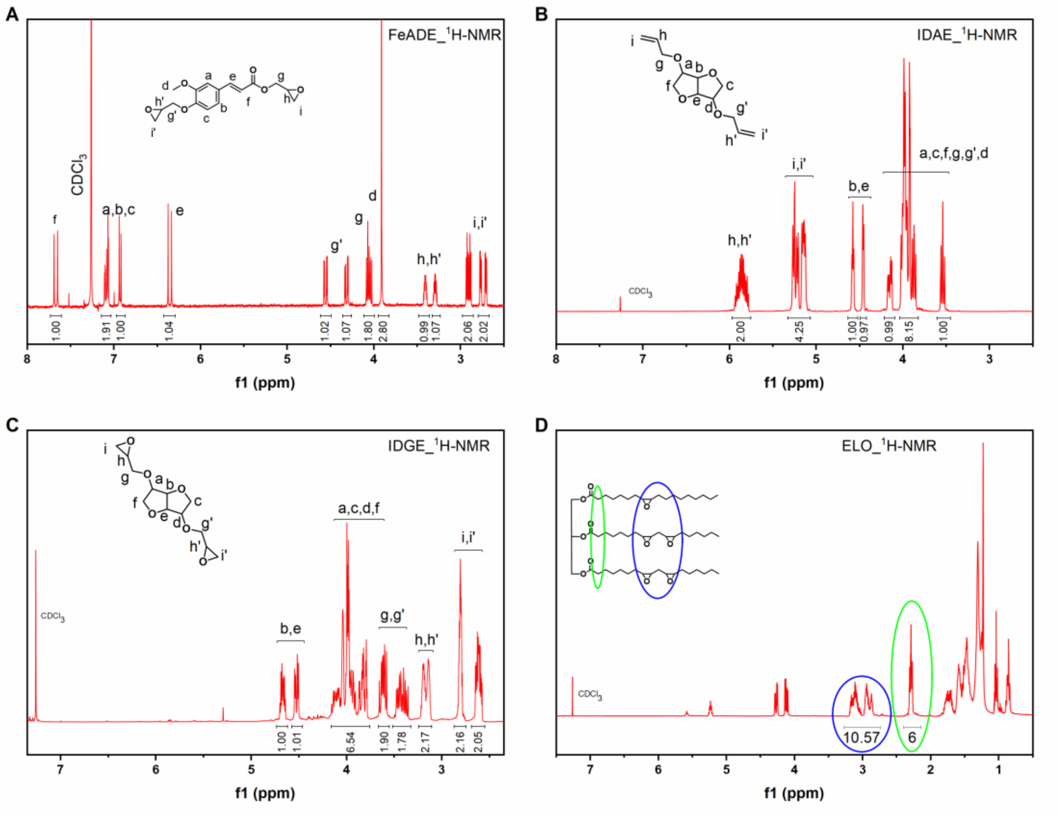

Figure 3.27. (A) ^{1}H-NMR of epoxy ferulic acid (FeADE); (B) ^{1}H-NMR of isosorbide-based allyl intermediate (IDAE); (C) ^{1}H-NMR of isosorbide-based epoxy (IDGE); (D) ^{1}H-NMR of epoxy linseed oil (ELO).

3.2.2.2. Filler characterization

The fillers used for the reinforced coatings and for the bio-based composites were characterized by SEM analysis to investigate dimension and morphology. Macadamia powder (**Figure 3.28**) had average dimension of 132 ± 72 um evaluated by image analysis where it also visible the irregular shape of the powder particles. Instead, the fillers used for the composites were received in two different mesh, 200 and 325. The mesh 200 indicate a minimum of 88 % of particles below 75 µm while the mesh 325 ensure that at least 88 % of particle have a diameter below 45 µm. **Figure 3.29** reports the ATR-FTIR analysis and the SEM analysis of the fillers to evaluate chemical and morphological features of the powders.

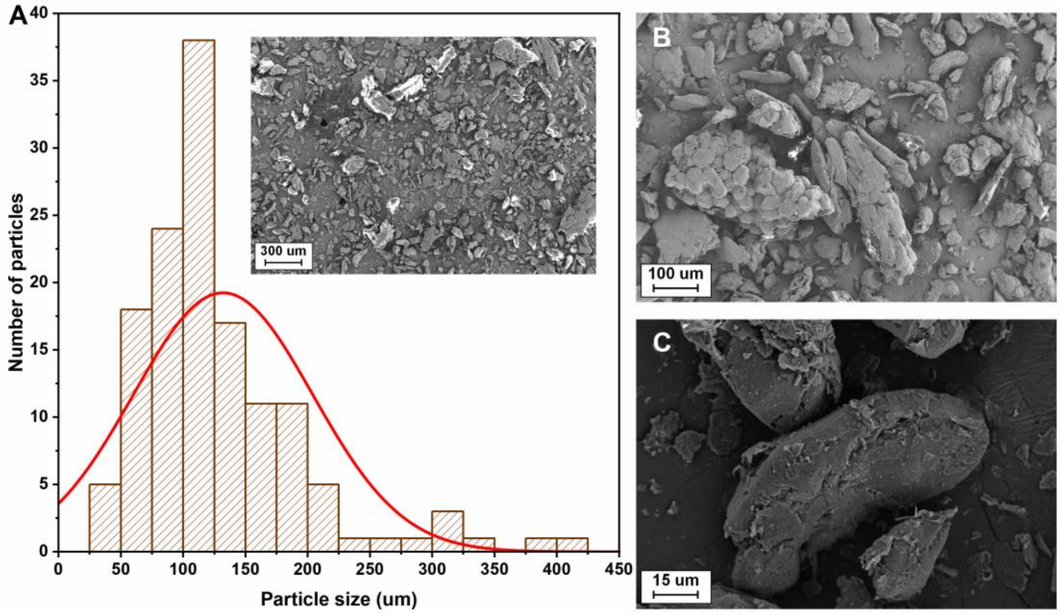

Figure 3.28. (A) Morphological analysis of macadamia filler performed by SEM analysis (image at 100× magnification); (B) Macadamia nut shell powder at magnification 300×; (C) image of the filler obtained at magnification 2000×.

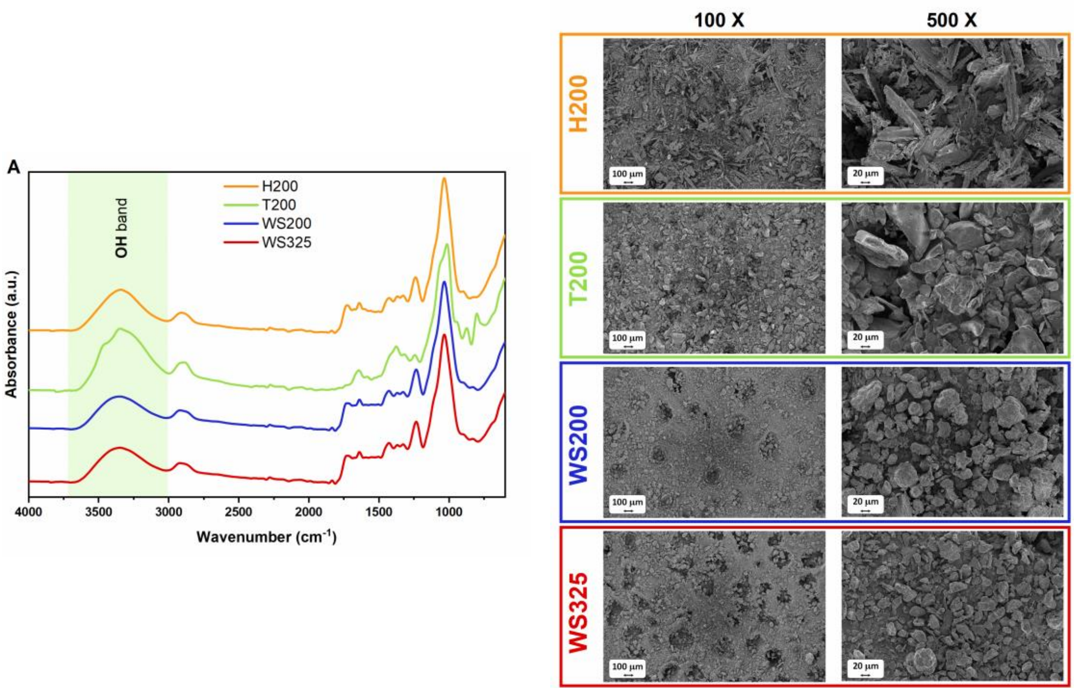

Figure 3.29. (A) ATR-FTIR analysis of the different fillers; (B) SEM analysis performed at 100× and 200× magnification of the different fillers (H200, T200, WS200, and WS325).

3.2.2.2. Multiple approaches for ferulic acid bio-based green thermoset

The growing need to expand the portfolio of green monomers to develop new resins for thermoset drives the attention to exploit ferulic acid-based epoxy monomer as main compound for UV-curable resin. In this framework, FeADE was used as epoxy monomer to develop a UV-curable green thermoset. Unfortunately, owing to the limit success of this approach, other two different strategies were explored to achieve proper formation of a polymer network: a thiol-epoxy anionic reaction and a thermally cationic reaction (**Figure 3.30**).

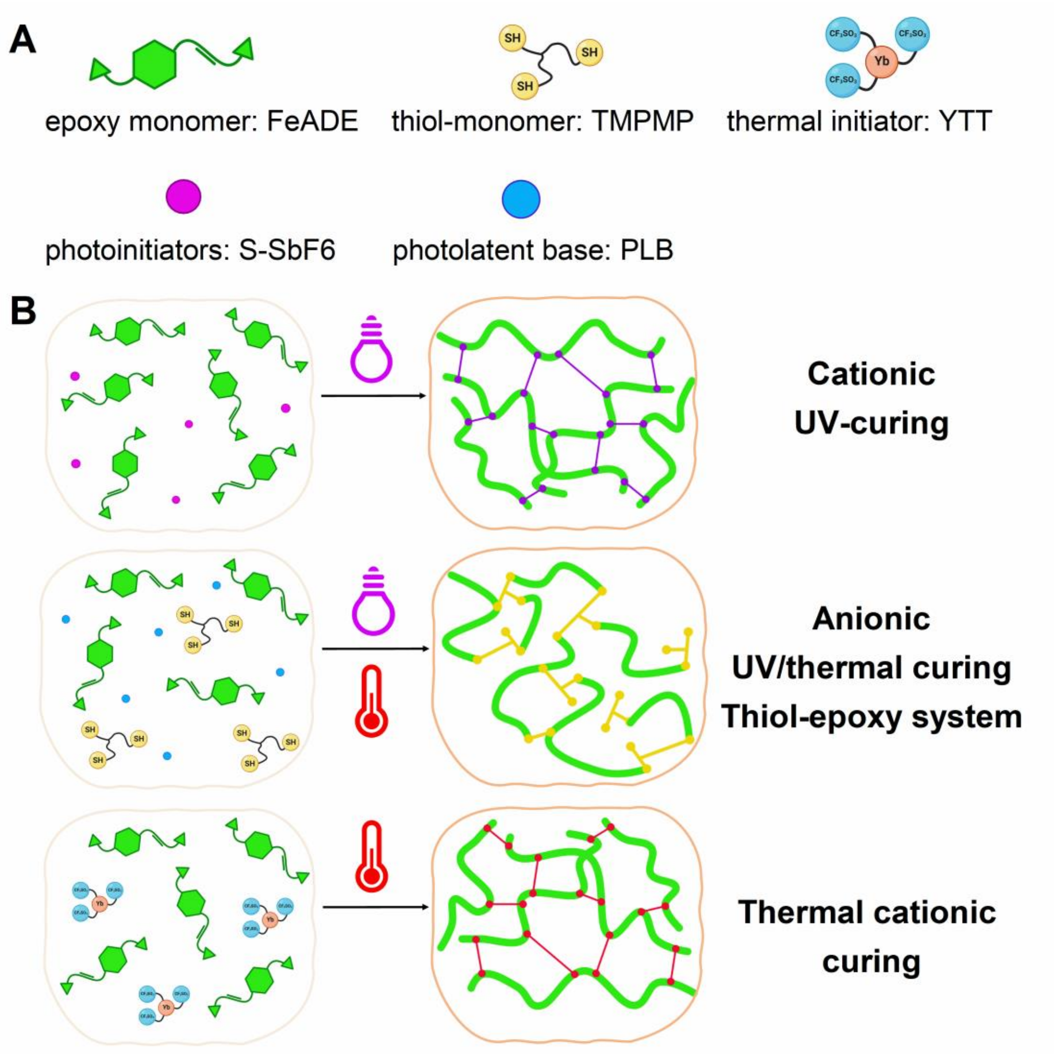

Figure 3.30. (A) Monomers and initiators used in the study; (B) Different approaches used in the study for the curing of FeADE.

Cationic UV-curing

The cationic UV-curing of FeADE was conducted in presence of I-SbF6 as photoinitiator and it was studied by means of ATR-FTIR and DSC analysis (**Figure 3.31**). It's worth noting that the epoxy ring opening was only partial/incomplete as can be notice by the slightly reduction of the epoxy peak located at 905 cm^{-1} and 855 cm^{-1}. The reaction was confirmed by the increase of the OH band located at 3500 cm^{-1}. Instead, as expected the C=C double bond was not affected by the cationic curing. The incomplete reaction was further confirmed by DSC analysis due to the presence of a T_g of 10 °C and an exothermic curing peak centered around 150 °C during the first heating run. Moreover, it was possible to assess the theoretical T_g of about 120 °C achievable with complete cross-linking. This is the result of the thermal curing of the first stage which started by thermal degradation of I-SbF6. Indeed, the photoinitiator can undergo thermal degradation, starting the epoxy curing [159].

The limitation encountered during curing can be elucidated by examining the UV-visible spectra of FeADE (as shown in **Figure 3.31C**), which reveals an exceptionally wide and intense absorption peak spanning from 200 to 400 nm. The monomer absorption competes with the absorption of the cationic photoinitiator, severely hindering the overall efficiency of the curing process. Additionally, the strong absorption of the monomer itself can restrict the penetration depth of the light.

Hence, we can conclude that the inherent chemical nature of the initial monomer is a constraining factor in the utilization of the cationic UV-curing process. Nevertheless, this challenge has motivated to rethink the system and explore two alternative solutions. Firstly, it was considered a thiol-epoxy system activated by photo-latent base, and secondly, a cationic thermal-curing method activated by Ytterbium initiator was employed to create ferulic-based thermosets.

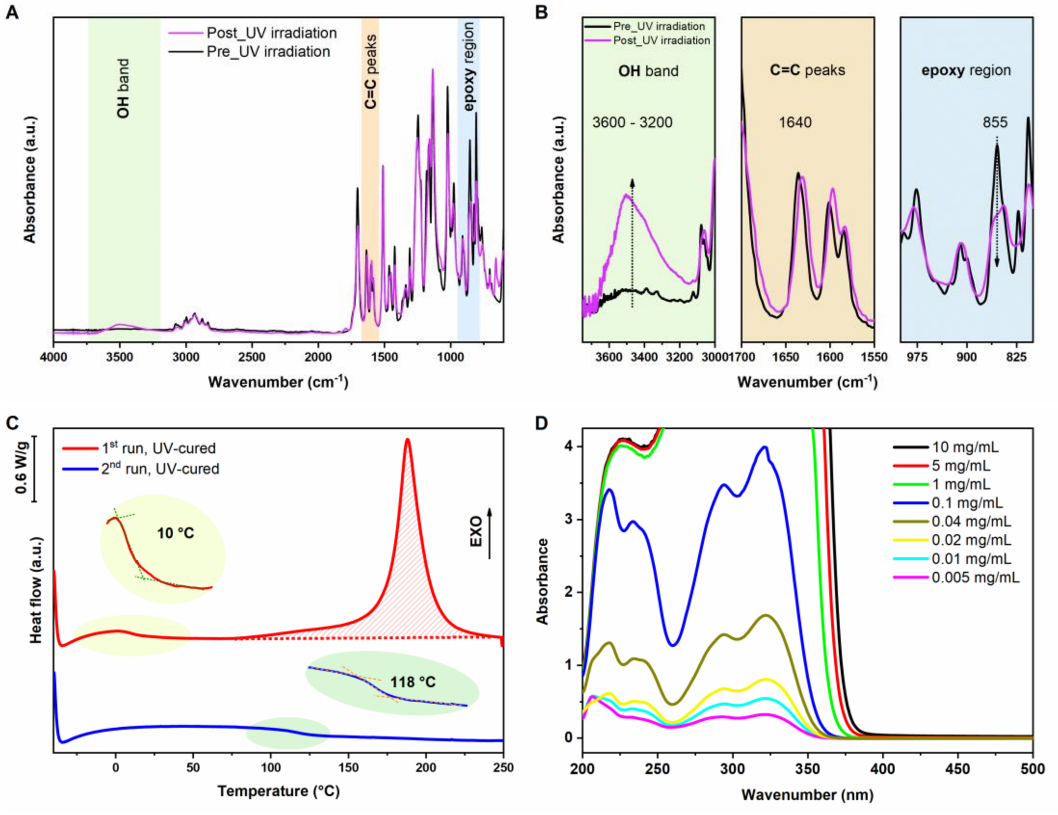

Figure 3.31. (A) ART-FTIR pre and post UV-irradiation of FeADE; (B) highlight of the OH band, C=C peak and epoxy region before and after UV-irradiation; (C) DSC analysis of cationic UV-cured FeADE, 1st and 2nd runs are presented; (D) UV-vis spectra of the FeADE monomer in acetonitrile at different concentration.

Thiol-epoxy anionic curing

Thiol-epoxy anionic curing systems are activated by UV-light, which leads to the generation of a strong base originating from the photo-latent base (PLB) [236]. PLB deprotonates the thiol group and the resulted anion initiates the opening of the epoxy ring thereby forming a thiol-epoxy crosslinked network [237]. Thus the reaction can be considered “click chemistry” [238–241].

ATR-FTIR analysis was used to monitor the UV-process of formulation containing a stochiometric ratio between the epoxy- and the thiol-groups. Following the ATR-FTIR analysis reported in **Figure 3.32**, the occurrence of the thiol-epoxy reaction was corroborated by the disappearance of the peaks related to epoxy and thiol groups. Additionally, an increase in the OH band was also noticed due to the opening of the epoxy-ring. Lastly, a decrease in the C=C signal was also observed, possible owing to the thiol-ene reaction. For clarity the reactions are showed in **Figure 3.33**, from the UV-activation step of the PLB to the thiol-epoxy and thiol-ene reaction which happen in the studied system.

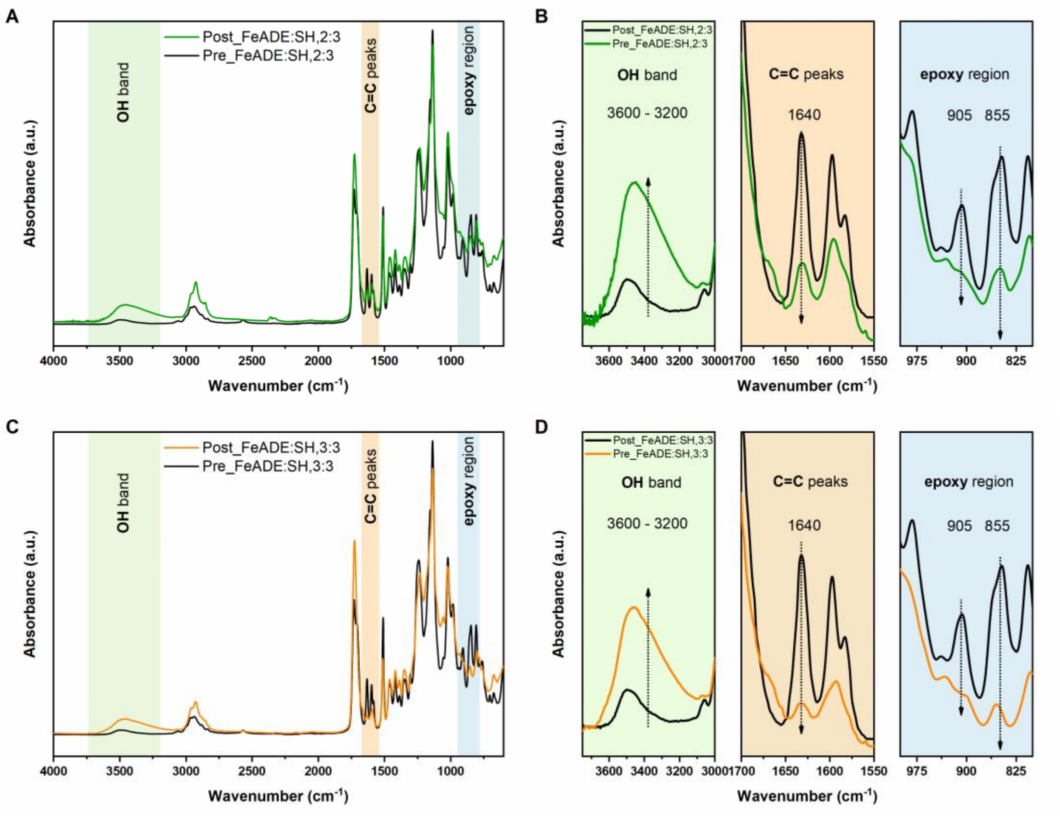

Figure 3.32. (A) ART-FITR of FeADE:SH,2:3 (black and green) and (B) FeADE:SH,3:3 (black and orange) pre and post irradiation with the highlights of the main changes in the bond peaks (B and D) involved into the cross-linking.

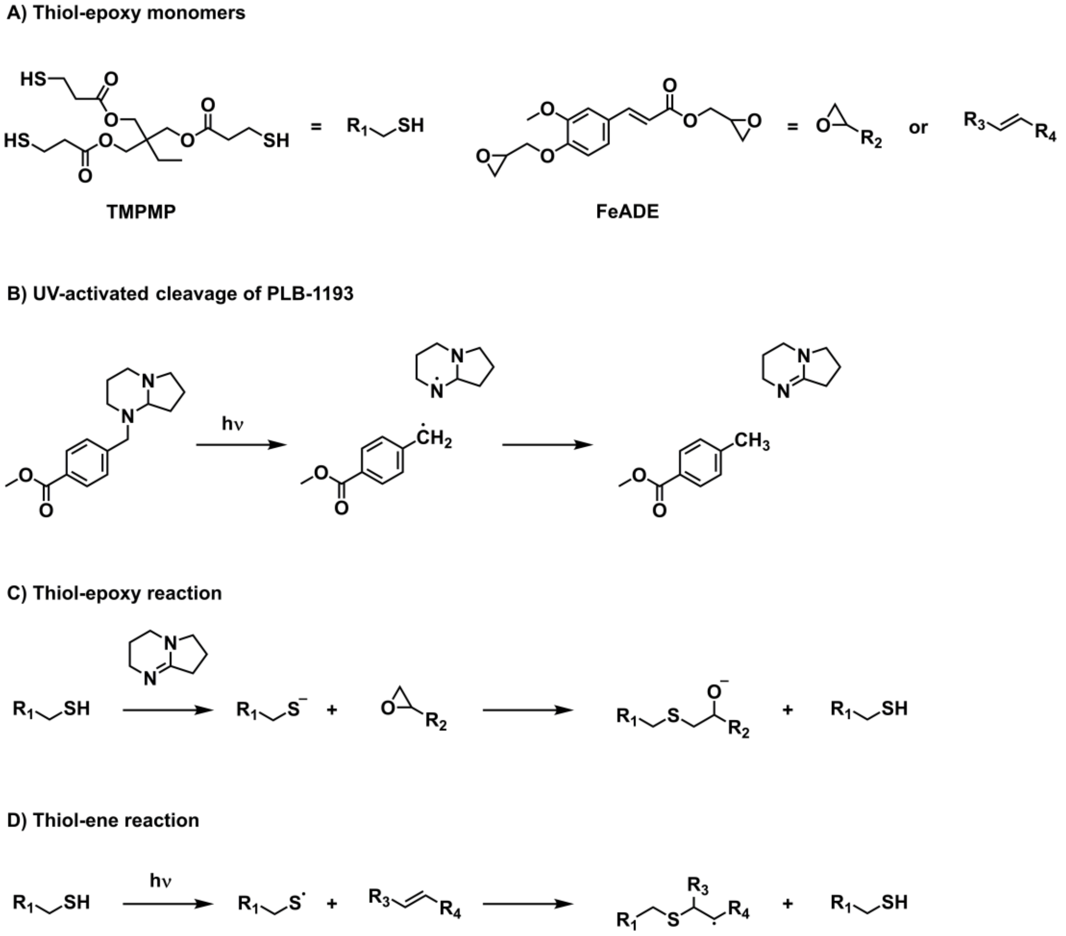

Figure 3.33. Reactions which take place in the thiol-epoxy system. (A) monomers involved in the system; (B) activation mechanism of PLB; (C) thiol-epoxy reaction; (D) thiol-ene reaction.

Considering that thiol-groups under UV-irradiation can also promote the thiol-ene reaction with the double bond of epoxidized ferulic acid besides participating to the thiol-epoxy crosslinking reaction promoted from the photolatent base, an excess of thiol was used to generate a different formulation. The possibility of the C=C double bond reaction in thiol-ene chemistry has been confirmed also in another study [242]. In this new system, a new formulation containing a 1:1 ratio between the thiol- and the functional groups of the FeADE (denoted as FeADE:SH,3:3) was explored. This assumption was done considering three reactive group in FeADE, two epoxy groups and one C=C double bond. ATR-FTIR analysis of the resulting thermoset (**Figure 3.32C**) confirmed the reactivity of the C=C double bond, as highlighted by the disappearance of the C=C peak. The decrease was more pronounced compared to the formulation with stochiometric ratio between epoxy and thiol, denoted as FeADE:SH,2:3 (**Figure 3.32A**), meaning a higher contribute of thiol-ene cross-links.

The last technique employed for the characterization of the curing process was photo-DSC analysis to evaluate the impact of the temperature on the curing (**Table 3.11**). Indeed, heating is required for the mixing of the formulations and it has been establish that the thiol-epoxy reaction can be triggered by heat or UV-irradiation [240,243]. Consequently, the effect of the two components was addressed by photo-DSC analysis and isothermal curing. It's evident that UV-light had a favorable effect on the overall reaction time, reducing it from hours to minutes for the formulations with stochiometric ratio between epoxy and thiol, FeADE:SH,2:3 (**Figure 3.34**). Furthermore, the rate of polymerization significantly increased with UV-irradiation; the peak height at 100 °C was approximately five times higher when the formulation was exposed to UV-light. Nonetheless, temperature played a crucial role in activating the reaction, as confirmed by isothermal curing performed at temperatures of 60, 80, and 100 °C, respectively. Simply increasing the curing temperature from 60 to 100 °C resulted in a substantial reduction in reaction time, directly leading to an acceleration of the reaction, as depicted in **Figure 3.34**. Conversion curves were derived from DSC thermograms by taking the dynamic curing as a reference. The FeADE:SH,2:3 had a total enthalpy of 528 ± 16 J/g while FeADE:SH,3:3 had 394 ± 15 J/g. The UV-irradiation was beneficial to activate the PLB, and hence thereby accelerating the cross-linking reaction. Both formulations showed the same trend confirming a decrease of the total time of the reaction by using UV-stimulus as listed in **Table 3.11**.

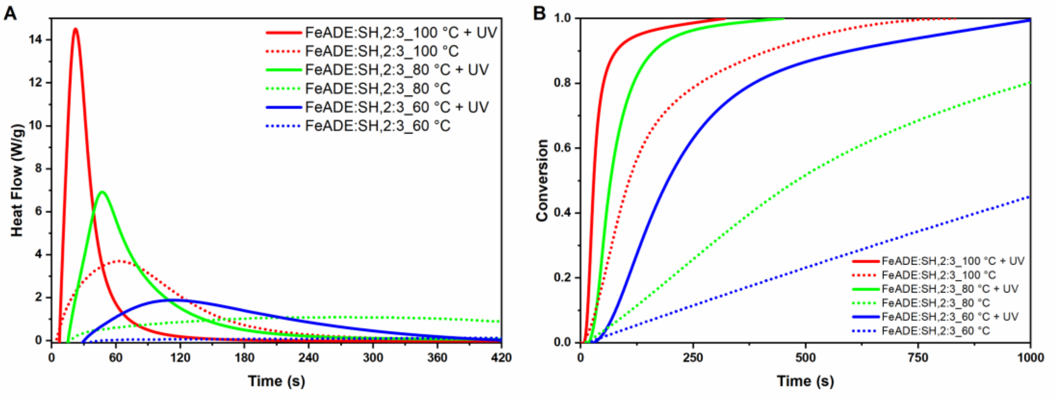

Figure 3.34. (A) Photo-DSC of FAE:SH,2:3 (stochiometric ratio between epoxy and thiol) with 2 wt% of PLB; (B) isothermal curing of FAE:SH,2:3; (C) comparison between the thermograms registered at 100 °C with UV-irradiation (solid line) and without UV-irradiation (dot line) for FAE:SH,2:3.

Table 3.11. DSC analysis of the thiol-epoxy curing performed for the two tested formulation containing a different ratio of thiol. The analyses were conducted in different conditions of temperature and UV-light as describe in the 2nd (T) and 3rd (UV-irradiation) column.

ENTRY	T	UV-irradiation	t_{peak}	h_{peak}	ΔH	Conversion
	(°C)		(s)	(W/g)	(J/g)	(%)
FeADE:SH,2:3	60	-	1290 ± 30	0.40 ± 0.09	498 ± 17	94
	60	UV	118 ± 20	2.18 ± 0.57	494 ± 20	94
	80	-	268 ± 10	1.26 ± 0.23	506 ± 25	96
	80	UV	50 ± 8	7.05 ± 1.63	486 ± 15	92
	100	-	66 ± 25	3.91 ± 0.68	492 ± 15	93
	100	UV	20 ± 2	14.73 ± 0.53	463 ± 10	88
FeADE:SH,3:3	60	-	967 ± 50	0.27 ± 0.04	383 ± 10	97
	60	UV	115 ± 30	1.05 ± 0.31	363 ± 40	92
	80	-	236 ± 25	0.64 ± 0.12	387 ± 37	98
	80	UV	46 ± 8	3.23 ± 0.77	378 ± 23	96
	100	-	80 ± 35	1.67 ± 0.50	384 ± 15	97
	100	UV	25 ± 2	7.87± 0.30	380 ± 10	96

The DMA analysis (**Figure 3.35A**) conducted on the thiol-epoxy system revealed that the varying ratio between TMPMP and FeADE had an interesting impact on the final properties explained considering the influence of thiol-ene network. In the FeADE:SH,2:3 system, the thiol-epoxy reaction were predominant prevailed contributing to higher T_g (47 °C) s compared to FeADE:SH,3:3 (30 °C) where thiol-ene dominated (**Figure 3.35A**). It is well-establish that the thiol-ene systems typically exhibit low T_g, close to room temperature [242,244]. Therefore, a greater contribution of this specific type of bond to the thermoset could contribute to lowering the final T_g. Furthermore, fewer cross-link's bonds (ν = 52 mmol/dm^3) were present in FeADE:SH,3:3 compared to FeADE:SH,2:3 which had a cross-link density of 85 mmol/dm^3. The results were confirmed by DSC analysis.

Lastly, tensile testing was carried out to explore the mechanical behavior (**Figure 3.30B**). The FeADE:SH,2:3 had higher mechanical response than FeADE:SH;3:3. This can be related to the chemical nature of the cross-links. The cross-links are mainly composed by S-C linkage resulting from thiol-ene reaction in the FeADE:SH,3:3 whereas FeADE:SH,2:3 predominantly featured β-hydroxythio-ether linkages derived from thiol-epoxy reaction which potentially could have increased the rigidity of the network. Furthermore, the analysis revealed that the lowest T_g of FeADE:SH,3:3 influenced the mechanical behavior imprinting the highest elongation with respect to FeADE:SH,2:3. Indeed, the polymer network is mainly in the rubbery region at 25 °C while the other had an higher strength with plastic behave due to the higher rigidity of the network.

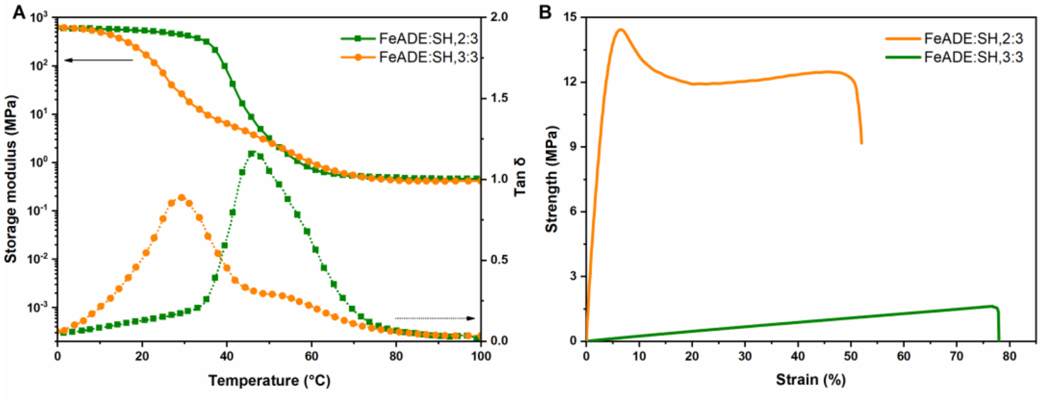

Figure 3. 35. (A) DMTA of FeADE:SH thermosets; FeADE:SH,2:3 (ratio epoxy:thiol = 1:1) reported in green and FeADE:SH,3:3 (ratio functional FeADE group: thiol = 1:1). Y-left axis presents the Storage modulus while Y-right axis shows the *Tan δ*; (B) tensile curves of thiol-epoxy thermosets.

Cationic thermal curing

The second adopted strategy was the pure thermal cationic curing involving the use of a thermal cationic initiator with ytterbium (YTT). Consequently, FAE was combined with YTT and subjected to thermal curing at 150 °C for 2 hours, followed by an additional 2 hours at 180 °C. The effectiveness of this specific initiator has already been demonstrated in previous studies for the thermal cationic curing of epoxy systems [245–247]. The ATR-FTIR analysis (**Figure 3.36**) confirmed the presence of the epoxy ring-opening reaction. Indeed, the disappearance of the epoxy peaks located at 905 and 855 cm^{-1} simultaneous with the appearance of the OH signal at 3450 cm^{-1} were proof of the ring opening. Furthermore, it's noteworthy that the signal associated with the C=C double bond (~1640 cm^{-1}) remained unchanged during the thermal treatment, indicating the occurrence of a pure cationic curing process.

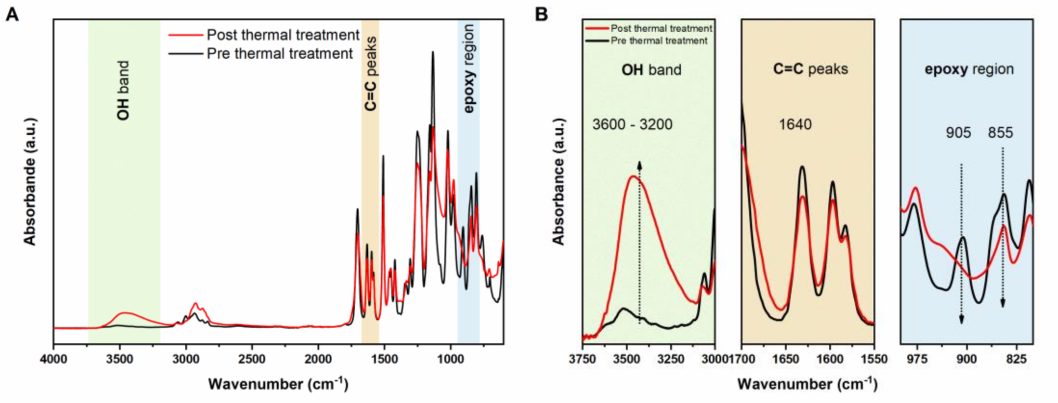

Figure 3.36. (A) ART-FTIR of thermally cured FeADE_YTT at 160 °C and for two hours and 180 °C for other 2 hours (red line) in comparison with the uncured formulation (black line); (B) highlights of the main changes in OH band, C=C region and epoxy one.

The kinetic study and the complete characterization of the thermal curing were conducted by dynamic and isothermal DSC analyses. The activation energy of the epoxy system, determined to be 71.96 KJ/mol, was obtained from the dynamic curing (**Table 3.12**) performed at different heating rate [230,248]. These data allowed the generation of the Arrhenius plot reported in **Figure 3.37**. The experimental E_a aligns with previously reported values for different epoxy systems [231,249]. Isothermal curing was additionally performed to better replicate the curing conditions, aiming for a more precise determination of the optimal time and temperature parameters for the curing process. Different temperatures were selected as listed in **Table 3.13** and illustrate in **Figure 3.37**. Considering the results, the curing method had two-step at 150 °C and 180 °C which needs to start the curing and complete the cross-linking reaction, respectively. The requirement for the second step was validate by DMTA analysis (**Figure 3.38**). Indeed, an increase of T_g was detected for the sample treated with two-step curing method and, in the sample treated only for 2 hours at 150 °C an increase of the storage modulus after the T_g was visible indicating a possible cross-linking due to incomplete curing.

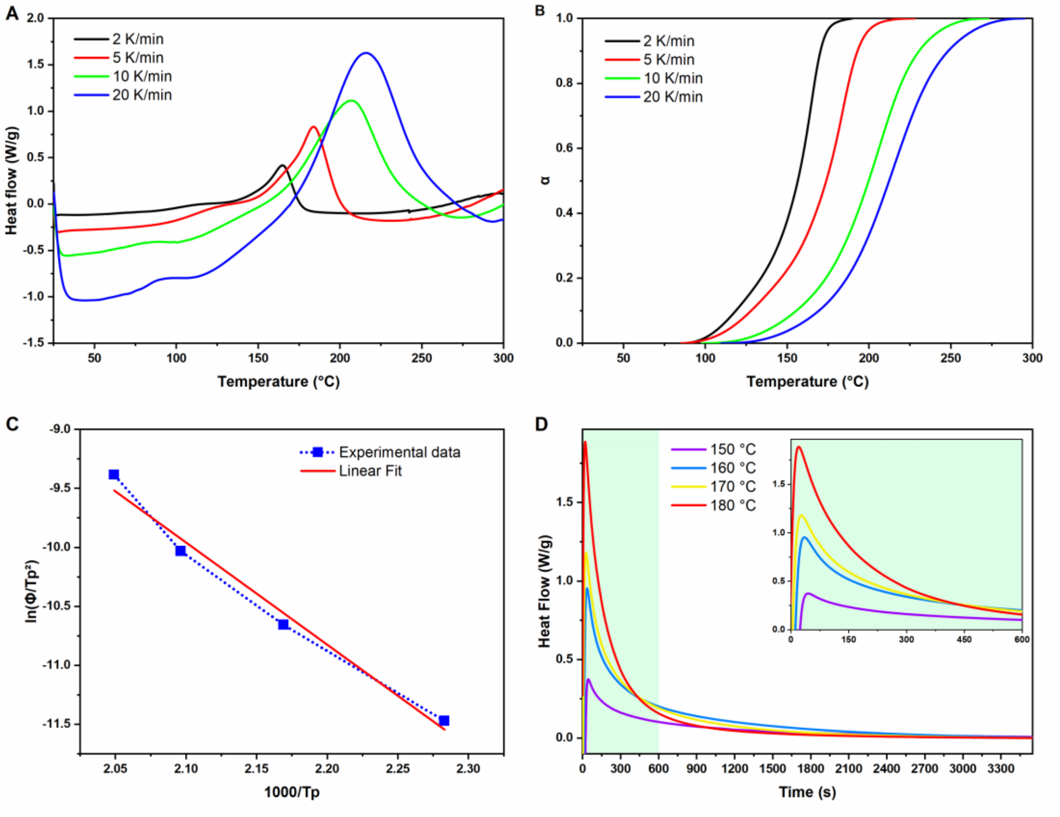

Figure 3.37. (A) Dynamic curing of the FeADE_YTT for different heating rate (2, 5, 10 and 20 K/min); (B) trend of α for the different heating rate in function of the temperature; (C)Arrhenius plot used to calculate the E_a of the epoxy thermal curing; (D) Isocuring performed on FeADE_YTT at different temperature: 150 °C (black line); 160 °C (red line); 170 °C (green line) and 180 ° (blue line).

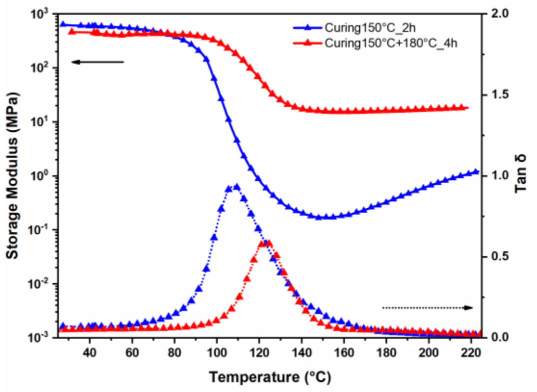

Figure 3.38. DMTA of FeADE_YTT system, left axis present the Storage Modulus while right axis presents the *Tan* δ curves in function of the temperature.

Table 3.12. Data of dynamic DSC curing performed on FeADE_YTT; heating rate (Φ); released enthalpy (*ΔH*); temperature's peak (*T_p); epoxy conversion (EC).*

ENTRY	ϕ	*ΔH*	*T_p*	*EC*
	(K/min)	(J/g)	(°C)	(%)
FAE_YTT	2	413 ± 20	155 ± 9	94
	5	460 ± 28	188 ± 4	≈ 100
	10	465 ± 22	205 ± 2	≈ 100
	20	442 ± 28	211 ± 5	≈ 100

Table 3.13. Results of isocuring of FeADE_YTT performed at different temperatures. Time to reach the peak (t_{peak}), heigh of the peak (h_{peak}), released enthalpy (*ΔH*), and epoxy conversion *(EC).*

ENTRY	Temperature isocuring	t_{peak}	h_{peak}	*ΔH*	*EC*
	(°C)	(s)	(W/g)	(J/g)	(%)
FAE_YTT	150	42 ± 2	0.42 ± 0.05	190 ± 20	43
	160	34 ± 2	0.96 ± 0.04	335 ± 45	76
	170	26 ± 4	1.15 ± 0.05	441 ± 30	≈ 100
	180	18 ± 4	1.88 ± 0.06	435 ± 18	≈ 100

Tensile test was carried out to compare the different thermoset obtained *via* thiol-epoxy and thermal cationic curing. The thermally cured FeADE_YTT showed the highest Young's modulus and strain at break of 774 MPa and 54 MPa respectively. The causes can be detected from the monomer chemistry, presence of aromatic ring, and from the cationic curing which form strong ether bonds (C-O-C). Instead, the thiol-epoxy thermosets were more flexible as mentioned in the previous paragraph. However, the high T_g of FeADE_YTT resulted in a brittle behavior at room temperature, as confirmed by the stress-strain curve under the tested condition (**Figure 3.39A**).

The high T_g and the exceptional mechanical performance open the possibility to investigate this formulation as adhesive. Three different substrates were tested, a ceramic matrix composite (CMC) made of carbon fiber reinforced Si/SiC matrix and two metal based material, aluminum and steel. Strength vs strain curves are reported in **Figure 3.39B** highlighting a brittle behavior of the joint as reported for commercially available fossil-based resin. The metal substrate showed a similar strength value between 20 ± 1 and 24 ± 4 MPa for aluminum and steel joints, respectively. Adhesive failure occurred at the interface between the substrate and epoxy adhesive in AISI/AISI and Al/Al joints, as evident from the samples after the test. Indeed, the adhesive was primarily present on one surface, signifying that the failure initiated at the adhesive-substrate interface.

In contrast, the CMC joints exhibited a cohesive failure within the adhesive, with the highest τ value of 32 ± 3 MPa. Very high adherence at the interface with the substrate can be evident, considering that the epoxy adhesive was present on both surface of the CMC and the failure must be located into the adhesive itself. It can be speculated that the epoxy adhesive spreads on the CMC surfaces infiltrates the open porosities, thus creating a stronger interface, compared to those of adhesive with metallic substrates. The τ achieved for steel and aluminum were consistent with a prior result reported for commercially available resin [250] while the τ for the composite was higher, demonstrating the high potentiality for the bio-based epoxy derivatives in industrial applications.

Table 3.14. Thermoset characterization performed by DSC (^{1}), DMTA (^{2}) analysis and tensile test (^{3}).

ENTRY	T_g ^{1}	T_g ^{2}	ν ^{2}	E ^{3}	σ ^{3}	ε ^{3}
	(°C)	(°C)	(mmol/dm^3)	(MPa)	(MPa)	(%)
FAE:SH,2:3	44 ± 2	48 ± 2	58	250 ± 50	13 ± 3	54 ± 20
FAE:SH,3:3	31 ± 4	29 ± 5	53	2.8 ± 0.3	1.9 ± 0.7	83 ± 16
FAE_YTT	117 ± 3	123 ± 5	1621	774 ± 30	25 ± 7	4.0 ± 1.5

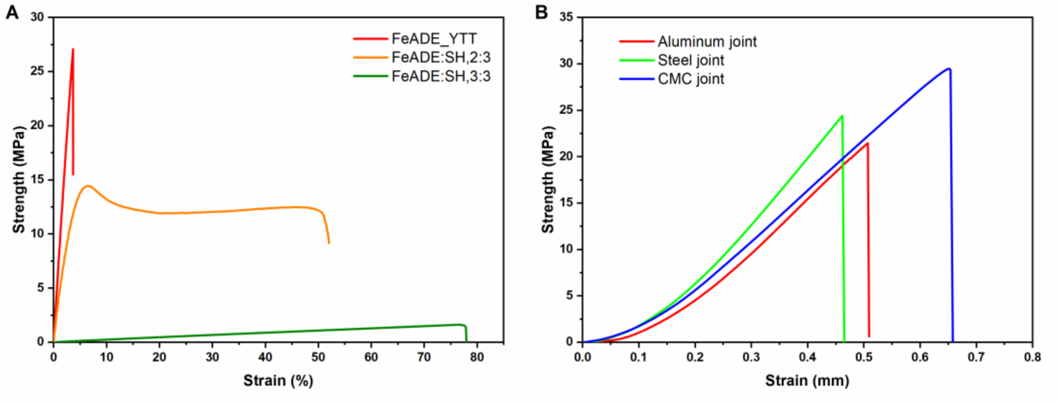

Figure 3.39. (A) tensile test for the FeADE-based thermoset; (B) Shear lap test curves of the FAE_YTT adhesive cured on different substrates, aluminum (red curve), steel (green line) and CMC (blue line). Representative curves are reported.

Additionally, the degradation of the thermosets under alkaline conditions over a period of 2 months was investigated to verify the possible chemical rupture of the network due to the ester bonds (**Figure 3.40**). The ester hydrolysis was significantly different comparing the thermally cured epoxy and thiol-epoxy systems, resulting in various rate of mass loss. This variation can be attributed to the presence of TMPMP, which contains ester bonds in its structure, increasing the susceptibility to degradation. As a result, FeADE:SH,3:3 degraded rapidly (within 4 hours), while FeADE:SH,2:3 required over 200 hours. On the other hand, the thermally cured FeADE_YTT, which contained only the ester bonds inherent to ferulic acid, exhibited the slowest degradation, taking one week to reach approximately 60 % mass loss. Even after two months, traces of about 20 % mass loss were still evident. The high T_g of FeADE_YTT, which allow the maintenance of a glassy state in the network, can contribute to reduce the mobility of polymer chains and the permeation of the degradation solution corroborating the highest resistance in alkaline environment.

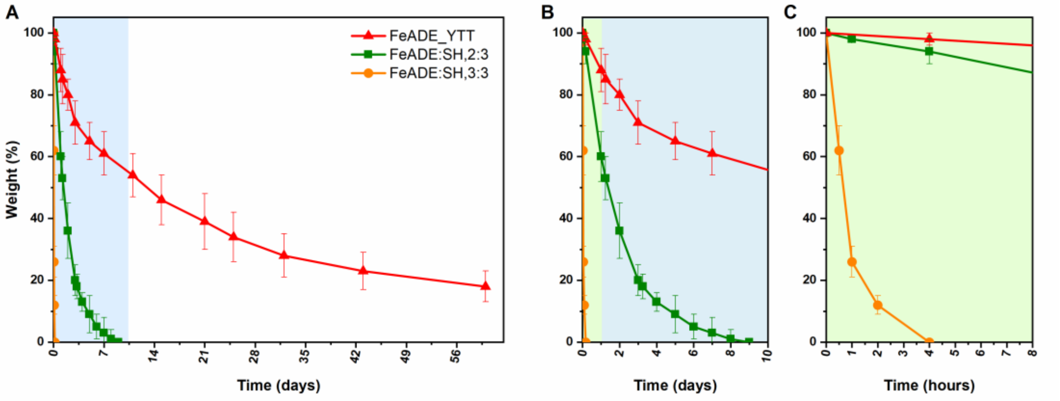

Figure 3.40. (A) degradation study in alkaline environment over 2 months; (B) zoom-in for FeADE:SH,2:3; (C) zoom-in for FeADE:SH,3:3.

3.2.2.3. Isosorbide-based UV-curable epoxy coating reinforced with macadamia nut shell powder

The isosorbide-based epoxy monomer (IDGE) was exploited for the formation of green coatings which were modified by adding macadamia nut shell powder (MAC) to arise the surface hardness (**Figure 3.41**).

Firstly, the UV-curing process was investigated employing different techniques to assess chemical and kinetics aspect of the curing. Real-time FTIR analysis was employed to follow the decrease of the epoxy peaks in the region between 900 and 850 cm^{-1} during the UV-irradiation (**Figure 3.42**). The first analyzed aspect was the amount of photoinitiator which has a crucial role in the UV-curing, thus the rate of photopolymerization was studied varying the amount of I-SbF6. There was a significant increase of the rate of polymerization and conversion passing from 1 to 5 wt% of I-SbF6 as presented in **Figure 3.42B**.

The FTIR data were confirmed by photo-DSC analysis (**Figure 3.42D**), where the conversion was evaluated as the area under the exothermic peak. Indeed, the heat generated during the polymerization process is attributed to ring-opening, thus a larger area under the curve corresponds to higher conversion levels achieved during UV-irradiation. Notably, formulations containing 3 and 5 wt% of photoinitiator exhibited significantly larger areas compared to those with 1 and 2 wt%, thus corroborating the findings from FTIR analysis. The increase in peak height (h_{peak}) with rising photoinitiator content, meant an accelerated rate of polymerization [114,152,159] which was further validated by the reduction in the time required to reach the maximum peak (t_{peak}), decreasing from 120 seconds to 20 seconds. This shift indicated that the maximum rate of polymerization was achieved more rapidly when utilizing 3 or 5 wt% of photoinitiator. Consequently, it was reasonable to employ 3 wt% of I-SbF6 in subsequent work due to its favorable combination of high conversion and rapid kinetics. For a comprehensive overview of the UV-curing data, please refer to **Table 3.15**.

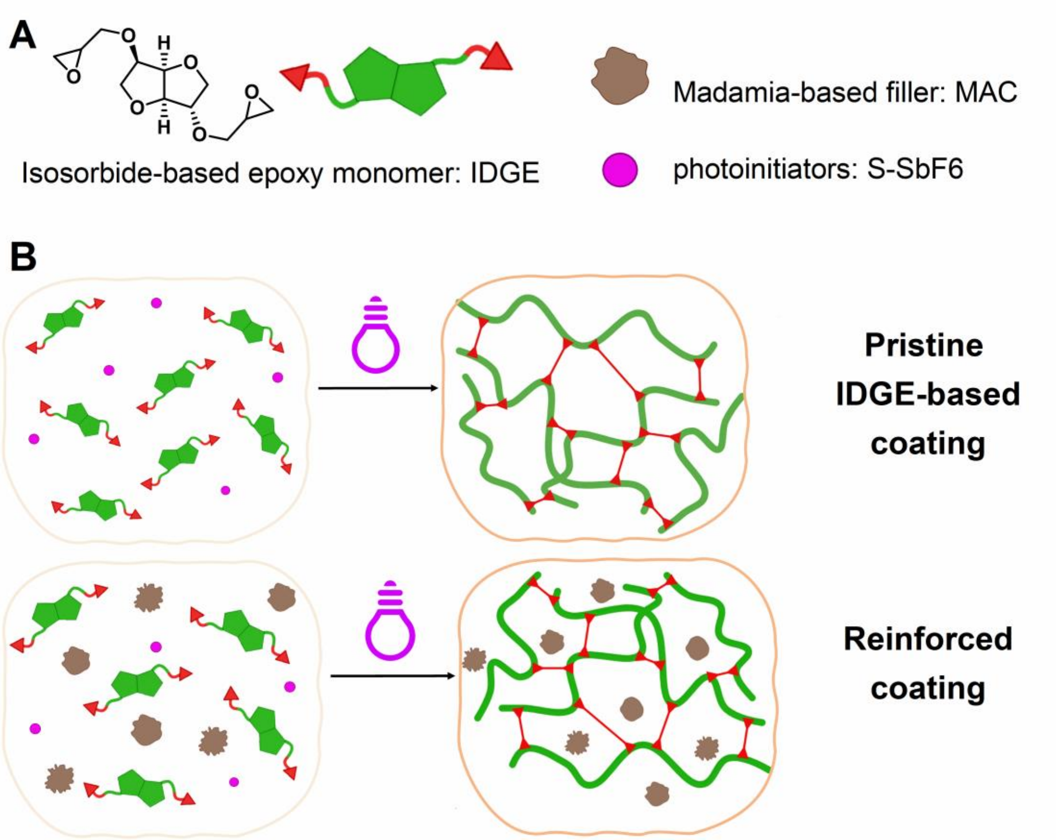

Figure 3.41. (A) Epoxy monomer, filler, and initiator used for the UV-curable formulations; (B) UV-curing of pristine and reinforced coatings.

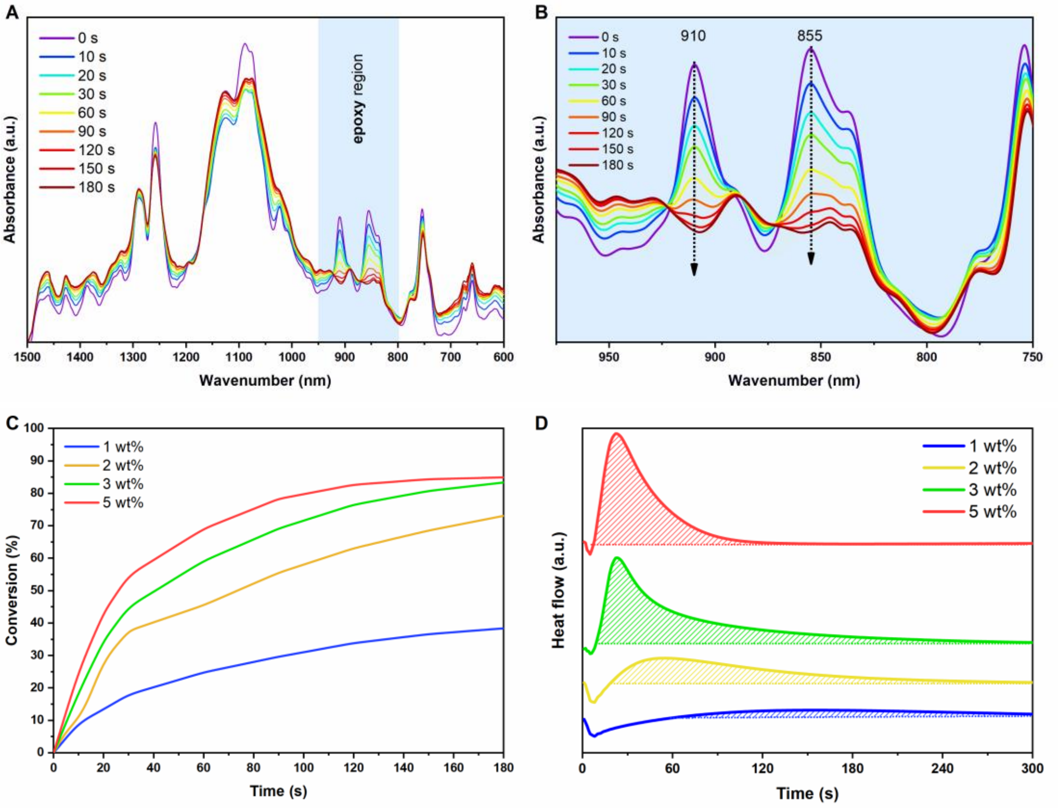

Figure 3.42. (A) FTIR spectra collected at different time for the IDGE with 3 wt% of I-SbF6 as photoinitiator; (B) zoom of the decrease of the epoxy peaks centered at 910 and 855 cm^{-1}; (C) Conversion in function of irradiation time for the IDGE with different amount of photoinitiator; (D) Photo-DSC thermograms for pristine IDGE with 1 wt%, 2 wt%, 3 wt%, and 5 wt% of I-SbF6.

Table 3.15. Epoxy conversion (EC) obtained by real-time FTIR (^{1}) and photo-DSC (^{2}) for the formulation containing IDGE and different amounts of photoinitiator. Height of the exothermic peak of the reaction (h_{peak}) and time of the peak (t_{peak}) evaluated by photo-DSC (^{2}).

FORMULATION	**I-SbF6**	EC^1	$EC_{DSC}{}^2$	$h_{peak}{}^2$	$t_{peak}{}^2$
	(wt%)	(%)	(%)	(W/g)	(s)
IDGE	1	38 ± 8	12 ± 5	1.9 ± 0.5	130 ± 8
IDGE	2	73 ± 3	57 ± 5	2.5 ± 0.4	58 ± 3
IDGE	3	83 ± 2	87 ± 4	10.2 ± 2.8	24 ± 4
IDGE	5	85 ± 1	85 ± 2	13.9 ± 2.8	20 ± 2

As mentioned previously, a common challenge in UV-curing is the limited penetration of light through thick samples, thus photorheology experiment were conducted at different layer thickness to examine light penetration effect. **Figure 3.43A** presents the results, revealing an extension of the induction time with increasing sample thickness, indicating a delay in the cross-linking reaction. To confirm a potential hindrance in the UV-process due to the inherent monomer absorption of the isosorbide-based resin, UV-visible analysis was conducted. As shown in **Figure 3.43B**, the bio-based monomer exhibited higher absorption between 250 and 350 nm, which coincides with the primary UV-emission region used for curing. Consequently, monomer absorption could hindrance the cross-linking of thick layers.

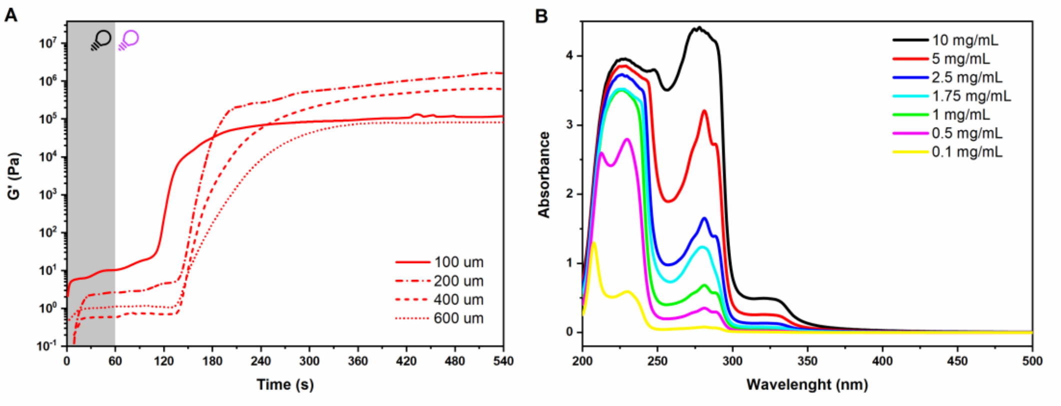

Figure 3.43. (A) Photorheology results of IDGE analyzed at various film thickness between the two plates; (B) UV-vis spectra of IDGE in acetonitrile at different concentrations.

The impact of macadamia nut shell (MAC) to the pristine formulation was investigated by photorheology, FTIR and photo-DSC. The photorheology analysis, presented in **Figure 3.44A** and performed with layer thickness of 200 μm, indicated that the addition of MAC increased the induction time, primarily due to reduced light transmittance through the thicker sample. The presence of the solid filler and its absorption effect limited light penetration, affecting the induction time in the photorheology test. The starting modulus, which can be related to the liquid formulation, has been affected by MAC. Indeed, the increased value can be reconducted to the viscosity which increased due to the filler, displaying a shear-thinning behavior particularly at low shear stress (**Figure 3.44B**).

Photo-DSC results confirmed that the inclusion of MAC hindered the photopolymerization process, evidenced by a reduction in the h_{peak} for formulations containing the filler, indicating slower kinetics and thus a slower polymerization rate (**Figure 3.44C**). However, as evident from the FTIR results, displayed in **Figure 3.44D**, the conversion at the coating's surface was less affected (maintained at a thickness of 32 µm to ensure IR-ray transmittance). This confirms the feasibility of formulating coatings while limitations in conversion for thick sample may arise problems for develop bulk objects. Last validation of network formation was given by gel content of UV-cured samples. The pristine IDGE showed a very high insoluble fraction of 97 % indicating a proper formation of the network. The incorporation of MAC marginally decreased this value, potentially due to reduced light penetration. Nevertheless, the result still exceeded 80 %, affirming the viability of introducing the filler without compromising the ability to process the coatings using UV-light. All the data about the photocuring process are listed in **Table 3.16**.

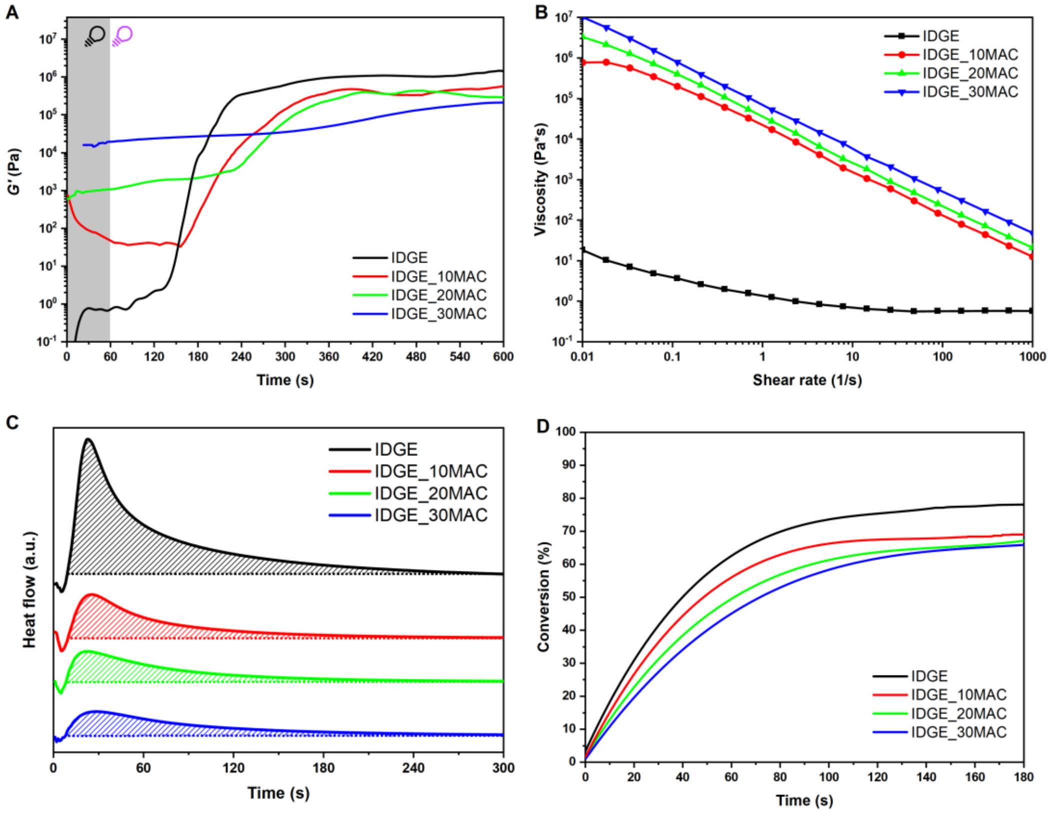

Figure 3.44. (A) Photorheology of pristine IDGE and formulation containing the different amounts of MAC as filler, 10, 20, and 30 wt% respectively; (B) viscosity test performed with the IDGE-based formulation; (C) Photo-DSC thermograms of the formulations; (D) Real-time FTIR conversion of the pristine IDGE and IDGE-based formulations with MAC.

Table 3.16. Epoxy conversion (EC) obtained by real-time FTIR ([1]) and photo-DSC ([2]) for the formulations containing IDGE and different loadings of macadamia nut shell powder. The heigh of the peak of the exothermic curing curves of the photo-DSC ($h_{peak}{}^{2}$) is reported and % gel result are listed for each cross-linked network.

ENTRY	***EC*** ^{1}	***EC*** ^{2}	$h_{peak}{}^{2}$	***% gel***
	(%)	(%)	(W/g)	(%)
IDGE	83 ± 2	87 ± 4	10.2 ± 2.8	97 ± 2
IDGE_10MAC	69 ± 4	55 ± 6	3.9 ± 1.9	87 ± 2
IDGE_20MAC	67 ± 3	53 ± 13	2.4 ± 1.2	83 ± 2
IDGE_30MAC	66 ± 5	57 ± 14	2.1 ± 0.8	85 ± 2

The thermo-mechanical properties of the composites were investigated by DMTA and DSC tests on the UV-cured coatings. **Figure 3.45A** illustrates the trend of *Tan δ* and Storage modulus for both the pristine IDGE and the UV-cured formulations containing MAC. Notably, the inclusion of MAC had a positive impact on the thermo-mechanical properties, resulting in an increase in T_g up to a MAC content of 20 wt%. The pristine IDGE UV-cured coatings displayed a T_g of approximately 24 °C, while coatings with 10 % and 20 % macadamia nut shell powder exhibited Tg values of about 37 °C and 39 °C, respectively. This enhancement in performance can be attributed to the interaction between the filler and the epoxy matrix, which benefits from the intrinsic properties of MAC powder and the strong interactions between the two materials.

Indeed, FTIR analysis of MAC revealed a notable presence of hydroxyl groups, which contributed to this effect. However, increasing the macadamia nut shell powder content to 30 wt% had an adverse effect, reducing the T_g of the UV-cured coating to approximately 29 °C, similar value of the pristine network. Several factors can be the causes. Firstly, the high filler content could hinder the UV-curing process, as observed in the investigation of the photocuring process by photo-DSC. Consequently, the reinforcing effect resulting from the filler's presence was counteracted by a reduction in epoxy group conversion, leading to a decrease in crosslinking density. This phenomenon is consistent with the observed trend in cross-link density, as reported in **Table 3.17**. A further support to this conclusion is the broadening of the *Tan δ*-transition upon the addition of MAC, implying the formation of a more heterogeneous network with irregular mesh structures. Lastly, the potential presence of hydroxyl groups on the surface of MAC, as previously mentioned, could react with the epoxy functionality, hindering the formation of an optimal network. In such case, the positive effects of filler addition, such as increased rigidity and improved mechanical properties, might be compromised and counterbalanced by the low cross-link density resulting in deterioration of mechanical properties. The DMTA analysis was corroborates by DSC analysis (**Figure 3.45C**) performed on UV-cured sample which were used to determine the trend of the T_g, revealing the consistency of the two analyses.

Tensile test was performed to explore the mechanical response of the reinforce coating comparing the pristine epoxy one (**Figure 3.45D**). The trend reflected the DMTA results, suggesting a beneficial effect up to 20 wt% of MAC with the best compromise using 10 wt% of filler. Indeed, IDGE_10MAC reached 16 MPa and 205 MPa, for strength at break and Young’s modulus respectively. On the contrary, the introduction of 30 wt% MAC into the photocurable formulation resulted in a reduction of mechanical properties, as detailed in **Table 3.17**. This observation can be attributed to the explanation provided for DMTA result.

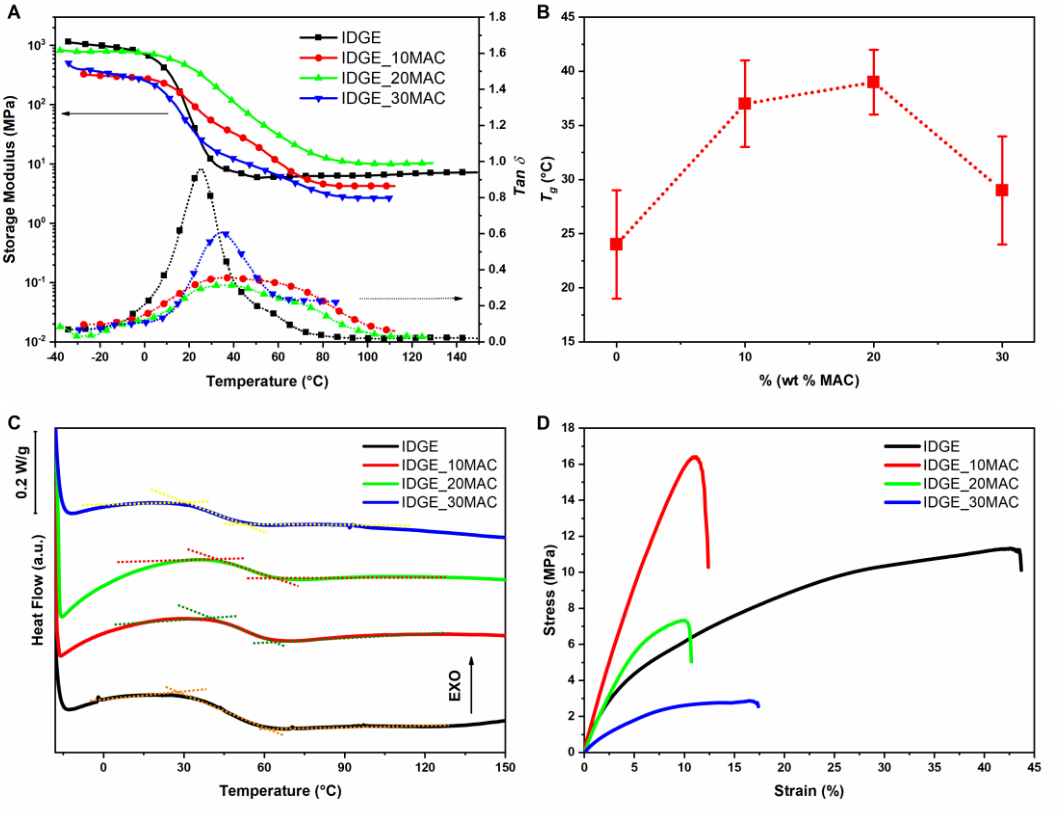

Figure 3.45. (A) Storage modulus and *Tan δ* trend in function of the temperature for the UV-cured IDGE-based coatings; (B) T_g of UV-cured coatings in function of temperature; (C) DSC thermograms of the second heating performed to detect the T_g; (D) Representative stress-strain curves obtained from pristine IDGE, IDGE_10MAC, IDGE_20MAC, and IDGE_30MAC.

Table 3.17. Data obtained from DMTA analysis, DSC and tensile test for the tested reinforced coatings. Glass transition ($T_g{}^1$) evaluated as the maximum of the *Tan δ*-peak in the thermograms obtained by DMTA; Storage modulus at the rubbery plateau obtained by DMTA (E^1); cross-link density assessed by Equation 3.3 with data obtained from DMTA ($v_c{}^1$); Glass transition evaluated as inflection point in the DSC thermogram ($T_g{}^2$).

ENTRY	Tg^1	E^1	$v_c{}^1$	$T_g{}^2$	E^3	σ^3	ε^3
	(°C)	(MPa)	(mmol/dm^3)	(°C)	(MPa)	(MPa)	(%)
IDGE	24 ± 5	6.3 ± 0.2	728	39 ± 3	123 ± 21	10 ± 5	40 ± 16
IDGE_10MAC	37 ± 4	4.3 ± 0.5	479	50 ± 3	205 ±18	16 ± 6	10 ± 2
IDGE_20MAC	39 ± 3	11.0 ± 0.5	1218	55 ± 2	131 ± 10	7 ± 1	9 ± 4
IDGE_30MAC	29 ± 5	3.4 ± 0.7	387	47 ± 2	47 ± 7	3 ±1	16 ± 5

SEM analysis was conducted on the fracture surfaces of the thermoset subjected to tensile testing, as illustrated in **Figure 3.46**. Strong interaction between filler and polymer matrix can be speculated due the lack of voids or irregularities. Upon closer inspection of the fracture surface, the pull-out mechanism expresses during the fracture process generates voids which can be highlighted. Expired to understanding more about the mechanism, real-time SEM analysis was performed during tensile testing to gain insights into the initiation and propagation of fractures in a sample containing 10 wt% of MAC. Cracks were observed to initiate at multiple points within the specimen. **Figure 3.47** provides a sequence of crack nucleation and propagation in a tensile specimen containing 10 wt% MAC. The green arrow shows the generation of a crack on the surface, followed by its propagation inward through the sample, behaving like a typical crack. Subsequently, other nucleation sites became evident. For instance, the red arrow indicates the formation of two defects and the subsequent growth and merging of two nearby pores under deformation. Lastly, the yellow circle highlights a series of cracks originating in two separate pores, aligned along the diameter perpendicular to the direction of loading, where the pore notch experiences a more significant stress intensification effect. The adverse effects observed with the use of 30 wt% macadamia nut shell powder can be attributed to the increased interface area between the matrix and filler, which serves as a starting point for crack initiation and debonding, thereby blocking the formation of a robust network, as previously explained.

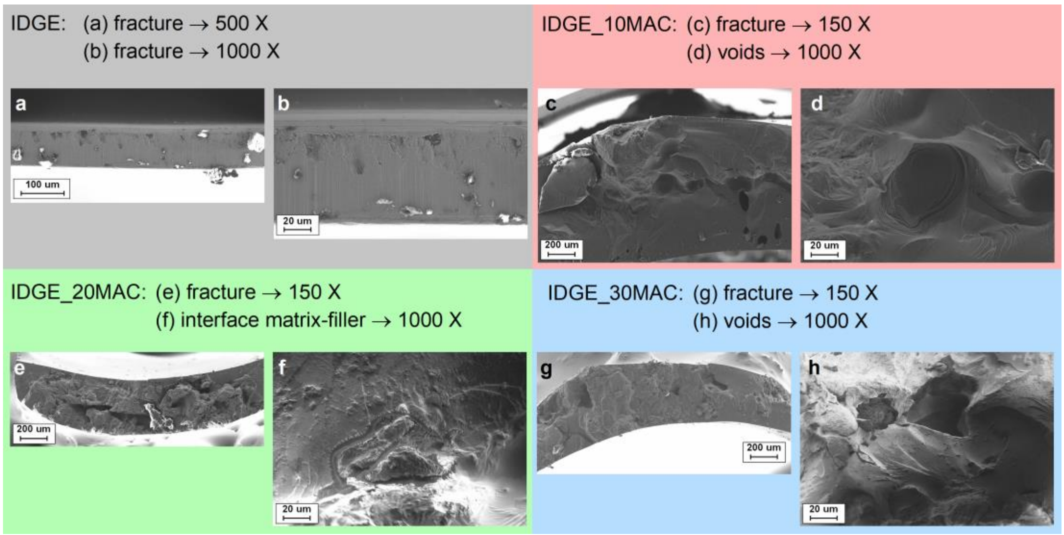

Figure 3.46. SEM analysis performed on the surface fracture of 5B type dog-bone specimens after tensile test.

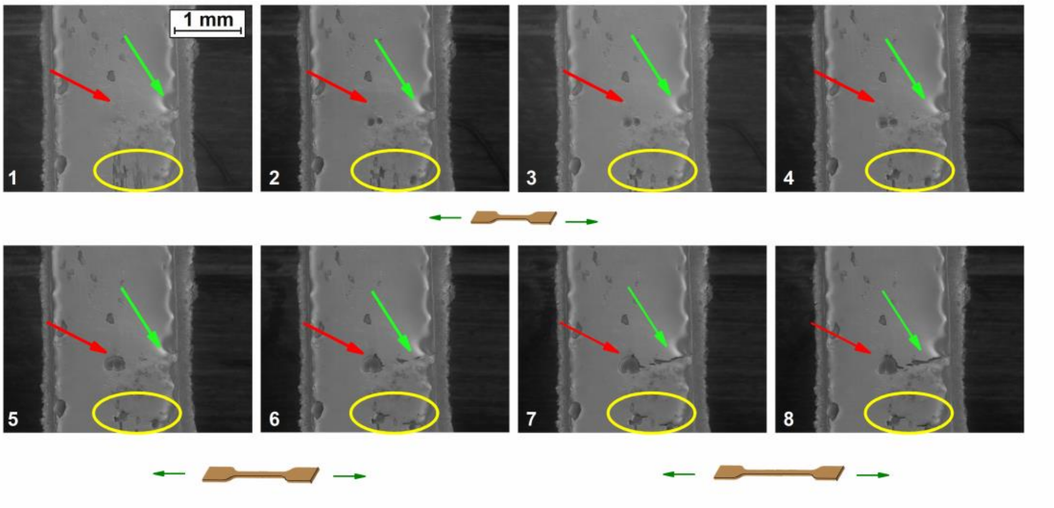

Figure 3.47. Online SEM analysis. Sequence of crack nucleation and propagation. Coalescence of defect (red arrows); debonding between matrix and filler (green arrows); region of crack nucleation (yellow circle). Magnification 300 × from 0.50 mm to 0.80 mm of extension.

The characterization of the bio-based coating continued with the analysis of the peculiar coating properties, such as surface hardness, contact angle, roughness and adhesion. The addiction of macadamia offered an improvement in the surface hardness, as shown in **Table 3.18**. Indeed, the value raised from 19 of pristine IDGE to 72 of coating containing 30 wt% of MAC. Not only hardness was affected, but also the roughness (*Ra*) of the surface was influenced by the filler. Overall, the *Ra* increased by increasing amount of the filler. Regarding adhesion, the bio-based epoxy resins demonstrated excellent performance. The IDGE coating exhibited excellent adhesion, classified as 5B on the ASTM scale, signifying completely smooth edges of the cuts without any detachments. Similarly, the addition of 10 wt% MAC did not affect the high adhesion. However, in the case of IDGE_20MAC, some detachment of flakes at the intersection of the cuts was observed, leading to a decrease in classification to 4B. Lastly, IDGE_30MAC was classified as 3B, primarily due to the increased presence of flakes along the cuts. This may be attributed to the hindrance of the UV-curing process, as previously described, which could limit adhesion to the glass substrate. The last investigated properties was the contact angle. The introduction of the filler increased the hydrophilicity of the coating meaning a decrease of the water contact angle from 50 ° to 9 ° for IDGE and IDGE_30MAC, respectively. This can be attributed to the nature of the filler, which has OH-groups on the surface imprinting a water-like nature of the coating.

Table 3.18. Data derived from surface analysis of the different coatings; hardness (*H*), the average surface roughness (*Ra*), adhesion, and contact angle.

ENTRY	***H***	***Ra* [silicon side]**	***Ra* [free side]**	**Adhesion**	**Contact angle**
	(Shore D)	(um)	(um)	(ASTM scale)	(°)
IDGE	19 ± 5	0.5 ± 0.2	0.7 ± 0.2	5B	50 ± 3
IDGE_10MAC	54 ± 10	0.8 ± 0.2	1.7 ± 0.3	5B	33 ± 2
IDGE_20MAC	68 ± 5	1.2 ± 0.3	4.7 ± 0.5	4B	14 ± 3
IDGE_30MAC	72 ± 2	2.9 ± 0.7	17.0 ± 0.9	3B	9 ± 2

In order to prove the feasibility of using the bio-based coating as alternative to commercially available fossil-based formulation, the study compared properties (T_g, Young's modulus, and hardness) achieved for the isosorbide-based thermoset with those reached by fossil-based epoxy thermoset, **Table 3.19**. Different glycidyl ether monomers, each featuring unique structural attributes, such as aliphatic (NPGDGE), cyclic (CDE), or aromatic (BADGE) structures, as well as cycloaliphatic epoxy (ECC), were selected as reference materials for this comparative analysis (chemical structures provided in **Figure 3.48**). It is evident that the isosorbide-based coating can compete effectively with certain epoxy resins when considering the T_g values. For instance, the T_g values obtained for IDGE were within the same range as those of neopentyl-based (7 °C) and cyclohexane-based (20 °C) resins. In contrast, resins containing rigid structures, such as aromatic rings in BADGE or cycloaliphatic rings in ECC, exhibited higher T_g values (over 100 °C) owing to the chemical structure of their starting monomers. The trends observed in Young's modulus (*E* values) reflected the trend of T_g, with IDGE demonstrating comparability with NPGDE and CEDGE, while resins featuring rigid structures (e.g., BAGDE, ECC) achieved higher *E* values. Concerning surface hardness, the values obtained for the reinforced coatings were on par with those of aromatic-based thermosets. These findings demonstrated the potential to enhance the surface properties of a bio-based resin, which might otherwise exhibit disparities when compared to commercially available resins.

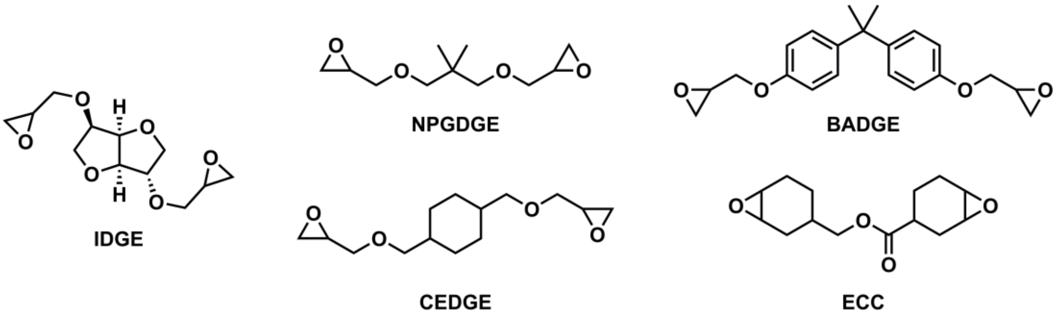

Figure 3.48. Chemical structure of bio-based isosorbide monomer (IDGE) and the commercially available epoxy monomers used for the comparison.

Table 3.19. Comparison between isosorbide-based coating and fossil-based ones; glass transition (T_g), Young's modulus (*E*) and surface hardness (*H*).

ENTRY	T_g	*E*	*H*
	(°C)	(Mpa)	(Shore D)
IDGE	24	123	19
IDGE_10MAC	37	205	54
IDGE_20MAC	39	131	68
IDGE_30MAC	29	47	72
NPGDGE	7	31	30
CDE	20	10	27
ECC	158	645	68
BADGE	129	709	70

3.2.2.4. Hot-lithography 3D printing of fully bio-based composites

Non edible epoxy vegetable oils present attractive bio-based resins which can be employed to move towards greener economy without affecting food primary resource, representing a validate alternative to fossil-based resins. Driven by the concerning about circular economy and sustainable materials, this study primarily aimed to leverage the potential of EVOs as epoxy resin for the development of green composite adding bio-derived filler. To effectively exploit EVOs, Hot-lithography was selected as process to develop composite materials with accurate geometry and high performances. Indeed, Hot-lithography enables to increase the reactivity of the resin reducing its viscosity, resulting in a feasible processability of non-conventional epoxy monomers.

Selection of photoinitiator system for Hot-lithography

The UV-curable formulations need to be adapted according to the process condition to ensure high storage stability, but at the same time high reactivity whenever the UV-stimulus is provided. Critical aspects of reactivity and thermal stability affect the stereolithography (SLA) process in the context of high-temperature printing. Therefore, the choice of the photoinitiator system holds immense importance. Three different systems, each containing a distinct photoinitiator were selected: I-SbF6 (with ITX serving as a sensitizer to enable activity in the wavelength of the printer's laser emission), S-SbF6, and S-BF5. Reactivity and thermal stability were assessed by photo-DSC, STA and rheology (**Figure 3.49**). The optimal performance for all the photoinitiator was consistently achieved at 100 °C by a linear increase with increased temperature. Moreover, it was suitable to avoid thermal activation; these aspects will be further discussed in detail below. S-BF5 exhibited the best performance due to its lowest t_{peak} and highest R_P compared to the other systems. Nonetheless, all systems demonstrated good reactivity at high temperatures, as indicated by the low t_{peak} values, which were all below 20 seconds. STA measurement served to investigate the possible thermal activation of the photoinitiators [114,159]. I-SbF6 exhibited an onset around 140 °C, S-SbF6 around 160 °C, and S-BF5 around 170 °C, suggesting that printing at around 100 °C would ensure a predominantly UV-activated reaction. Nevertheless, thermal stability tests at 100 °C were conducted by maintaining the formulations at an isothermal condition to simulate the conditions of the Hot-lithography process. It was observed that I-SbF6 solidified in less than 24 hours, while cross-linking of the S-SbF6 occurring within 3 days. In contrast, the formulation containing S-BF5 remained stable over the course of 3 days, maintaining a liquid state throughout the entire testing period. Considering the aforementioned results, S-BF5 was selected as the preferred system for investigating the UV-curing process and Hot-lithography of the bio-based composites. The ongoing investigation continued with the inclusion of S-BF5 as a photoinitiator at a concentration of 3 phr.

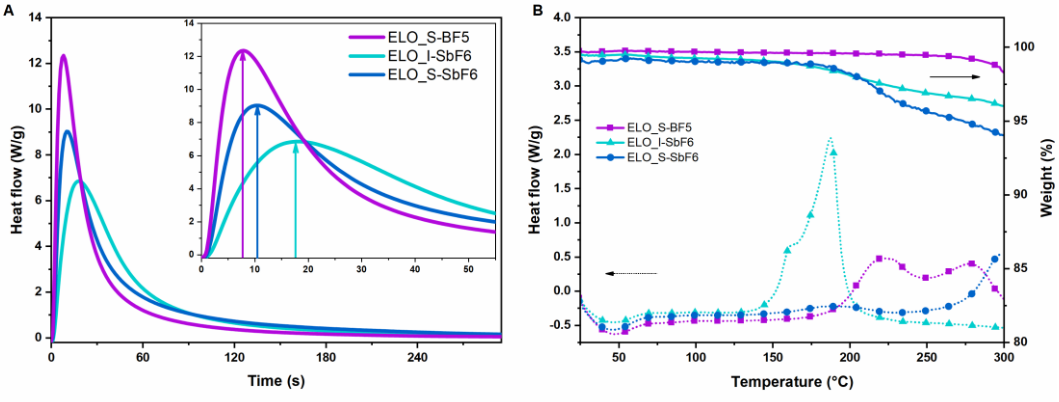

Figure 3.49. (A) Photo-DSC thermogram of the ELO containing the different photoinitiator systems. The analysis was performed at 100 °C; (B) STA analysis of the uncured formulations containing ELO with the tested photoinitiators.

UV-curing process

The UV-curing process of the pristine bio-based epoxy vegetable oils was investigated at various temperatures using photo-DSC, ART-FTIR and photorheology techniques (**Figure 3.50**). Specifically, the temperature-dependent effects on the kinetics during the UV-curing process was assess by test at 25, 50, 75, and 100 °C. Notably, a significant increase in epoxy group conversion was observed as the temperature was raised, with values exceeding 90 % for both vegetable epoxy oils when the UV-curing process was carried out at 100 °C (**Figure 3.50A**). Furthermore, it is evident that operating at higher temperatures led to a significant increase in R_P, increasing from approximately 25 mmol/s×L at 25 °C to about 200 mmol/s×L when UV-curing was conducted at 100 °C. These findings collectively demonstrate that higher temperatures can facilitate the 3D printing of epoxy vegetable oils by enhancing both kinetic reactions and conversion. The maximum reaction rate was attained at 100 °C, with values of 196 mmol/s×L for ELO and 141 mmol/s×L for ESO, respectively. The temperature influence is a well-known effect in cationic photopolymerization described by Crivello et al. [251] which showed that cationic epoxy ring-opening polymerization can be markedly accelerated when carried out at higher temperature. This is particularly true when the aliphatic epoxy ring is exploited in cationic photopolymerization since a stable intermediate structure is formed during the ring-opening, slowing down the curing speed. Polymerization does not proceed spontaneously at room temperature in such systems. However, if photopolymerization is performed at higher temperature, the ring-opening reaction starts much faster [155,156,251]. Photorheology was used to investigate the development of the solid network by t_{gel} which is defined at the intersection between Storage modulus (G') and Loss modulus (G''). This critical feature acts as a crucial indication for establishing the appropriate printing parameters to ensure the creation of self-sustaining layers which do not collapse during the additive manufacturing process. A clear decrease of t_{gel} from 16.0 ± 1.0 s at 25 °C to 4.5 ± 1.5 s at 100 °C for ELO was detected by increment of temperature. The trend in G', recorded for ELO (**Figure 3.50D**), showed a decrease in the induction time by increasing temperature as well as an increase in the slope can be observed, confirming the faster kinetic at higher temperature. The trend registered for ESO was in agreement with the result of ELO above discussed. Finally, the conversion data were confirmed by ATR-FTIR analysis conducted over the sample cured at different temperatures. The epoxy peak at 825 cm^{-1} progressively disappeared passing from UV-curing at 25 °C to UV-curing at 100 °C (**Figure 3.50C**). Considering the epoxy group conversion reached operating at 100 °C and the faster kinetics, this was selected as printing temperature for the Hot-lithography 3D printing process.

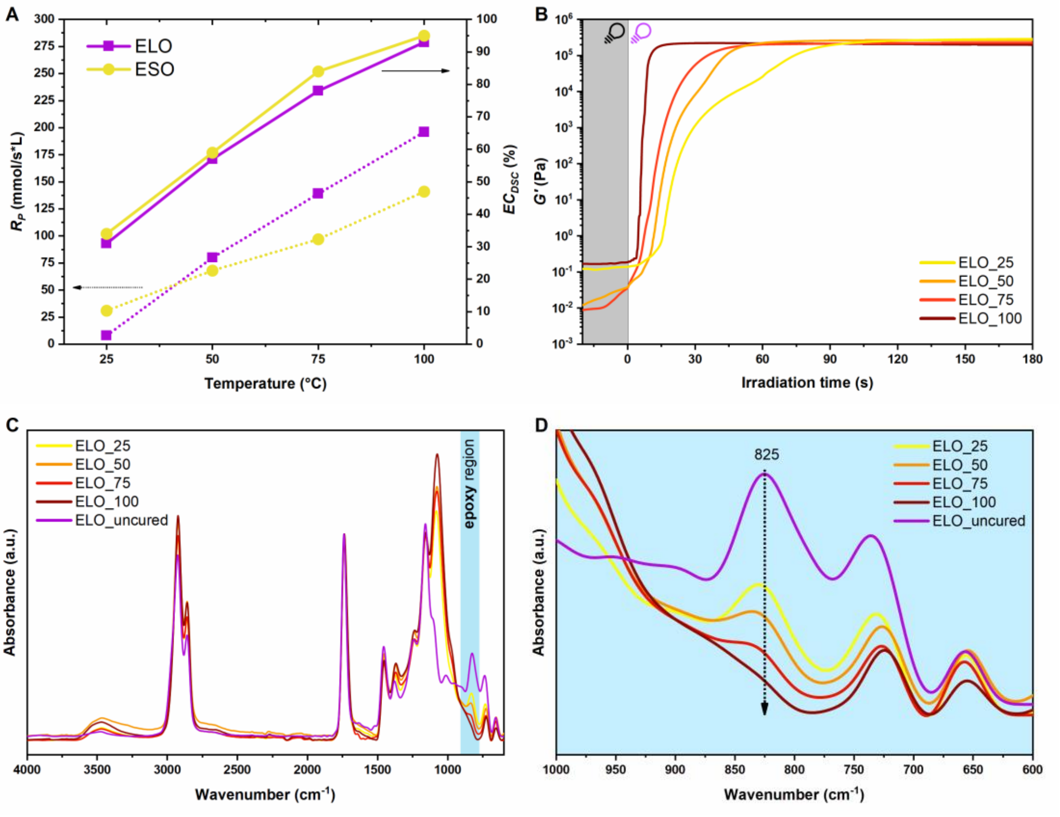

Figure 3.50. (A) Photo-DSC data: rate of polymerization (R_P) and epoxy conversion (E_{CDSC}) in function of the temperature for ELO (purple lines) and ESO (yellow lines); (B) photorheology curves collected for ELO at different temperatures; (C) ATR-FTIR analysis of the UV-cured ELO at different temperatures; (D) highlight of ATR-FTIR spectra in the epoxy region with the peak centered at 825 cm^{-1}.

Fillers influence on UV-curing process

Lastly, the UV-curing process was studied in presence of varying filler quantities to investigate a possible hindrance of the cross-linking reaction. The chemical nature and the morphology of the different fillers were investigated by ATR-FTIR analysis and SEM (**Figure 3.29**) in order to have a comprehensive view of the possible influence and interaction with the UV-process. The results of the UV-curing in presence of the fillers revealed that their presence did not significantly affect the final conversion, with all formulations achieving over 80 % of EC_{DSC}. Noticeable high conversion was reached by formulation containing H200 (**Table 3.20**). This could be explained considering that the fillers surface contains a high number of OH-groups, verified by ATR-FTIR, which can interact with the carbocationic growing chain *via* a chain transfer reaction, with a consequent enhancement of the final epoxy group conversion [80].

The presence of fillers might be expected to hinder the curing process by competing for absorption with the photoinitiator and reducing the available UV-light intensity [252]. However, the chain transfer process induced by the OH groups present on the filler's surfaces counteracts the decrease of the photogenerated acid, leading to an enhancement of the curing process [253,254]. The two phenomena are somehow balanced and so the overall UV-curing is not significantly affected by the present of the filler in the photocurable formulations.

However, the nature of the filler had an influence on the UV-process. A higher R_P reduction for strong brown colored fillers of wall nutshell powder was observed, whereas white fillers like tagua and hemp may have a lesser effect on light penetration depth limiting the reduction of R_P. Another important parameter to consider is the amount of the filler present into the formulation. **Figure 3.51A** illustrates the photo-DSC analysis of the formulation containing different amount of H200, highlighting the trend of R_P (proportional to the h_{peak}) as well as the decrease of the total ΔH release during the reaction. The lowest epoxy conversion of 55 % was reached by the formulation containing 20 phr of H200, which was also attributed its higher viscosity. Indeed, the propagation of the carbocationic growing chains was limited by the viscosity thus this relevant feature requires to be addressed for the printing. The formulations suitable for SLA need to have proper viscosity to flow forming homogeneous layers on the vat for each platform movement. A standard value below 20 Pa×s indicates a limit for successful printing [114,159]. Viscosity test was run at printing temperature of 100 °C revealing that most of the formulations had appropriate value which were kept over 6 days. The ELO_H200_20 due to high viscosity and impossibility to properly flow was deemed unsuitable for printing. Therefore, further investigation was limited to so UV-curable formulations containing 5 and 10 phr of H200 as filler. The cause of high viscosity can be researched in the filler geometry. The reason of the higher viscosity can be attributed to the filler geometry. The wedge-shape of hemp generate a strong increase in the viscosity varying from 5 to 20 phr (**Figure 3.51B**) which generate a limitation in the filler addition into the resin. On the other hand, the more-round shape filler, as wall nut shell (WS) and tagua (T), has lower impact on the final viscosity of the formulations allowing the addition of 20 phr (**Figure 3.52A**).

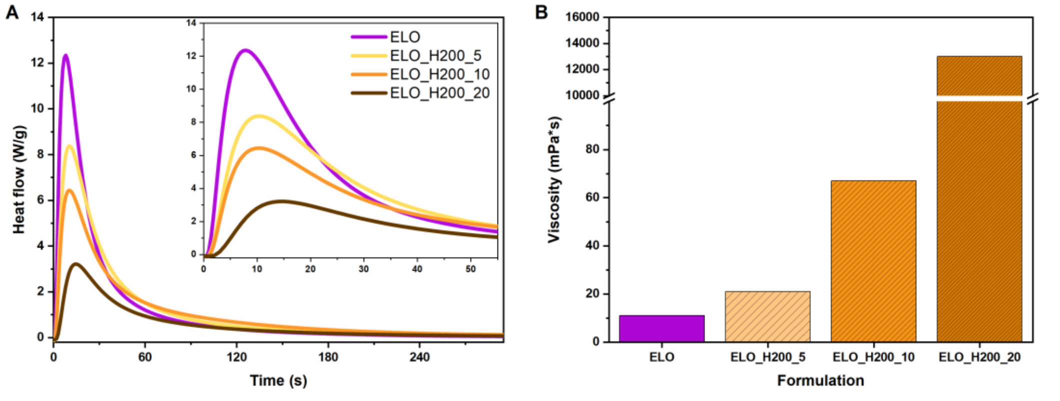

Figure 3.51. (A) Photo-DSC result for ELO-based formulation containing different amounts of H200; (B) Viscosity measurements for the ELO formulation with 5, 10, and 20 phr of hemp (H200).

ATR-FTIR analysis and photorheology test were carried out to confirm photo-DSC data on the epoxy UV-curable formulations with the highest amount of filler to investigate the final conversion ($EC_{\text{ATR-FTIR}}$) and a possible delay in the t_{gel} which should be considered when setting parameters for additive manufacturing. The results of the different techniques indicated minimal influence of the fillers on the UV-curing process at the given quantities, confirming the feasibility of additive manufacturing. Even when the fillers were added, the conversion evaluated both *via* ATR-FTIR or photo-DSC was comparable (**Table 3.20**) with the results obtained for the pristine epoxy resin, confirming the efficiency of the UV-curing process. The photorheology results aligned with the photo-DSC outcomes, which previously indicated a similar range of R_P, indicative of a fast reaction even for epoxy formulations containing fillers (**Figure 3.52**). Lastly, STA confirmed a fully cross-linked network resulting in absence of exothermic peak. The formulation containing 20 phr of WS200 showed a minor exothermic peak around 150 °C which can be due to the incomplete epoxy group conversion. The analysis established also the starting point of the thermal degradation which varied from 270 to 290 °C for the studied composites.

Table 3.20. UV-curing process data for the different composites studied by photo-DSC, ATR-FTIR analysis and photorheology. Experimental parameters t_{peak}, h_{peak}, and ΔH; R_P, ΔH_{EXP}, EC_{DSC}, $EC_{ATR\text{-}FTIR}$ calculated parameters.

FORMULATIONS	t_{peak}	h_{peak}	R_P	ΔH	ΔH_{EXP}	EC_{DSC}	$EC_{ATR\text{-}FTIR}$	t_{gel}
	(s)	(W/g)	(mmol/s×L)	(J/g)	(J/mol)	(%)	(%)	(s)
ELO	7.7±0.2	12.7±0.8	196	339±5	61.1	93	92±6	4.5±1.5
ELO_WS200_10	8.4±0.9	6.6±0.9	101	267±13	53.4	81	*	*
ELO_WS200_20	8.4±1.0	5.7±0.4	87	237±5	55.6	84	94	5.0±1.0
ELO_WS325_10	8.7±0.8	10.6±1.4	163	312±18	62.5	95	*	*
ELO_WS325_20	8.5±0.9	7.3±2.6	113	257±39	60.4	92	98	5.5±0.5
ELO_T200_10	7.7±0.6	16.1±2.5	206	348±10	69.6	≈100	*	*
ELO_T200_20	8.7±1.5	11.8±1.8	182	340±12	70.8	≈100	94	5.5±1.5
ELO_H200_5	9.7±1.0	9.2±1.4	142	314±6	59.6	90	*	*
ELO_H200_10	10.9±1.5	5.9±1.7	91	251±31	55.8	85	*	5.0±1.5
ELO_H200_20	12.2±1.3	3.6±0.5	55	161±10	36.3	55	*	*
ESO	8.1±0.2	9.9±0.7	141	287±1	65.8	95	95±4	3.5±1.5
ESO_WS200_10	8.8±0.8	9.0±0.4	128	275±2	70.1	94	*	*
ESO_WS200_20	7.6±0.8	7.6±0.8	108	238±8	68	91	97	3.5±1.0
ESO_WS325_10	8.2±0.5	9.5±0.6	135	283±5	72.4	96	*	*
ESO_WS325_20	8.5±0.9	7.4±0.7	106	242±7	69.4	93	96	4.0±1.0
ESO_T200_10	7.2±1.3	13.6±1.8	194	305±6	77.7	≈100	*	*
ESO_T200_20	7.7±0.7	12.7±0.4	181	280±10	75.6	≈100	94	4.0±1.0
ESO_H200_5	7.1±1.2	12.4±0.3	177	295±3	75.2	≈100	*	*
ESO_H200_10	8.8±0.5	7.8±0.7	111	272±2	73.4	≈100	97	3.5±1.0

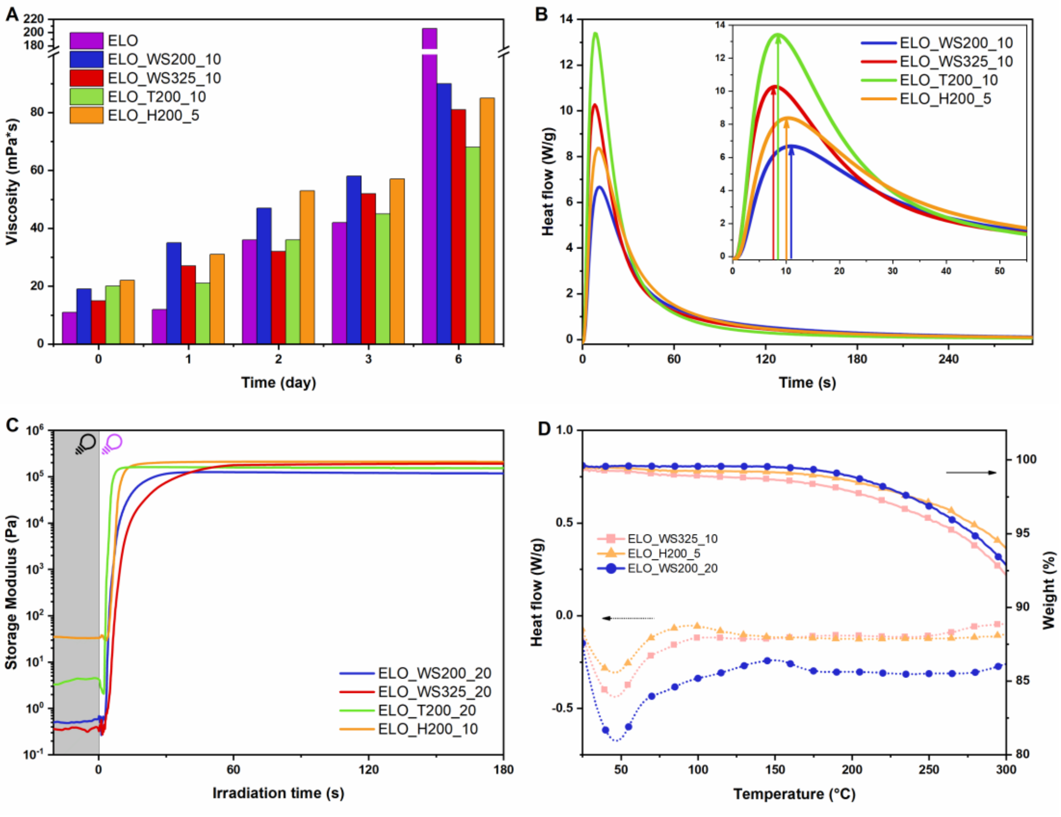

Figure 3.52. (A) Stability test performed at 100 °C for 6 days; (B) Photo-DSC result for the ELO-based formulation with 10 phr of WS200, WS325, T200, and 5 phr of H200; (C) Photorheology test of ELO-based formulations with the highest amount of different fillers used; (D) STA data of ELO-based composites.

SLA Hot-lithography 3D printing and mechanical testing

Hot-lithography was employed to 3D print composites for mechanical testing; DMTA specimens and tensile 5B type dog bone samples were successfully printed at 100 °C with a layer thickness of 100 µm. Remarkably, the 3D printing was performed not only on pristine EVOs but also it was performed for bio-based composites. This noteworthy result with epoxy monomers opens up new possibilities for expanding the range of bio-based materials that can replace fossil-based resins and composites. Furthermore, the utilization of bio-based fillers has increased the overall content of bio-derived products. This highlights the feasibility of effectively employing bio-based fillers derived from industrial side-streams. The primary aim of additive manufacturing is often the creation of intricate, self-supporting structures that are challenging to produce using other manufacturing processes. The potential for developing complex geometries is showcased in **Figure 3.53** where printed ELO-based composite object demonstrated excellent reproducibility and printing accuracy, enabling the creation of small, precisely detailed square grids. Moreover, 3D scanning analysis was carried out to verify the accuracy of the 3D printing comparing the CAD model to the 3D printing object. **Figure 3.54** reports the analysis performed on the different 3D printed nets highlighting the regions of major fidelity in the green zone. The best performance was attributed to the ELO_WS325_20 with a green zone of about 38 % meaning a high accuracy in the selected range of ± 50 um. The other resins were less accurate with value around 20 %, however the mean values as well as the variances were tight and narrow for all the objects demonstrating a good reproducibility of the CAD file. The artefacts and irregularities can be attributed to several factors. Firstly, the resin composition can explain part of the errors due to the presence of the filler which generate scattering and absorption phenomena hindering the light path. Then, some process-dependent errors such as printer resolution, printing errors and scanner precision can have impacts on the result. Imperfections can be also created by the inhomogeneous distribution of magnesium stearate used to increase the efficiency of the 3D scanner as well as the presence of the support (visible in **Figure 3.54**) which enable a correct acquisition of the imagines. As future prospective, the creation of proper printing formulations with dye and inhibitors of cationic UV-curing to maximize and optimize the light absorption could lead to increase the accuracy and precision of the 3D printing objects.

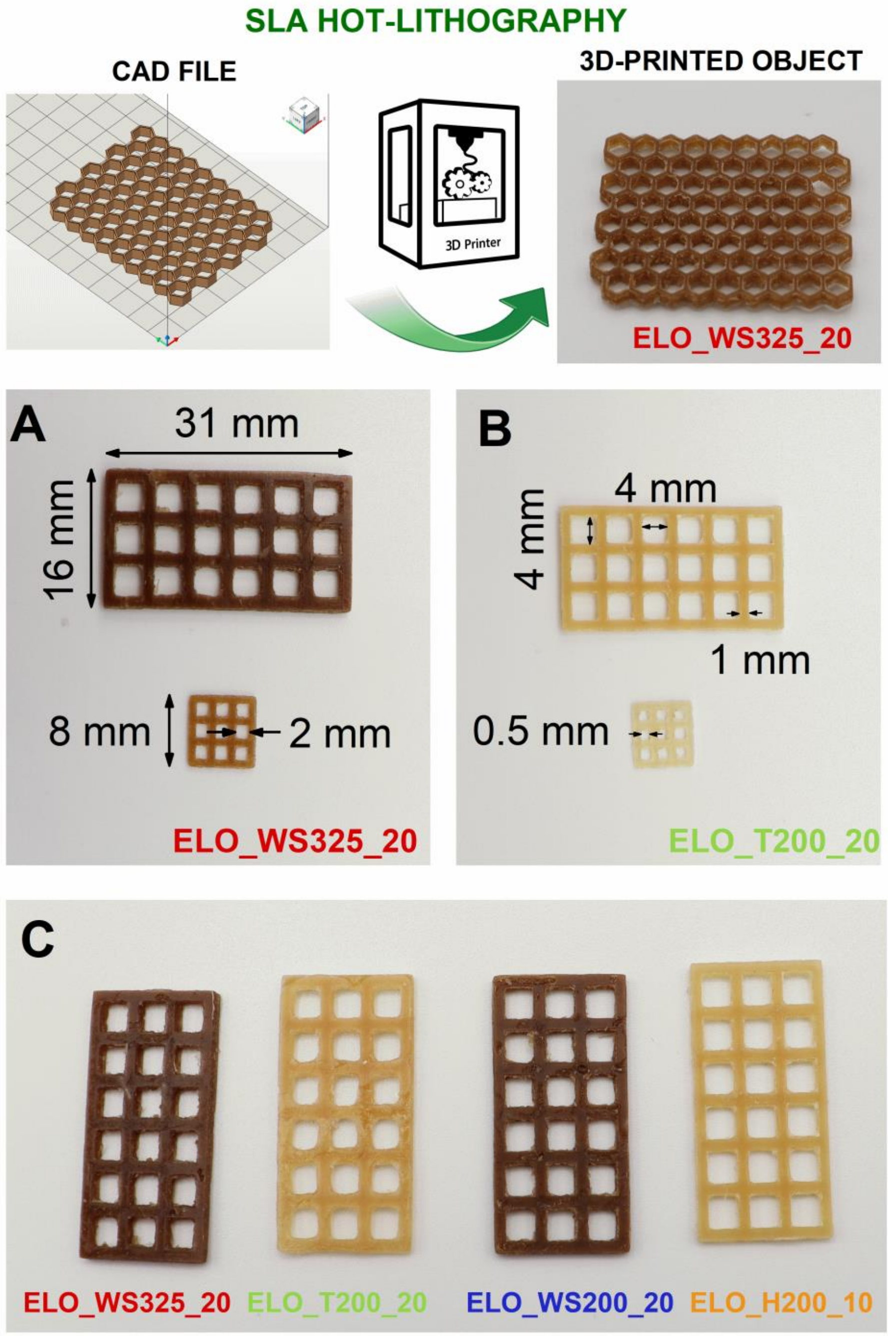

Figure 3.53. 3D printing specimens by SLA Hot-lithography performed at 100 °C. Each layer was 100 μm. Honeycomb net made of ELO_WS325_20 (total volume of 70 x 40 x 4 mm). 3D printed net ELO-based with the different fillers in the highest amount and squared-based pyramid of ELO and ELO_WS200_20.

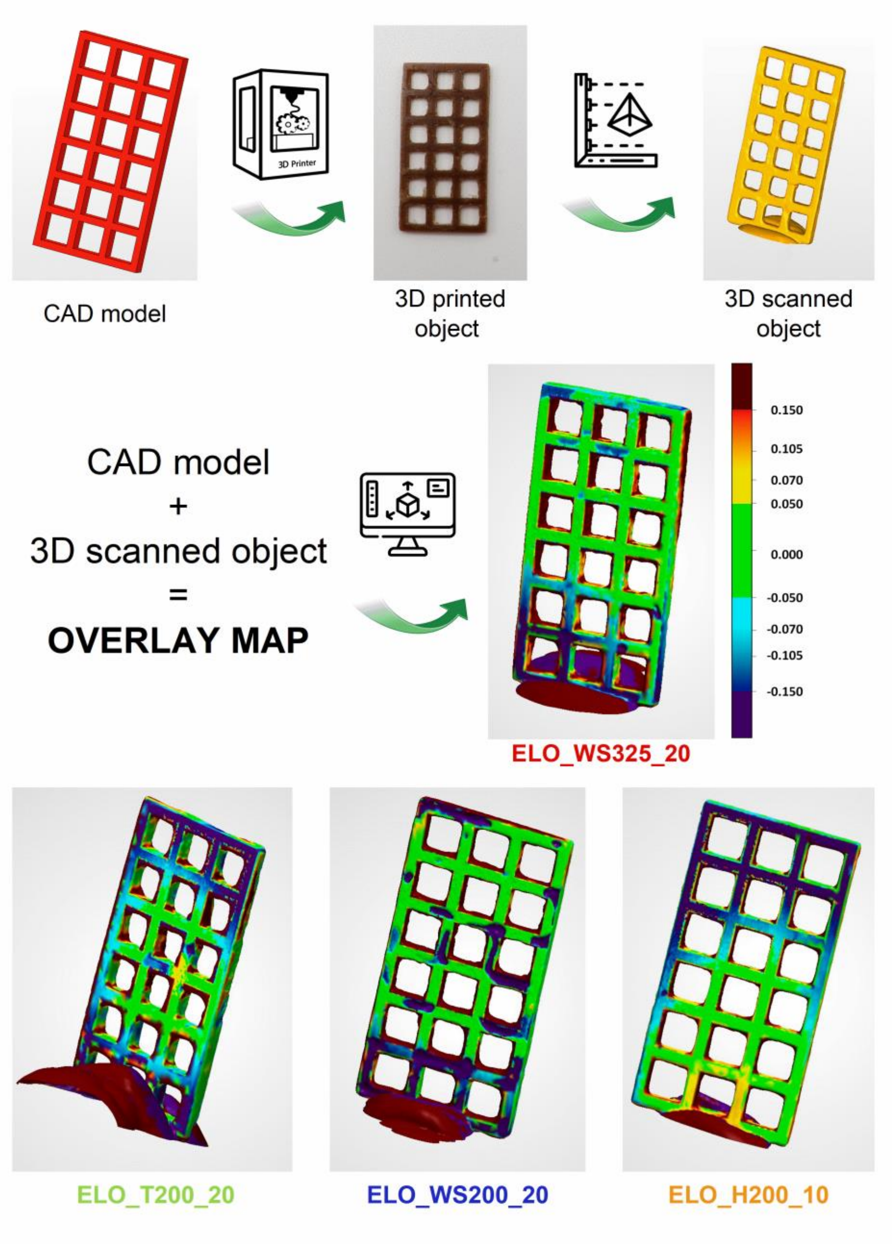

Figure 3.54. Overlay maps created by 3D scanning analysis of the ELO-based 3D printed square nets with the different fillers. From the CAD model to the 3D printed object to evaluate the accuracy of the printing.

The thermo-mechanical properties of the composites were assessed through DMTA analysis. Distinct T_g was observe for pristine ELO and ESO, which can be attributed to the epoxy values of the oils. A higher epoxy value implies a greater cross-linking density and, consequently, increased overall rigidity of the polymer network. Therefore, ELO, with an epoxy value of 5.55, achieved a T_g of 47 °C and a ν of 4300 mmol/cm^3, while ESO, with an epoxy value of 4.36, exhibited a T_g of

7 °C and a cross-link density of 1835 mmol/dm^3 (as depicted in **Figure 3.54**). This outcome underscores the potential to tailor the properties of the crosslinked polymer network by simply choosing the epoxy value. The availability of various epoxy vegetable oils offers a broad spectrum of initial properties that can be customized to meet specific application requirements, as previously demonstrates for coating application [56]. Once the effect of the polymer matrix was assessed, the influence of bio-derived fillers was examined. Interestingly, the fillers did not notably affect the final T_g of the network. As previously discussed, the presence of fillers did not significantly hinder UV-curing, allowing the proper formation of the network, *via* chain transfer mechanism. Typically, the addition of reinforcing fillers is expected to raise the T_g by restricting the mobility of the polymeric network. However, in this case, this benefit is balanced by the anticipated reduction in crosslinking density due to the chain transfer reaction. Consequently, the addition of the filler did not significantly modify the final T_g of the cured materials. This is confirmed by the results presented in **Figure 3.55**, where the UV-cured formulations containing 10 phr of various fillers exhibited nearly identical T_g values as the pristine UV-cured resin.

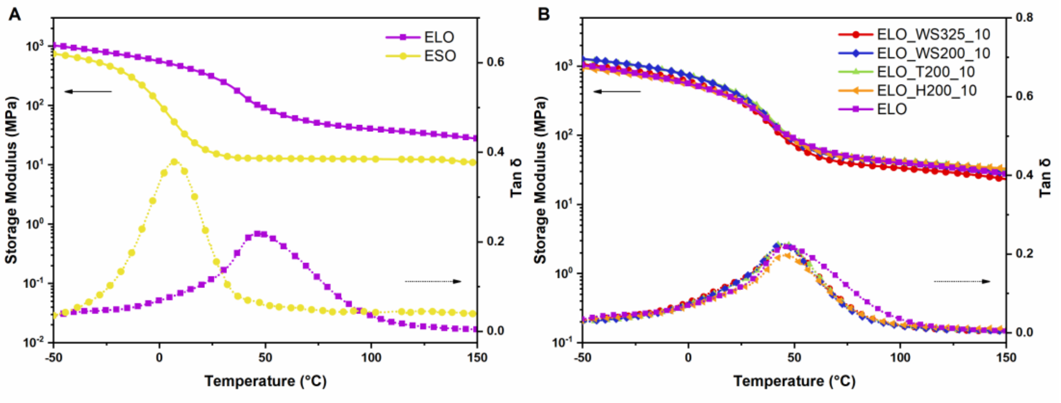

Figure 3.55. (A) DMTA of pristine ELO and ESO 3D printed at 100 °C; (B) DMTA of ELO-based composites with 10 phr of the different filler used in the study.

To complete the characterization of the composites investigating the benefit of the fillers, tensile test was carried out. The results corroborated the findings from DMTA analysis, with the epoxy vegetable oil possessing the highest epoxy value, ELO, displaying the best mechanical performance, as illustrated in **Figure 3.56A**. The higher epoxy content contributed to increased network rigidity and gave superior mechanical performance in terms of ultimate strength. Crosslinked ELO exhibited a strength of 10 MPa, in contrast to the 1.1 MPa observed for crosslinked ESO epoxy resin. E increased from 0.27 MPa for UV-cured ESO to 3.30 MPa for crosslinked ELO meaning a roughly increment of about 10 times just acting on the chemical functionalization of the epoxy matrices.

The filler had a beneficial impact on composite's strength and rigidity as confirmed by higher Young's modulus (**Figure 3.56B**). The analysis of the different fillers allowed to compare results based on morphology, dimension and quantity of the filler. The intrinsic shape of Tagua and Hemp, with their wedge-shaped geometry, determined higher values of E and σ. Additionally, it's interesting to note how the filler dimensions can affect the properties. When comparing the wall-nut shell composites (WS200 and WS325), the influence of the mesh sizes (200 and 325) is evident, revealing how the larger dimension of the filler contributes to achieving higher strength at break, but with a consequent decrease in elongation due to the increased rigidity imparted to the composite.

The customizing the final properties can be done by playing with the filler amount. Taking WS200 or T200 as examples, **Figure 3.56** reports the result with different filler quantity. It is evident that passing from 10 to 20 phr (or 5 to 10 phr for H200) resulted in higher values of E, σ, and U, as detailed in **Table 3.21**. The highest toughness was achieved in the case of ELO_WS325_20, with a value of 2950 $Jm^{-3}10^{4}$, which was eight times greater than the toughness of pristine ELO.

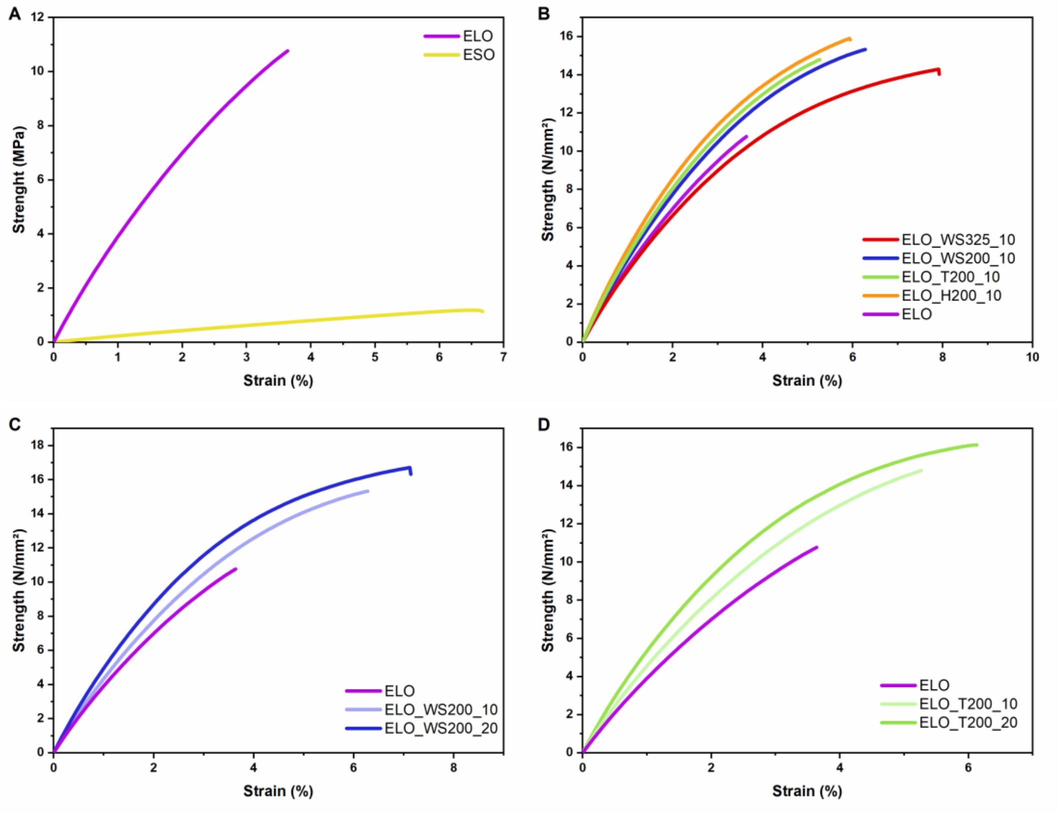

Figure 3.56. (A) tensile test for 3D printed samples of ELO and ESO; (B) stress-strain curves for ELO-based composites with 10 phr of the different fillers; (C) tensile test for ELO-based 3D printed composites with wall nut shell; (D) influence of tagua on the tensile properties of ELO-based composites.

Matrix-filler interface investigation

The WS-filler was incorporated into the polymer matrix exhibiting the highest toughness, especially when it has been used in the ELO epoxy resin at 20 phr. The presence of these fillers had a remarkable impact on the mechanical properties of the composites. Consequently, the investigation point out the origin of this benefit. As previously demonstrated through ATR-FTIR analysis, the surfaces of the different fillers displayed OH groups (**Figure 3.29**). Cellulose, hemicellulose and lignin are the main components of the bio-derived fillers, and it is well-known that OH functionality is strongly present in the chemical structure of these natural polymers [13,168,255–257]. The great potential of OH groups is the feasibility to interact with the epoxy matrix *via* chain transfer reactions (**Figure 3.57**). This could directly translate into strong surface interactions between the polymer and filler, contributing significantly to the enhancement of the composite properties. To validate this hypothesis, the WS325 filler was subjected to a silanization process. This reaction step involved most of the OH groups on the surface, generating Si-O bonds by reaction with silane reagent as illustrated. ATR-FTIR analysis confirmed the success of this process by comparing the spectra before and after functionalization which evidenced the presence of the $Si(CH_3)_3$ peak at 837 cm^{-1} and the reduction of the OH band, as depicted in **Figure 3.58**.

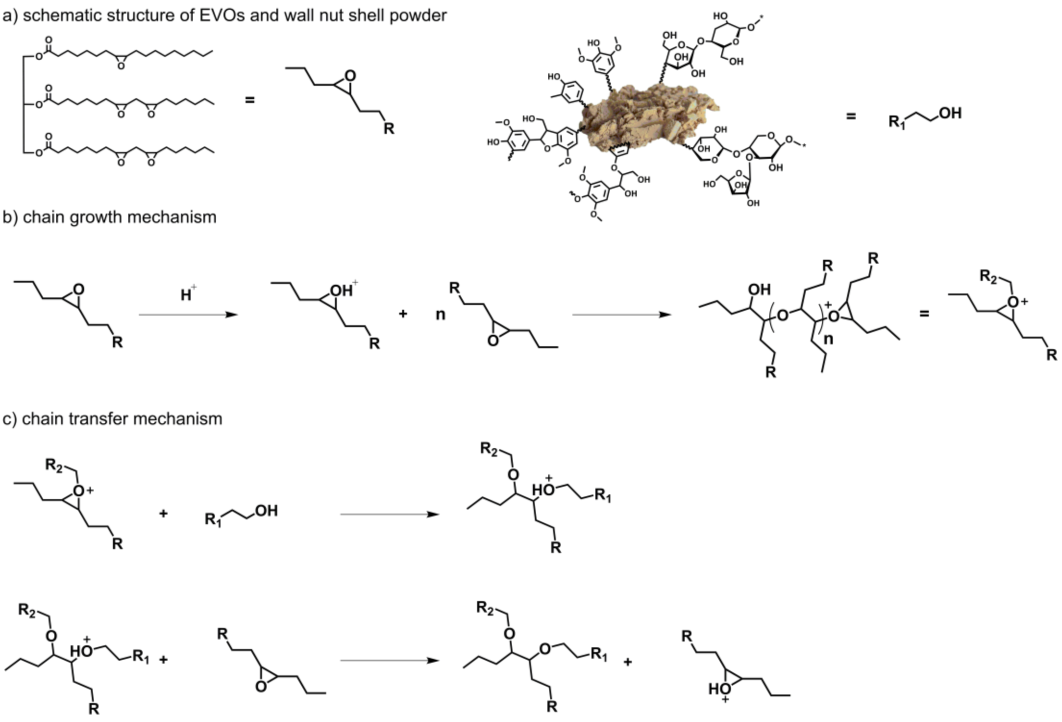

Figure 3.57. Schematic view of mechanisms involved in the UV-curing of the EVOs.

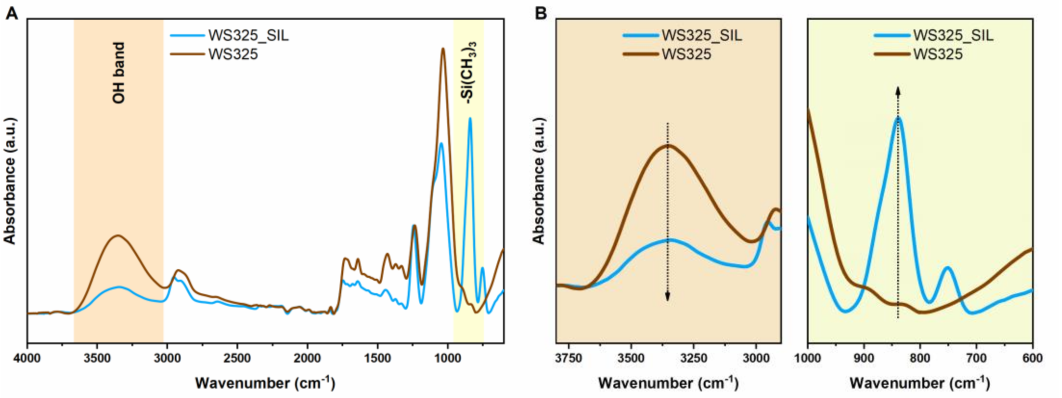

Figure 3.58. (A) ATR-FTIR pre and post functionalization; (B) highlight on the OH band at 3300 cm^{-1} and on the $Si(CH_3)_3$ peak at 835 cm^{-1}.

The modified WS325 filler was employed in the SLA Hot-lithography of DMTA and tensile specimens to assess and confirm the impact of the interaction between the bio-derived filler and the bio-based epoxy polymer matrix. **Figure 3.58** illustrates the comparison between the ELO UV-cured composite containing unmodified WS325 filler and the ELO_WS325_20_SIL composite with silanized filler at a content of 20 phr. The weaker interaction between filler and matrix can cause the slight decrease in T_g, approximately 5 °C, for ELO_WS325_20_SIL. Stress-strain curves (**Figure 3.59**) further confirmed the decrease of mechanical response due to surface modification. The reduced interaction between the polymer and the filler has an impact on the final properties, leading to a decrease in E, σ, and U. Specifically, the E decreased from 4.6 MPa for the ELO UV-cured composites containing the original WS325 filler at 20 phr to 3.3 MPa for the same ELO composites containing the silanized filler. Furthermore, the strength decreased from 16.8 MPa for the 3D printed composites containing the original filler to 8.6 MPa for the composites containing the silanized filler. Finally, the toughness decreased by a factor of 10 when the silanized filler was incorporated into the UV-curable epoxidized vegetable oil, as evident from the area under the stress-strain curves. Thus, the presence of OH groups on the surface of the bio-derived filler is truly beneficial, allowing for a strong interaction at the interface which provides advantages in the composites.

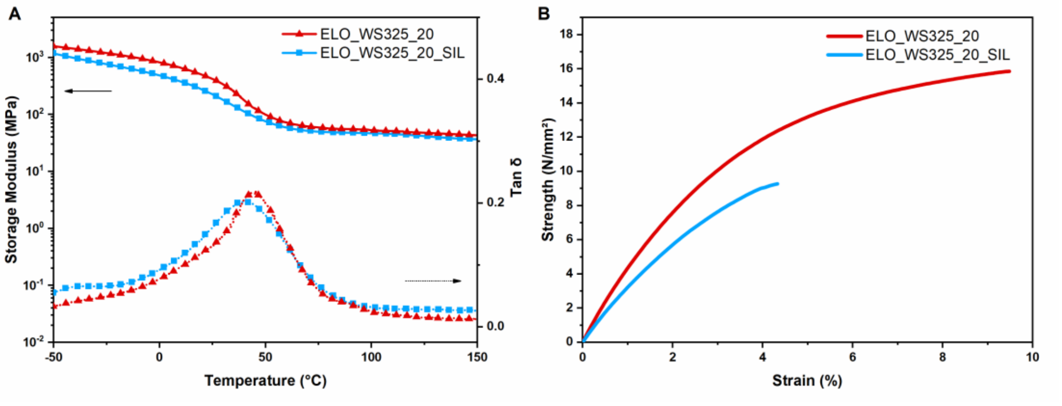

Figure 3.59. (A) DMTA analysis of ELO-based composite containing WS325 unmodified and silanized WS325; (B) stress-strain curves for ELO-based 3D printed composites specimens with pristine WS325 and silanized WS325.

The morphology of the composite as well as the interaction between polymer matrix and bio-derived filler were investigated by SEM analysis of the fractured specimens derived from tensile test. **Figure 3.60** illustrates the distinction between ELO_WS325_20 and ELO_WS325_20_SIL. Firstly, no clumping or settling were evident proving that the fillers were uniformly distributed throughout the composite. Additionally, the examination of the interface in ELO_WS325_20_SIL revealed issues related to the compatibility between the matrix and the filler. In this case, voids between the matrix and filler were visible at high magnification. These voids may be attributed to the poor interaction between the matrix and the filler and could also explain the observed weak tensile properties. On the other hand, when examining the interface between unmodified WS325 and ELO, a strong interaction was visible, as indicated by the absence of voids and a uniform distribution throughout the sample thickness.

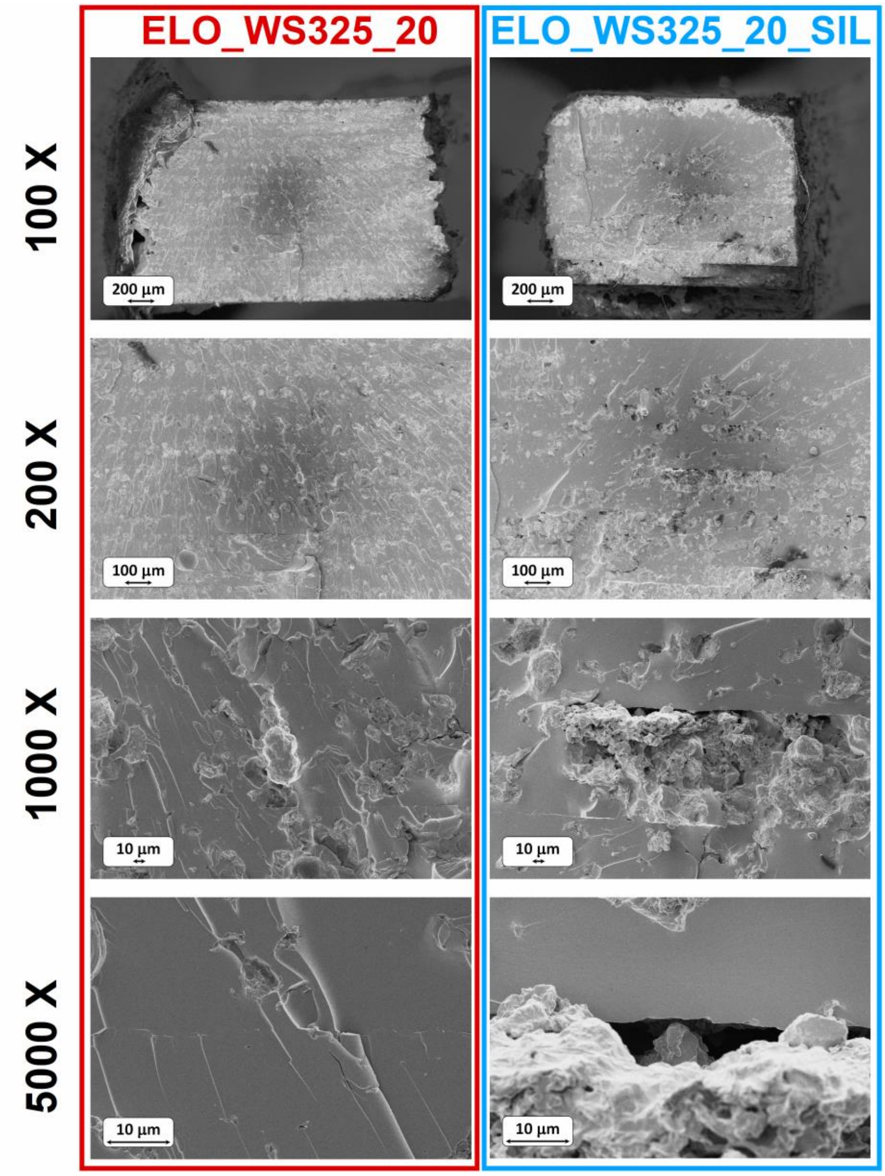

Figure 3.60. SEM analysis of fracture surface of 3D printed dog-bone specimens ELO-based containing pristine WS325 and silanized WS325.

Moreover, a comprehensive SEM analysis of pristine ELO and the composites containing 10 phr of various bio-derived fillers was made, demonstrating the uniform distribution of the powders and the favorable interface with all the bio-derived fillers, from hemp to tagua (**Figure 3.61**). The analysis was also conducted on ESO and its derived composites, which exhibited similarly favorable results as those observed for ELO-based composites. The distribution and interface were as satisfactory as those seen in the ELO-based composite. Lastly, it was possible to observe the distinct printed layers, each approximately 100 µm thick, in accordance with the 3D printing parameters set for Hot-lithography (**Figure 3.61**).

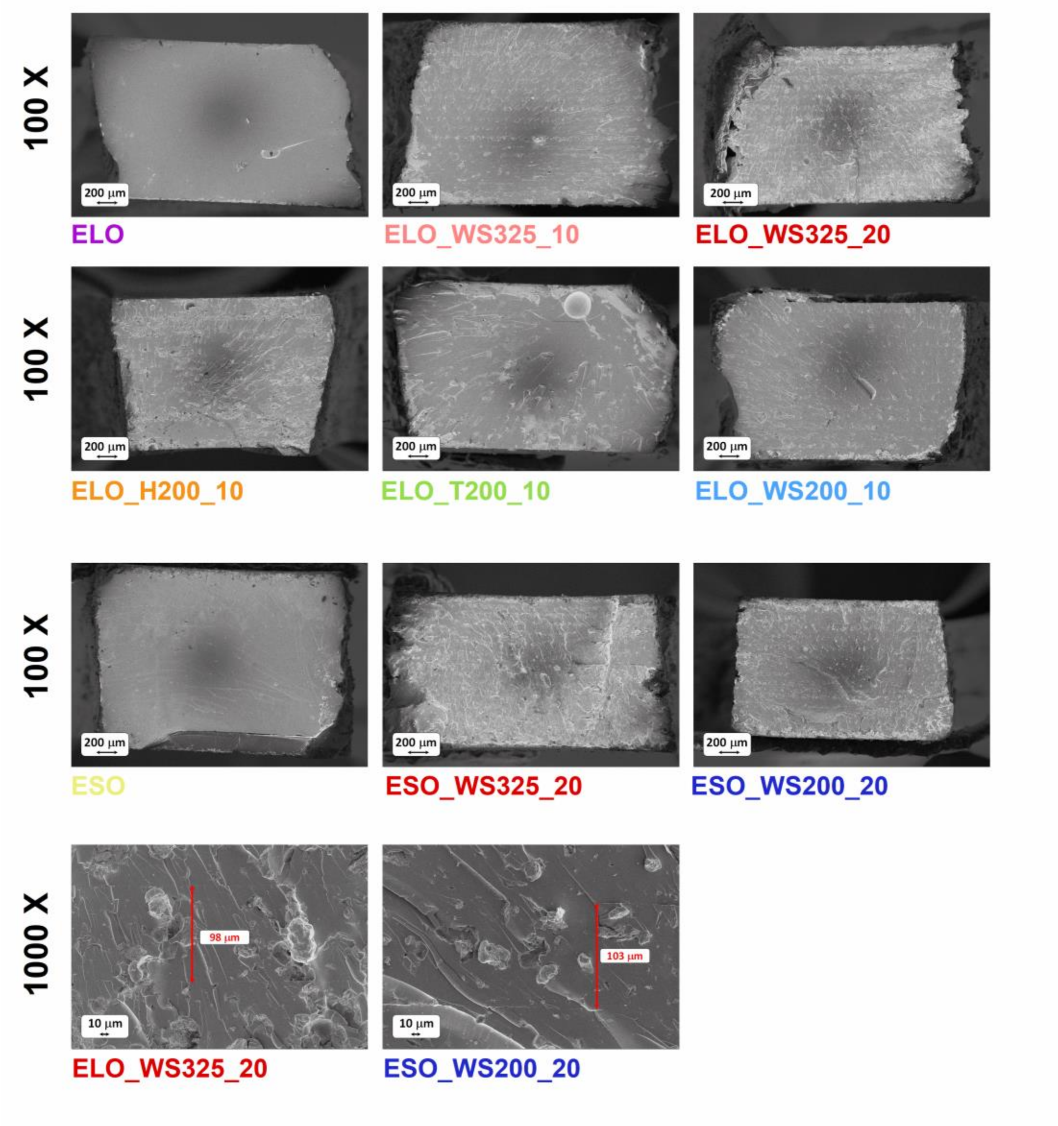

Figure 3.61. SEM analysis of the fractured dog-bone composite specimens derived from tensile test.

Chemical degradation of the bio-composites

The concept of circular economy is attracting more and more attention nowadays to overcome the problem of waste, pollution and plastic disposal. To embrace this aim, chemical degradation of the thermoset was carried out to prove the possibility to decompose the polymer reusing it for different purposes. This proof of concept was conducted in a strongly alkaline environment (NaOH 10 M) at high temperatures (80 °C) to accelerate the degradation process which was monitored over time through mass loss analysis. It's worth noting that the strong alkaline conditions also affected the bio-derived fillers since they primarily consist of cellulose, hemicellulose, and lignin. Indeed, these natural products degrade under strong alkaline conditions [258,259]. **Figure 3.62** illustrates the chemical degradation of the composites, which was more pronounced for the ESO-based composite due to the high treatment temperature (80°C). ESO had a T_g of 7°C, which was significantly lower than the treatment temperature thus, the increased mobility in the rubbery state could accelerate the degradation process. On the other hand, the high cross-link density of ELO could contribute to its resistance slowing the degradation process, which required up to two weeks to completely dissolve in the alkaline condition. The bio-derived composites exhibited a similar trend compared to the pristine matrix (**Figure 3.62**). The presence of bio-based fillers in the ESO-based composites containing 20 phr slightly accelerated the weight loss due to the degradation of the fillers themselves. Specifically, when considering ESO, ESO_WS325_10, and ESO_WS325_20, there was an observable increase in the degradation rate with an increase in the filler amount. **Figure 3.62D** illustrates the degradation of ESO and ESO_WS325_10, in which the degradation of the 3D printed samples is evident, followed by a change in the color of the alkaline solution.

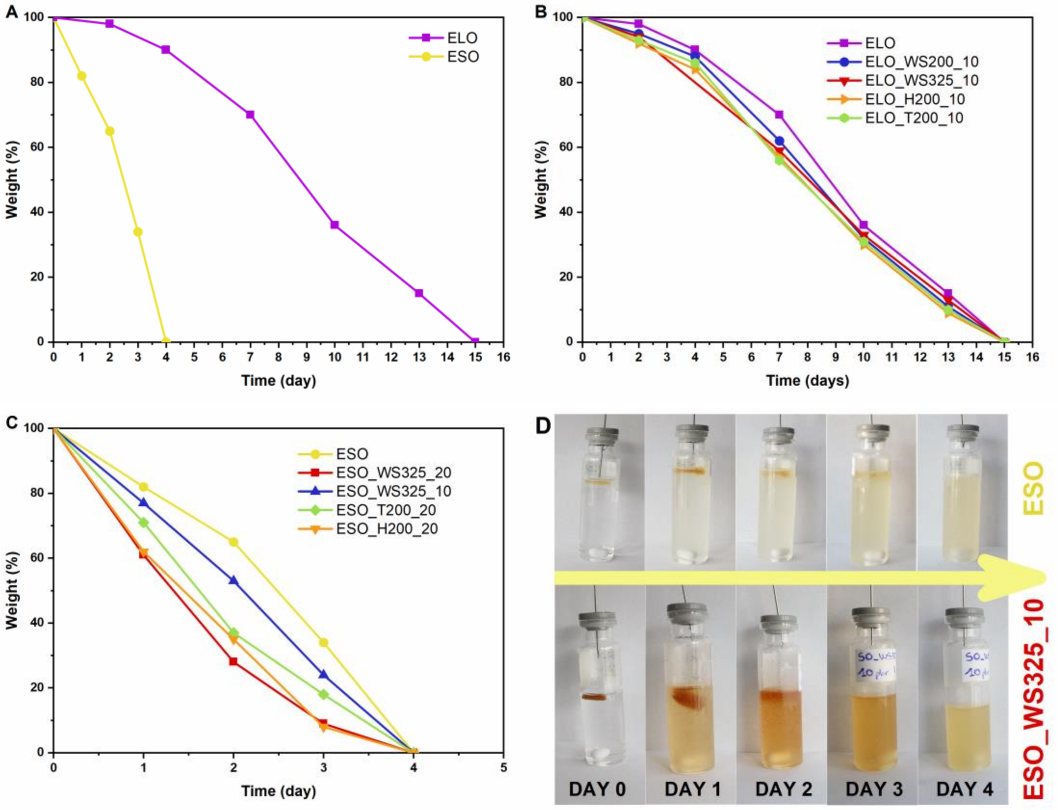

Figure 3.62. (A) Mass loss of the ELO and ESO in alkaline environment; (B) Degradation of ELO-based composites in alkaline environment (NaOH 10 wt%, 80 °C); (C) Mass loss of ESO-based composite; (D) Photos of the ESO and ESO_WS325_10 during the chemical degradation followed through the time.

The hydrolysis of the ester bond of the EVOs in the alkaline environment was responsible for the degradation of the polymer network [260]. NMR analysis was employed to verify this process, highlighting the differences between the uncured ELO and the degraded ELO-based product (**Figure 3.63A**). Three main changes can be seen: firstly, the epoxy peak disappeared in the degraded product due to the previous UV-curing step. Then, the characteristic glycerol peaks disappeared as a result of the hydrolysis of the ester bonds. Additionally, the formation of acids derived from ester hydrolysis can be observed due to the peak at 12 ppm. ATR-FTIR analysis (**Figure 3.63B**) was used to corroborate and confirm the results, comparing the pristine ELO, the UV-cured epoxy resin, and the degraded product. Three regions can be highlighted to confirm the UV-curing and the degradation process. The epoxy peak disappeared after curing, as previously demonstrated due to the formation of cross-links. This resulted in the formation of ether linkages, which were present in both the UV-cured ELO and the degraded product at around 1070 cm^{-1}. Interestingly, the ether region at 1160 cm^{-1} exhibited a decreased peak intensity from ELO to ELO-degraded, attributed to breaking of ester bonds in the glycerol-based linkage. Notably, the peak associated with the C=O of the ester bonds at 1737 cm^{-1} shifted to a lower wavenumber, indicating the formation of acid in the degraded product (1708 cm^{-1}). These analyses confirmed the possibility of recovering a degraded thermoset material that could be valuable in the production of polyester, in the view of a potential reuse of degraded products derived from 3D printed composites.

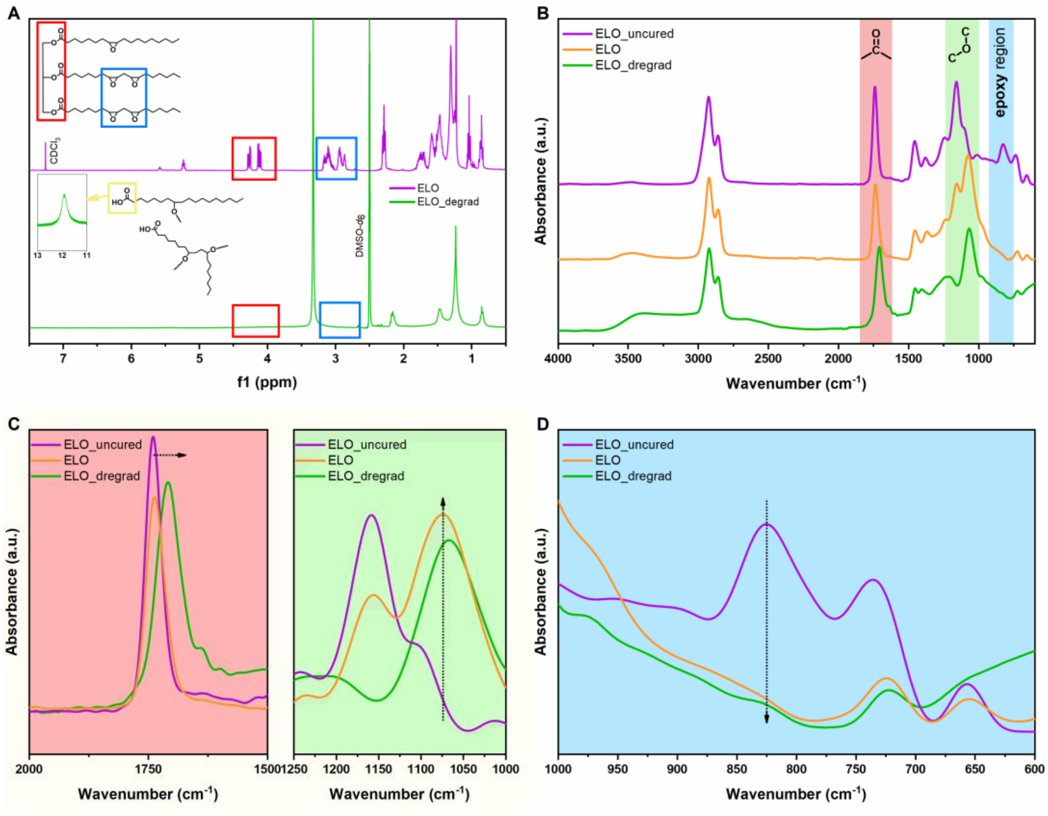

Figure 3.63. (A) ^{1}H-NMR analysis of uncured ELO and degraded ELO with highlighted peak changing. Epoxy groups, glycerol, and proton of acid group of degrade product; (B) ART-FTIR spectra of ELO_uncured, ELO UV-cured, and ELO_degrad; (C) zoom into the carbonyl region with the shit of the peak and ether region with the increase of the signal due to the curing; (D) decrease epoxy peak due to the UV-curing.

3.2.3. Conclusions

In this chapter, I have summarized our works where possible exploitation of different bio-based monomers for cationic UV-curing were investigated. The challenge of using new green monomers from cellulose, lignin or hemicellulose is an actual concern which open up several possibilities to move toward greener and more sustainable society. Among the several results reported in literature, these works highlight the feasibility of employing ferulic acid, isosorbide and epoxy vegetable oils to create adhesive, coating and bio-composites.

Ferulic acid was successfully functionalized and used by multiple approaches to overcome the initial UV-curing problem. Indeed, the epoxy monomer absorption limited the efficacy of UV-light as trigger for the curing. Thus, the study moved from cationic UV-curing to UV-assisted thermal cationic curing by analyzing two thiol-epoxy formulations and a fully epoxy one to find the best system. The different chemical nature of the cross-links generated in the thermosets allowed the customization of the properties with a wide spectrum of T_g and mechanical response. Indeed, thiol-epoxy thermosets had T_g of about 30 °C while the thermally cured pure epoxy thermoset achieved about 130 °C. Furthermore, it was possible to discover interesting adhesive properties (τ of 32 MPa) of this ferulic-based epoxy material which can be compared to the commercially BADGE-based available epoxy adhesives.

Cellulose and its interesting chemical nature drive the attention about isosorbide which has been functionalized introducing diglycidyl ether functionality and employed in coating applications. The aim of reaching high surface coating properties lead toward the use of bio-based filler to reinforce the pristine IDGE-based coating. Macadamia nut shell was successfully employed achieving interesting results in terms of surface hardness and mechanical response. Indeed, a maximum of 72 Shore D was achieved with 30 wt% of macadamia into the isosorbide-based epoxy polymeric matrix which is comparable with BADGE and ECC values.

Epoxy vegetable oils represent a noteworthy category of non-edible monomers with potential applications in various fields. Their utilization has been somewhat hampered due to their limited reactivity and resulting properties. Nevertheless, the addition of cross-linker or the incorporation of fillers can enhance their mechanical characteristics, making them appealing for several applications. To increase mechanical properties, bio-derived fillers, ranging from wall-nut shell to tagua powder, were used to produce bio-based composites. Moreover, SLA Hot-lithography was employed to promote reactivity and conversion, yielding promising outcomes. Conversions above 90 % were achieved exploiting temperature-assisted UV-curing. The study highlighted the significant effect of the epoxy functionality on the mechanical behavior being responsible of T_g variation from 7 to 47 °C for ESO and ELO respectively due to the high epoxy value of ELO. Complex and self-stain structures were properly generated fulfilling the advantages of 3D printing. The investigation emphasized the importance of the filler-matrix interface and the relative benefit in terms of mechanical response. Indeed, the chain-transfer mechanism between filler and matrix was the origin of the positive impact given by the filler and it was demonstrated by silanization. Finally, to join the concept of circular economy, the degradation of the material was assessed to prove a possible reuse of the bio-based composites.

4. Radical UV-curing of allyl-functional bio-based monomers

UV-curing is a significant technique employed to form thermoset material. Not only cationic UV-curing can be exploited, but also radical UV-curing offers a broad spectrum of monomers which can be used to generate different networks to meet specific requirements. This chapter showcases the results obtained through the utilization of various bio-based monomers in the radical UV-curing process. Through an exploration of different features, we highlight the significance of each stage in this process, collectively aiming for a more sustainable material development approach.

These studies aim to underscore the importance and effectiveness of substituting fossil-based monomer with bio-based counterparts to attain essential material properties. The entire process is composed of different stages which are deeply investigated. From the synthesis of suitable monomers for the curing process; followed by an examination of the optimization of UV-curing procedures; to the final tuning of the properties by playing with chemical aspects to accommodate diverse demands. This strategy promotes sustainability aiming to achieve valuable and unique properties. The chapter is centered around the exploration of various bio-based monomers within the context of thiol-ene UV-curing (**Figure 4.1**), encompassing diverse applications ranging from coatings to 3D printing. The research primarily delves into the utilization of ferulic acid (Paper I), isosorbide (Paper II), furan monomers (Paper III) and levoglucosenone (Paper IV) as primary monomer for the development of cross-linked network. Finally, a brief excursus on itaconic acid and the use of UV-induce thiol-ene reaction for surface post-functionalization (Paper V).

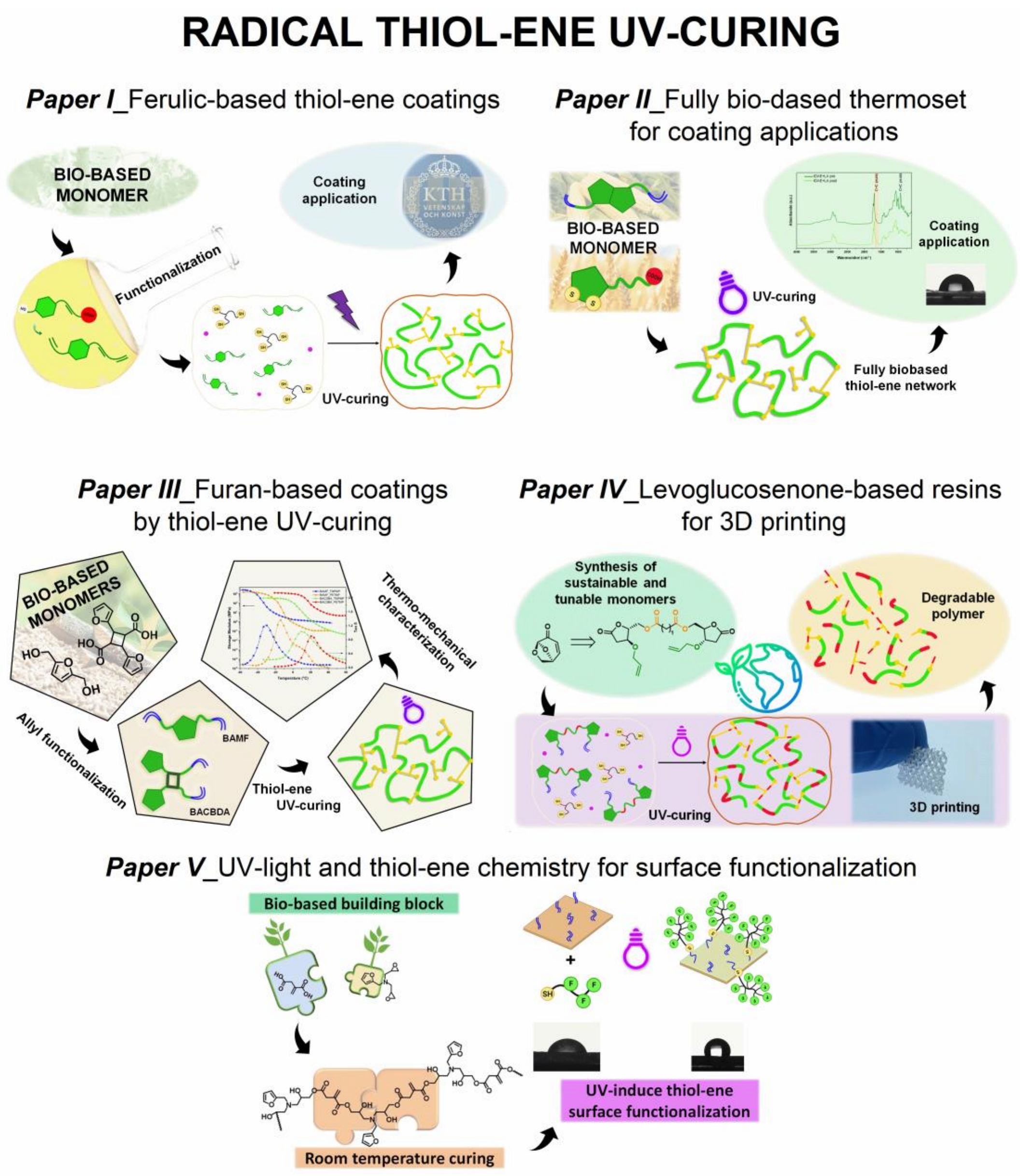

Figure 4.1. Schematic representation of the subjects addressed in the different papers presented in this thesis chapter.

4.1. Where are the eco-friendly monomers for radical thiol-ene UV-curing?

Promoting sustainability and reducing the use of fossil-based monomers are the boosts toward the use of bio-based monomers as key-players in the green transition for a more eco-friendly plastic world [10,261]. Performance and cost production are prerequisites which need to be addressed for the bio-based monomers in order to be competitive with respect to the well-known and establish fossil-based monomers [50]. Derivatives of lignin, cellulose and hemicellulose are more and more used due to the advantages of been largely available on world-wide scale and moreover they can be retrieved form the side stream of food industry, agricultural waste or forestry residue [9,45]. The use of building blocks from sugar, polysaccharides, cellulose, vegetable oils, and lignin are gaining competitiveness in terms of industrial and socio-economic features due to the wide application range which can cover different application requirements [46,262,263]. Among this building blocks, the research has been focused on some interesting monomers which can be functionalized to be suitable for UV-radical curing.

A lignin derivative, ferulic acid (FeA), employed in the **Chapter 3** as an epoxy-functional monomer, has been used in a new version as allyl-based monomer. The green origin is insight in its lignin's origin being a key component for the vegetable cells [170,173,184,264]. The interest in FeA explained by the fascinating achievable properties makes it attractive for developing new bio-based formulation for radical UV-curing which has been proposed for other cinnamic acid [265,266].

Another important platform for bio-based monomers is cellulose which represent an adaptable starting point to develop a wide range of different classes of monomers, terpenes [125,188–190], furans [92], isosorbide-based derivatives [191], carboxylic acids and bio-derived multifunctional alcohols [9,49,192]. Among the several possibilities, isosorbide was selected as starting point to develop a study about a bio-based thiol-ene network formed by isosorbide-based allyl monomer. The choice is driven by the potential of isosorbide as promising platform for biobased monomers across several application has been previously described in **Chapter 3** [193,197–199] pointing out the wide spectrum of possible employment from medical application to UV-curable coatings [55,201,203]. Here, isosorbide was used to develop a new fully bio-based coating exploiting thiol-ene chemistry by reacting with lipoic acid. Lipoic acid (LA) is a natural molecule which is present in both human and vegetable cells;

specifically it can be found in potatoes, spinaches, and it is present in either wheat's roots or leaves wheat [267,268]. The peculiarity is insight in the presence of a disulfide bond in the five member ring present in the chemical structure of LA [269]. The reactivity towards UV-light was already proved in 1954 [270], and since then LA has been used for copolymerization of styrene and vinyl monomers [271,272]. More recently, LA has been employed for the generation of degradable network due to the reversibility of the rupture of the disulfide bond [273], and it has been further studied with vinyl monomers [137,274].

Moving to other platform chemicals in the investigation of bio-based monomers for radical UV-curing, furanic compounds, derived from carbohydrate biomass [84,91,92], have been used to develop green coatings. As deeply discussed before, furans are originated from cellulose and hemicellulose [45,50]; they are available on large scale and the low cost makes them a valid alternative to petroleum-based monomers, especially considering that furans can be produce from side streams of several industries [10,93,94]. A well-known furan monomer, 2,5-furandicarboxylic acid (FDCA), has been adapted to classical thiol-ene chemistry by functionalization of acid group by allyl reaction. A vast array of bio-based thermosets was obtained *via* UV-curing with different thiol monomers [275]. Inspired by this result and driven by the advantages of UV-assisted thiol-ene reaction, two different furanic monomers were used for developing a thiol-ene cross-linked network: 2,5-furandimethanol (FDM) and cyclobutane furan dicarboxylic acid (CBDA-2). FDM has already been used for coating applications [108,109]. CBDA-2, produced under UV-light through the [2+2] cycloaddition [276], has been employed as building block for polyester [277] or as cross-linker for epoxy vegetable oils [278].

My research continued in scouting for green candidates to be employed in the UV-curing. One promising cellulose-derived monomer is be levoglucosenone (LGO) which has the benefit of being produced by a carbon-neutral process, as illustrated in **Figure 4.2** [279]. LGO offers reactive functionalities and commercial availability of 1000 tons per year which make it attractive for new types of functional polymers [279]. Polyacrylates [280], polycarbonates [281], polycyclic olefin [282], and polyesters [283] represents some LGO-based polymers recently developed. Since no studies cover the UV-curing of LGO derivatives, this investigation aimed to develop a new set of bio-based LGO-derived monomers suitable for UV-curing, addressing the exploitation of additive manufacturing (AM) by the digital light process (DLP). One current challenge in AM is the lack of bio-derived resins which are suitable for 3D printing [284,285]. Hence, after the detailed investigation of the radical UV-curing process to optimize and select the best formulation, DLP was used to verify the printability of the LGO-derived resin opening new possible application for bio-based monomers.

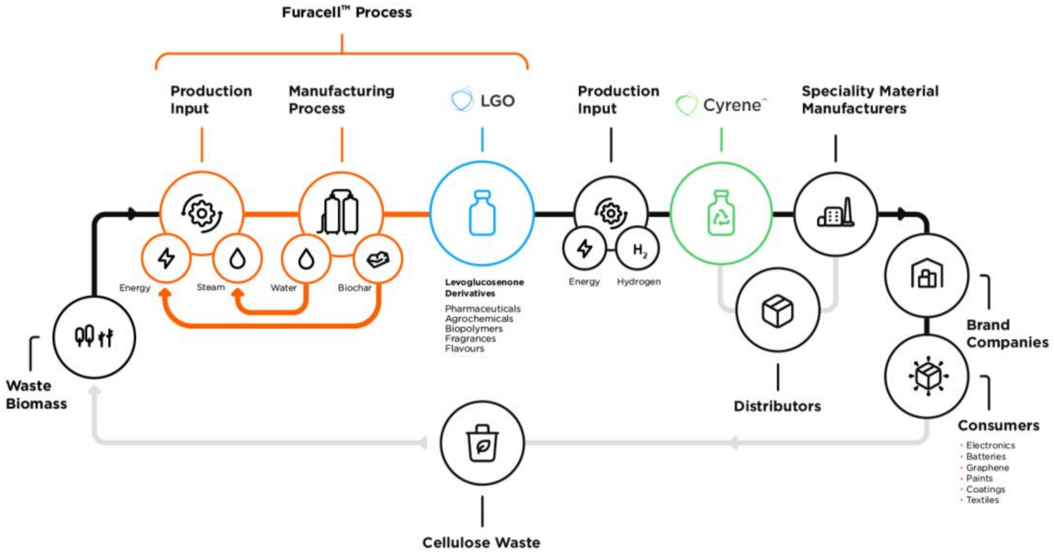

Figure 4.2. Schematic view of the production process of LGO from biomass waste [279].

The final investigation focused on the utilization of itaconic acid (IA) and furanic-based monomers to create environmentally friendly thermoset materials. Itaconic acid has gained recognition as one of the 12 top building blocks by the US Department of Energy [286]. The natural diacid is produced by sugar fermentation exploiting the fungus *Aspergillus terrus* [287,288]. Its abundant availability of approximately 80 ktons per year and its low cost of 2 €/kg represent remarkable requisites which encourage the exploitation of this interesting monomer [289]. The presence of the α,β-unsaturated functionality makes IA promising for several chemical modifications [290] which can be suitable for the use in UV-activated radical photopolymerization [54,291]. Interestingly, our study exploited UV-light for a surface treatment to customize the final properties of an itaconic-based thermoset. Thiol-ene chemistry is employed to functionalize the surface of the coating, imprinting different properties by thiol-ene reaction with the instauration present in the backbone after the curing stage.

Part of the work described in this chapter has been already published and it is available at the references:

[242] **Pezzana, L.**; Mousa, M.; Malmström, E.; Johansson, M.; Sangermano, M. Bio-based monomers for UV-curable coatings: allylation of ferulic acid and investigation of photocured thiol-ene network. *Prog. Org. Coatings* **2021**, *150*, 105986, DOI: https://doi.org/10.1016/j.porgcoat.2020.105986.

[244] **Pezzana, L.**; Sangermano, M. Fully biobased UV-cured thiol-ene coatings. *Prog. Org. Coatings* **2021**, *157*, 106295. DOI: https://doi.org/10.1016/j.porgcoat.2021.106295.

[292] **Pezzana, L.**; Melilli, G.; Delliere, P.; Moraru, D.; Guigo, N.; Sbirrazzuoli, N.; Sangermano, M. Thiol-ene biobased networks: Furan allyl derivatives for green coating applications. *Prog. Org. Coatings* **2022**, *173*, 107203. DOI: https://doi.org/10.1016/j.porgcoat.2022.107203.

[293] Flourat, A.L.; **Pezzana, L.**; Belgacem, S.; Dosso, A.; Sangermano, M.; Fadlallah, S.; Allais, F. Levoglucosenone to 3D-printed green materials: synthesizing sustainable and tunable monomers for eco-friendly photo-curing. *Green Chem.* **2023**, DOI:10.1039/D3GC01833D.

[294] **Pezzana, L.**; Melilli, G.; Sangermano, M.; Sbirrazzuoli, N.; Guigo, N. Sustainable approach for coating production: Room temperature curing of diglycidyl furfuryl amine and itaconic acid with UV-induced thiol-ene surface post-functionalization. *React. Funct. Polym.* **2023**, *182*, 105486, DOI: https://doi.org/10.1016/j.reactfunctpolym.2022.105486.

4.2. Experimental section

4.2.1. Material and Chemicals

Ferulic acid (FeA), lipoic acid (LA), trans-3-(2-furyl)acrylic acid (FAA), furfuryl amine (FfA), and itaconic acid (IA) were provided by Sigma Aldrich and used as received. Isosorbide diallyl (IDAE) was supplied by Specific Polymer (Castries, France). 2,5-Furandimethanol (FDM) was purchased from Apollo Scientific (97 % purity). Levoglucosenone (LGO) was graciously provided by Circa group. The trimethylolpropane tris(3-mercaptopropionate) (TMPMP) and the pentaerythritol tetrakis(3-mercaptopropionate) (PETMP) were provide by Bruno Bock Gmbh. 1H,1H,2H,2H-perfluorodecanethiol (PFDT) was supplied from Sigma Aldrich.

Allyl bromide, sodium hydroxide (NaOH), potassium carbonate (K_2CO_3), Pd (10 % on activated carbon) were obtained from Sigma Aldrich. Magnesium sulphate ($MgSO_4$) was provided by Acros Organic. Acetone and methanol (MeOH), ethyl acetate (EtOAc) were supplied by VWR Chemicals, dichloromethane (DCM) from Merck KGaA, and dimethyl sulfoxide (DMSO), diethyl ether were provided by Carlo Erba. Hydrochloric acid, (HCl 37 %) and sulphuric acid (H_2SO_4, 95 %) were supplied by VWR Solvent. NMR analysis was performed with either deuterated chloroform, $CDCl_3$, or dimethyl sulfoxide, DMSO-d_6 provided by VWR Chemicals. The photoinitiators were Irgacure 819, phenylbis(2,4,6-trimethylbenzoyl)phosphine oxide (BAPO) and Darocure 1173 provided by BASF.

4.2.2. Procedures

4.2.2.1. Allylation of ferulic acid (A2FeA)

The allylation was performed according previous protocol, adapting the conditions according to the preliminary result obtained with ferulic acid [265,266]. FeA (2.08 g, 10.7 mmol) and potassium carbonate (5.91 g, 42.8 mmol) were placed in a two-neck round-bottomed flask and dissolved in acetone (40 mL). The initial stirring allowed the dissolution of FeA whereafter allyl bromide (2.35 mL, 26.7 mmol) was added. The reaction was then run for about 20 hours under reflux (~55 °C). The mixture was then filtered, and the solvent evaporated. The crude product was dissolved in DCM (20 mL) and extracted with water. The water phase was extracted three times with DCM then the organic fractions were combined together and dried over $MgSO_4$ to obtain the product. Finally, the solvent was removed under reduced pressure on a rotavapor. A2FeA was obtained as yellow-orange liquid (2.39 g, 82 % yield) and it was used without further purification. The schematic view of the reaction path followed for the multiple reactions performed on ferulic acid is reported in **Figure 4.3**.

^{1}H NMR (400 MHz, DMSO-d_6) δ = 7.61 (d, J = 15.9 Hz, 1H), 7.37 (d, J = 2.0 Hz, 1H), 7.21 (dd, J = 8.3, 1.9 Hz, 1H), 6.97 (d, J = 8.3 Hz, 1H), 6.58 (d, J = 15.9 Hz, 1H), 6.01 (dddt, J = 20.9, 17.4, 10.6, 5.4 Hz, 2H), 5.43 – 5.20 (m, 4H), 4.63 (ddt, J = 29.3, 5.4, 1.5 Hz, 4H), 3.82 (s, 3H) ppm.

^{13}C NMR (101 MHz, DMSO-d_6) δ = 166.10, 149.82, 149.17, 144.88, 133.42, 132.84, 127.02, 122.78, 117.75, 117.70, 115.34, 112.89, 110.70, 68.81, 64.30, 55.64 ppm.

4.2.2.2. Hydrogenation of ferulic acid (h-FeA)

FeA (20.0 g, 103 mmol) was dissolved in MeOH (100 mL) under stirring. The catalyst, Pd on activated carbon (2 g), was added to a round-bottomed flask which was sealed with a septum. Argon was supplied to degas the reaction flask. The FA-solution was added to the flask with a syringe whereafter H_2 atmosphere was applied using a H_2-balon. The mixture was stirred 24 hours at room temperature then the Pd/C was filtered off through a glass filter (NS 5). The solvent was then evaporated using a rotavapor to obtain the product, h-FeA, as a whitish powder (19.2 g, 95 % yield). The schematic view of this reaction step is reported in **Figure 4.3**.

^{1}H NMR (400 MHz, $CDCl_3$) δ = 6.86 – 6.70 (m, 3H), 3.87 (s, 3H), 2.89 (t, *J* = 7.7 Hz, 2H), 2.66 (t, *J* = 7.7 Hz, 2H) ppm.

^{13}C NMR (101 MHz, $CDCl_3$) δ = 178.95, 146.59, 144.25, 132.21, 120.99, 114.55, 111.07, 56.02, 36.10, 30.49 ppm.

4.2.2.3. Allylation of hydrogenated ferulic acid (h-A2FeA)

h-FeA (3.22 g, 16.4 mmol) and potassium carbonate (9.10 g, 65.7 mmol) were added to a two-neck round-bottomed flask and dissolved in acetone (~50 mL). The mixture was stirred to allow the dissolution of h-FA whereafter allyl bromide (3.45 mL, 39.4 mmol) was added. The reaction was then left for 24 hours under reflux. Then the mixture was filtered, the solvent was evaporated, and DCM was used for the extraction of the organic phase. The water layer was extracted three times with DCM, then the combined organic phases were dried using $MgSO_4$. Finally, evaporation of the solvent was performed with rotavapor. The h-A2FeA retrieved as yellow liquid (4.24 g, 93 % yield), was used without further purification (**Figure 4.3**).

^{1}H NMR (400 MHz, $CDCl_3$) δ = 6.80 (d, *J* = 8.1 Hz, 1H), 6.75 – 6.65 (m, 2H), 6.07 (ddt, *J* = 17.4, 10.6, 5.4 Hz, 1H), 5.90 (ddt, *J* = 17.3, 10.5, 5.7 Hz, 1H), 5.44 – 5.18 (m, 4H), 4.58 (dq, *J* = 5.7, 1.4 Hz, 4H), 3.86 (s, 3H), 2.91 (t, *J* = 7.7 Hz, 2H), 2.64 (dd, *J* = 8.4, 7.1 Hz, 2H) ppm.

^{13}C NMR (101 MHz, $CDCl_3$) δ = 172.58, 149.39, 146.47, 133.53, 133.51, 132.16, 120.07, 118.22, 117.83, 113.65, 112.06, 70.00, 65.13, 55.89, 36.10, 30.59 ppm.

4.2.2.4. Mono-allylation of hydrogenated ferulic acid (h-A1FeA).

h-FA (3.33 g, 17.0 mmol) was dissolved in acetone (50 mL). K_2CO_3 (9.38 g, 67.8 mmol) was added to the solution and then allyl bromide (3.55 mL, 40.7 mmol) was added using a micropipette. The mixture was kept at reflux for 24 hours under vigorous stirring. After cooling down to r.t., the solution was filtered, and the solvent was removed under reduced pressure. The residue was dissolved in a mixture aqueous NaOH (75 mL, 2 M) and EtOH (50 mL), then the solution was heated to reflux for 2 hours. After cooling, the solvent was partially evaporated. HCl (6 M) was added dropwise to precipitate the final product which was filtered and dried in a vacuum oven over night. Yellowish powder was recovered (h-A1FeA, 3.85 g, 96 % yield, **Figure 4.3**).

^{1}H NMR (400 MHz, $CDCl_3$) δ = 10.67 (s, 1H), 6.83 (d, J = 8.1 Hz, 1H), 6.79 – 6.70 (m, 2H), 6.10 (ddt, J = 16.2, 10.6, 5.4 Hz, 1H), 5.46 – 5.37 (m, 1H), 5.33 – 5.25 (m, 1H), 4.61 (d, J = 5.4 Hz, 2H), 3.88 (s, 3H), 2.93 (t, J = 7.7 Hz, 2H), 2.69 (t, J = 7.7 Hz, 2H) ppm.

^{13}C NMR (101 MHz, $CDCl_3$) δ = 178.94, 149.41, 146.55, 133.48, 133.17, 120.03, 117.87, 113.66, 112.06, 69.99, 55.90, 35.81, 30.25 ppm.

4.2.2.5. Esterification of allylated hydrogenated ferulic acid (h-EA1FeA)

h-A1FeA (2.0 g, 8.5 mmol) was dissolved in MeOH (40 mL) where after H_2SO_4 was added in a catalytic amount. The solution was refluxed 24 hours under stirring. After cooling to r.t. the mixture, the product was extracted with EtOAc. The organic layers were combined and washed with portions of saturated $NaHCO_3$ and brine, respectively, and dried over $MgSO_4$. Finally, the solvent was evaporated on a rotavapor. The product (h-EA1FeA) was an orange-brown liquid (1.99 g, 94 % yield, **Figure 4.3**).

^{1}H NMR (400 MHz, $CDCl_3$) δ = 6.79 (dd, J = 8.1, 1.9 Hz, 1H), 6.74 – 6.66 (m, 2H), 6.07 (dddd, J = 15.9, 12.7, 6.5, 4.4 Hz, 1H), 5.43 – 5.20 (m, 2H), 4.57 (ddt, J = 5.4, 2.8, 1.5 Hz, 2H), 3.85 (d, J = 2.1 Hz, 3H), 3.66 (d, J = 2.5 Hz, 3H), 2.89 (td, J = 7.7, 1.8 Hz, 2H), 2.60 (td, J = 7.9, 1.8 Hz, 2H) ppm.

^{13}C NMR (101 MHz, $CDCl_3$) δ = 173.48, 149.49, 146.57, 133.65, 120.14, 117.92, 113.75, 112.15, 70.09, 55.99, 51.70, 36.06, 30.71 ppm.

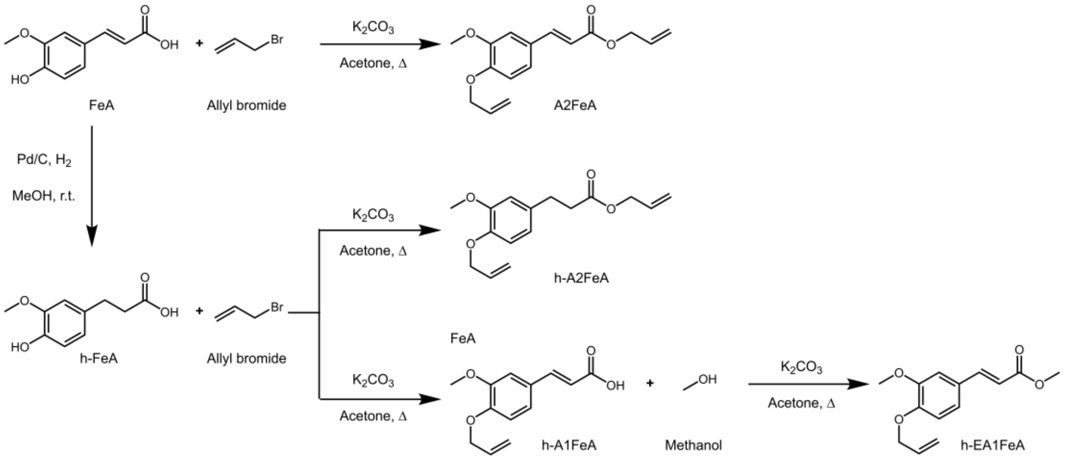

Figure 4.3. Synthetic pathways used to develop the different monomers from ferulic acid.

4.2.2.6. Allylation of 2,5-furandimethanol (BAMF)

Following and adapting previous protocols [295,296], FDM (3.00 g, 23.4 mmol) was placed in a round bottom flask and dissolved in acetonitrile (150 mL). Pulverized NaOH was added (3.75 g) and the mixture was stirred for 30 min then allyl bromide (7.02 mL, 8.1 mmol) was slowly added at 0°C. The reaction was left for 3 days at room temperature under agitation. After the precipitate was filtered off and rinsed with acetonitrile. The solvent was evaporated, and the extraction of the organic phase was performed using diethyl ether. The water phase was extracted three times then the collected organic phases were washed with water and dried over $MgSO_4$. The solvent was removed under reduced pressure and the product obtained as brownish liquid was used without other purification (3.96 g, yield 81 %). The chemical reaction is presented in **Figure 4.4**.

^{1}H NMR (400 MHz, DMSO-d_6) δ 7.67 – 7.62 (m, 2H), 6.43 (d, J = 1.7 Hz, 4H), 5.88 (ddt, J = 17.3, 10.6, 5.4 Hz, 2H), 5.26 (dq, J = 17.3, 1.8 Hz, 2H), 5.20 – 5.12 (m, 2H), 4.41 (s, 4H), 3.95 (dt, J = 5.4, 1.5 Hz, 4H).

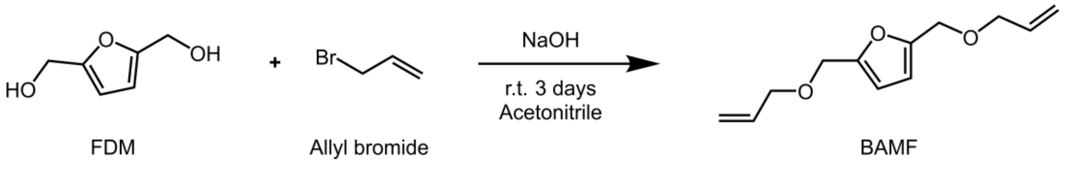

Figure 4.4. Allylation of furandimethanol by reaction with allyl bromide to create BAMF.

4.2.2.7. Allylation cyclobutane dicarboxylate (BACBDA)

The allylation of furfuryl acrylic acid (FAA) to obtain a bifunctional monomer is a two-step reaction as shown in **Figure 4.5**. The first step was done according to previous syntheses [278,297]. FAA (25 g, 181 mmol) was suspended in hexane (250 mL) in a 1000 mL flask. Strong mixing was provided, and two commercially available lights (intensity 30 W with emission ranged from 385 to 400 ηm, purchased from Onforu) were used to provide the UV-irradiation. The reaction was left until the total conversion of the reagent was reached by measuring it through ^{1}H-NMR. The solid product was filtrated through a glass filter G4 and then was left to dry overnight to remove all the hexane. The final brownish solid product was CBDA-2 obtained in a of yield 97 % (24 g).

The second step was done following other synthesis [298]. CBDA-2 (7.00 g, 25.4 mmol) was dissolved in DMSO (100 mL). NaOH (4.06 g) was pulverized and added into the solution. Then allyl bromide (8.78 mL, 10 mmol) was finally added. The reaction was left for 3 days at 50 °C. The reaction was stopped by decreasing the temperature and DCM was used to extract the organic product. Three extractions against water were performed. The organic phases were collected and then washed with water and brine. Finally, the organic phase was dried over $MgSO_4$ and the solvent was removed by evaporation under reduced pressure obtaining BACBDA as a viscus brown liquid as final product (8.5 g, yield 94 %).

^{1}H NMR (400 MHz, DMSO-d_6) δ 6.60 (d, J = 1.9 Hz, 2H), 5.47 – 5.27 (m, 4H), 5.14 – 5.00 (m, 2H), 4.58 – 4.32 (m, 4H), 3.80 – 3.66 (m, 4H), 3.36 – 3.25 (m, 2H), 3.07 (dq, J = 4.9, 1.6, 1.1 Hz, 2H).

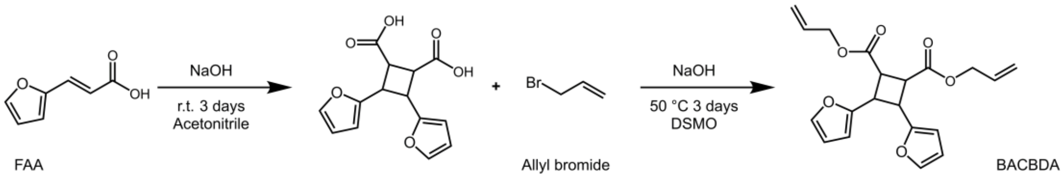

Figure 4.5. Synthesis of bis allyl CBDA-2 in two-step reaction starting from trans-3-(2-furyl) acrylic acid.

4.2.2.8. Photopolymerization and 3D-printing of LGO derivatives

The allyl derivatives from levoglucosenone (LGO) were synthetize in the laboratory of URD Agro-Biontechnologies Industrielles (ABI). For more details refers to Flourat et al. [293]. The allylation of LGO was performed by reaction through a one-pot two-steps reaction (**Figure 4.6**), involving the oxa-Michael addition of allyl alcohol and then the Baeyer-Villiger oxidation of the crude mixture using H_2O_2. Allyl alcohol was added to LGO in presence of triethylamine at r.t. for 20 h. After concentration of the medium, 1 mL of water was added. At 0 °C, a solution of hydrogen peroxide 30% was added dropwise, then the reaction mixture was allowed to reach room temperature and then was heated at 45 °C for 16 h. Absence of remaining peroxide was tested using quantofix strip and reaction medium was concentrated prior flash purification over silica gel. Pure HBO-*O*-All was recovered as a pale-yellow oil (63 %). The second step of the reaction was a transesterification of the allyl derivative which complete the production of the final bi-functional LGO derivative. Diethyl malonate, diethyl adipate and diethyl azelate were the three different esters used as chain extender between the HBO-*O*-All moieties. The transesterification was conducted in presence of Novozyme 435® and the best parameters were found according to DoE performed varying temperature, Novozyme 435®/diethyl malonate ratio and equivalence of HBO-*O*-Allyl to diethyl malonate. The schematical view of the two-step reaction is reported in **Figure 4.6**.

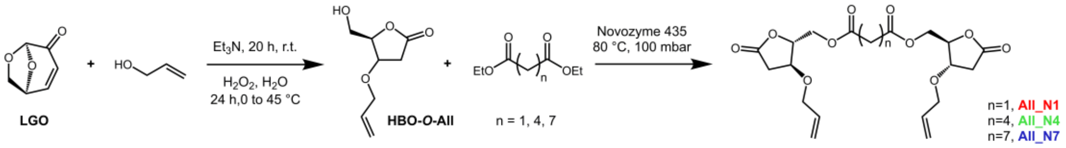

Figure 4.6. Synthesis pathway of LGO-based allyl derivatives. Oxa-Michael addition of allyl alcohol and transesterification reaction in presence of Novozyme 435.

4.2.2.9. Formulation and photopolymerization of ferulic acid derivatives

The synthesized allylated-monomers were used to develop a series of different photocurable formulations, **Table 4.1**. Trimethylolpropane tris(3-mercaptopropionate) (TMPMP) was used as thiol-functional crosslinker in all formulations. The formulations were prepared by adding stoichiometric amounts of thiols and enes (1:1 molar ratio). A2FeA was, however, used in two different ratios, either in a 1:1 molar ratio thiol:allyl ether, or 1:1 molar ratio thiol:total enes. The photoinitiator used was BAPO in accordance to previous works [299,300] and used in 0.5 wt% of the total of mass of the resin. The photocurable formulation were prepared according to the amounts listed in **Table 4.1**. As example, Entry 3 is explained in detail. A2FeA (200 mg) was placed in a test tube together with h-EA1FA (10 mg) and then TMPMP (204 mg) was added. The test tube was stirred for 5 min in an ultrasonic bath. The photoinitiator (2 mg) was finally added whereafter the test tube was covered with aluminum foil and stirred for another 2/3 min to ensure a complete dissolution of PI. A set of films was prepared using a silicon mold (8 × 12 mm, with a variable thickness of 0.1, 0.2, 0.3, 0.4, and 0.6 mm respectively). The UV irradiation was ensured by means of a DYMAX ECE 5000 Flood lamp. The irradiation time was 1 or 2 minutes (~ 100 mW/cm^2).

Table 4.1. Summary of the prepared photocurable formulations. TMPMP was used as a crosslinking trifunctional thiol and BAPO (0.5 wt%) as a photoinitiator in all formulations. (^{1}) The monoallylated monomer was added in molar amount 5 %, 10 % or 15 % relative to the diallylated monomer.

		Diallylated monomers		**Monoallylated monomer ^{1}**	**Thiol monomer**
ENTRY	**MOLAR RATIO 1:1**	**A2FeA**	**h-A2FeA**	**h-EA1FeA**	**TMPMP**
		(mg)	(mg)	(mg)	(mg)
1	Thiol : allyl ether	215	-	-	208
2	Thiol : total ene	195	-	-	283
3	Thiol : allyl ether	200	-	10 [5 %]	199
4	Thiol : allyl ether	204	-	21 [10 %]	209
5	Thiol : allyl ether	207	-	33 [15 %]	218
6	Thiol : allyl ether	-	220	-	212
7	Thiol : allyl ether	-	216	10 [5 %]	213
8	Thiol : allyl ether	-	222	22 [10 %]	225
9	Thiol : allyl ether	-	209	33 [15 %]	219

4.2.2.10. Radical UV-curing of isosorbide diallyl

Thio-ene photocurable formulations were prepared using isosorbide dially (IDA) as allyl monomer and lipoic acid (LA) or TMPMP as thiol functional monomers. The mixing was performed in equimolar ratio between ene and thiol functionality with 5 phr of photoinitiator for IDA + LA and 1 phr for IDA + TMPMP. LA (400 mg) was placed in a test tube together with IDA (439 mg). The test tube was stirred for 10 min in an ultrasonic bath at room temperature to allow complete solubilization of LA and mixing. The photoinitiator, Darocure 1173 (42 mg), was finally added covering the test tube with aluminum foil and stirred for another 2/3 min to ensure a complete dissolution. A set of films was prepared coating the formulation on a glass slide and irradiating with the UV-lamp for 5 min at 150 mW/cm^2. The thickness of the coatings was 50 μm. The UV-irradiation was performed with a DYMAX ECE 5000 Flood lamp. Considering IDA + TMPMP, the procedure followed the same step using the UV-irradiation for only 1 min.

4.2.2.11. Formulation and photo cross-linking of furan-based allyl monomers

The synthetized furan-based allyl-monomers were mixed with two different commercially available thiols, the trimethylolpropane tris(3-mercaptopropionate) (TMPMP) and the pentaerythritol tetrakis(3-mercaptopropionate) (PETMP) to investigate the thiol-ene UV-activated chemistry. The stoichiometric ratio between allyl group and thiol group was fixed at 1:1 to have the exact equivalent of both functional groups (ene and thiol). The monomers were weighed and then, the BAPO photoinitiator was added to the formulations. The different formulations are listed in the **Table 4.2**. The three components, allyl monomer, thiol monomer and photoinitiator were mixed in an ultrasound bath until the BAPO was completely dissolved. The formulations were kept in brown vials to avoid light contact. Preliminary tests were carried out to assess the exact concentration of BAPO into the formulations. For this reason, photocuring process was investigated varying the BAPO concentration from 0 to 3 phr. Finally, the photoinitiator was set at 3 phr to produce the specimens for the further characterizations. The formulations were spread on a Telfon substrate with a film bar ensuring a thickness of 150 μm. The photocuring was carried out by exposing the formulation to UV-light for 5 min. A DYMAX flood lamp was used as the UV-light source with the light intensity set around 130 mW/cm^2. The emission spectrum of the UV lamp was from 275 to 500 nm with a maximum located to 365 nm.

Table 4.2. Formulation tested in the study with the synthetized allyl monomer and the commercial thiols, TMPMP and PETMP. The photoinitiator (BAPO) was added in 3 phr evaluating the total amount of the resin.

ENTRY	ALLYL MONOMER	Mass	THIOL MONOMER	Mass
		(g) / [mmol]		(g) / [mmol]
BAMF_TMPMP	BAMF	0.500 [2.4]	TMPMP	0.638 [1.6]
BAMF_PETMP	BAMF	0.500 [2.4]	PETMP	0.587 [1.2]
BACBDA_TMPMP	BACBDA	0.500 [1.4]	TMPMP	0.373 [0.9]
BACBDA_PETMP	BACBDA	0.500 [1.4]	PETMP	0.343 [0.7]

4.2.2.12. Formulations and DLP 3D-printing of allyl derivatives from LGO

The three synthetized allyl ethers were tested for thiol-ene photocuring process, so a commercial thiol (TMPMP) was used as cross-linker in the formulations. The ratio between ene and thiol was kept at 1:1 molar ratio and 3 wt% of photoinitiator, Darocure 1173, was added to the mixture. All the data are collected in **Table 4.3**. The formulations containing ALL_N1 and ALL_N7 were heated to allow the melting of the ene monomers in order to mixing properly. Then all the formulations were kept in an ultrasound bath for 5 minutes in order to disperse uniformly all compounds. Successively, the formulations were cured in silicon mold to create the samples for further analysis. A Flood DYMAX UV lamp was used as a UV-source. The light intensity was set around 100 mW/cm^2 and the irradiation time was one minute. The emission spectrum of the UV lamp was from 275 to 500 nm with a maximum located to 365 nm. The left-over formulations were kept in brown vials to avoid the light contact and used for successive curing and sample preparation.

Table 4.3. Schematic report of the different amount used for the thiol-ene formulations studied.

FORMULATION	ENE MONOMER		THIOL MONOMER		MOLAR RATIO THIOL-ENE	PI 3 wt%
	/	(g)	/	(g)	/	(g)
All_N1_TMPMP	All_N1	1.000	TMPMP	0.643	1:1	0.051
All_N4_TMPMP	All_N4	1.000	TMPMP	0.585	1:1	0.049
All_N7_TMPMP	All_N7	1.000	TMPMP	0.535	1:1	0.047

The 3D-printing DLP process was performed with an Asiga MAX X UV 27 DLP printer operating a 385 nm LED light source. CAD models were designed and exported to .stl files to be uploaded into the proprietary printer software Asiga Composer. Light intensity was set to 40 mW/cm^2 and the layer thickness was 50 nm. The printing parameters were set according to the best result achieved. After the printing process, samples were immersed in isopropanol and left for 15 minutes in an ultrasound bath to remove the unpolymerized formulations present on the surface. Subsequently, samples were subjected to UV-postcuring performed in a RobotFactory (Mirano, Italy) UV-chamber equipped with a medium-pressure mercury lamp for 1 min.

4.2.3. Characterization

Nuclear magnetic resonance (NMR)

NMR analysis was conducted on a Bruker AM 400 MHz. $CDCl_3$ and DMSO-d_6 were used as solvent and internal reference for the chemical shift given in ppm. ^{1}H-NMR was recorded at 400 MHz while ^{13}C-NMR was at 101 MHz.

Fourier transform infrared spectroscopy (FTIR)

The thiol-ene reaction was followed by means of FTIR analysis. A Nicolet iS 50 spectrometer was used in transmittance mode to record the data. The samples were spread on Si wafer by film bar guaranteeing a thickness of 32 μm. The conversion curves were collected by spectral resolution of 4 cm^{-1}. The thiol peak was monitored by the band located around 2600 cm^{-1} while the reaction of C=C was followed by the peaks at 1640 cm^{-1} and 925 cm^{-1}. The spectra were normalized considering a peak which remained unaffected during the reaction. Considering the study with ferulic acid derivatives, the peak at 1550 cm^{-1} of the stretching of C=C of the aromatic ring was taken as reference; the ester peaks around 1750/1700 cm^{-1} were considered references for the studies with lipoic acid, furan derivatives and levoglucosenone. Equation 4.1 was used to evaluate the conversion.

$$Conversion = \frac{\left(\frac{A_{fun}}{A_{ref}}\right)_{t=0} - \left(\frac{A_{fun}}{A_{ref}}\right)_{t}}{\left(\frac{A_{fun}}{A_{ref}}\right)_{t=0}} \qquad \text{Equation 4.1}$$

Where A_{fun} is the area of the functional group under investigation (e.g. thiol group at 2570 cm^{-1}) while A_{ref} is the area under the selected reference peak. The evaluation is done at different time to elaborate the conversion curve for the real-time analysis. All the FTIR data were handled with the software Omnic from Thermo Fisher Scientific.

Photorheology

The UV-curing process was studied by means of photo-rheology with an Anton Paar MC 302 rheometer (Physica MCR 302, Graz, Styria). The rheometer was set with a plate-plate geometry; the outside diameter of the upper metal disk was 25 mm and a quartz disk was used as bottom support in order to guarantee the irradiation of the sample. A Hamamatsu LIGHTINGCURE LC8 was used as UV-source and the light was directed on the sample by means of an optic fiber. The measurements were performed in oscillatory condition at frequency of 1 Hz, with strain of 1 %. The distance between the plate was set as 200 μm which correspond about 150 μL of the formulation between the plates. The UV-light intensity provided on the surface of the sample differs according to the performed study. The ferulic acid derivatives were tested with 30 mW/cm^2, the isosorbide-based formulation were tested with 75 mW/cm^2, 40 mW/cm^2 were used for furan-based formulations, and for levoglucosenone-based ones 5% of the intensity of the lamp that correspond to 4 mW/cm^2 was used. The achievement of the proper photorheological curve explained the difference of the intensity, which correlate the different reactivity of the tested systems. The lamp was turned on after 60 s of stabilization. The tests performed for levoglucosenone-based formulations were done in isothermal condition at three different temperatures, 25 °C, 50 °C and 80 °C. A thermal stability at high temperature was performed after 2000 seconds by starting the irradiation.

Differential scanning calorimetry (DSC)

The UV-curing process was investigated by means of photo-DSC. A Mettler TOLEDO DSC-1 equipped with Gas Controller GC100 was used to perform the analysis. The DSC was equipped with a mercury lamp, Hamamatsu LIGHTINGCURE LC8, with an optic fiber to direct irradiate the samples. The emission of UV-light was centered at 365 nm. About 5-10 mg of photocurable formulation were placed in an open aluminum pan (40 μL), whereas an empty pan was used as reference. The tests were done at room temperature (25 °C), or in isothermal condition at 50 and 80 °C for levoglucosenone-based formulations, and in controlled atmosphere (N_2 flow of 40 mL/min). The samples were irradiated two times in order to proper evaluate the UV-curing. The second run was done to confirm the complete curing and create the base line. The second curve was subtracted from the first to obtain the curve related to the curing only. The integration of this curve gave the total enthalpy (ΔH_{exp}). The other important parameter detected through this analysis was the height of the exothermic peaks (h_{peak}). All measurements were performed in triplicate with satisfactory reproducibility. The final conversion was evaluated by exploiting the Equation 4.2.

$$Conversion\,(\%) = \frac{\Delta H_{exp}}{\Delta H_{theo}} \times 100 \qquad \text{Equation 4.2}$$

Where ΔH_{exp} is the experimental value obtained by the analysis while ΔH_{theo} is the theoretical value of the thiol-ene cross-linking reaction which was 79.5 kJ/mol [301].

The thermal properties of cured sample were analyzed by DSC. A Mettler TOLEDO DSC-1 equipped with Gas Controller GC100 was employed to carry the tests. Samples of about 5-10 mg were sealed in 40 µL aluminum pans and analyzed by DSC. After each dynamic steps, isothermal steps of 5 min were done to stabilize the chamber and the sample. The heating and the cooling rates were set at 10 °C/min and the analyses were performed in a controlled atmosphere with a N_2 flow rate of 40 mL/min. All the data were analyzed with Mettler Toledo STARe software V9.2. The following methods were used to analyze the different green thermosets.

Ferulic-based thermoset were tested setting the starting temperature at 30 °C; the first heating went from 30 to 100 °C; then the temperature was maintained at 100 °C for 2 min in order to stabilize the sample, after that the chamber was again cooled until −50 °C was reached and then this temperature was maintained for 4 min, finally was a second heating from −50 °C to 100 °C applied.

For the isosorbide-based materials, the first heating went from 25 to 100 °C in order to eliminate the thermal history of the polymers; after that the chamber was cooled until – 70 °C and finally a second heating from – 70 °C to 100 °C was applied.

The evaluation of the T_g of furan-based cured samples was done with starting temperature set at 25 °C, then the first heating goes from 25 to 100 °C; after that the chamber was cooled until – 50 °C and finally a second heating from – 50 °C to 300 °C was applied to detect the T_g.

The T_g of the levoglucosenone thermoset by an analysis from – 40 °C to 250 °C anticipated by a first heating from 25 to 100 °C to eliminate the thermal history of the polymers.

UV-vis spectroscopy

The measurement of ferulic-derivatives monomers was done with a Jenway 6850 UV/Vis Spectrophotometer. The spectra were recorded from 450 ηm to 200 ηm. Quartz cuvettes were used. DCM was used as solvent, and the concentration were 0.03 g/L and 0.04 g/L for A2FeA and h-A2FeA respectively.

An UV2600 Shimadzu Spectrophotometer was used for furan-monomers. The spectra were recorded from 600 ηm to 200 ηm. Quartz cuvettes were used, and the monomer were dissolved in acetonitrile in concentration ranging from 3 g/L to 0.2 g/L.

Gel content

The gel content percentage (% gel) of the UV-cured polymers was determined by measuring the weight loss after 24 h extraction with chloroform. The samples were about 500 mg and after the immersion they were allowed to completely dry for 24 h in air. % gel was calculated according to Equation 4.3.

$$\% \, gel = \frac{W_\mathrm{f}}{W_\mathrm{i}} * 100 \qquad \text{Equation 4.3}$$

where W_f is the weight of the dry film after the treatment with chloroform and W_i is the weight of the dry sample before the treatment.

Dynamic mechanical thermal analysis (DMTA)

The thermal mechanical analysis of the thermoset was carried out with a Triton Technology instrument. The instrument applied uniaxial tensile stress at frequency of 1 Hz with a heating rate of 3 °C/min. The initial temperature of – 40 °C was achieved by cooling down the test chamber with liquid nitrogen. The samples were UV-irradiated in rectangular silicon mold with dimensions of 12×4×0.3 mm^3.

The measurements were done to detect the T_g as maximum of *Tan δ* curve and were stopped after the rubbery plateau. *Tan δ* is the loss factor, thus the ratio between the loss modulus (E'') and storage modulus (E'). The DMTA analysis allowed the evaluation of the cross-link density (ν_c) calculated by Equation 3.3 derived from the statistical theory of rubber elasticity [117,118].

$$\nu_c = \frac{E'}{3RT} \qquad \text{Equation 4.4}$$

where E' is the storage modulus in the rubbery plateau (T_g + 50 °C), R is the gas constant and T is the T_g expressed in Kelvin.

Tensile test

The mechanical properties of the green thermosets were investigated by tensile test. The stress-strain curve was registered using a tensile instrument (MTS QTestTM/10 Elite, MTS System Corporation) combined with a measurement software (TestWorks® 4, MTS System Corporation). A 1 kN load cell was used, and the traverse speed of the machine was set as 5 mm/min. The Young's modulus (*E*) was evaluated as the tangent of the curve up to the linear region (around 20 % of total elongation). The toughness (*U*) was calculated as the area under the stress-strain curve. Moreover, strength at break (σ) and strain (ε) were retrieved from the curves. The result was the average value of 5 measurement.

Thermogravimetric analysis (TGA)

The thermal stability of the isosorbide and levoglucosenone-based coatings was studied by means of a Mettler Toledo TGA1. The test was done imposing a heating ramp of 10 °C/min from r.t. to 700 °C under N_2 atmosphere with flow of 40 mL/min. The analysis was done considering different features: T_5, temperature at which the sample lost 5 wt%; T_{peak}, temperature at peak of degradation, evaluated as peak of the first derivative, and *Char*, analyzed as final char residue in wt%.

Coating properties: contact angle, hardness, adhesion

The contact angle measurements were performed by Drop Shape Analyzer, DSA100, Krüss. The reported results are an average of at least 5 water droplets spread on free film surfaces.

The pencil hardness of ferulic and isosorbide-based was measured according to the standard ASTM D3363 [302]. For the hardness different pencils were used from 8 B to 8 H. Instead, a Sauter HMO mobile Leeb Hardness Tester, ASTM A956, was used to evaluate the hardness of the furan-based coating.

The adhesion was measured by Eclometer 107, as cross hatch cutter, according to ASTM D3359 [303]. The insert number 2 was used as cutter. The films were photocured on glass substrate. The ASTM scale ranging from 5B to 0B was used to evaluate the results.

Chemical degradation

The levoglucosenone UV-cured samples (50-75 mg) were tested again chemical degradation. They immersed into an alkaline solution of NaOH 2 M (2 mL) and gently stirred on a thermoregulate mixer at 25 °C, 120 rpm. The samples were recovered from the solution, washed with deionized water, dried and weight. A weight loss evaluation was done considering the initial weight of the samples, triplicate measures of each time were performed. The Equation 4.5 was used for the evaluation.

$$\text{Not degraded sample }\% = \frac{W_1}{W_0} * 100 \qquad \text{Equation 4.5}$$

Where W_1 is the weight of the dry film after the treatment in NaOH and W_0 is the weight of the dry sample before the treatment.

3D-Scanning

The 3D-printed levoglucosenone-based object was scanned with a 3Shape E3 scanner to verify the precision and accuracy of the print. The sample was coated with magnesium stearate in order to limit the reflection of light on the transparent structure, and then positioned on a platform by means of a sticky paste to ensure the correct acquisition of images. The resulting scanned image was then compared to the original CAD model by means of CA Analyzer software to generate the deviation analysis and map.

X-ray photoelectron spectroscopy (XPS)

The surface functionalization of itaconic-based coatings was investigated by means of X-ray photoelectron spectroscopy (XPS). The instrument used for the experiment was an XPS, PHI 5000 Versaprobe II, ULVAC-PHI, Kanagawa (Japan). The X-ray source was an Al-Ka radiation. The take-off angle was set at 45° so that the system is able to detect photoelectrons to a depth of 1–5 nm from the surface. 400×400 µm areas were analyzed on each sample. Survey spectra were acquired between 0 and 1200 eV. High-resolution spectra of C were taken on the pristine and the functionalized sample to detect the presence of the PFDT.

4.3. Result and discussion

4.3.1. Synthesis route and characterization of bio-based allyl monomers

Ferulic acid, isosorbide, furans and levoglucosenone were versatile bio-based starting monomers capable of several modifications among which allyl functionalization is one. Most of the reactions were carried out using allyl bromide as main reagent to react the OH groups present in the chemical structure of the monomers, as alcohol, phenol or acid functionality. High yields were obtained for all the allyl products, moreover the allylation has been proven to be very selective reaction without the occurrence of significant side reactions. The ferulic acid (FeA) demonstrated to be a very versatile monomer since functionalities, such as allyl aryl ethers, coumaryl alkenes, carboxylic acids, methyl esters, allyl esters, and phenols were combined in different ways. Furthermore, levoglucosenone (LGO), also demonstrated its versatility, which enables multiple chemical functionalizations. The allylation of LGO, obtained through chemo-enzymatic pathway, was optimize by DoE analysis to maximize *Productivity* of the dimers and the catalytic kinetic of the enzyme (pseudo K_{cat}). Eco-Scale and E-factor assessed the greenness of the synthesis. To ensure a complete characterization, the synthetized products were investigated by NMR analysis. The specific protons signal of allyl-based monomers were assessed by ^{1}H-NMR analysis, as reported in **Figure 4.7**.

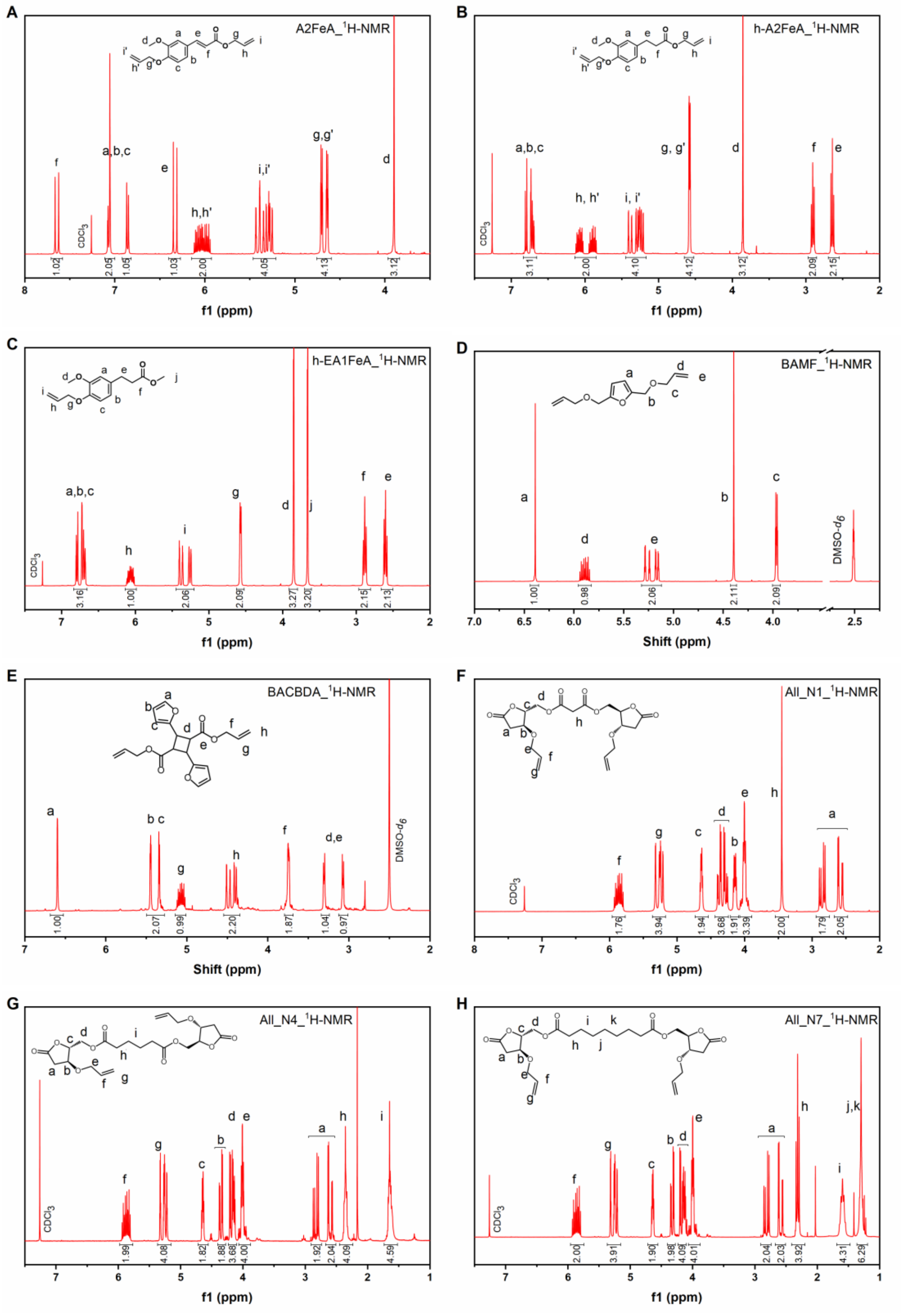

Figure 4.7. ¹H-NMR of the synthetized products. (A, B, C) ferulic-based allyl monomers; (D, E) furan-based allyl monomers; (F, G, H) levoglucosenone-based allyl monomers.

4.3.2. Ferulic-based thiol-ene networks

This chapter will be dedicated to the exploitation of ferulic-based allyl derivatives for UV-activated thiol-ene chemistry. FeA is a suitable candidate for the utilization of a bio-based monomer in different applications. Indeed, the ability to score different functionalization allowed a vast portfolio of different properties covering wide spectrum of thermo-mechanical behave. Here, the investigation started with the investigation of the UV-curing process of thiol-ene formulations followed by the characterization of the thermoset for coating applications also addressing thermos-mechanical performances. The monomers used in the study are reported in **Figure 4.8**.

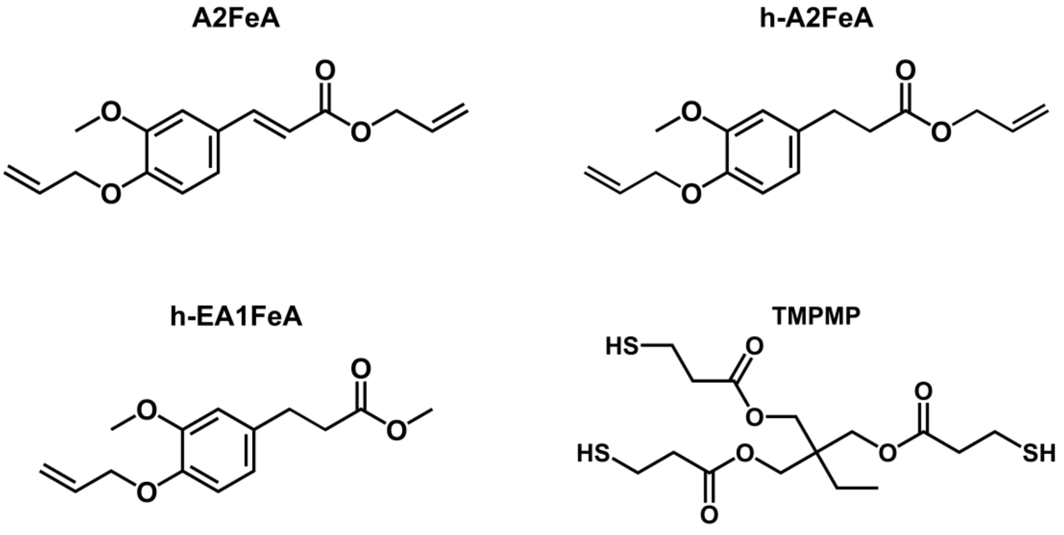
A2FeA
h-A2FeA
h-EA1FeA
TMPMP

Figure 4.8. Chemical structures of the monomer used in the study; bifunctional ferulic-based allyl monomers (A2FeA and h-A2FeA), monofunctional allyl monomer (h-EA1FeA), and trifunctional thiol (TMPMP).

Investigation of the UV-curing process of FeA-based formulations

The investigation of the thiol-ene UV-activated cross-linking of the ferulic acid-based monomer was performed by photorheology and FTIR analysis. The two bifunctional allyl monomers, h-A2FeA and A2FA, were tested in 1:1 molar ratio thiol-to-ene with TMPMP, a commercially available thiol. **Figure 4.9**. shows the photorheology curves, which highlight the faster reaction of h-A2FeA compared to A2FeA. This can be proved by the steeper increased of the modulus and the absence of induction time. This last feature can be attributed to several reasons, among them, the UV-absorption intrinsic properties of A2FeA linked to the resonance structure of the monomer. This light absorption may compete with the photoinitiator limiting the efficacy of the UV-curing [304]. When the cinnamoyl carbon double bond is removed by hydrogenation, as in h-A2FeA, the absorption shifted towards shorter wavelengths allowing faster photopolymerization without competition. The hypothesis was confirmed and corroborated by UV-vis analysis performed on the two ally monomers as illustrated in **Figure 4.9B** where is visible the difference of the absorbance of the two monomers, A2FeA and h-A2FeA, with a higher absorption peak between 275 and 375 nm for the non-hydrogenated monomer.

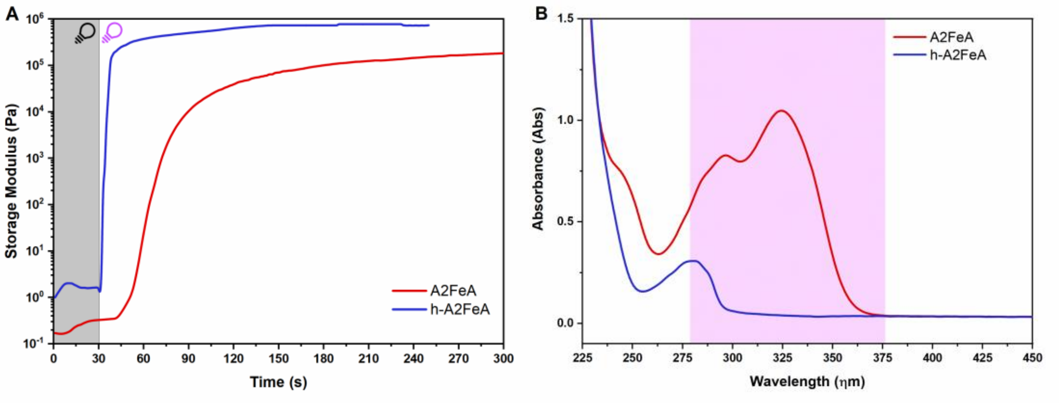

Figure 4.9. (A) photorheology curves obtained for A2FeA and h-A2FeA; (B) UV-vis analysis of the two allylated monomers dissolved in DCM.

FTIR analysis was used to assess the chemical feature of the cross-linking by the investigation of the disappearance of the thiol- and ene-reactive groups. The conversion reached for h-A2FeA was higher than A2FeA which was 85 % for the thiol group. The C=C decrease, investigated with the stretching band around 1640 cm^{-1}, was significant lower for A2FeA with respect h-A2FA as it can be visible from **Figure 4.10**. Impressively, the shoulder of the carbonyl peak at 1700 cm^{-1} was strongly reduced after the irradiation, implying that most of the cinnamoyl alkenes have been consumed. Thus, the remain unreacted allyl ethers provide the residual signal at 1640 cm^{-1}. This suggest that the initial addition of a thiyl-radical is faster in adding to the cinnamoyl alkene than to the allyl ether. Consequently, the hydrogen abstraction of the thiol hydrogen by a carbon-centered radical is the rate-determining step. This corroborates well with the reduced slope observed in **Figure 4.9**. The validation of this hypothesis was performed modifying the thiol-content in the formulation containing A2FeA. Indeed, A2FeA-monomer was considered as trifunctional monomer (therefore increasing the thiol molar content in the photocurable formulation) and it was thus evaluated in two distinct formulations, where the thiol-crosslinker was added either in a 1:1 molar ratio thiol:allyl ether, or 1:1 molar ratio thiol:total enes (**Table 4.1**, entries 1 and 2). The results obtained by altering the formulation ratio showed nearly complete thiol conversion, **Figure 4.10E**. Moreover, the reduction of the peak related to the ene double bond was more pronounced than in the formulation in which A2FeA was assessed as a bifunctional monomer, as depicted in **Figure 4.10A**.

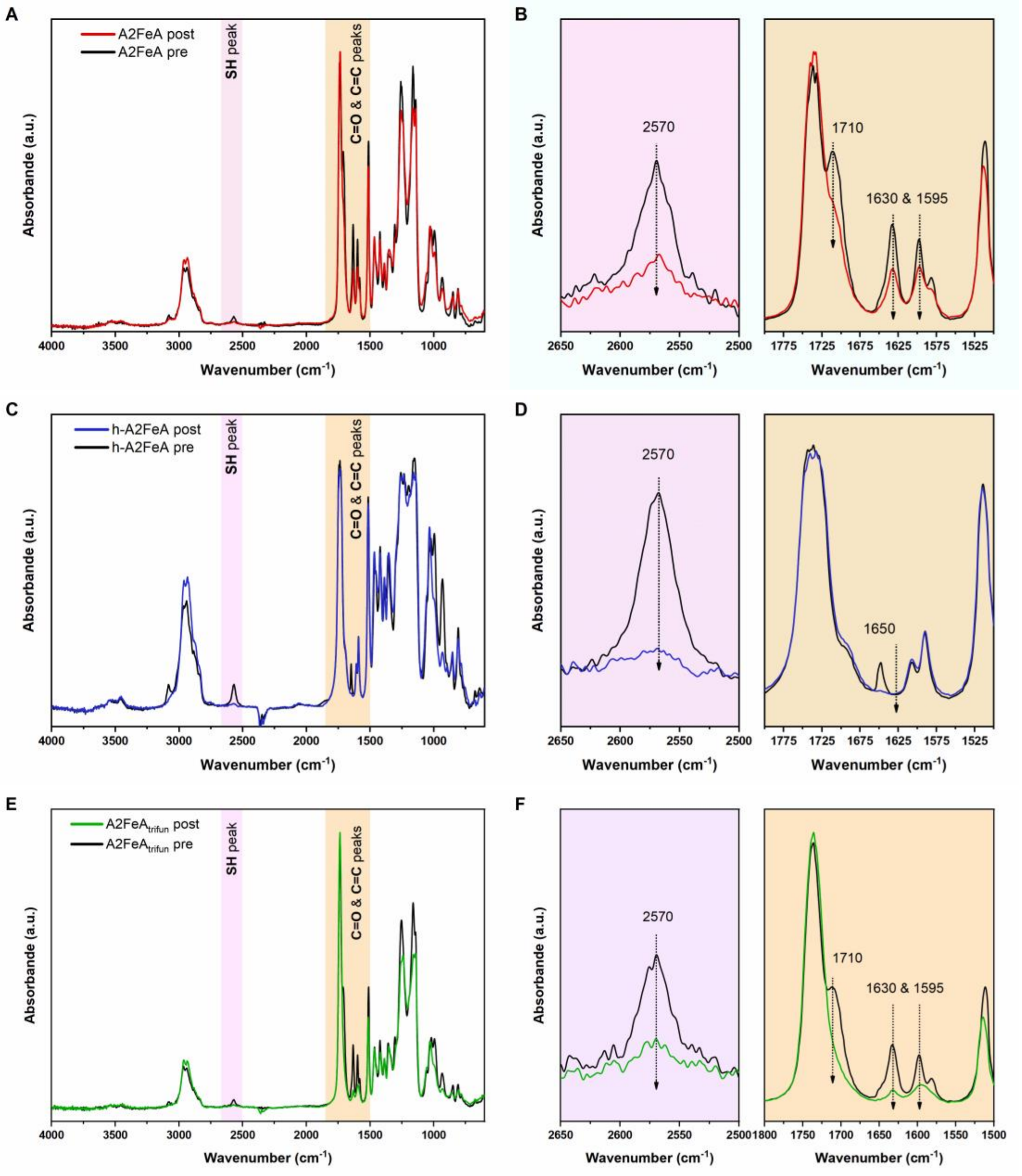

Figure 4.10. (A, B) FTIR spectra of formulation containing A2FeA pre and post UV-irradiation; (C, D) FTIR spectra resulted from formulation with h-A2FeA; (E, F) FTIR spectra of formulation with allyl A2FeA$_{\mathrm{trinfun}}$ considered as trifunctional monomer before and after UV-irradiation.

Mechanical behavior of cross-linked ferulic-based polymers

DSC and DMTA analysis were used to investigate the properties of the thiol-ene network cross-linked *via* UV-irradiation. The DMTA analysis allowed the evaluation of the trend in E' highlighting interesting features. Firstly, the modulus above the T_g reflect the photorheology result with the higher value for h-A2FeA respect to bifunctional A2FeA. Then the T_g of the films varied from 1 °C for h-A2FeA, 20 °C for bifunctional A2FeA, and 24 °C for the trifunctional A2FeA, as visible in **Figure 4.11A**. The different chemical structures explained the difference of about 20 °C between the two T_g. Indeed, the presence of a conjugated double bond in the A2FeA structure, linked to the benzyl ring, resulted in increased network stiffness due to the hindrance of chain rotation. On the other hand, the absence of this double bond in the h-A2FeA monomer imparted greater flexibility to the polymer network, consequently leading to a reduction in the T_g-value. The highest T_g reached by the network formed by thiol added in stochiometric amount with respect to the ene functional groups (**Table 4.4**, entry 2) can be attributed to the higher number of reactive sites, resulting in higher final cross-link density.

The DSC analysis served as corroboration and validation of DMTA analysis proving the same T_g-trend of the UV-cured films as presented in **Figure 4.11B** where it is shown the inflection point in the thermograms due to the glass transition of the polymer network associated to the decrease in the heat capacity of the thermoset.

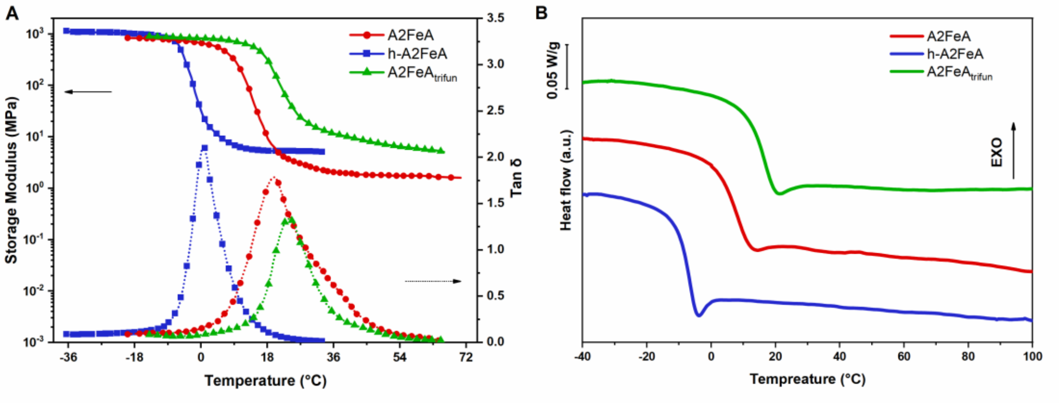

Figure 4.11. (A) DMTA analysis of the UV-cured thiol-ene thermosets containing TMPMP and the allyl monomers, A2FeA, h-A2FeA, and A2FeA$_{trifun}$ respectively; (B) DSC thermogram of the UV-cured samples.

Table 4.4. Properties of the photocured networks assessed by FTIR analysis of thiol peak at 2590 cm^{-1} (^{1}), DMTA analysis (^{2}), T_g evaluated as maximum of Tan δ and cross-link density calculated from Equation 4.4., and DSC (^{3}).

ENTRY	FORMULATION NAME	CONVERSION	T_g	T_g	E'	ν_c
		(%)	(°C)	(°C)	(MPa)	(mmol/dm^3)
1	A2FeA	86	20	6.0	2.08	258
2	A2FeA$_{\text{trifun}}$	99	24	15.0	6.38	781
3	A2FeA+5% h-EA1FeA	85	18	4.5	1.04	130
4	A2FeA+10% h-EA1FA	85	17	2.5	5.65	71
5	A2FeA+15%h-EA1FeA	83	13	0.5	2.60	33
6	h-A2FeA	99	1	-7.5	5.38	711
7	h-A2FeA+5% h-EA1FeA	100	0	-8.0	4.87	645
8	h-A2FeA+10% h-EA1FeA	100	-2	-9.5	3.75	500
9	h-A2FeA+15% h-EA1FeA	99	-5	-11.0	2.85	384

Copolymerization with the synthesized monofunctional monomer

The investigation of the mechanical properties proceeded with the evaluation of the influence of the introduction of a monofunctional allyl monomer, h-EA1FeA, into the formulations. The aim was the customization of the final properties playing with the functionality and the chemical structure of the monomers. Firstly, the UV-curing process was assessed by photorheological analysis showing barely any influence of the h-EA1FeA in the studied range (**Figure 4.12**). The kinetics of the formulations containing the monofunctional monomer followed the pristine ones either for A2FeA and h-A2FeA, demonstrated by the same curve slope of the Storage modulus in the initial stage. However, a linear lowering of the modulus upon curing was observed. Instead, the effect on T_g was markable and visible as showed in **Figure 4.13**. As expected, the introduction of a monofunctional monomer induced a decrease of cross-link density of the thiol-ene network implying a reduction in the rigidity and finally an ultimate decrease in the T_g. The trend of *Tan δ* was correlated to a decrease in the E' in the rubbery plateau.

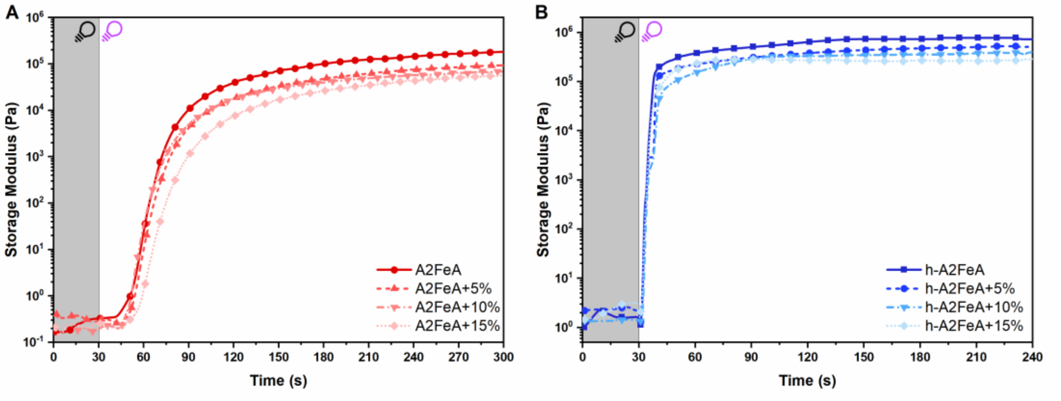

Figure 4.12. (A) photorheology curves of pristine A2FeA and A2FeA with monofunctional monomer in 5, 10, and 15 % respectively; (B) trend in Storage modulus for h-A2FeA-based formulations with and without the h-EA1FeA monofunctional monomer.

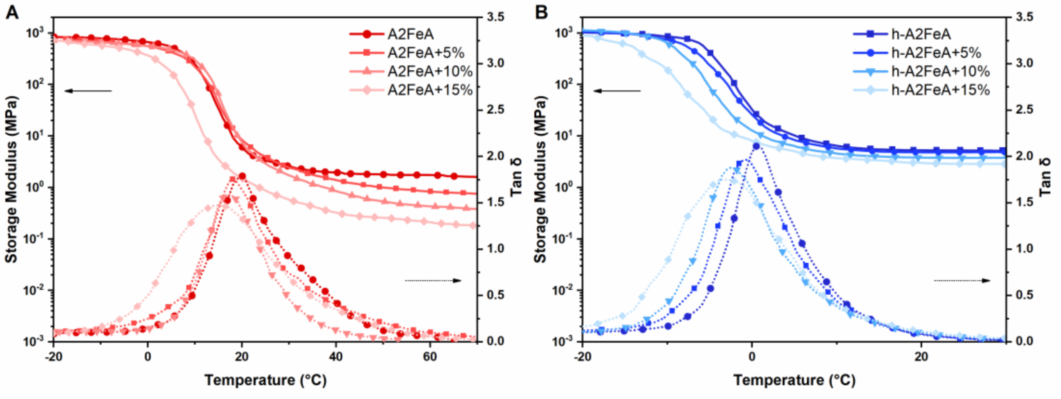

Figure 4.13. (A) Effect of monofunctional monomer h-EA1FeA on T_g and Storage modulus; (B) DMTA of h-A2FeA-based formulation with h-EA1FeA.

Properties of ferulic-based coatings

The comprehensive characterization of the ferulic-based coating ended with the evaluation of the peculiar requirements for organic coating. Among them the investigation was focused on formulation viscosity, surface hardness of UV-cured films, contact angle, and adhesion.

Viscosity measurements were conducted to assess the processability of the formulation before curing. The formulations containing the monomer h-A2FeA exhibited lower viscosity compared to A2FeA. This can be explained by considering that the presence of the cinnamoyl double bond increases the molecule's rigidity and electron density through conjugation with the carbonyl bond. The contact angle against water was investigated on UV-cured films, and revealed similar wettability among all samples, with contact angles close to 67° (as shown in **Table 4.5**). The UV-cured coatings obtained from formulation with A2FeA, used as a trifunctional monomer (ratio 1:1 thiol-total ene), exhibited the highest contact angle of 75 °, attributed to the higher concentration of TMPMP which contain water-like bonds as ester group. Excellent surface hardness (6 H to 7 H) as determined by pencil hardness tests, was assessed to all UV-cured films. Adhesion was assessed through a cross-hatch test, with the A2FeA-based coatings showing the best adhesion. On the other hand, the h-A2FA films exhibited lower adhesion, likely due to their lower polarity and T_g.

Table 4.5. Coating properties of the UV-cured ferulic-based films.

ENTRY	FORMULATION NAME	CONTACT ANGLE	VISCOSITY	PENCIL HARDNESS	ADHESION
		(°)	(Pa × s)	/	(%) - ASTM
1	A2FeA	66 ± 1	0.21 ± 0.05	7 H	82 – 3B
2	$\text{A2FeA}_{\text{trifun}}$	75 ± 1		7 H	92 – 5B
3	A2FeA+5% h-EA1FeA	68 ± 1		7 H	87 – 4B
4	A2FeA+10% h-EA1FeA	68 ± 2		7 H	88 – 4B
5	A2FeA+15%h-EA1FeA	68 ± 2		6 H	90 – 5B
6	h-A2FeA	66 ± 2	0.05 ± 0.01	7 H	55 – 1B
7	h-A2FeA+5% h-EA1FA	67 ± 2		7 H	60 – 1B
8	h-A2FeA+10% h-EA1FeA	68 ± 2		7 H	59 – 1B
9	h-A2FeA+15% h-EA1FeA	68 ± 1		6 H	65 – 2B

4.3.3. Bio-derived thiol and bio-derived ene monomer for a fully bio-based polymer network

The exploitation of isosorbide (IA) and lipoic acid (LA) allowed the development of a fully bio-based formulation. Indeed, IA, derived from cellulose, was exploited as ally-monomer while the thiol counterpart was provided by the LA which is also a bio-derived monomer, as previously described. The UV-triggered opening of the five-member cyclic disulfide ring to generate the thiol reactive group has been previously demonstrated [137,274] and here exploited to form a thiol-ene network (**Figure 4.14**). The new green formulation was compared with a standard formulation containing the isosorbide-based diallyl ether (IDAE) and a commercially fossil-based thiol (TMPMP). This comprehensive study allowed to assess the feasibility of the bio-based formulation as UV-curable coating polymer resin.

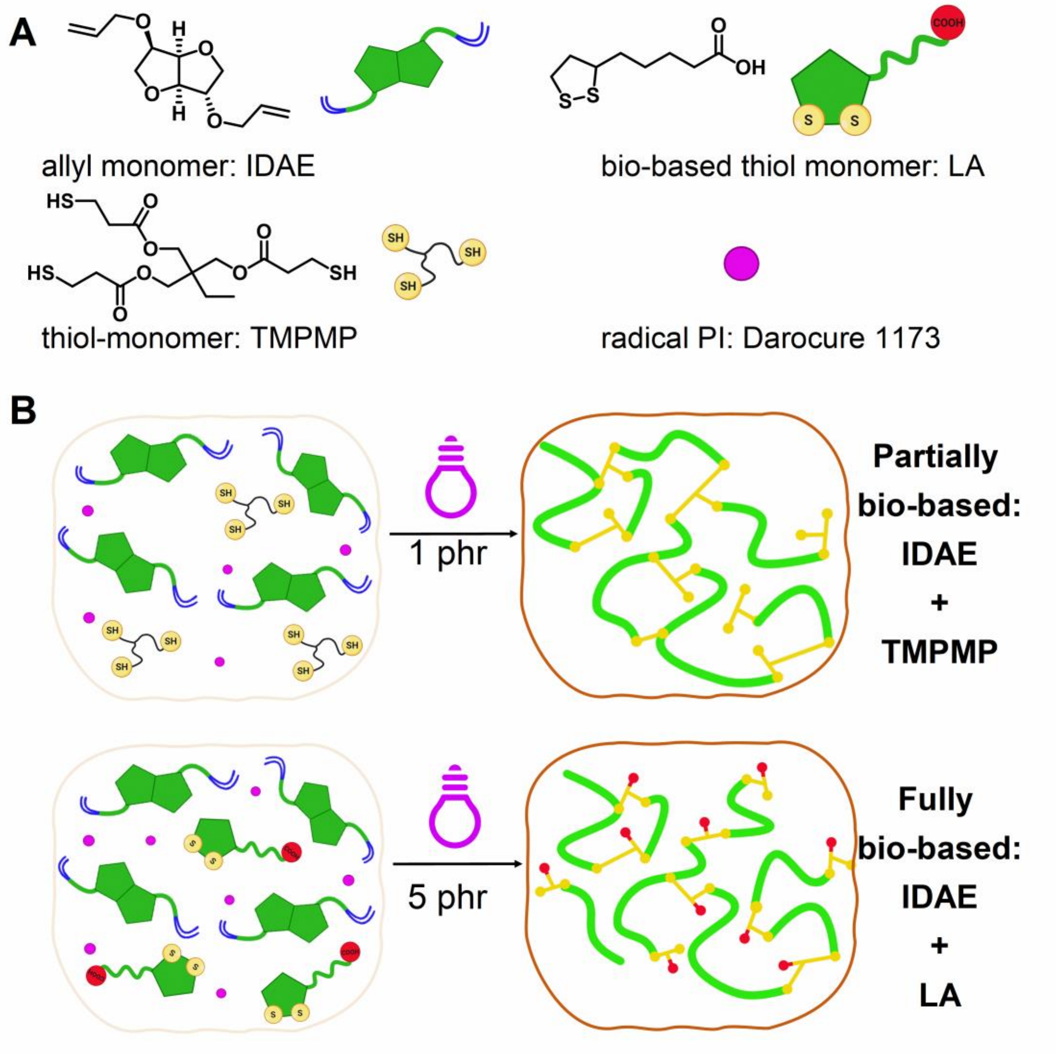

Figure 4.14. (A) compound involved into the UV-curing process of the partially and fully bio-based thiol-ene coatings; (B) Schematic view of the UV-curing of the two different isosorbide-based formulation studied.

Firstly, the UV-curing was investigated by means of photorheology and FTIR to evaluate kinetic and chemical features of the process. The trend of G' as a function of the irradiation time is reported in **Figure 4.15**, highlighting two distinct kinetics for the tested formulations. Indeed, IDAE+TMPMP showed remarkably high reactivity since no induction time was detected and moreover the plateau in few seconds was reached. On the contrary, the thiol-ene reaction of IDAE+LA was slower, as indicated by the extended induction time of approximately 120 s. Furthermore, when the reaction started, the kinetic was slower with respect IDAE+TMPMP confirmed by the slope of G'. The linear fitting of the increment can provide a direct means of comparison between the curing rate of the two formulations. Analyzing this factor, IDAE+TMPMP revealed a slope value of 0.72 while IDAE+LA revealed a slope of 0.02 which is 36 time smaller confirming the difference in the kinetic. The nature of the thiol monomer can explain this behave since TMPMP has available SH bonds which can directly start the reaction upon UV-irradiation. Instead, LA has a disulfide bond which must first undergo UV-induced cleavage generating the reactive species (-S•) crucial for the click thiol-ene reaction [273,305]. The generation of the radicals required energy supplies by UV-irradiation, which accounts for the observable delay in the reaction onset, a phenomenon primarily attributed to the time required for radical formation.

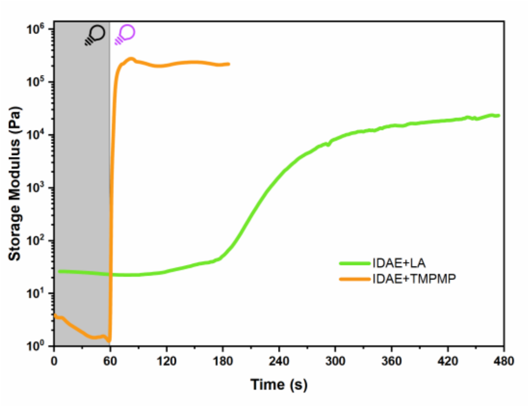

Figure 4.15. Photorheology curves for IDAE+LA and IDAE+TMPMP tested at 25 °C.

The occurrence of the thiol-ene reaction was verified by ATR-FTIR analysis, performed on both the liquid resin and on UV-cured samples. The spectra are reported in **Figure 4.16** illustrating the thiol and allyl peaks before and after UV-irradiation. Considering IDAE+TMPMP, the disappearance of both stretching vibration peak of thiol and allyl group centered at 2565 cm^{-1} and 1645 cm^{-1} is evident. Furthermore, the signal related to vibration of C-H bond of the allyl group at 925 cm^{-1} corroborates the result of the stretching vibration of C=C peak. On the other hand, since the structure of LA has only disulfide bonds and no free thiols, the analysis was performed evaluating the signal relative to the allyl groups. The analysis confirmed the disappearance of the signal related to the C=C corroborating the occurring of the thiol-ene reaction.

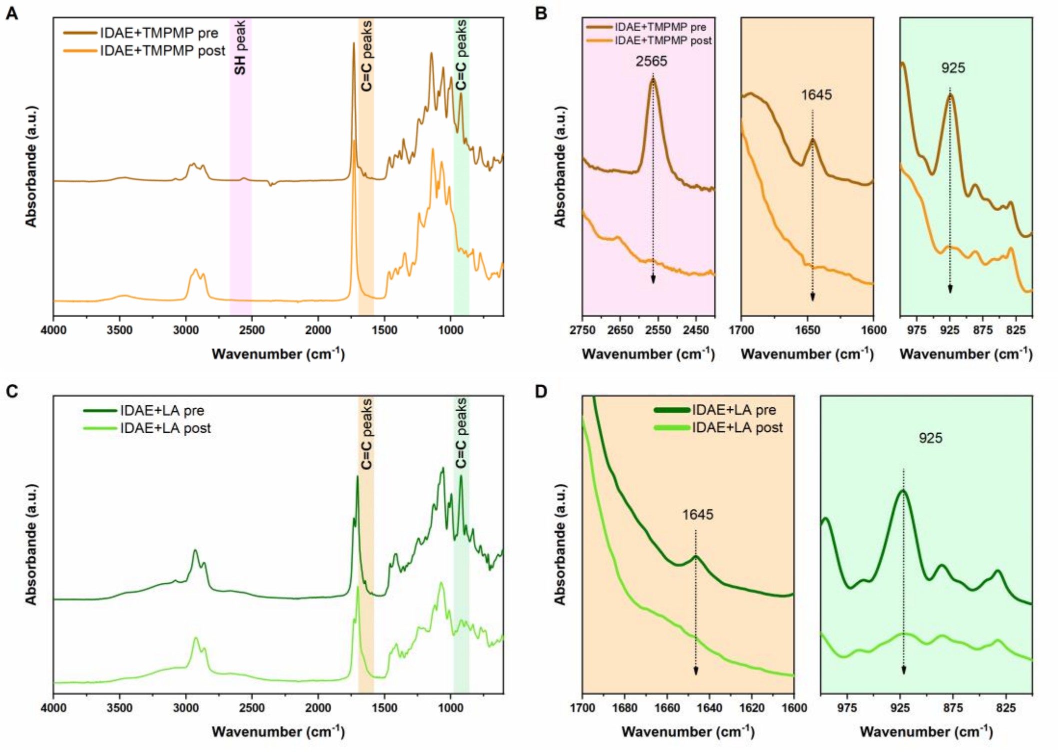

Figure 4.16. (A, B) ATR-FTIR spectra of IDAE+TMPMP before and after UV-irradiation; (C, D) ATR-FTIR spectra of the formulation containing IDAE+LA pre and post UV-irradiation.

Tack-free films were successfully obtained after UV-irradiation and their corresponding gel content was assessed after 24 h by immersion in chloroform. The fully biobased formulation achieved an 88 % gel content, while the partially biobased 95 %, (**Table 4.6**). Despite the slower kinetics, the fully biobased formulation exhibited high gel content implying a formation of fully cross-linked network. However, possibly due to the slow reaction, some disulfide bonds might not have reacted properly, as supported both by the residual presence of ene peaks in FTIR spectra and by the marginal difference of gel content between the two thermosets (IDAE+LA and IDAE+TMPMP). Indeed, the use of TMPM allowed astonishing gel content value in accordance with the previous study [64].

Subsequent thermal analysis was performed on the crosslinked films by DSC (**Figure 4.17A**). The T_g of the two crosslinked materials were similar, the fully biobased coating exhibit a T_g of −14 °C while the partially biobased –12 °C. These results align with previous findings reported in literature [306]. This underscored the lipoic acid's potential as a bio-derived alternative to the commercially available thiol, capable of yielding similar properties in crosslinked coatings.

The thermal degradation of the two different crosslinked films was evaluated by TGA. **Figure 4.17B** reports the weight loss as a function of time, highlighting that the fully biobased coating degraded at lower temperature compared to IDAE+TMPMP one. Indeed, the T_{peak} was around 320 °C for IDAE+LA, while the decomposition temperature for IDAE+TMPM was at 370 °C demonstrating higher thermal stability. The onset temperatures, T_5, evaluated as the start of the degradation (5 % weight loss), reflect the trend of T_{peak}. In fact, the fully biobased IDAE+LA had lower T_5 than partially biobased formulation IDAE+TMPM (235 °C and 345 °C respectively). The difference in the degradation profile could be explained considering the chemical structure of the utilized thiols: bifunctional LA and trifunctional TMPMP. Furthermore, as confirmed by FTIR, the incompletely crosslinked network based on IDAE+LA could provide an additional explanation of the T_5 variation with respect to the IDAE+TMPMP. The fully cross-linked network generated by IDAE+TMPMP ensured higher thermal stability as previous reported [64].

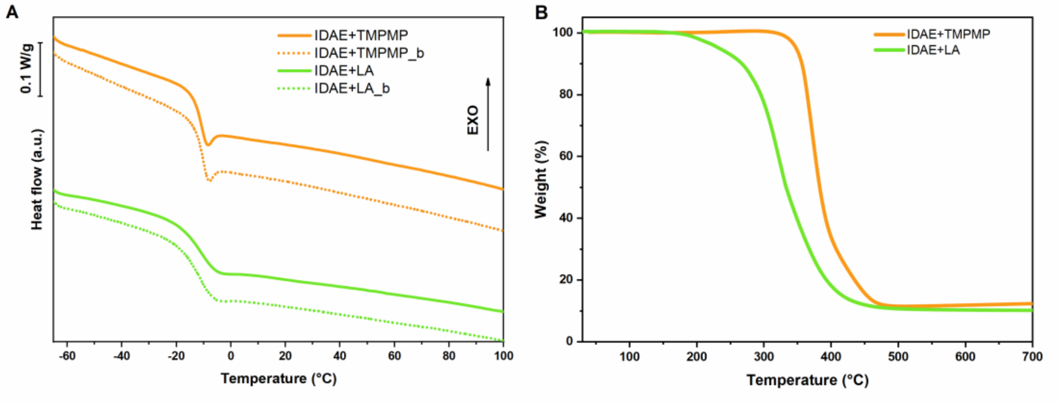

Figure 4.17. (A) DSC thermograms of UV-cured isosorbide-based coating containing TMPMP and LA; (B) TGA curves of IDAE+TMPMP and IDAE+LA.

The characterization of the bio-based coatings covered the specific film properties, such as adhesion, surface hardness and contact angle. Impressive results were achieved considering the adhesion on glass substrates. Indeed, IDAE+LA achieved 92 % (5B in ASTM scale) adhesion while IDAE+TMPMP only 85 % (4B in ASTM scale). The acidic nature of LA can be the reason behind this increment due to the promotion of strong interactions with the substrate surface. Interesting result of pencil hardness were reached for both coatings, with 5H and 8H for IDAE+LA and IDAE+TMPMP respectively. The contact angle, influenced by the thiol-ene nature of the networks, was very similar for both compositions, measuring around 85 °for IDAE+TMPMP and 88 ° for IDAE+LA.

Table 4.6. Result obtained for the tested formulations. Curing rate (evaluated by slope of photorheology curves [1]), glass transition (evaluated by DSC [2]), gel content, and coating properties.

FORMULATION	CURING RATE [1]	T_g [2]	% gel	CONTACT ANGLE	PENCIL HARDNESS	ADHESION
	/	(°C)	(%)	(°)	/	(%) – ASTM
IDAE+TMPMP	0.70	− 12 ± 1	95 ± 2	85 ± 2	8 H	84 – 4B
IDAE+LA	0.02	− 14 ± 1	88 ± 1	88 ± 3	5 H	92 – 5B

4.3.4. Furan-based allyl monomers for bio-based coating applications

Furan monomers have gained significant attention and utilization over recent years due to their remarkable versatility and interesting features which can be obtained in the final furan-based derived material. An overview of their applications in the epoxy field has been already presented in Chapter 3. However, here the attention is shifted towards the radical UV-curing, specifically to the thiol-ene chemistry. A detailed investigation of the UV-curing using allyl-functional furan-based monomers (**Figure 4.18**) has been conducted, with a special emphasis to identify the optimal curing conditions through real-time FTIR analysis, photo DSC and photorheology. Moreover, the mechanical response of the polymer network was analyzed by DMTA and tensile analysis aiming to assess the feasibility of utilizing this cellulose-based resins for coating applications.

UV-curing process

Three different techniques were exploited to investigate the thiol-ene UV-curing aiming to evaluate the chemical as well as kinetics aspects. Specifically, real-time FTIR, photo-DSC and photo-rheology will be discussed.

For instance, real-time FTIR monitored the decrease of the thiol peak, S-H (2570 cm^{-1}), and the carbon-carbon double bond peak, located at C=C (930 cm^{-}1), through the irradiation time confirming the progress of the thiol-ene reaction. **Figure 4.19** illustrates the real-time spectra over time for BAMF_TMPMP formulation with 3 phr of photoinitiator. It can be seen that the area of the peaks decreased, and it was possible to verify the "click" features of the thiol-ene reaction [43] by comparing the conversion trend of both functional groups (S-H and C=C) as reported in **Figure 4.19C**. The trend was the same, proving that the reaction adhered to the 1:1 ratio between the two functional groups, which is a defining characteristic of the thiol-ene click reaction.

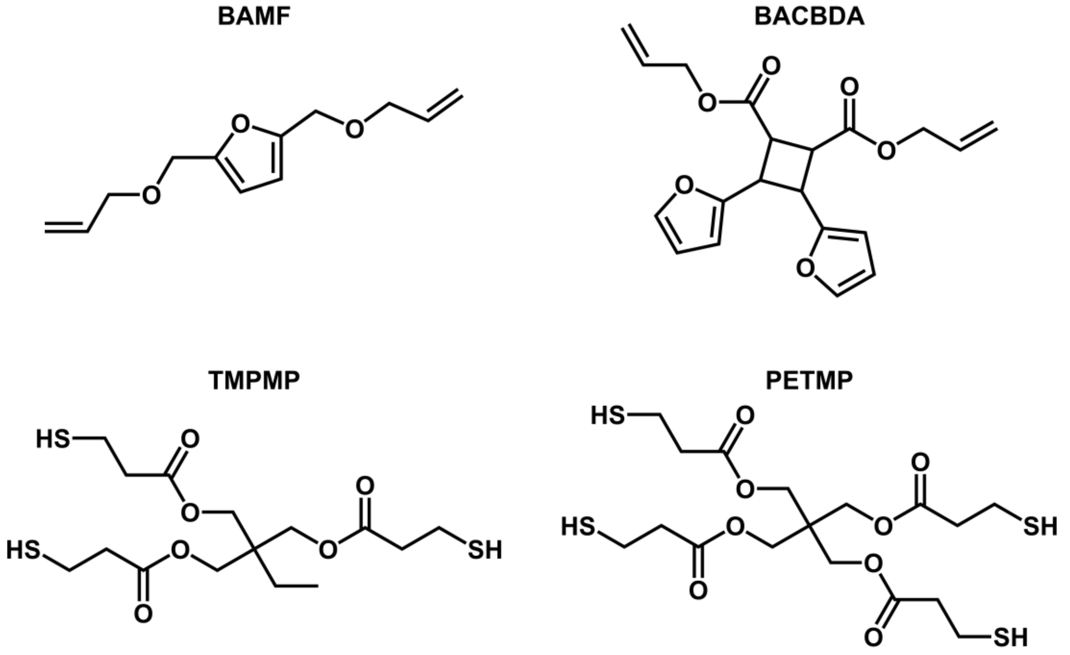

Figure 4.18. Chemical structures of the bio-based ene monomers used in the study (BAMF and BACBDA) and the two thiols, a trifunctional one (TMPMP) and a tetra functional one (PETMP).

The optimization of the curing deals with the amount of photoinitiator, hence the influence of the photoinitiator on the UV-curing process was assessed to optimize the reactive groups conversion. The conversion trend of S-H, as a function of the irradiation time, was investigated by varying the concentration of BAPO from 0 to 3 phr (**Figure 4.19D**). With respect to the BAMF_TMPMP formulation, the increment of the amount of BAPO led to increase final conversion, along with a slight increase of rate of photopolymerization. This increase can be attributed to the increased amount of radicals generated by the photoinitiator upon irradiation. The additional radicals facilitated the polymerization process, resulting in a faster kinetics and a higher degree of conversion. While it's possible to perform the thiol-ene reaction without any photoinitiator [307], the evidence of a faster reactivity and a higher thiol-ene conversion in the presence of 3 phr of the photoinitiator led to formulate the UV-curable resins in the presence of 3 phr of BAPO for further characterization.

The real-time FTIR analysis was conducted for all formulations, and the conversion results are reported in the **Table 4.7**. It is evident that the final conversion achieved was comparable for all formulations involving both BAMF and BACBDA. The slightly lower value observed for the formulations with BACBDA could be attributed to the higher steric hindrance of the allyl monomer with respect to the BAMF monomer. Nevertheless, all the conversion value exceeded 70 %, indicating that all the synthetized allyl monomers demonstrated good reactivity to UV-light and strong interaction with the thiol-based monomers.

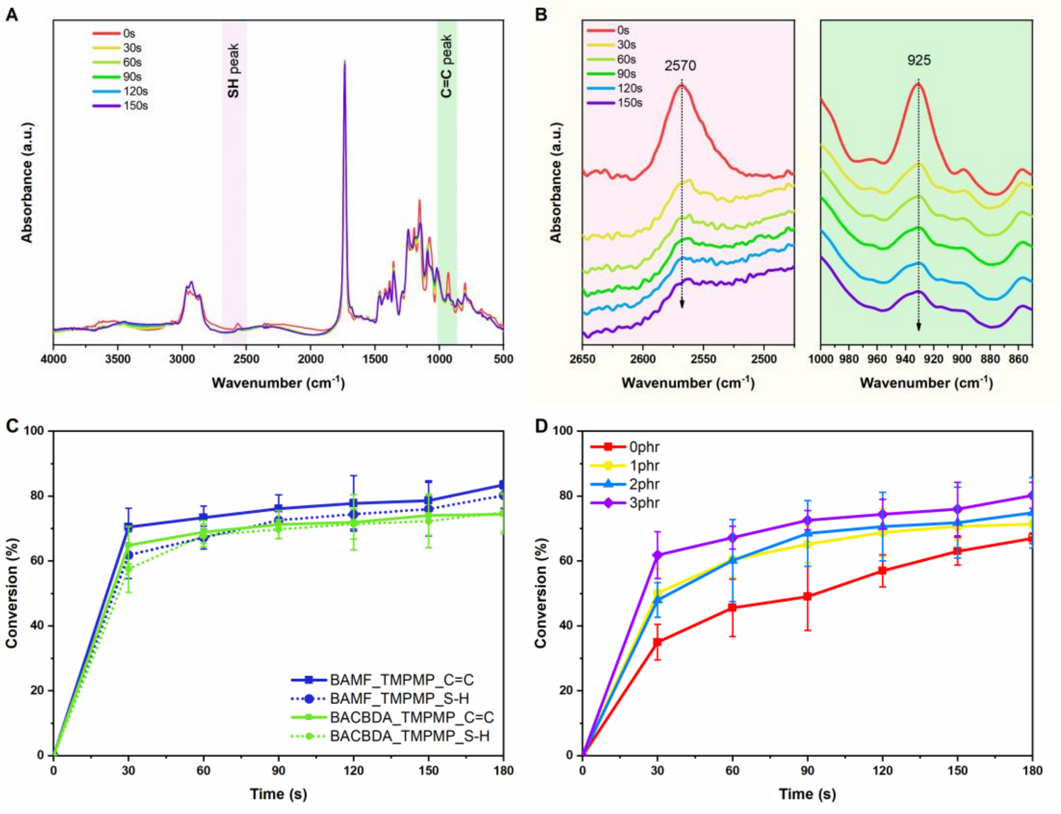

Figure 4.19. (A) FTIR spectra collected over time for BAMF_TMPMP with 3 phr of BAPO; (B) zoom on thiol and carbon double bond peaks; (C) Conversion of functional group in function of the time for two distinct formulations with 3 phr of photoinitiator. C=C is reported in solid line, S-H is reported in dot line; blue lines for BAMF_TMPMP and BACBDA_TMPMP; (D) Conversion curves of S-H bond in function of the irradiation time obtained for the BAMF_TMPMP with different amount of BAPO.

The FTIR results were consistent with the photo-DSC findings. The impact of the amount of photoinitiator was further explored by means of photo-DSC, evaluating the curing peak. **Figure 4.20** displays the thermograms for BAMF_TMPTP (3 phr of BAPO). It is clear that the addition of the photoinitiator significantly influenced the heat release (*ΔH*). Indeed, the conversion calculated by *ΔH* generated (Equation 4.2) increased by addition of photoinitiator, aligning with the previous real-time FTIR results. The maximum *ΔH* value of 210 J/g was reached for 3 phr of BAPO. Additionally, the investigation of h_{peak} showed that the highest value was reached with 3 phr of photoinitiator. This confirmed the beneficial impact on the kinetic of the reaction considering that the h_{peak} is known to be proportional to the rate of polymerization. As a last observation, the t_{peak} (time at maximum rate of polymerization) decreased as the amount of photoinitiator increased. Specifically, it reduced from 18 s to 10 s when going from 0 phr to 3 phr of photoinitiator corroborating the previous data.

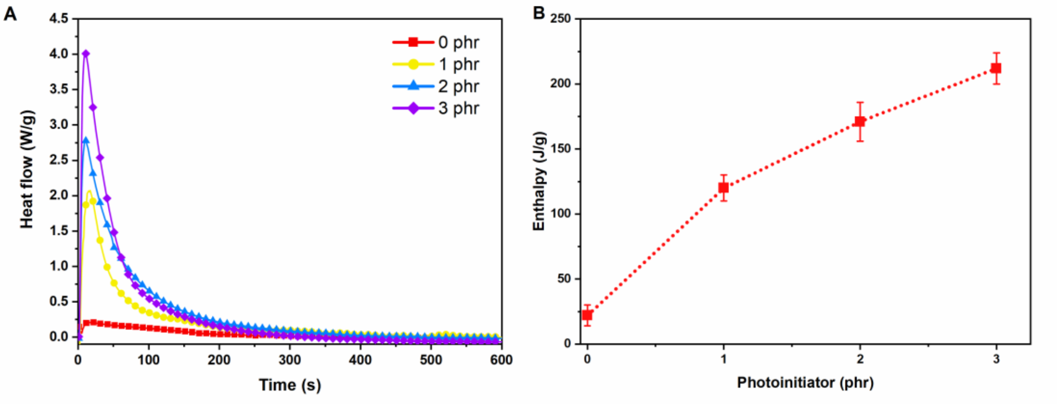

Figure 4.20. (A) photo-DSC thermograms of BAMF_TMPMP formulation with varing amount of BAPO; (B) *ΔH* released in function of the amount of BAPO for BAMF_TMPMP.

The lower degree of conversion observed in the photo-DSC analysis (**Figure 4.21** and **Table 4.7**) with respect to the real-time FTIR data can be explained considering the different sample arrangements. In the real-time FTIR, the sample was spread with a thickness of 32 um, so the light absorption by the monomer itself and the formed polymer had a negligible effect. In contrast, the light penetration effect in the DSC pan is noticeable. To explore the possible absorption of ene-monomers, UV-vis analysis was conducted to assess this impacting feature. Both monomers exhibited absorption peaks due to the presence of the furan ring, as illustrated in Figure **4.21B**. However, BACDBA displayed a broader absorption region compared to BAMF, resulting in higher potential for interferences with the UV-light and consequently constraining the conversion process during bulk polymerization. Indeed, the same absorption spectra was obtained when BACDBA was diluted 10 time more with respect to the BAMF, 0.03 g/L and 0.2 g/L respectively.

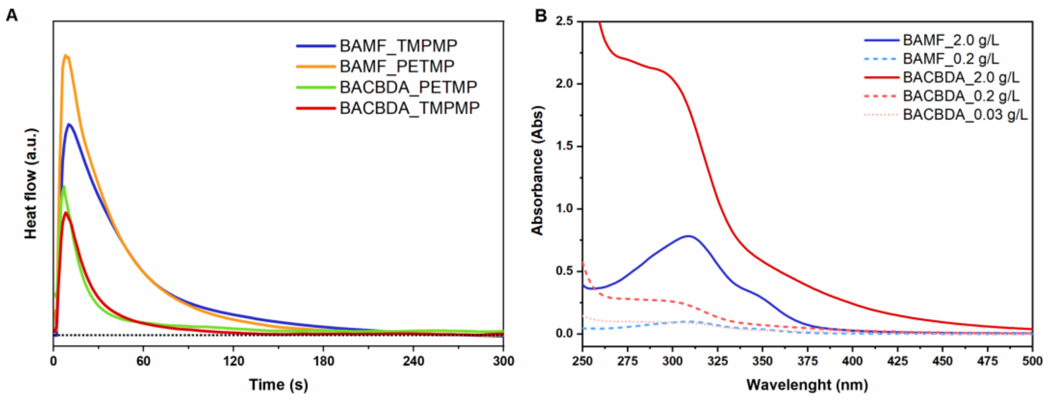

Figure 4.21. (A) Photo-DSC thermograms obtained for the tested formulation with 3 phr of BAPO; (B) UV-vis spectra of allyl monomers, BAFM and BACBDA, dissolved in acetonitrile at different concentrations.

Real-time photorheology was conducted as the final analysis to explore the photocuring process. The progression of UV-curing was assessed by evaluating the trend in the storage modulus and its increment due to the cross-linking reaction until reaching of a plateau indicating that the reaction is terminated. **Figure 4.22A** displays the results obtained for BAMF_TMPMP and BAMF_PETMP which differs for the initial induction time of the reaction. The thermoset containing BACBDA (**Figure 4.22B**) exhibited a longer induction time as visible by the delayed increase in the storage modulus. Moreover, both formulations had a slower slope of the curves, confirming slow kinetics (**Table 4.7**). After approximately 360 s, the curves of the BAMF-based network reached a constant modulus value, while the formulation containing the BACBDA-based monomer required 900 s. This behavior can be attributed to the light absorption of the ene monomers. Indeed, two processes can occur when UV-light is directed at the sample. The first process involves the absorption of light by the photoinitiator, which generates radicals, initiating the curing reaction. In the second process, the UV-light is absorbed by chromophore groups present in the monomer's structure, and thus no radicals are generated. When considering the allyl derivatives, it's important to note the UV-vis spectra obtained and presented in **Figure 4.21B**. Monomer’s light absorption can interfere with the UV emitted from the lamp, reducing the available radiation for the formation of radical species. Consequently, formulations containing BACBDA required a longer induction time to receive the necessary radiation dose to initiate the curing reaction.

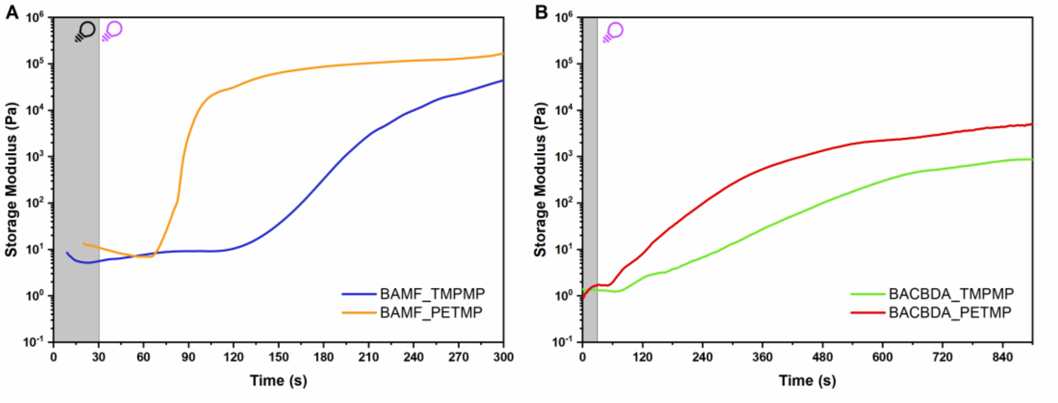

Figure 4.22. Photo-rheology measurement for the four formulations. (A) BAMF_TMPMP (blue) and BAMF_PETMP (orange) curves of Storage modulus in function of the time; (B) Storage modulus trend for BACBDA_TMPMP (green curve) and BACBDA_PETMP (red curve).

To investigate the potential for cross-linking bulk samples for mechanical characterization, % gel analysis was performed on the UV-cured samples to determine the gel fraction after irradiation. The highest values of 80 % was revealed by BAMF_TMPTP. BAMF_PETMP based thermosets had a value of 78 %. The value slightly decreased with the introduction of BACBDA, reaching 72 % and 68 % for the coatings with TMPMP and PETMP, respectively. The lower gel content for the thermosets containing BACBDA confirmed the DSC results highlighting the limitations on polymerization due to steric hindrance and light penetration. However, the % gel values confirmed the effective formation of an insoluble fraction resulting from cross-links between the polymer chains, thus demonstrating the feasibility of creating coatings.

Table 4.7. UV-curing process data. C_{FTIR}: conversion evaluated by FTIR analysis (^{1}) for thiol and ene groups; DSC derived data (^{2}), C_{DSC}: conversion evaluated by DSC analysis, released enthalpy (ΔH_{exp}), and height of the peak (h_{peak}); Curing rate obtained from the slope of the storage modulus from photo-rheology analysis (^{3}).

ENTRY	*C_{FTIR} S-H ^{1}*	*C_{FTIR} C=C ^{1}*	*C_{DSC} ^{2}*	*ΔH_{exp} ^{2}*	*h_{peak} ^{2}*	*Curing rate ^{3}*
	(%)	(%)	(%)	(J/g)	(W/g)	/
BAMF_TMPMP	80 ± 4	83 ± 1	62	210 ± 12	3.9 ± 0.4	0.03
BAMF_PETMP	75 ± 1	74 ± 1	64	225 ± 10	4.5 ± 0.5	0.12
BACBDA_TMPMP	74 ± 2	77 ± 2	35	90 ± 13	2.5 ± 0.4	0.004
BACBDA_PETMP	72 ± 3	69 ± 5	28	75 ± 15	3.1 ± 0.8	0.007

Thermo-mechanical characterization of furan-based coatings

Once the UV-curing process was optimized, different samples were UV-cured to evaluate the thermo-mechanical properties of thiol-ene networks by DMTA, DSC, and tensile analysis. The aim of the study was the designing of the final properties of the polymer network by varying the thiol functionalities and the ene structures. Indeed, the thiols were tris and tetra functional (TMPMP and PETMP, respectively) while the ene monomers were both bifunctional but with different chemical back bone.

The influence of the different thiols was investigated in BAMF-based formulations. As observed in **Figure 4.23**, the UV-cured BAMF_PETMP resin shows higher T_g (− 13 °C) compared to BAMF_TMPMP (− 26 °C). This result is a directly linked to the tris- and tetra- thiol functionality present in TMPMP and PETMP, respectively. A higher number of thiol groups can be associated with a higher rigidity and T_g of final coating as previously reported [275,308], due to an expected increase of crosslinking density. Hence, the thiol-monomer with four functionalities led to a crosslinked network with a higher glass transition. The high crosslinking density is in accordance with the high gel content previously reported. On the other hand, the influence of the bis allyl structures can be investigated by selecting BACBDA and BAMF with the same thiol, e.g. TMPMP. The change in the ene structure allowed an increment of T_g around 38 °C when employing BACBDA instead of BAMF. This can be attributed to the intrinsic rigidity of the CBDA-2 derivatives, which bear a stiff cyclobutane ring. Indeed, the cyclobutane ring ensures higher structural stability, resulting in better thermo-mechanical properties. A similar effect can be observed in PETMP-based thermosets, where the chemical structure of BACBDA led to an increase of the final *Tg* of about 35 °C compared to the BAMF. Remarkably, the T_g of the thiol-ene networks were consistent with the previous studies [242,244,298]. Furthermore, the BACBDA_PETMP (T_g = 24 °C) revealed higher *Tg* with respect to other biobased thiol-ene thermosets derived from ferulic acid [113], isosorbide [244] and eugenol [298]. The evaluation of the cross-link density revealed an increment from BACBDA_PETMP to BAMF_PETMP. Despite the low conversion, BACBDA_PETMP reached the highest value of the T_g and cross-link density. This underscores the potential to achieve excellent performance exploiting the rigid chemical structure and high monomer functionality of CBDA-2. BAMF_TMPMP has a cross-link density value of 149 mmol/dm^3 comparable to the value of BACBDA_TMPMP despite the lower T_g. This can be explained by the highest degree of conversion for the formulation containing BAMF and TMPMP which overcome the 80 % leading to very high cross-link density. All the results are reported in the **Table 4.8**. DSC analysis was used to confirm and corroborate the DMTA findings in terms of T_g. The formulations were UV-cured in the same conditions and then tested in DSC, resulting in a validation of the trend observed for DMTA. Indeed, BACBDA_PETMP achieved the highest T_g value at 19 °C, while FDM_TMPMP exhibited the lowest T_g at -14 °C.

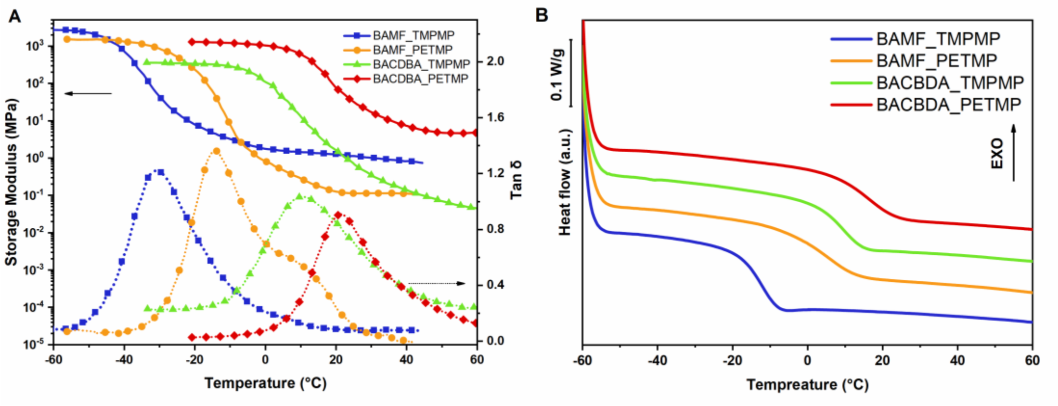

Figure 4.23. (A) DMTA curves for thiol-ene UV-cured networks both Storage Modulus and *Tan δ* in function of temperature; (B) DSC thermograms of the thiol-ene networks (2nd heating run).

Table 4.8. Thermo-mechanical properties evaluated by means of DMTA (^{1}) and DSC (^{2}). Glass transition (T_g); Storage modulus (E'), and cross-link density (ν_c).

ENTRY	T_g ^{1}	T_g ^{2}	E' ^{1}	ν_c ^{1}
	(°C)	(°C)	(MPa)	(mmol/dm^3)
BAMF_TMPMP	− 26 ± 4	− 14 ± 8	1.10	149
BAMF_PETMP	− 13 ± 4	− 3 ± 7	0.14	18
BACBDA_TMPMP	+ 12 ± 3	+ 8 ± 5	0.50	60
BACBDA_PETMP	+ 24 ± 3	+ 19 ± 4	4.25	490

A further characterization was performed by tensile testing on UV-cured coatings to investigate their mechanical behavior. **Figure 4.24** displays typical stress-strain curves acquired for the thiol-ene UV-cured networks. Elastic behavior can be visualized, with a notable strain at break, which can be explained by the relatively low T_g values of the networks. Remarkably, under the tested conditions (room temperature) all the bis-allyl coatings were in the rubbery region, above the T_g. A general trend emerged when PETMP was employed instead of TMPMP in the thiol-ene resins. Indeed, the increased number of thiol functionalities in PETMP led to higher elastic modulus and stress at break in the measured samples. This result correlates with the higher T_g reported for PETMP-based thermoset with respect to the bis TMPMP-based ones. The highest stress at break and elastic modulus were reached for BACBDA_PETMP exhibited the highest value of σ with a value of 9.3×10^5 Pa, and Yong's modulus of 9.7 MPa. The tuning of the tensile properties was confirmed, and it aligned and corroborated the results obtained for the DMTA analysis. Detailed data are available in **Table 4.9**.

Furthermore, the assessment of toughness, calculated as the area under the stress-strain curve, was performed. The trend indicated that BACBDA_PETMP with 11.44 J/m^3 10^4 reached the highest value. The use of BACBDA enhanced the toughness of the thermoset comparing to the coatings containing BAMF. This improvement can be attributed to higher rigidity of the structure derived from the cyclobutane ring could contribute as well as the higher cross-link density reached.

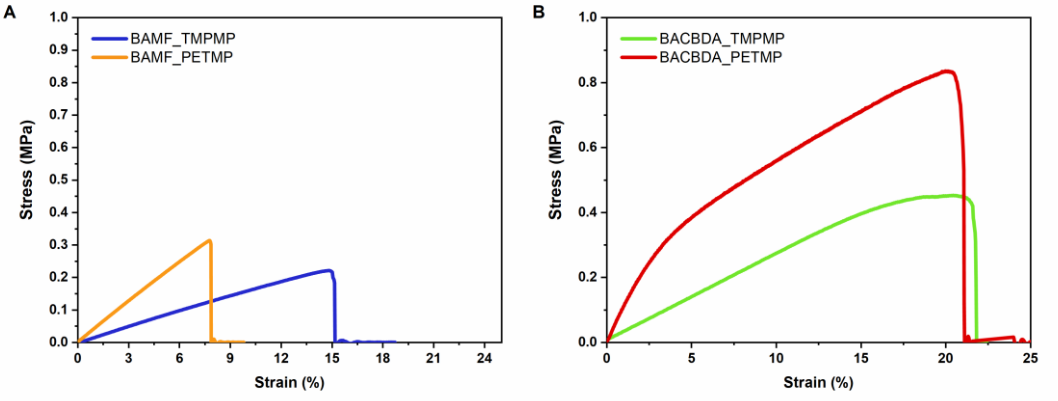

Figure 4.24. Stress-strain curves for the tested thermoset. (A) BAMF-based thermosets; (B) Thermoset produced with BACBDA as ene monomer. The reported curves are the representative ones taken from the 5-replica performed for each thermoset.

The thiol-ene thermosets has been studied to be employed in coating application, thus the surface properties were tested to investigate the feasibility of these in this specific field (**Table 4.9**). Contact angle measurements were performed, indicating comparable values for all the tested samples. Notably, the surface hydrophobicity increased as the thiol transitioned from TMPMP to PETMP and when switching from bis-allyl BAMF to BACBDA. This change in surface properties may be attributed to differences in chemical structure as well as the relatively low conversion of thiol groups, which could contribute to increased contact angles on the surface [309]. Instead, considering the hardness, the presence of the PETMP, tetrafunctional thiol, led to an enhancement of the surface hardness comparing the same thermoset with TMPMP. Such difference could be attributed to the higher T_g reached by PETMP-based samples.

Table 4.9. Mechanical properties evaluated through tensile test: Young's modulus (*E*), strength at break (σ), elongation at break (ε), and toughness (*U*). Coating properties: contact angle and surface hardness measured by Leeb scale.

ENTRY	***E***	***σ***	**ε**	***U***	***Contac angle***	***Hardness***
	(MPa)	(MPa)	(%)	(J/m^3 10^4)	(°)	(HL)
BAMF_TMPMP	1.7 ± 0.3	0.21 ± 0.02	14.5 ± 0.6	1.33 ± 2.7	62 ± 4	156 ± 12
BAMF_PETMP	4.1 ± 0.4	0.33 ± 0.06	8.5 ± 1.3	1.78 ± 5.0	66 ± 3	245 ± 29
BACBDA_TMPMP	2.2 ± 0.3	0.37 ± 0.07	20.5 ± 0.8	4.83 ± 5.6	72 ± 2	195 ± 23
BACBDA_PETMP	9.7 ± 1.3	0.93 ± 0.13	20.8 ± 1.3	11.44 ± 3.23	74 ± 4	296 ± 33

4.3.5. Levoglucosenone for DLP 3D printing of green degradable networks: towards eco-friendly photo-curable materials

Tunable bis-allylated compounds were efficiently synthesized from cellulose-derived levoglucosenone via a chemo-enzymatic pathway whose greenness has been assessed by E-factor and Eco-Scale demonstrating a suitable sustainable process to achieve the formation of allylated monomers. The allyl ether monomers were used as ene counterpart in a thiol-ene reaction activated by UV-light. The UV-curing was investigated by means of real-time FTIR, photo-DSC and photo-rheology to assess chemical and kinetic features of the curing. Then, thermo-mechanical properties were explored by DMTA, DSC and tensile analysis to investigate the effect of tunable ene on the final material properties. Owing the high reactivity of the resins, DLP 3D printing was investigated to achieve the formation of precise and complex structure aiming for a broader application of these bio-derived polymer networks. Finally, aiming to pursuit the concept of circular economy, the degradation of the polymers *via* chemical or thermal was studied to investigate possible reuses of these polymers. **Figure 4.25** illustrates the scheme of the different steps previously described as an example for All_N4 and TMPMP.

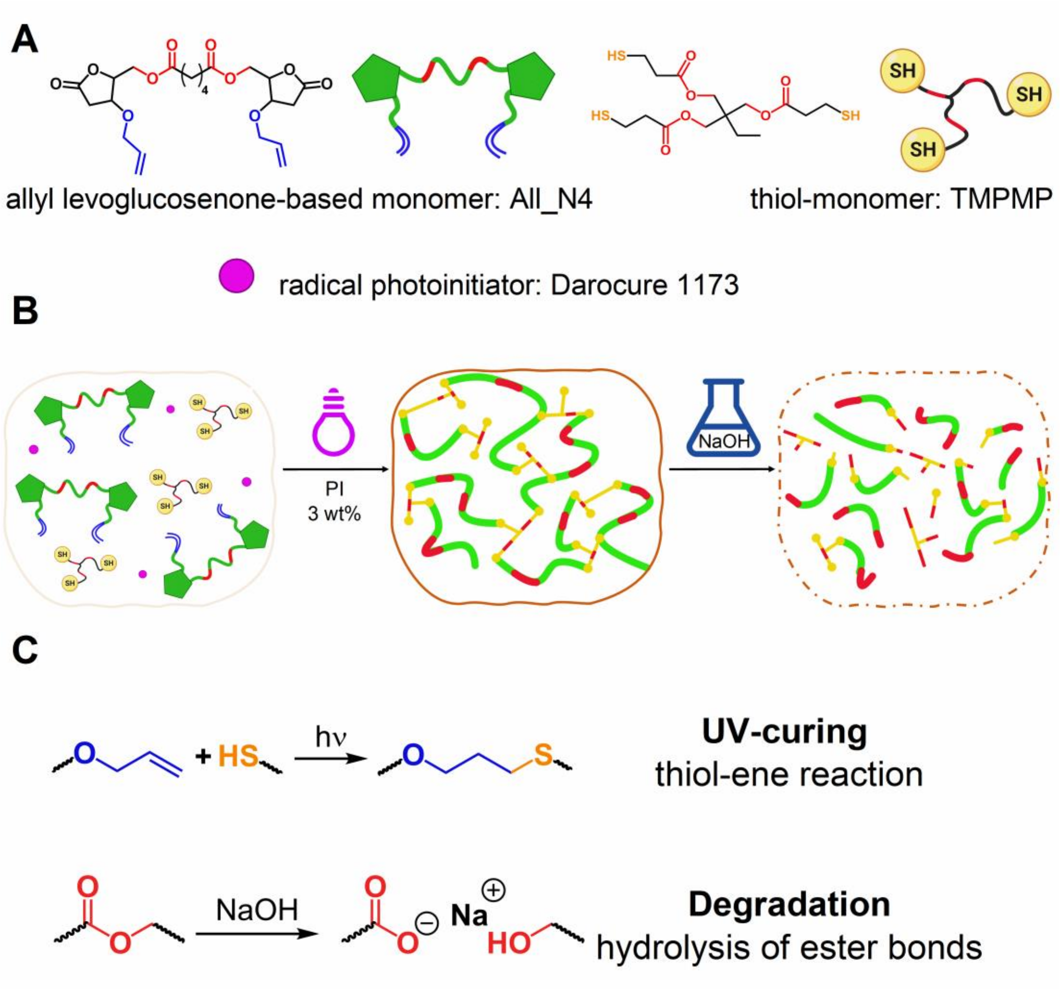

Figure 4.25. (A) Structure of All_N4, TMPMP and photoinitiator involved into the UV-curing; (B) UV-curing of the liquid formulation (step 1) and degradation of the cured network (step 2); (C) S-C bond created during the UV-curing and rupture of COO bond during the chemical degradation.

UV-curing process

Firstly, the UV-curing process was investigated aiming to optimize the conditions for reaching fast reactivity and good final conversion. The formation of the network was followed by real-time FTIR considering thiol and peaks centered at 2750 cm^{-1} and 1640 cm^{-1}, respectively. Looking to the conversion curves in function of the time, presented in **Figure 4.23**, it is possible to ensure that all the photocurable formulations were extremely reactive, with a slightly difference of the induction time. Moreover the "click" feature, significant of the thiol-ene system, has been confirmed due to the similar conversion trend of S-H and C=C. All_N1_TMPMP showed the shortest induction time, followed by All_N4_TMPMP and then All_N7_TMPMP. However, the photocuring reaction for the analyzed thin films was found to be complete within approximately 30 s for all the investigated formulations.

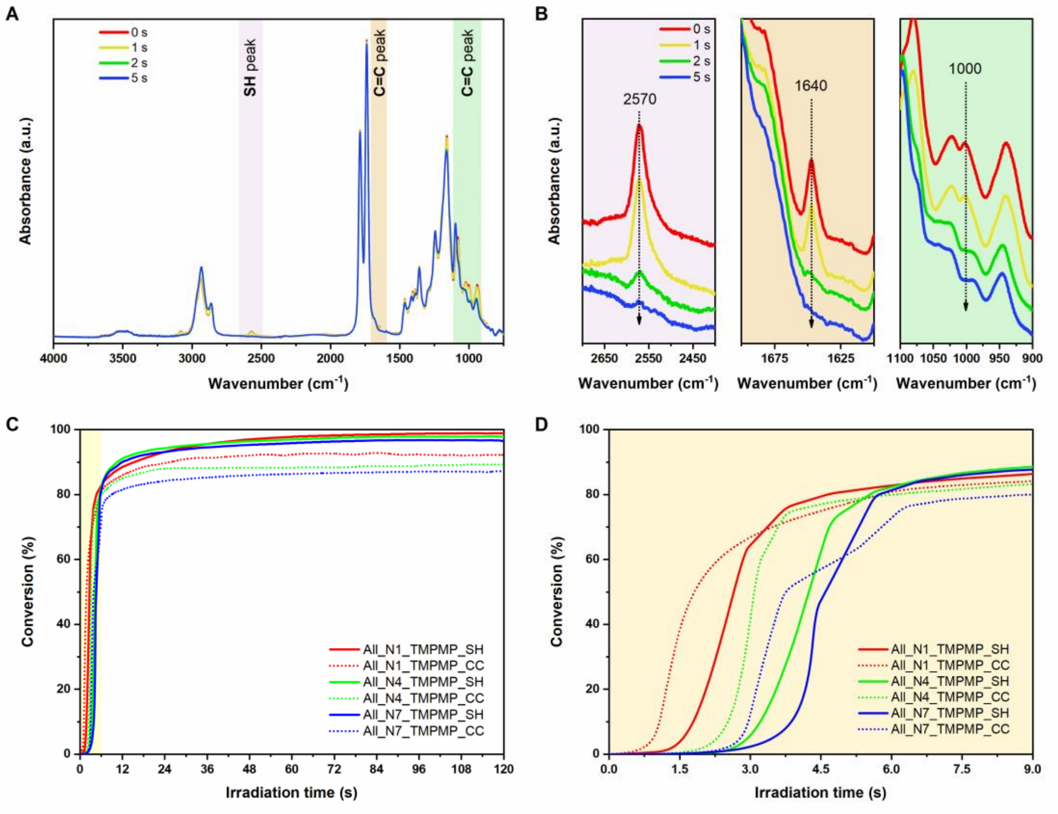

Figure 4.26. (A) FTIR spectra detected for the thiol-ene formulation containing All_N7 recorded at different irradiation time; (B) Inserts of thiol peak at 2570 $\mathrm{cm^{-1}}$ (purple box), carbon double bond peak at 1640 $\mathrm{cm^{-1}}$ (orange box) and the other region characteristic of C=C around 1000 $\mathrm{cm^{-1}}$ (green box); (C) Conversion vs. irradiation time for thiol and ene peaks of the different thiol–ene formulations. The continuous lines report the conversion for the S–H peak, while the dotted lines represent C=C. Red lines indicate All_N1_TMPMP, green lines indicate All_N4_TMPMP and blue lines indicate All_N7_TMPMP; (D) Highlight on the starting of the UV-curing.

Validation and confirmation of the FTIR findings was carried out with photo-DSC analysis, where the influence of the temperature was assessed. Indeed, All_N1 melted around 80 °C, thus the processing of this resin required heating which could influence the UV-curing. The photo-DSC analyses were carried out at 25, 50, and 80 °C for all formulations (**Figure 4.24**) monitoring the released enthalpy (ΔH) which is correlated with the advancement of the curing. The physical state of All_N1 affected the ΔH at room temperature limiting the final conversion. On the contrary the formulation with All_N4 and All_N7 reached the total conversion already at 25 °C. The beneficial effect of the temperature was visible analyzing the h_{peak} of the All_N1_TMPMP, which can be associated with the kinetic of the cross-linking. The rate of polymerization was faster at higher temperature compared to room temperature. A complete overview of the data is reported in **Table 4.10**.

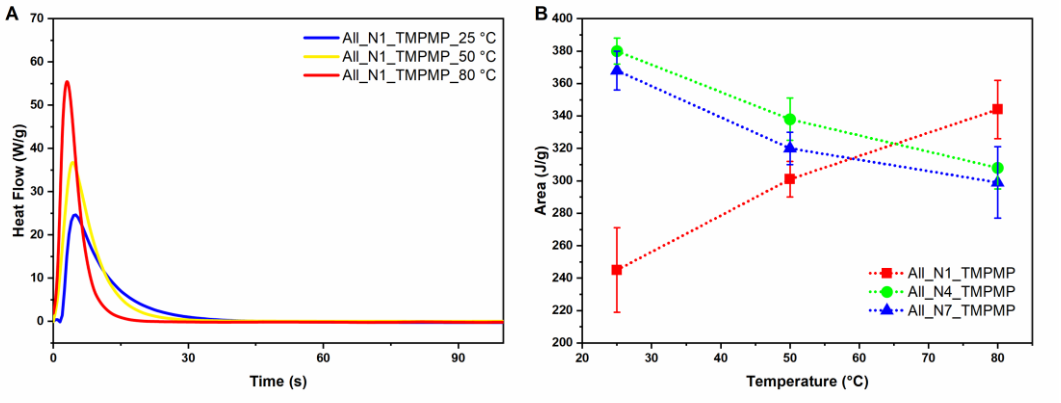

Figure 4.27. (A) Thermograms of All_N1_TMPMP tested at different temperatures (25, 50, and 80 °C) with 3 wt% of photoinitiator; (B) Released enthalpy (*ΔH*) at different temperatures for the three different thiol–ene photocurable resins, containing All_N1 (red), All_N4 (green) and All_N7 (blue), respectively.

Table 4.10. Results obtained from DSC analysis. Temperature of analysis, height of the peak (h_{peak}), Time at peak (t_{peak}), total heat flow (*ΔH*), double bond conversion (DC_{DCS}) evaluated as ratio between heat flow at the set temperature and heat flow for theoretical total conversion (ΔH_{max}).

FORMULATION	**Temperature**	h_{peak}	t_{peak}	ΔH	DC_{DCS} $(\Delta H/\Delta H_{max.})$
	(°C)	(W/g)	(W/g)	(J/g)	(%)
All_N1_TMPMP	25	26 ± 2	5.0 ± 1.0	245 ± 26	71
	50	38 ± 3	4.0 ± 0.5	301 ± 11	88
	80	51 ± 8	3.5 ± 1.0	344 ± 18	≈ 100
All_N4_TMPMP	25	59 ± 5	4.0 ± 1.0	380 ± 8	≈ 100
	50	46 ± 4	4.0 ± 1.0	338 ± 13	89
	80	50 ± 10	3.5 ± 0.5	308 ± 13	81
All_N7_TMPMP	25	61 ± 6	3.5 ± 0.5	368 ± 12	≈ 100
	50	34 ± 5	4.5 ± 1.0	320 ± 10	87
	80	45 ± 8	4.0 ± 1.0	299 ± 22	81

Furthermore, to gain deeper insights into the UV-curing process, photo-rheology was employed. In this analysis, the evolution of the storage modulus was tracked over the irradiation time as reported in **Figure 4.28**. The reaction started immediately as the light was directed on the sample, leading to a steep increase in G'. This increase is a direct consequence of the cross-linking reaction, which transforms the liquid resin into a solid thermoset, imparting rigidity. The photorheology highlighted the high reactivity of these formulations to UV-light, in line with the results obtained from the real-time FTIR analysis. It was observed that the All_N1_TMPMP formulation exhibited a shorter induction time compared to the other two formulations. However, all formulations demonstrated exceptionally high reactivity, evidenced by the steep rise in modulus and the completion of the reaction within approximately 60 s. In fact, the modulus plateau was rapidly reached, indicating a quick cross-linking reaction.

Lastly, the pot-life of the formulation was evaluated at 80 °C, a temperature at which all resins were liquid. The investigation was carried out leaving the resin under isothermal condition at 80 °C for about 40 minutes, then UV-light was turned on. As depicted in **Figure 4.28**, the storage modulus displayed no substantial increase over time; it remained nearly identical to the initial value. This observation indicated that no cross-linking reaction occurred due to the influence of temperature, as any such reaction would have led to an increase in the modulus. After 40 minutes, the UV-light was activated, and the subsequent development of the storage modulus followed the same pattern as in the previous test (i.e., UV irradiation began after 60 seconds).

The cross-linking reaction was finally evaluated by assessing the gel content in order to verify the formation of insoluble networks. All the thiol-ene polymers showed values above 95 %, confirming the UV-curing.

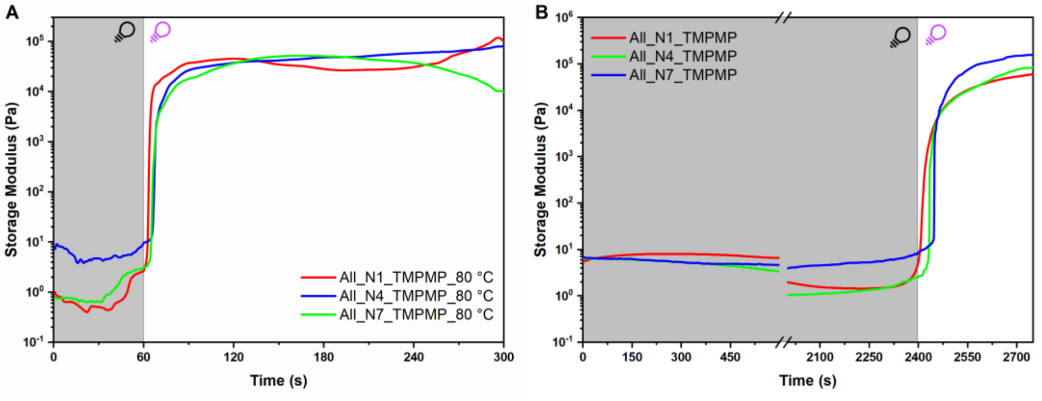

Figure 4.28. (A) Storage modulus as a function of the irradiation time at 80 °C for the thiol-ene formulations containing the different levoglucosenone-based resins; (B) Thermal stability investigation by means of photo-rheology conducted at 80 °C for the bio-based thiol-ene resins.

Thermo-mechanical & surface properties

After the detailed investigation of the curing process, the UV-cured samples were fully characterized by different analyses, such as DSC, DMTA, to attain a comprehensive thermo-mechanical characterization of the thermoset's properties.

DSC analysis was employed to evaluate the thermal properties of the thiol-ene networks (**Table 4.11**). The aim was to understand the influence of the chemical structure of the LGO-based allyl monomers (highlighted in **Figure 4.29**) on the final T_g. The thermogram displayed in Figure **4.26A** illustrates the results obtained during the second heating cycle, ranging from -40 °C to 250 °C. Notably, the presence of the shorter CH_2-based chain spacer in the allyl monomer structure gave the highest rigidity to the final network. Indeed, the formulation with All_N1 which had the lowest aliphatic chain between the two main unit and resulted in the highest T_g among the thermosets of 11 °C. In comparison, the network bearing the ene monomer with the middle number of aliphatic carbon (i.e. 4) had the medium T_g of the set and finally the azelate-based allyl with the longest aliphatic chain (i.e. 7) presented the lowest T_g of – 8 °C. This significant 20 °C difference in T_g was exclusively attributed to the chemical structure of the allyl monomers, as the ene:thiol functionality ratio remained constant, and the same thiol was consistently used across various photocurable formulations. This result aligns with prior research where the chemical structure of monomers was found to influence the final T_g [242,292].

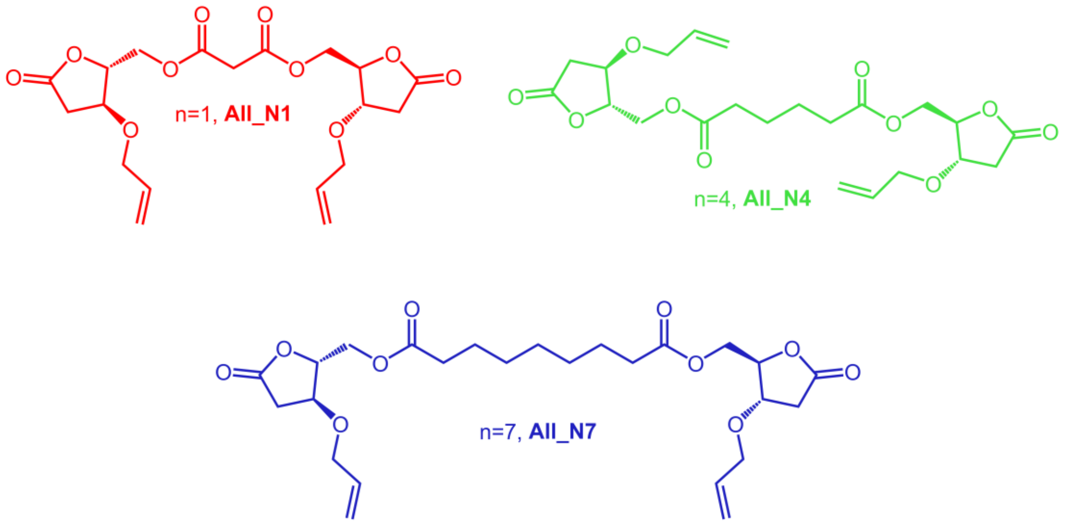

Figure 4.29. Chemical structure of the different allyl LGO-based monomers used in the study. All_N1 with the shortest spacer (1 CH_2), All_N4 with 4 CH_2 units between the LGO-ring, and All_N7 with an aliphatic chain of 7 units.

Viscoelastic properties of the crosslinked networks were investigated by means of DMTA analysis, exploring the storage modulus and Tan δ curves in function of the temperature for all the UV-cured formulations (**Figure 4.30B**). The trend observed for the T_g, determined as the maximum of Tan δ curve, was in agreement with the DSC analysis, highlighting the highest T_g value (17.5 °C) for thiol-ene formulation containing All_N1_TMPMP. A different aspect that can be investigated by DMTA analysis was the evolution of the storage modulus over the temperature. As depicted in the **Figure 4.30**, the three thermosets behave equally below the T_g showing almost the same storage modulus. At the T_g there was the decrease of *E'* that ended at the rubbery plateau. The highest value of *E'* in this region (2.45×10^6 Pa) was provided by the All_N1-based formulation, then the formulation containing All_N4 showed an intermediate value and finally the All_N7 had the lowest (9.50×10^4 Pa). The variation of storage modulus had a tangible effect on the cross-linking density of the cured samples, evaluated according to Equation 4.4 and reported in the **Table 4.11**. Once again, it possible to state that the chemical structure of the ene monomer influenced the cross-link density, playing a crucial role in the rigidity of the network giving an increase in the T_g when the "spacer" length of the allyl monomer is reduced.

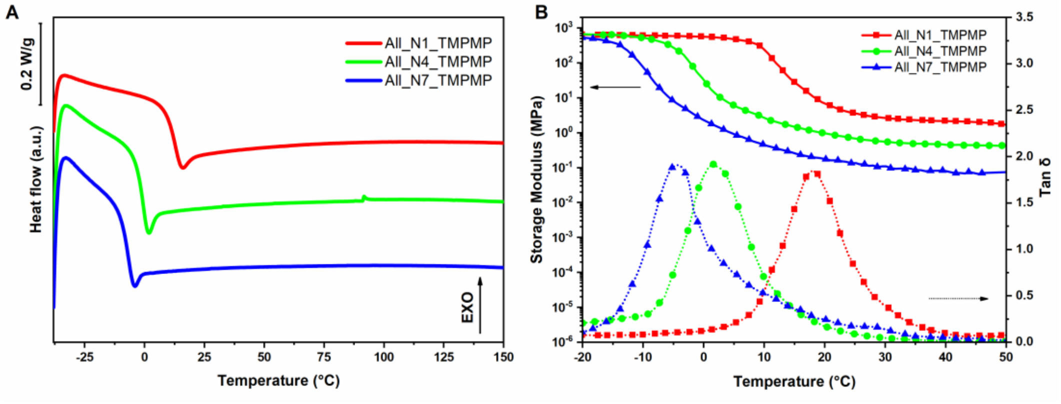

Figure 4.30. (A) Thermograms of the three different UV-cured thiol-ene formulations; red line for the network with All_N1, green line for the thermoset containing All_N4 and blue line for the thiol-ene material containing All_N7; (B) DMTA result for the UV-cured thiol-ene networks; Storage modulus and *Tan δ* development as a function of temperature.

Table 4.11. Characterization of the UV-cured networks by DSC analysis (1) and DMTA analysis (2).

FORMULATION	Tg^{1}	Tg^{2}	E'^{2}	ν^{2}	*% gel analysis*	*Contact angle*
	(°C)	**(°C)**	**(Pa)**	**(mmol/dm^3)**	**(%)**	**(°)**
All_N1_TMPMP	11.0 ± 0.5	17.5 ± 2.0	2.45×10^{6}	883	98 ± 1	73.5 ± 4.0
All_N4_TMPMP	− 1.0 ± 1.0	1.5 ± 1.5	2.85×10^{5}	108	97 ± 2	78.0 ± 1.5
All_N7_TMPMP	− 8.0 ± 0.5	− 4.0 ± 0.5	9.50×10^{4}	37	96 ± 1	83.0 ± 2.0

The mechanical behavior was investigated by tensile test on UV-cured samples. **Figure 4.31** present the typical stress-strain curves obtained from the rupture of the thiol-ene network at room temperature. All_N1_TMPMP showed the highest Young's modulus due to the remarkable rigidity of the network which allowed to also achieve the highest strength at break with about 3 MPa. It is worthy to emphasize that the high ε can be attributed to the teste condition above the T_g for all polymer networks. The spacer of the other allyl-monomers had a crucial role in the customization of the final material affecting the rigidity of the network resulting in different mechanical properties (**Table 4.11**).

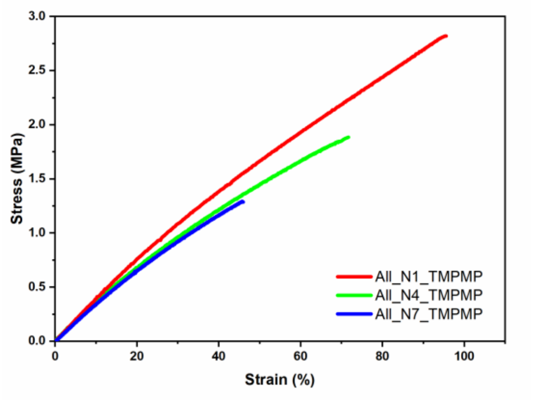

Figure 4.31. Stress-strain curves obtained at 25 °C for the UV-cured thiol-ene thermosets containing the different levoglucosenone-based monomers. Representative curves are reported among the five tested samples.

Table 4.12. Tensile test outcomes obtained for the three thermosets. Young's modulus (*E*), strength at break (σ), elongation at break (ε).

FORMULATION	***E***	σ	ε
	(MPa)	**(MPa)**	**(%)**
All_N1_TMPMP	4.2 ± 0.7	3.1 ± 0.5	100 ± 12
All_N4_TMPMP	3.5 ± 0.2	1.7 ± 0.3	62 ± 10
All_N7_TMPMP	3.2 ± 0.3	1.2 ± 0.3	46 ± 10

The chemical structure of the ene monomer can influence also surface properties such as the contact angle. Thus, the free surface of UV-cured film was tested. The results indicated a rise in the contact angle when transitioning from the network containing All_N1 to All_N7. This increase can be understood by taking into account the longer spacer of the allyl monomers. The extended aliphatic chain associated with the allyl ether monomer contributed to increase the hydrophobicity, ultimately resulting in a maximum contact angle of 83 ° for All_N7_TMPMP. These findings are detailed in **Table 4.11**.

Thermal and chemical degradation of thiol-ene networks

The concept of circular economy is capturing increasing attention, primarily due to the alarming amount of waste and the ongoing depletion of raw materials essential for monomer's supply. In this context, the bio-based monomers can help in the research of new materials that can replace the traditional fossil-based counterparts.

However, the transition to bio-based monomers is not sufficient. Therefore, it's crucial to address material reuse to minimize waste and enhance opportunities for recycling, thereby reducing the environmental footprint of polymeric materials. The investigation of the thermal and chemical degradation aiming to explore the thermal stability of the thiol-ene network and possible end-of-life scenarios which conjugate further utilizations of the monomers into the value chain.

The thermal stability was investigated by weight loss analysis (TGA), **Figure 4.32**. Notably, the UV-cured formulation based on All_N1 displayed the highest thermal stability, likely due to the increased cross-link density within the polymeric network. Nevertheless, all three thermosets exhibited a similar weight loss pattern. The reason can be searched is into the shared chemical nature of the main bonds that constitute these networks. The primary cross-links of the network composed by S-C bonds are responsible for the main degradation peak around 350 °C. A secondary peak appeared at around 450 °C, potentially due to the decomposition of the aliphatic chains (C-C bonds). A support of this hypothesis, the crosslinked network achieved in the presence of All_N7 exhibited a more pronounced contribution compared to the others. The latter can be explained by the longer spacer and consequently, a higher contribution of aliphatic components within the network. The last peak around 550 °C marked the network's final degradation, resulting in almost no residual char. These distinctions observed in the derivatives are outlined in **Table 4.13**.

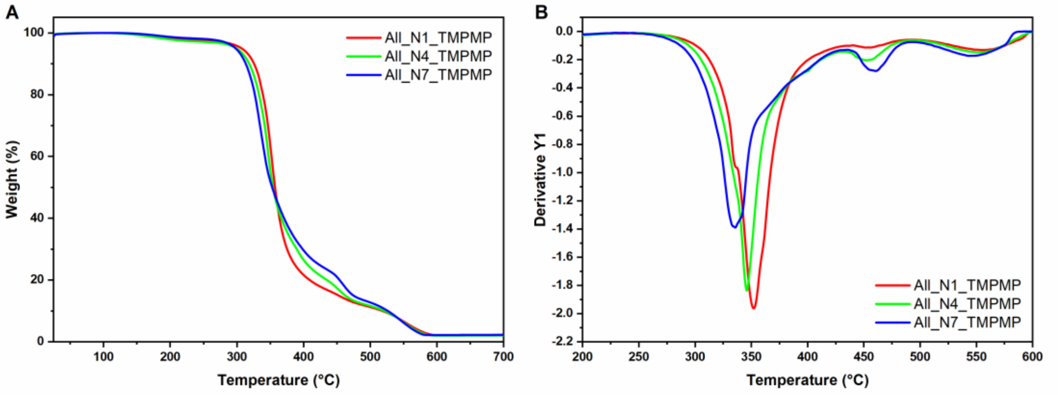

Figure 4.32. (A) TGA thermograms of thiol-ene UV-cured thermoset performed in air; (B) Derivatives of TGA curves of the thiol-ene thermosets.

Table 4.13. Results derived from TGA, T_5 (temperature at 5% weight loss), T_{peak} (temperature at derivative peak), and *Char* (percentage of residual weight at 700 °C).

FORMULATION	T_5	T_{peak}	*Char*
	(°C)	(°C)	(%)
All_N1_TMPMP	308	352	2.3
All_N4_TMPMP	301	346	2.2
All_N7_TMPMP	298	335	2.3

Chemical degradation was carried out under alkaline condition (NaOH 2 M) where the ester bonds present into the thiol-ene network can undergo to hydrolysis [310,311] resulting in a mass loss over time, **Figure 4.33**. Once more the influence of the chemical composition was evident in the degradation path. Indeed, All_N1_TMPMP showed the more pronounced degradation, followed by All_N4_TMPMP, while All_N7_TMPMP lasted for about 15 days. Considering that the analysis was conducted at room temperature, thus all the networks were above T_g, the only affecting factor was linked to the chain length of the diester moiety in the diallyl monomers. Then it was possible to assume that an increase of the chain spacer led to higher hydrophobicity resulting in slower hydrolysis. The network containing All_N1 degraded completely in 48 h with the fastest kinetic despite the highest rigidity of the network.

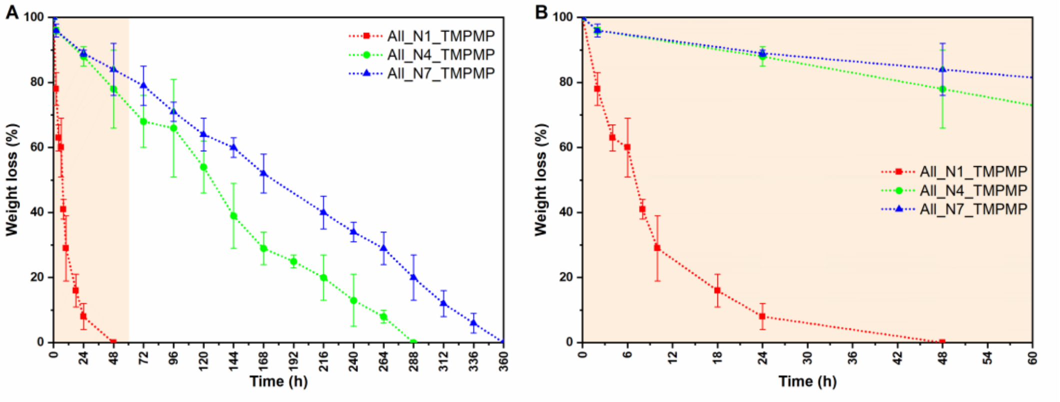

Figure 4.33. (A) Degradation study for the three UV-cured thiol-ene system, All_N1_TMPMP (red), All_N4_TMPMP (green), and All_N7_TMPMP (blue); (B) Insert with the zoom on All_N1_TMPMP mass loss over time.

DLP 3D-printing of thiol-ene resins

Digital Light Processing (DLP) 3D printing is a well-established and highly used additive manufacturing (AM) technique in the field of 3D printing and rapid prototyping. This method embraces the power of digital light projection to create intricate and precise three-dimensional objects. DLP 3D printing has gained widespread attraction and application across various industries from biomedical to aerospace due to its numerous advantages and capabilities [142,144]. One of the primary features that makes DLP 3D printing so attractive is its speed and efficiency. This method can rapidly cure and solidify entire layers of liquid resin in a single exposure, making it suitable for high-volume production, reducing energy cost and time. The use of a liquid crystal display (LCD) ensures precise control of the light projection, resulting in accurate and consistent part production [146,312]. Moreover, DLP 3D printing offers versatility in material choices. An actual challenge is the growth and expansion of the portfolio of possible bio-based resins which can be employed in AM [284,285]. Integrating both the selection of sustainable material, as levoglucosenone-based material, and the optimization of eco-friendly process, as DLP 3D printing, the investigation aimed to evaluate the feasibility of the bio-based thiol-ene resins for AM.

Firstly, based on the characterization on the UV-curing process, photo-rheology analysis demonstrated high reactivity to UV-light and short induction time for all formulations. These features are essential for achieving reaction times compatible with the speed of 3D printing and for creating self-sustaining structures. Remarkably in less than 30 s the curing reaction was complete corroborating the feasibility of AM. However, another crucial factor is the viscosity of the resin, which if is maintained in a proper range allows the formation of uniform layer properly covering the VAT (resin container) to successfully be able to print the entire object. Good viscosity was exhibited by all the resins at 80 °C (**Figure 4.34A**); nevertheless, All_N1_TMPMP required constant heating to stay in the liquid state, so the selection for the r.t. 3D printing was limited to the All_N4- and All_N7-based resins which retained suitable viscosity also at 25 °C (**Figure 4.34B**).

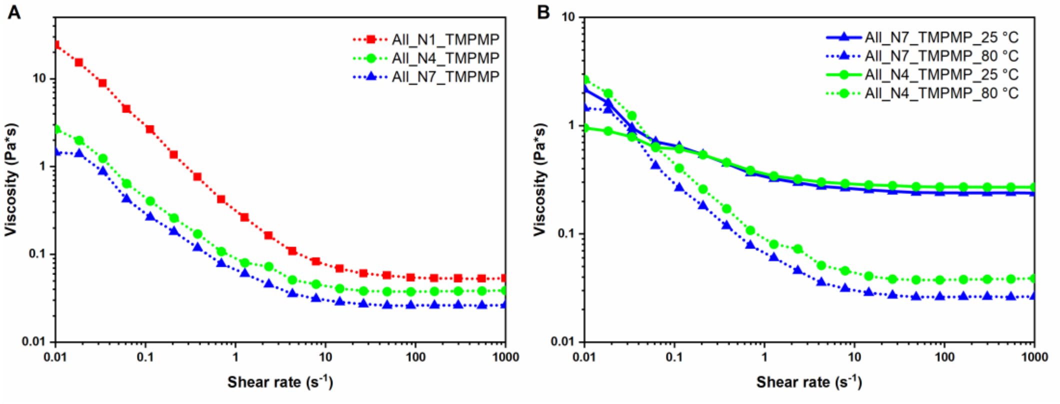

Figure 4.34. (A) Viscosity tested for the thiol-ene formulation at 80 °C; (B) Viscosity comparison at 25 and 80 °C for All_N4_TMPMP and All_N7_TMPMP for evaluation of printability.

The printing parameters regarding the UV-curing (i.e., light intensity, exposure time, burn-in layers) were empirically set according to photo-rheology, and real-time FTIR analysis, while the platform's parameters (i.e, velocity, acceleration and deceleration of the platform) were set considering the viscosity.

Promising results were obtained for the formulation containing All_N4 and All_N7. A honeycomb structure was successfully produced using both resins, and an additional hexagonal net structure was created by All_N7_TMPMP resin. As mentioned before, the precision of the 3D printing is crucial features hence using a 3D scanner a comparison analysis between the model CAD and the 3D printed object was performed (**Figure 4.35**). An overlay map has been created to define the accuracy of the AM comparing the model CAD dimensions to the effective ones of the object. As can be clearly seen in the comparative analysis, the mean deviation remained in a tight range of 0.42 % compared to the CAD file. The "green zone" indicative of the area of the highest fidelity and accuracy, ranging from – 100 μm to + 100 μm, represented the major portion of the 3D printed object (**Figure 4.35**). Nonetheless, certain discrepancies and irregularities observed can be attributed to various factors, including machine-related errors, resin limitations, and scanning issues. Printer resolution, printing imperfections, scanner precision, and the detection of complex structural areas can represent some of machine's errors. In addition, the non-uniform distribution of magnesium stearate powder on the object's surface, used for improving the scanning efficiency, as well as the presence of a support structure for accurate image acquisition, could create artefacts. Lastly, the lack of a comprehensive and tailored printing formulation, incorporating elements such as color dyes or radical inhibitors to mitigate over-polymerization and enhance light absorption within the desired spectrum can cause limitation in the final accuracy. These considerations represent potential avenues for further research to maximize the efficiency and precision of 3D printing using these types of resins.

To conclude, the study demonstrated the feasibility of using DLP 3D-printing for bio-derived resins achieving important results in terms of accuracy and precision of final 3D objects. This open the possibility to really think about green alternatives to the commercially available polymer resins which nowadays cover the highest world-wide market sales.

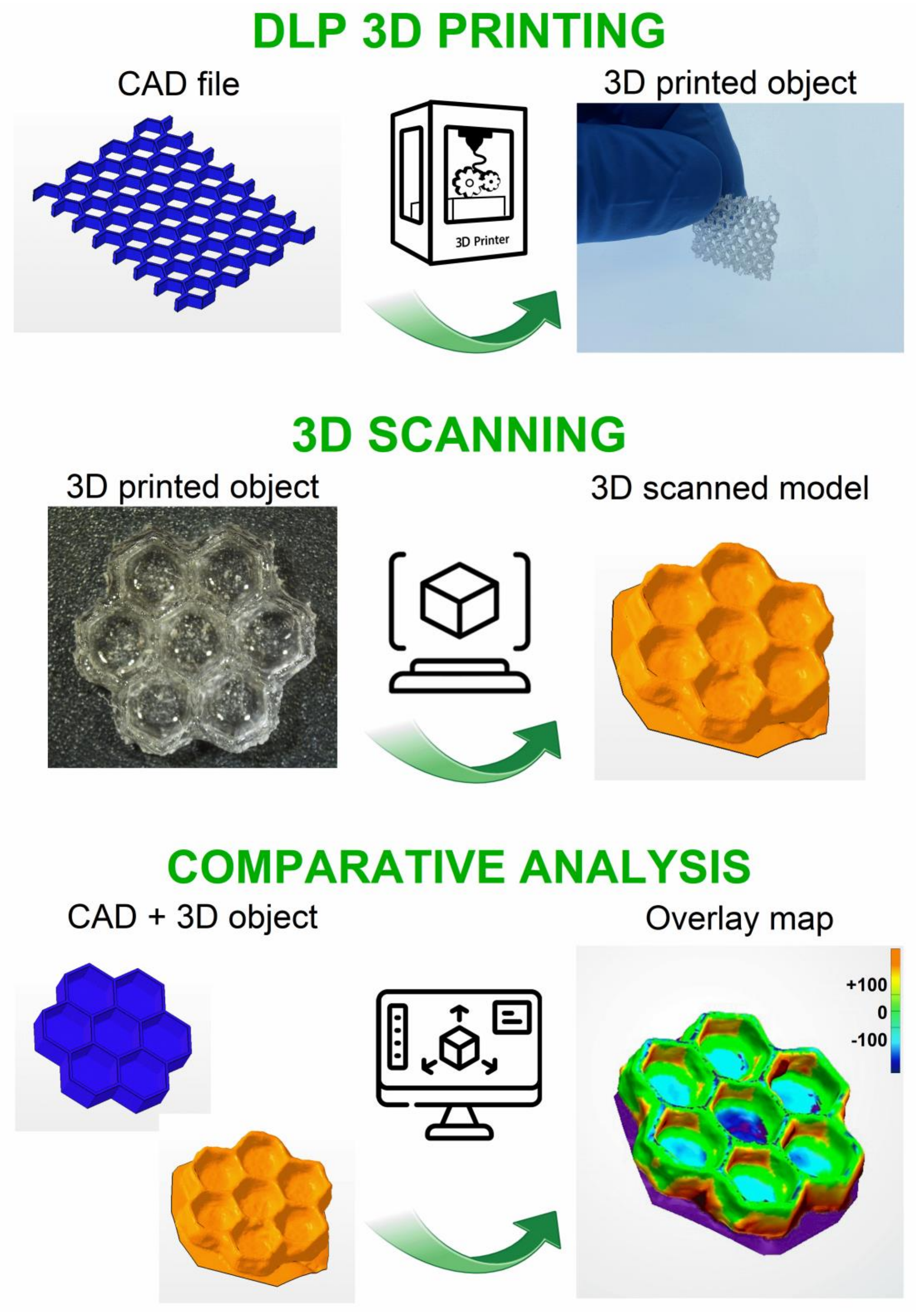

Figure 4.35. DLP 3D printing results with the schematic view of the step for the comparative analysis carried out with the 3D scanner operated with a honeycomb with dimensions of 11.27 × 11.66 × 2.12. mm (x, y, and z axes, respectively).

4.3.6. UV-induced thiol-ene reaction as interesting tools for surface post-functionalization

As presented in the previous chapter, UV-induced thiol-ene reaction has been used to cross-link different bio-based resins covering distinct applications form coating to 3D printing. Here, a different way to use the UV-induce thiol-ene curing is shown aiming to increase the spectrum of potential uses of this of chemistry. Indeed, UV-induce thiol-ene reaction offers the possibility to perform post-functionalization treatments to modify the material surface tailoring the final properties according to specific requirements. In the biomedical field this technique has been employed to graft proteins on coating surface opening interesting possibilities for controlled assemblies [313]. Antibacterial properties were provided to an epoxy coating by grafting glutathione on the surface through UV-induced thiol-ene reaction [314] or other specific molecules exploiting the orthogonal thiol-ene reaction [137]. Furthermore, isoprene unit of natural rubber can be functionalized modifying the final properties [315].

This study focus the attention of surface modification of bio-based epoxy coating through the grafting of a fluorinated-based monomer. Firstly, an epoxy-based thermoset has been produced by thermally curing at room temperature (**Figure 4.36**) the furfuryl amine diglycidyl ether (DGFA) and itaconic acid (IA).

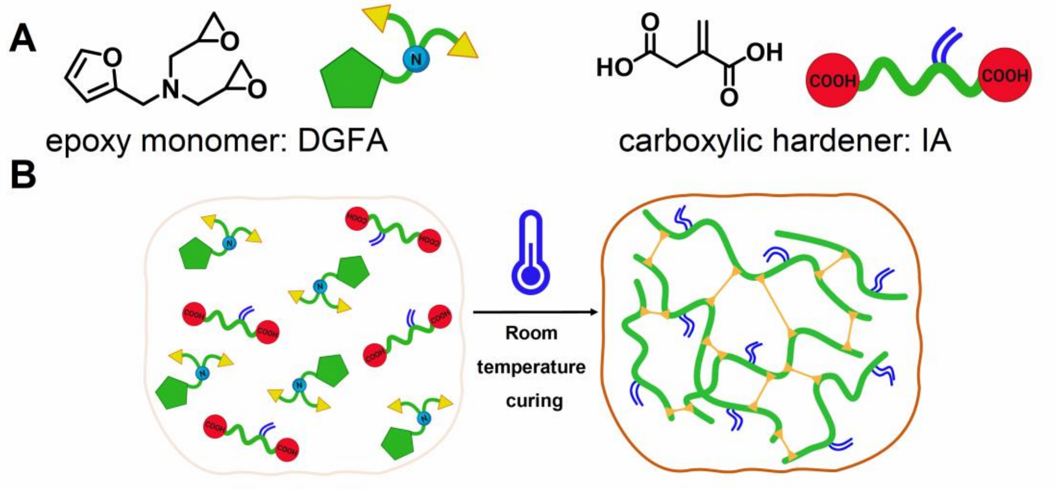

Figure 4.36. (A) Monomers used for the formation of epoxy-based network; (B) schematic view of the reaction between DGFA and IA for r.t. curing.

The ratio selected was 1:1 after a deep evaluation of the released enthalpy investigating various epoxy-carboxylic acid ratios, which is well-describe in the published paper [294]. DGFA has been extensively employed in epoxy resin with maleimide and anhydride as curing agents imprinting self-healing properties [316,317]. The great impact of DGFA is visible in the final mechanical properties which can be compared with the bisphenol A-based thermoset [318]. Natural acids represent an important class of hardness which can be used for curing of epoxies [168,319]. Recently fruit-based acid mixtures have been used to cure ELO at room temperature by exploitation of eutectic hardeners [278,320]. Here, IA has been used as hardener for DGFA in a room temperature curing to promote the formation of bio-based thermoset. The comprehensive curing investigation was carried out by deep investigation through FTIR, DSC and rheological analysis. The FITR analysis carried out at r.t. emphasized the decrease of the epoxy peaks of the oxirane signal located at 824 and 855 and 916 cm^{-1} with a complementary increased of OH band due to the opening of the epoxy rings (**Figure 4.37**). The validation of the reaction was showed by DSC analysis conducted at different curing time monitoring T_g and residual enthalpy, ΔH_r, as depicted in **Figure 4.38**. Lastly, rheology analysis was conducted to monitor the trend of storage and loss moduli over time (**Figure 4.39**). The final proof of the curing was the increase in the moduli over time highlighting the presence of the gel point after about 24 h. The vitrification of the system was reached in about 65 h in correspondence of the plateau of G', G'', and η.

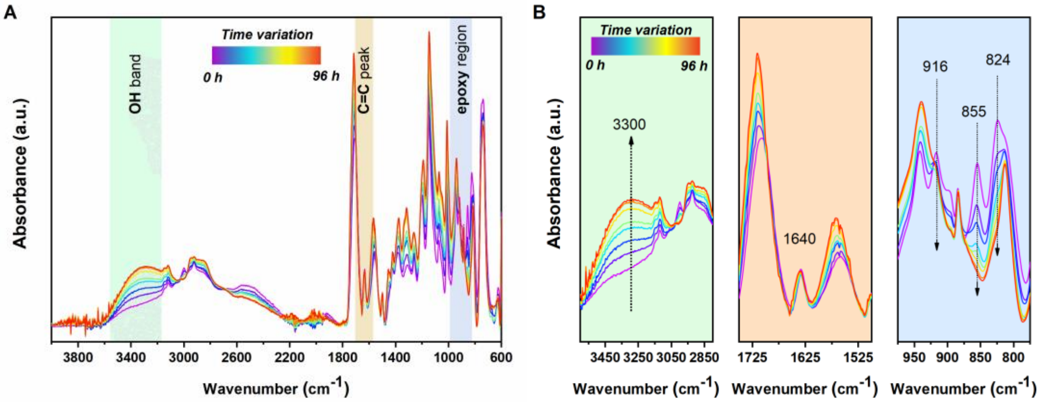

Figure 4.37. (A) ATR-FITR analysis conducted at room temperature of curing process of DGFA/IA; (B) highlight of specific OH, C=C, and epoxy region.

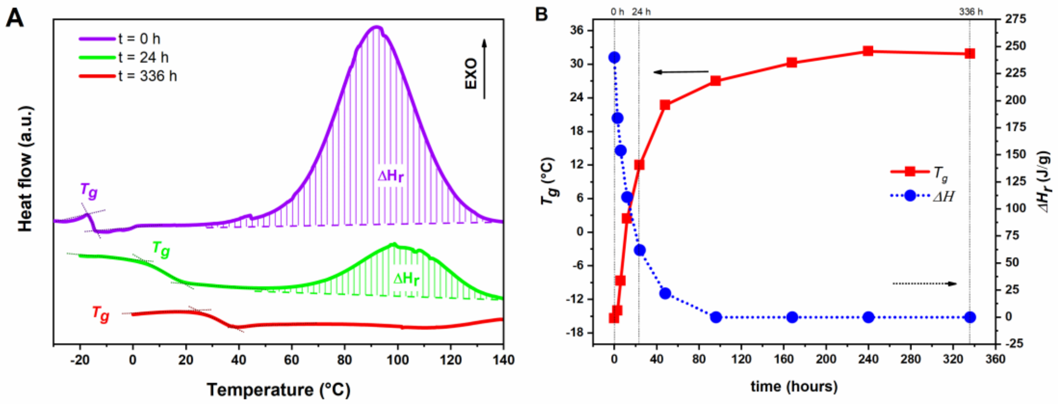

Figure 4.38. (A) DSC thermogram of the progress of the curing at different time, 0 h, 24 h, and 336 h; (B) Trend of T_g and *ΔH* in function of the curing time.

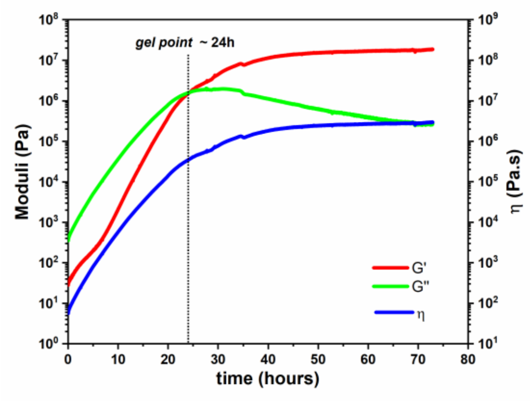

Figure 4.39. Variation of storage (*G′*), loss (*G″*) modulus, and complex viscosity (η) in function of the curing time at 25 °C.

Once the thermoset was formed, UV-induced thiol-ene reaction serves to post-functionalized the coating surface. **Figure 4.40** shows a schematic view of the significant chemical bonds present on the surface. The chemical-physical properties of the surface were significantly affected by the fluorinated compound. Specifically, the use of F-based compound aims to develop low energy hydrophobic coating [315]. The validation was performed by contact angle measurement before and after the functionalization revealing an increase from 56 ± 5 ° of the pristine surface to 99 ± 4 ° for the treated surface. This result was in accordance with previous treatment conducted with F-based compounds [321,322].

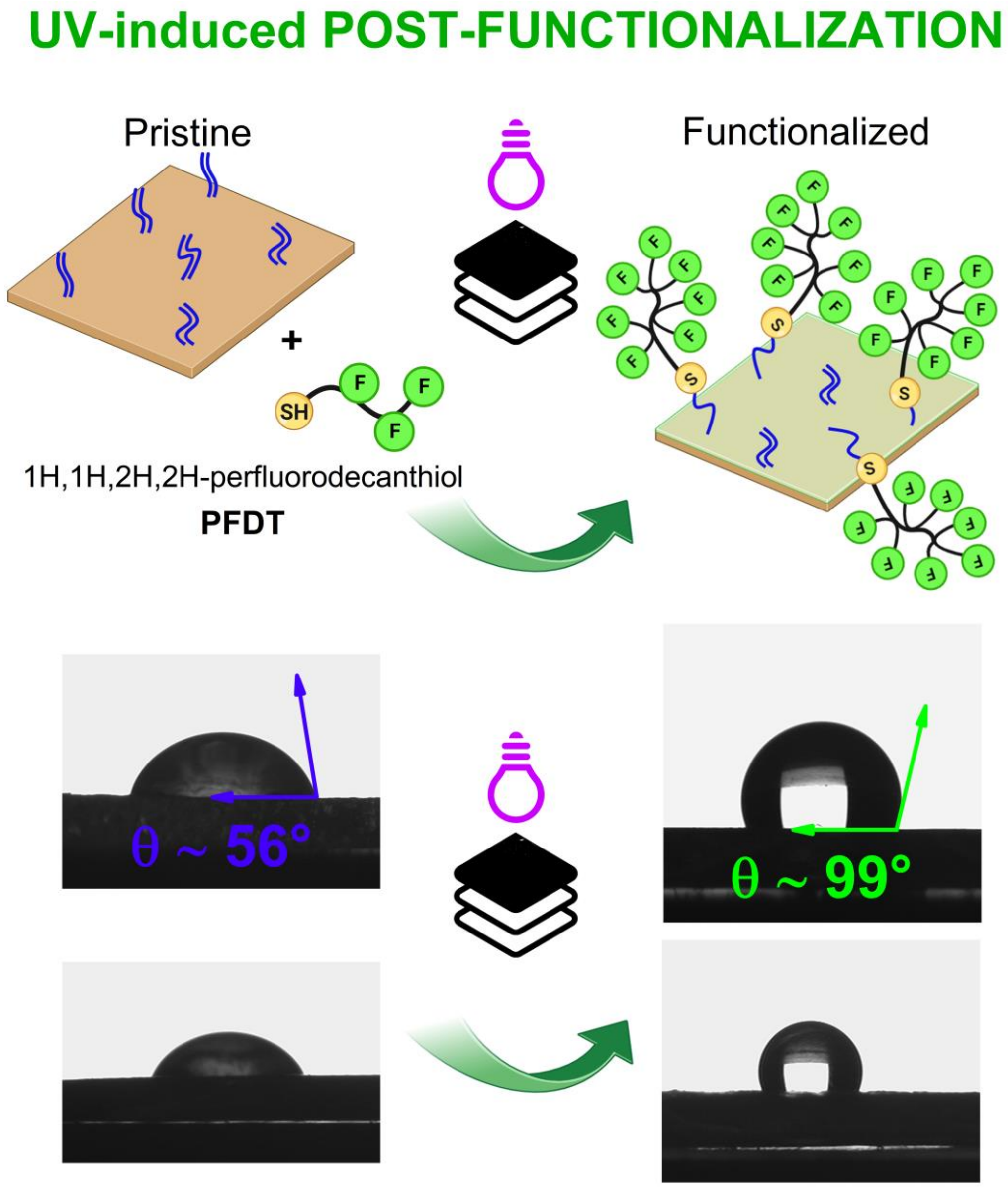

Figure 4.40. Schematic view of the UV-induced post-functionalization by thiol-ene reaction, highlighting the effect on the surface contact angle.

The formation of S-C bond was the result of the linking between the pendant C=C double bonds present on the surface, residual from the IA structure and the S-H moieties of the fluorinated monomer. The presence of unreacted C=C bonds was confirmed by ATR-FTIR analysis performed on the surface of the coating previous functionalization. It is possible to affirm that the r.t. preserved the vast majority of the double bond which could undergo to undesired reaction in case of high curing temperature such as cross-linking through oxa-Michael addition [323], radical reaction via C=C [324], and isomerization from itaconate to mesaconate [325]. The conversion of the C=C bonds was calculated around 60 % after the UV-irradiation; moreover, the presence of the C-F peak in the region between 1360 and 1000 cm^{-1} confirmed the success of the functionalization (**Figure 4.41**).

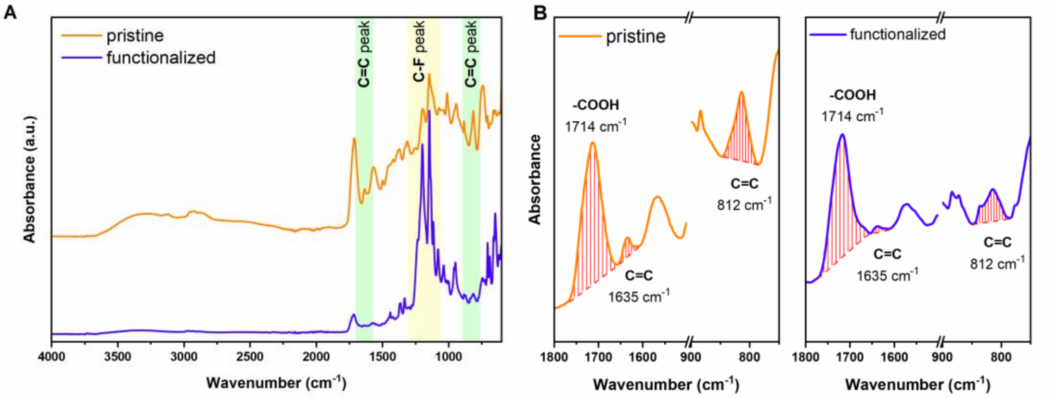

Figure 4.41. (A) ATR-FTIR spectra of pristine and functionalized coating surface; (B) Zoom of the area of the peaks used for the calculation of the conversion, COOH as reference, and C=C at 812 cm^{-1} as experimental peak.

XPS was conducted to provide additional insights into the chemical composition present at the modified DGFA/IA coating surface. In comparison to the pristine surface, XPS survey spectrum (**Figure 4.42**) of the functionalized DGFA/IA coating pointed out the presence of characteristic peaks (F KLL and F1s) associated with fluorine atoms. Additionally, the presence of the PFDT was verified and confirmed through the detection of the S2s and S2p peaks as consequence of the thiol-ene reaction and formation of C-S bond [326].

A more detailed scan of the carbon peak C1s and its deconvolution confirmed the result of the survey. The signal of both pre- and post- functionalization are reported in the **Figure 4.43**. The pristine surface of the thermoset displayed the peaks relative to Csp2 (283.5 eV), Csp3 (284.8 eV) and O-C=O (287.6 eV) which correspond to the chemical bonds within the polymer backbone [327,328]. Whereas in the UV-functionalized surface of the coating the new signal of CF_2 and CF_3 clearly appeared at 290 and 292 eV, attributed to the presence of PFDT [329]. Furthermore, it was possible to show that the Csp2 decrease with respect Csp3 as demonstrate by the deconvolution of the C1s peak. This decrease of Csp^2 aligned with the FTIR data confirming the reaction of the carbon double bond involved in the thiol-ene reaction. The increase in the Csp^3 can be also due to the presence of the carbon chain of the PFDT (hybridization C sp3).

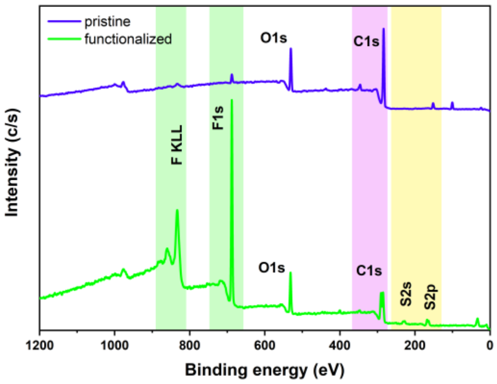

Figure 4.42. XPS analysis of the pristine (blue) and functionalized (green) coating with insert showing the F peaks, C peaks, and S peaks.

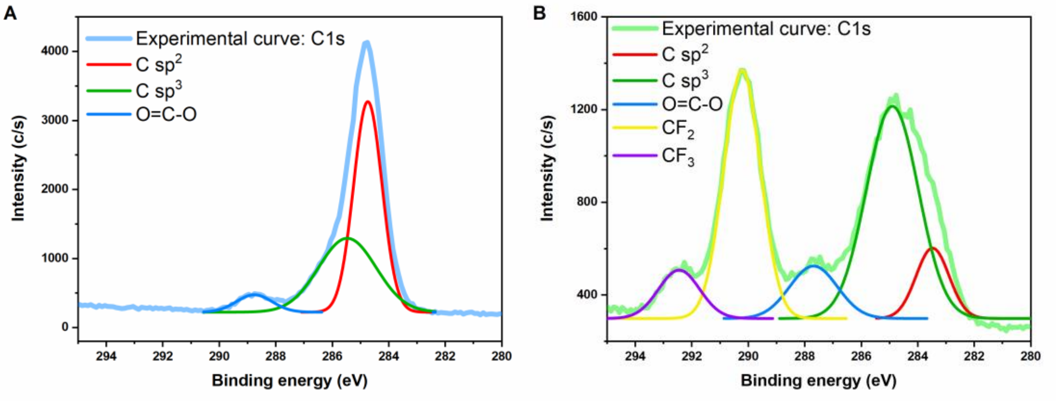

Figure 4.43. (A) Deconvolution of the C1s peak for the pristine surface; (B) Deconvolution of the carbon peaks, C1s, of the UV-functionalized surface with PFDT.

By employing this array of techniques, from FTIR to XPS, the success of the UV-induced post-functionalization of the polymer coating was demonstrated and verified, resulting in a transformation of its surface properties. More specifically, the establishment of a chemical bond between the surface and PFDT was strengthened through the in-depth analysis of variations in the signal associated with C=C bonds, as carried out using ATR-FTIR. This discovery was further corroborated by the presence of evident signals indicative of PFDT within the results of XPS analysis. Lastly, the impact of the introduced fluorine compound on the hydrophobicity of the surface was quantified through contact angle measurements, revealing a substantial increase of approximately 40 ° in the water contact angle. This observation underscores the profound enhancement in the surface's resistance to wetting, attributed to the incorporation of the fluorinated compound.

4.4. Conclusion

The works performed in the field of UV-induce radical thiol-ene curing complete the overview of the multiple strategies used along with the cationic UV-curing presented in Chapter 3 to exploiting green monomers developing interesting materials which applications can spread from coating to 3D printing.

Indeed, ferulic acid was successfully used as allyl-based monomer for developing green coatings. Thus, not only possible usage in cationic UV-curing was explored but also radical UV-curing was proven to be effective with this versatile molecule. On the same prospective, isosorbide showed its versatility resulting in the production of thiol-ene based green coating beside the previous investigation of epoxy-based ones. In this case, the impressive novelty needs to be located into the formation of a fully bio-based resin involving the use of lipoic acid as thiol counterpart. Moreover, furan compounds demonstrated the impressive portfolio of applications appearing into the radical UV-induce curing by thiol-ene chemistry. The formation of different green coating can promote the further growth in the use of these interesting naturally cellulose-based green compounds. Speaking of UV-curing, levoglucosenone showed its impressively reactivity as allyl-based compounds in thiol-ene reaction allowing the exploitation of DLP 3D printing. This impressive result opened the door for AM, meeting the specific and restrict requirements of 3D printing. Complex and self-stain structures were successfully printed increasing the possible application in an industrial point of view. The last described work aimed to point out a different approach in which UV-induce thiol-ene chemistry can play a crucial role for the efficiency and efficacy of an UV-induce techniques. The rapid post-functionalization proved the possibility to exploit UV-light for the customization of surface properties meeting different requirements. In this way, choosing the proper chemical network which can impart good bulk properties and possible surface functionalization, the best compromise of properties can be achieve.

In conclusions the results reported here, besides proving the versatility of the chosen bio-based system for the preparation of thiol-ene resin, further confirmed the effectiveness of moving toward sustainable approaches maintaining impressive performance of the final bio-based networks.

General conclusions

Through this thesis, the production of bio-based thermosetting materials, exploring the intricate relationships between structure and properties, was investigated in-depth. The purpose has been to encourage the use of renewable resources for material design to mitigate the adverse effects of global warming which has been demonstrated for various fields, from coatings to 3D printing applications. In this thesis, the synergy between environmentally green and efficient processes, and the use of renewable materials was examined in the field of the UV-curing, a powerful tool with the potential to develop green materials.

The effective utilization of bio-based polymers has the potential to play a main role in advancing the achievement of the Sustainable Development Goals (SDGs), thus promoting the development of a more sustainable and circular economy. By embracing bio-based polymers, a myriad of global challenges, including those related to environmental sustainability, social well-being, and economic growth, can be addressed. Bio-based polymers may offer a sustainable alternative to conventional, petroleum-derived plastics and materials, making them a key contributor to the global effort to combat resource depletion, reduce environmental degradation, and mitigate the effects of climate change.

Here, different chemical platforms have been chosen as source of monomers varying from cellulose to lignin, which are valuable feedstocks for sustainable energy and bio-based material production. Throughout the thesis, several monomers have been used, from furan to ferulic acid. Firstly, chemical functionalizations were performed to render the bio-based monomers sensitive to UV-light. Different approaches were developed to meet two different UV-activated mechanisms: cationic and radical UV-curing. The former was deeply investigated in **Chapter 3** while the latter focused on radical thiol-ene UV-curing was explored in **Chapter 4**.

The several works involved the chemical functionalization of monomers by reaction of OH-functional groups on the various starting molecules. The hydroxyl groups of furan monomers, isosorbide and ferulic acid have been reacted with epichlorohydrin (ECH) and allyl bromide to produce epoxy- and allyl-functional monomers respectively. The versatility of the bio-based monomers was demonstrated by the multiple reactions successfully achieved forming interesting UV-active monomers. It is noteworthy to mention that the employment of fossil-based chemical, such as ECH and ally bromide, facilitated the reaction, resulting in high purity and yield of the final products limiting the sustainability of the overall reactions. However, the evaluation of a sustainable production need to consider reagents, solvents, purification methods, reaction conditions, and all factors contributing to the reaction's environmental impact. In certain instances, the traditional and standard methods may still more efficient than the new greener methods. However, it is important to scout for different sustainable pathways to overcome the use of hazardous reagents, to reduce the overall impact of chemicals, and to meet the SGDs. An example reported in the thesis is the allylation of LGO-based monomer through sustainable reactions using green reagents and enzymes to achieve the synthesis of the different products.

In **Chapter 3** several experimental contributions related to cationic UV-curing was presented, exploring the epoxy world. Specifically, furan-based monomers were functionalized by introducing glycidyl ether groups aiming to perform a detailed investigation of the cationic UV-curing.

Firstly, the production of hybrid coating was achieved by cationic cross-linking of furan diglycidyl ether (FDE) and the exploitation of TEOS as precursor of silica particles which contribute to the inorganic part of the network. Aiming to a final customization of the properties of the polymer network, the formation of hybrid coatings helped to increase the mechanical performance achieving T_g above 100 °C. On the other hand, the introduction of a monofunctional furan-based glycidyl ether (FGE) derived from furfuryl alcohol allowed the tailoring of the properties, decreasing cross-link density, rigidity and ultimately T_g.

Within the coating frameworks, a second work presented the cross-linking of a monofunctional monomer (FGE) by interesting and innovative two-step method embracing UV-light and thermal curing. Indeed, the UV-irradiation of monofunctional FGE raised the formation of furan-based linear chains which were subsequently cross-linked by thermal treatment exploiting the cross-linking reaction of furan ring at high temperature. The cross-linking was validated using several techniques which studied both the kinetic and chemical features of the thermal step and the final effect on the material properties of the cross-linked furan-coating.

Lastly, aiming to increase the spectrum of the possible applications of these interesting monomers, FDE was investigated as main component for a 3D printable resin with remarkable results. Indeed, the high photoreactivity displayed by FDE reflected into an excellent Hot-lithography printability. The effect of the temperature was investigated to optimize the printing condition aiming to achieve fast and high conversion. The success of the printing was confirmed by the feasibility of printing intricate, complex and self-stain structures embracing one of the scopes of additive manufacturing (AM), which was born as technology to develop unique, complex structure by layer-by-layer method reducing time and cost productions. Furthermore, the FDE demonstrated fascinating mechanical performance comparable with conventional, petroleum-based resin used in AM. In the framework of a growing interest for a greener and sustainable manufacturing, these findings gave extra evidence that bio-based molecules can be successfully used to prepare significant alternatives to the current palette of printable photopolymers.

Not only furan was a valid source for bio-based monomers, but also other source were exploited for cationic UV-curing. Ferulic acid, derived from lignin, serves as platform to synthesize a diglycidyl ether (FeADE) which was exploited in different ways aiming for a production of green thermosets. In this case, the facing with UV-curing problem, such as monomer absorption, limitation of curing deep, and solid state of the starting monomer, challenged the exploitation of alternatives to fulfill the primary scope of thermoset productions. Thus, a thiol-epoxy system was investigated to achieve the formation of green thermoset using the synergistic combination of UV-light and temperature. Lastly, a cationic thermal curing method was investigated to demonstrate the potential of this monomer for utilization in a green adhesive for different substrates showing promising results. Indeed, the achieved value of strength were comparable with the one obtained with fossil-based resins.

Another interesting monomer, isosorbide, achieved notably results, as epoxy derivative (IDGE) for coating applications. Indeed, it demonstrated its potential for reinforced coating application in combination with macadamia nut shell powder (MAC) used as filler into the green resins. In this work, the cationic UV-curing was exploited to form interesting green coating which showed properties comparable with commercial fossil-based resins used in the same field. These interesting results proved once more the feasibility of not only thinking about green alternatives but starting to use them for real applications since they can compete performing in the same manner or even better with respect to the traditional counter parts.

Lastly, embracing once more the 3D printing field, epoxy vegetable oils were proven to be useful monomers to produce green thermosets in combination with bio-derived fillers, such as wall-nut shell, tagua or hemp powders. The Hot lithography method allowed an increasing of conversion and reactivity by the beneficial effect of operating at high temperatures, as demonstrated by the comprehensive analysis of the UV-curing stage by photo-DSC, photorheology and FTIR analyses, which assessed the temperature effect studying the curing varying the temperature. Ultimately, the mechanical characterization highlighted the beneficial effect of the filler on the mechanical properties with a tremendous increase in the tensile features. The cause of the benefit was assessed by characterization of modified filler, finding the core of the benefit in the surface interface between polymer matrix and bio-derived fillers.

Going through the **Chapter 4**, it is evident how bio-based precursors can also serve as platforms from which new monomers can be derived, making it possible to exploit another interesting UV-curing technique, the thiol-ene “click” chemistry. In this case the functionalization showed the versatility of furan monomers, ferulic acid, isosorbide and levoglucosenone as source for allyl derivatives employable for thiol-ene reactions. In the different showcases, the versatility the OH functionality of alcohol, carboxylic acid and phenol groups of the bio-based monomers was proved by successfully multiple functionalization conducted to achieve ene-based monomers useful in thiol-ene chemistry.

Ferulic acid proved to be suitable for allylation and subsequent use in thiol-ene resin for coating applications. Interestingly the chemical nature of the UV-curing, studied by FTIR, offered explanations for the different reactivity of the functional groups of the ferulic acid, allyl groups and cinnamic carbon double-bond. This achieved level of knowledge allowed to understand the influence of the chemical structure reaching a broad spectrum of properties playing with the nature of the allyl monomer involved into the reaction.

Same behave was demonstrated for isosorbide, with an innovative fully bio-based resin with the lipoic acid (LA) as thiol counterpart. The study demonstrated the feasibility to produce a fully green coating with comparable properties to a partial bio-based film formed using a commercially available thiol (TMPMP).

Moving in the in-depth analysis of thiol-ene chemistry, furan monomers showed remarkable properties in the same field. Furthermore, they raised the possibility of customization of final polymer properties, such as T_g, ultimate strength, toughness, by changing either structure or functionality of the monomers involved into the cross-linking reaction. Specifically, a more rigid furan-based ene structure bearing cyclobutane ring (BACBDA) allowed a T_g above 20 °C that were impressive considering the thiol-ene nature of the network. Moreover, the tailoring can be done employing different functionality modifying the cross-link density and thus rigidity, T_g and tensile properties according to the specific requirements.

Last innovation was studied using levoglucosenone for allyl derivatives. The extremely high photoreactivity of these ene monomers with thiol allowed the investigation as photocurable resins employable in 3D printing. The in-depth analysis of the UV-curing by photo-rheology and photo-DSC allowed the optimization of the curing conditions achieving satisfactory results in terms of kinetic and final conversion. The final properties were tailored according to the ene used into the resin highlighting the massive influence of the chemical structure. Aliphatic long spacer between the ene units decreased the T_g without affecting the photoreactivity. Thus, to open the spectra of the possible bio-based formulations spendable in the 3D printing, an investigation of the feasibility of digital light processing (DLP) of bio-based resins was carried out showing the success in printing complex structure with remarkable results in terms of efficiency and accuracy of the 3D printing.

As the last presented work, a different use of thiol-ene chemistry was displayed considering not the proper UV-curing of a thermoset, but the surface functionalization of an already cured green thermoset exploiting the residual double bonds present on the surface. In this case, the UV-light served to activate the linkage of a fluorine monomer on the surface to modify the surface hydrophobicity of the coating. The UV-induce thiol-ene reaction was fully demonstrated by several techniques showing how this powerful tool can be used also for post curing treatment useful to meet specific requirements.

Overall, different learnings can be retrieved from the thesis. Firstly, new methods for chemical functionalization need to be wisely characterized to prove an effective benefit. Then, the presented research places a strong emphasis on understanding the structure-properties relationship, resulting in interesting findings. The chemical backbone variation, the change in the number of reactive groups, the use of different reactive species, and presence of filler particles were identified as key faction to tailor the properties of the final thermosets. Thus, it is possible to customize the properties knowing the effect of a component introduced into a UV-curable resins to meet specific requirements. Additionally, the thesis addresses challenges inherent to UV-curing, such as monomer absorption, reactivity, and the presence of fillers, offering solutions to enhance the feasibility of UV-curing processes. Considering AM, the presented studies highlighted the feasibility of using bio-based monomer adopting the right condition to arise reactivity and conversion employing Hot-lithography and DLP. Within all these works presented, embracing epoxy- and allyl-functional monomers, the thesis aimed to further open possibility for the innovation and the sustainability of material and process with a specific attention into the replacement of traditional and conventional polymer resins to meet the actual challenges in the direction of a greener eco-friendly society.

Appendix A

A1 List of Abbreviations

% wt	Weight percent
.cli	Command line interface
^{13}C-NMR	Carbon NMR
^{1}H-NMR	Proton NMR
3D	Three dimensional
A2FeA	Diallyl ferulic acid
Ally_N	Ester of ally-based levoglucosenone derivative
AM	Additive manufacturing
ASTM	American Society for Testing and Materials
ATR	Attenuated total reflectance
BACBDA	Bisallyl cyclobutane dicarboxylate
BADGE	Bisphenol A diglycidylether
BAMF	2,5-Bis((allyloxy)methyl) furan
BAPO	Bis(acyl)phosphine oxide
C=C	Carbon-carbon double bond
C=O	Carbonyl bond
C5	Pentose unit
C6	Hexose unit
CAD	Computer aided design
CAGR	Compound Annual Growth Rate
CBDA-2	Cyclobutane furan dicarboxylic acid
C-C	Carbon-carbon bond
$CDCl_3$	Chloroform
CDE	1,4-Cyclohexanendimethanol diglycidyl ether

C-H	Carbon-hydrogen bond
CMC	Ceramic matrix composite
CO_2	Carbon dioxide
COO	Ester bond
Darocur 1173	2-Hydroxy-2-methyl-1-phenyl-propan-1-one
DC	Double bond conversion
DCM	Dichloromethane
DGFA	Diglycidyl ether of furfuryl amine
DLP	Digital light processing
DMSO	Dimethyl sulfoxide
DMTA	Dynamic mechanical thermal analysis
DoE	Design of experiment
DSC	Differential scanning calorimetry
E	Young’s modulus
E'	Storage modulus
E_a	Activation energy
EC	Epoxy conversion
ECC	3,4-Epoxycyclohexylmethyl-3,4-epoxycyclohexanecarboxylate
ECH	Epichlorohydrin
ELO	Epoxy linseed oil
ESI	Electronspray mass spectroscopy
ESO	Epoxy soybean oil
EtOAc	Ethyl acetate
EtOH	Ethanol
EVO	Epoxy vegetable oil
FA	Furfuryl alcohol
FAA	Trans-3-(2-furyl)acrylic acid
FDCA	2,5-Furandicarboxylic acid
FDE	Furan diglycidyl ether
FDM	2,5-Furandimethanol

FeA	Ferulic acid
FeADE	Diglycidyl ether of ferulic acid
FESEM	Field emission scanning electron microscopy
Ffa	Furfuryl amine
FGE	Furan glycidyl ether
FTIR	Fourier-transform infrared spectroscopy
G'	Storage modulus
G''	Loss modulus
H	Hardness
H200	Hemp 200 mesh
H_2O_2	Hydrogen peroxide
h-A1FeA	Hydrogenated monoallyl ferulic acid
h-A2FeA	Hydrogenated diallyl ferulic acid
HBO-*O*-Allyl	Allyl (*S*)-γ-hydroxymethyl-α,β-butenolide
HCl	Hydrochloric acid
h-EA1FeA	Hydrogenated monoallyl methyl ester of ferulic acid
Hept	Heptane
h-FeA	Hydrogenated ferulic acid
Hg-lamp	Mercury-lamp
h_{peak}	Heigh of the peak
IA	Itaconic acid
IDAE	Isosorbide diallyl
IDGE	Isosorbide diglycidyl ether
Irgacure 290	Tris(4-((4-acetylphenyl)thio)phenyl) sulfonium tetrakis(pentafluorophenyl) borate
Irgacure 819	Phenylbis(2,4,6-trimethylbenzoyl)phosphine oxide
IS	Isosorbide
I-SbF6	p-(octyloxyphenyl)phenyl iodonium hexafluoroantimonate
ISC	Intersystem crossing
ISO	International Organization for Standardization

ITX	Isopropylthioxanthone
LA	Lipoic acid
LCD	Liquid crystal display
LCQ	Quadrupole ion trap
LED	Light emitting diod
LevA	Levunillic acid
LGO	Levoglucosenone
MAC	Macadamia nut shell powder
m-CPBA	3-Chloroperbenzoic acid
MeCN	Acetonitrile
MeOH	Methanol
$MgSO_4$	Magnesium sufphate
MS	Mass spectrometry
Mw	Molecular weight
NaOH	Sodium hydroxide
NIR	Near infrared
NMR	Nuclear magnetic resonance spectroscopy
NPGDGE	Neopentyl glycol diglycidyl ether
NT1	Norrish type 1
NT2	Norrish type 2
OH	Hydroxyl group
OPA	One phonon absorption
PAG	Photoacid generator
PEF	Poly(ethylene 2,5-furandicarboxylate)
PET	Polyethylene terephthalate
PETMP	Tetrakis(3-mercaptopropionate)
PFA	Polyfurfuryl alcohol
PFDT	1H,1H,2H,2H-perfluorodecanethiol
PI	Photoinitiator
phr	Per hundred resin

PLB	4-(hexahydro-pyrrolo[1,2-a]pyrimidin-1-ylmethyl)-benzoic acid methyl ester
ppm	Part per million
r.t.	Room temperature
$R\bullet$	Initiating radical
RDE	Resorcinol diglycidyl ether
RP	Rapid prototyping
R_P	Rate of polymerization
$S\bullet$	Thiyl radical
S_0	Ground state
S_1	Singlet state
S-BF5	Tris(4-((4-acetylphenyl)thio)phenyl) sulfonium tetrakis(pentafluorophenyl) borate
SDGs	Sustainable developments Goals
SH	Thiol group
$Si(CH_3)_3$	Trimethylchlorosilane
SLA	Stereolithography
S-SbF6	Triarylsulfonium hexafluoroantimoniate
STA	Simultaneous thermal analysis
STL	Standard triangulation language
T_1	Triplet state
T200	Tagua 200 mesh
T_5	Temperature at 5 wt% weight loss
$Tan\ \delta$	Damping factor
TBAB	Tetrabutylammonium bromide
TBHS	Tetrabutylammoium hydrogenosulphate
TEA	Trietylenammine
TEOS	Tetraethyl orthosilicate
T_g	Glass transition temperature
TGA	Thermogravimetric analysis
t_{gel}	Gel time

THF	Tetrrahydrofuran
TMPMP	Trimethylolpropane tris(3-mercaptopropionate)
T_{peak}	Temperature of peak
t_{peak}	Time of the peak
U	Toughness
UV	Ultraviolet
VAT	Resin container
v_c	Crosslinking density
Vis	Visible
VOC	Volatile organic compound
VOs	Vegetable oils
VP	Vat polymerization
WS	Wall nut shell powder
WS200	Wall nut shell 200 mesh
WS325	Wall nut shell 325 mesh
XPS	X-ray photoelectron
YTT	Ytterbium(III) trifluoromethanesulfonate
ε	Elongation at break
σ	Strength at break
Φ	Heating rate
ΔH	Enthalpy
η	Viscosity

A2 List of Figures

A3 List of Tables

Appendix B

B1 List of publications

Related to the PhD project

[1] **Pezzana, L.**; Mousa, M.; Malmström, E.; Johansson, M.; Sangermano, M.; Bio-based monomers for UV-curable coatings: allylation of ferulic acid and investigation of photocured thiol-ene network. *Prog. Org. Coatings*. **2021**, 150, 105986. DOI: https://doi.org/https://doi.org/10.1016/j.porgcoat.2020.105986.

[2] **Pezzana, L.**; Sangermano, M. Fully biobased UV-cured thiol-ene coatings. *Prog. Org. Coatings* **2021**, *157*, 106295. DOI: https://doi.org/10.1016/j.porgcoat.2021.106295

[3] **Pezzana, L.**; Malmström, E.; Johansson, M.; Sangermano, M. UV-Curable Bio-Based Polymers Derived from Industrial Pulp and Paper Processes. *Polymers.* **2021**, 13 (9), 1530. DOI: https://doi.org/10.3390/polym13091530.

[4] **Pezzana, L.**; Melilli, G.; Guigo, N.; Sbirrazzuoli, N.; Sangermano, M. Cationic UV Curing of Bioderived Epoxy Furan-Based Coatings: Tailoring the Final Properties by In Situ Formation of Hybrid Network and Addition of Monofunctional Monomer. *ACS Sustainable Chem. Eng.* **2021** 9 (51), 17403-17412 DOI: 10.1021/acssuschemeng.1c06939

[5] **Pezzana, L.**; Wolff, R.; Melilli, G.; Guigo, N.; Sbirrazzuoli, N.; Stampfl J.; Liska, R.; Sangermano, M. Hot-lithography 3D printing of biobased epoxy resins. *Polymer* **2022**, 254, 12507. DOI: https://doi.org/10.1016/j.polymer.2022.125097

[6] **Pezzana, L.**; Melilli, G.; Delliere, P.; Moraru, D.; Guigo, N.; Sbirrazzuoli, N.; Sangermano, M. Thiol-ene biobased networks: Furan allyl derivatives for green coating applications. *Prog. Org. Coatings* **2022**, *173*, 107203. DOI: https://doi.org/10.1016/j.porgcoat.2022.107203.

[7] **Pezzana, L.**; Melilli, G.; Guigo, N.; Sbirrazzuoli, N.; Sangermano, M. Photopolymerization of furan-based monomers: Exploiting UV-light for a new age of green polymers. *React. Funct. Polym.* **2023**, 185, 105540. DOI: https://doi.org/10.1016/j.reactfunctpolym.2023.105540.

[8] **Pezzana, L.**; Melilli, G.; Guigo, N.; Sbirrazzuoli, N.; Sangermano, M. Cross-Linking of Biobased Monofunctional Furan Epoxy Monomer by Two Steps Process, UV Irradiation and Thermal Treatment. *Macromol. Chem. Phys.* **2023**, 224, 2200012 DOI: https://doi.org/10.1002/macp.202200012

[9] **Pezzana, L.**; Melilli, G.; Sangermano, M.; Sbirrazzuoli, N.; Guigo, N. Sustainable approach for coating production: Room temperature curing of diglycidyl furfuryl amine and itaconic acid with UV-induced thiol-ene surface post-functionalization. *React. Funct. Polym.* **2023**, *182*, 105486, DOI: https://doi.org/10.1016/j.reactfunctpolym.2022.105486.

[10] Flourat, A.L.; **Pezzana, L.**; Belgacem, S.; Dosso, A.; Sangermano, M.; Fadlallah, S.; Allais, F. Levoglucosenone to 3D-printed green materials: synthesizing sustainable and tunable monomers for eco-friendly photo-curing. *Green Chem.* **2023**, DOI:10.1039/D3GC01833D.

[11] **Pezzana, L.**; Emanuele, A.; Sesana, R.; Delprete, C.; Malmström, E.; Johansson, M.; Sangermano, M. Cationic UV-curing of isosorbide-based epoxy coating reinforced with macadamia nut shell powder. *Prog. Org. Coatings* **2023**, 185, 107949, DOI: https://doi.org/10.1016/j.porgcoat.2023.107949.

[12] **Pezzana, L.**; Malmström, E.; Johansson, M.; Casalegno, V.; Sangermano, M. Multiple approaches to exploit ferulic acid bio-based epoxy monomers for green thermosets. *Industrial Product and Crops*, **SUBMITTED**

[13] **Pezzana, L.**; Wolff, R.; Stampfl J.; Liska, R.; Sangermano, M. Hot-lithography Hot-lithography 3D printing of fully bio-based composites: green vegetable oil epoxy matrix & bio-derived filler powder. *Additive Manufacturing*, **ACCEPTED**

Unrelated to the PhD project

[1] **Pezzana, L.**; Riccucci G.; Spriano, S.; Battegazzore, D.; Sangermano, M.; Chiappone, A. 3D Printing of PDMS-Like Polymer Nanocomposites with Enhanced Thermal Conductivity: Boron Nitride Based Photocuring System. *Nanomaterials* **2021** 11 (2) 373. DOI: https://doi.org/10.3390/nano11020373

[2] Riccucci, G.; **Pezzana, L.**; Simone Lantean, S.; Tori, A.; Spriano, S.; Sangermano, M.; Investigation of the Thermal Conductivity of Silicon-Base Composites: The Effect of Filler Materials and Characteristic on Thermo-Mechanical Response of Silicon Composite. *Applied Sciences* **2021** 11 (12), 5663. DOI https://doi.org/10.3390/app11125663

[3] Giacomo, R.; Angelo, R.; **Lorenzo, P.**; Tori, A.; Spriano, S.; Sangermano, M.; Magnetic-Oriented Nickel Particles and Nickel-Coated Carbon Nanotubes: An Efficient Tool for Enhancing Thermal Conductivity of PDMS Composites. *Macromol. Chem. Phys*. **2022**, 223, 2200199. DOI: https://doi.org/10.1002/macp.202200199

[4] Papadopoulos, L.; **Pezzana, L.**; Malitowski, N. M.; Sangermano, M.; Bikiaris, D. N.;Robert, T.; UV-Curing Additive Manufacturing of Bio-Based Thermosets: Effect of Diluent Concentration on Printing and Material Properties of Itaconic Acid-Based Materials. *ACS Omega* **2023** 8 (34), 31009-31020. DOI: 10.1021/acsomega.3c02808.

B2 List of conferences attended by the author

[1] **Virtual European Symposium of Photopolymer Science 2021**, online (Poster session: Bio-based monomers for UV-curable coatings: allylation of ferulic acid and investigation of photocured thiol-ene network).

[2] **European Polymer Congress 2022**, Prague (Oral session: Hot-lithography 3D printing of biobased epoxy resins)

[3] **European Symposium of Photopolymer Science 2022**, Istanbul (Oral session: Epoxy biobased furan monomers for cationic UV-curing)

[4] **Coating Science International Conference 2023**, Noordwjik (Oral session: Photocured furan-based organic coatings)

[5] **Polymer meeting 15**, 2023 Bratislava (Oral session: Bio-based monomers for UV curable thiol-ene formulations)

References

1. European commission The EU and the United Nations – common goals for a sustainable future Available online: https://commission.europa.eu/strategy-and-policy/sustainable-development-goals/eu-and-united-nations-common-goals-sustainable-future_en (accessed on Oct 9, 2023).

2. United Nations The Paris Agreement Available online: https://www.un.org/en/climatechange/paris-agreement (accessed on Oct 9, 2023).

3. Owusu, P.A.; Asumadu-Sarkodie, S. A review of renewable energy sources, sustainability issues and climate change mitigation. *Cogent Eng.* **2016**, *3*, 1167990, doi:10.1080/23311916.2016.1167990.

4. Rogelj, J.; den Elzen, M.; Höhne, N.; Fransen, T.; Fekete, H.; Winkler, H.; Schaeffer, R.; Sha, F.; Riahi, K.; Meinshausen, M. Paris Agreement climate proposals need a boost to keep warming well below 2 °C. *Nature* **2016**, *534*, 631–639, doi:10.1038/nature18307.

5. Khalid, M.Y.; Arif, Z.U.; Ahmed, W.; Arshad, H. Recent trends in recycling and reusing techniques of different plastic polymers and their composite materials. *Sustain. Mater. Technol.* **2022**, *31*, e00382, doi:https://doi.org/10.1016/j.susmat.2021.e00382.

6. Statista Plastic Market 2022 Available online: https://straitsresearch.com/report/plastic-market (accessed on Dec 12, 2023).

7. Statista Global plastic market size value 2021-2030 Available online: https://www.statista.com/statistics/1060583/global-market-value-of-plastic/ (accessed on Oct 9, 2023).

8. Mordor Intelligence Research & Advisory Bio-based Polymers Market Size & Share Analysis - Growth Trends & Forecasts (2023 - 2028). Available online: https://www.mordorintelligence.com/industry-reports/bio-based-polymers-market (accessed on Oct 9, 2023).

9. Gandini, A. Polymers from renewable resources: A challenge for the future of macromolecular materials. *Macromolecules* **2008**, *41*, 9491–9504, doi:10.1021/ma801735u.

10. Bozell, J.J.; Petersen, G.R. Technology development for the production of biobased products from biorefinery carbohydrates—the US Department of Energy's "Top 10" revisited. *Green Chem.* **2010**, *12*, 539–554, doi:10.1039/B922014C.

11. John, G.; Nagarajan, S.; Vemula, P.K.; Silverman, J.R.; Pillai, C.K.S. Natural monomers: A mine for functional and sustainable materials – Occurrence, chemical modification and polymerization. *Prog. Polym. Sci.* **2019**, *92*, 158–209, doi:10.1016/j.progpolymsci.2019.02.008.

12. Ragauskas, A.J.; Beckham, G.T.; Biddy, M.J.; Chandra, R.; Chen, F.; Davis, M.F.; Davison, B.H.; Dixon, R.A.; Gilna, P.; Keller, M.; et al. Lignin Valorization: Improving Lignin Processing in the Biorefinery. *Science (80-.).* **2014**, *344*, 1246843, doi:10.1126/science.1246843.

13. Upton, B.M.; Kasko, A.M. Strategies for the conversion of lignin to high-value polymeric materials: Review and perspective. *Chem. Rev.* **2016**, *116*, 2275–2306, doi:10.1021/acs.chemrev.5b00345.

14. Scranton, A.B.; Bowman, C.N.; Peiffer, R.W. *Photopolymerization: fundamentals and applications*; ACS Publications, 1997; ISBN 0841235201.

15. Mordor Intelligence Research & Advisory UV Curable Resin Market Size & Share Analysis - Growth Trends & Forecasts (2023 - 2028) Available online: https://www.mordorintelligence.com/industry-reports/uv-curable-resin-market.

16. Chatani, S.; Kloxin, C.J.; Bowman, C.N. The power of light in polymer science: photochemical processes to manipulate polymer formation, structure, and properties. *Polym. Chem.* **2014**, *5*, 2187–2201, doi:10.1039/C3PY01334K.

17. Andrzejewska, E. Photopolymerization kinetics of multifunctional monomers. *Prog. Polym. Sci.* **2001**, *26*, 605–665, doi:https://doi.org/10.1016/S0079-6700(01)00004-1.

18. Baret, V.; Gandini, A.; Rousset, E. Photodimerization of heteroarylene-vinylenes. *J. Photochem. Photobiol. A Chem.* **1997**, *103*, 169–175, doi:https://doi.org/10.1016/S1010-6030(96)04525-X.

19. Peters, M.V.; Stoll, R.S.; Kühn, A.; Hecht, S. Photoswitching of Basicity. *Angew. Chemie Int. Ed.* **2008**, *47*, 5968–5972, doi:https://doi.org/10.1002/anie.200802050.

20. Krompiec, S.; Bujak, P.; Malarz, J.; Krompiec, M.; Skórka, Ł.; Pluta, T.;

Danikiewicz, W.; Kania, M.; Kusz, J. An isomerization—1,3-dipolar cycloaddition tandem reaction towards the synthesis of 3-aryl-4-methyl-5-O-substituted isoxazolines from O-allyl compounds. *Tetrahedron* **2012**, *68*, 6018–6031, doi:10.1016/J.TET.2012.05.027.

21. Ding, L.; Chen, Y.F.; Zhong, Z.; Lu, F.; Du, Y.; Liu, L.; Huang, Y. Preparation of the flexible soybean oil-based material via [2 + 2] cycloaddition photo-polymerization. *J. Appl. Polym. Sci.* **2020**, doi:10.1002/app.49925.

22. Crivello, J. V; Lam, J.H.W. Diaryliodonium Salts. A New Class of Photoinitiators for Cationic Polymerization. *Macromolecules* **1977**, *10*, 1307–1315, doi:10.1021/ma60060a028.

23. Decker, C. Kinetic Study and New Applications of UV Radiation Curing. *Macromol. Rapid Commun.* **2002**, *23*, 1067–1093, doi:https://doi.org/10.1002/marc.200290014.

24. Kiskan, B.; Yagci, Y. Thermally curable benzoxazine monomer with a photodimerizable coumarin group. *J. Polym. Sci. Part A Polym. Chem.* **2007**, *45*, 1670–1676, doi:https://doi.org/10.1002/pola.21934.

25. Purbrick, M.D. Photoinitiation, photopolymerization and photocuring. J.-P. Fouassier. Hanser Publishers, Munich, 1995. pp. xii + 375, price DM198.00, sFr175.00, öS1466.00, US$138.00, £84.00. ISBN 3-446-17069-3. *Polym. Int.* **1996**, *40*, 315, doi:https://doi.org/10.1002/(SICI)1097-0126(199608)40:4<315::AID-PI566>3.0.CO;2-T.

26. Fouassier, J.P.; Allonas, X.; Lalevée, J.; Dietlin, C. Photoinitiators for Free Radical Polymerization Reactions. *Photochem. Photophysics Polym. Mater.* **2010**, 351–419, doi:10.1002/9780470594179.ch10.

27. Lalevée, J.; Fouassier, J.-P. *Photopolymerisation initiating systems*; Royal Society of Chemistry, 2018; ISBN 1788014944.

28. Griesser, M.; Neshchadin, D.; Dietliker, K.; Moszner, N.; Liska, R.; Gescheidt, G. Decisive reaction steps at initial stages of photoinitiated radical polymerizations. *Angew. Chemie - Int. Ed.* **2009**, *48*, 9359–9361, doi:10.1002/anie.200904473.

29. Andrzejewska, E.; Zych-Tomkowiak, D.; Andrzejewski, M.; Hug, G.L.; Marciniak, B. Heteroaromatic thiols as co-initiators for type II photoinitiating systems based on camphorquinone and isopropylthioxanthone. *Macromolecules* **2006**, *39*, 3777–3785, doi:10.1021/ma060240k.

30. Cosola, A.; Chiappone, A.; Martinengo, C.; Grützmacher, H.; Sangermano, M. Gelatin Type A from Porcine Skin Used as Co-Initiator in a Radical Photo-Initiating System. *Polymers (Basel).* 2019, *11.*

31. Sangermano, M.; Razza, N.; Crivello, J.V. Cationic UV-curing: Technology and applications. *Macromol. Mater. Eng.* **2014**, *299*, 775–793, doi:10.1002/mame.201300349.

32. Crivello, J. V The discovery and development of onium salt cationic photoinitiators. *J. Polym. Sci. Part A Polym. Chem.* **1999**, *37*, 4241–4254, doi:https://doi.org/10.1002/(SICI)1099-0518(19991201)37:23<4241::AID-POLA1>3.0.CO;2-R.

33. Olah, G.A.; Prakash, G.K.S.; Sommer, J.; Molnar, A. Superacid chemistry. **2009**.

34. Crivello, J. V; Lam, J.H.W. Photoinitiated cationic polymerization by dialkylphenacylsulfonium salts. *J. Polym. Sci. Polym. Chem. Ed.* **1979**, *17*, 2877–2892, doi:https://doi.org/10.1002/pol.1979.170170924.

35. Decker, C. The use of UV irradiation in polymerization. *Polym. Int.* **1998**, *45*, 133–141, doi:10.1002/(SICI)1097-0126(199802)45:2<133::AID-PI969>3.0.CO;2-F.

36. Stanford, J.L.; Ryan, A.J.; Yang, Y. Photoinitiated cationic polymerization of epoxides. *Polym. Int.* **2001**, *50*, 986–997, doi:10.1002/pi.730.

37. Sangermano, M. Advances in cationic photopolymerization. *Pure Appl. Chem.* **2012**, *84*, 2089–2101, doi:https://doi.org/10.1351/PAC-CON-12-04-11.

38. Crivello, J. V.; Reichmanis, E. Photopolymer materials and processes for advanced technologies. *Chem. Mater.* **2014**, *26*, 533–548, doi:10.1021/cm402262g.

39. Yagci, Y.; Jockusch, S.; Turro, N.J. Photoinitiated Polymerization: Advances, Challenges, and Opportunities. *Macromolecules* **2010**, *43*, 6245–6260, doi:10.1021/ma1007545.

40. Hoyle, C.E.; Bowman, C.N. Thiol-ene click chemistry. *Angew. Chemie - Int. Ed.* **2010**, *49*, 1540–1573, doi:10.1002/anie.200903924.

41. Kolb, H.C.; Finn, M.G.; Sharpless, K.B. Click Chemistry: Diverse Chemical Function from a Few Good Reactions. *Angew. Chemie - Int. Ed.* **2001**, *40*, 2004–2021, doi:10.1002/1521-3773(20010601)40:11<2004::AID-ANIE2004>3.0.CO;2-5.

42. Kade, M.J.; Burke, D.J.; Hawker, C.J. The power of thiol-ene chemistry. *J. Polym. Sci. Part A Polym. Chem.* **2010**, *48*, 743–750, doi:https://doi.org/10.1002/pola.23824.

43. Lowe, A.B. Thiol-ene “click” reactions and recent applications in polymer and materials synthesis. *Polym. Chem.* **2010**, *1*, 17–36, doi:10.1039/b9py00216b.

44. Cramer, N.B.; Bowman, C.N. Kinetics of thiol-ene and thiol-acrylate photopolymerizations with real-time Fourier transform infrared. *J. Polym. Sci. Part A Polym. Chem.* **2001**, *39*, 3311–3319, doi:10.1002/pola.1314.

45. Pezzana, L.; Malmström, E.; Johansson, M.; Sangermano, M. UV-Curable Bio-Based Polymers Derived from Industrial Pulp and Paper Processes. *Polym.* 2021, *13*.

46. Pezzana, L.; Melilli, G.; Guigo, N.; Sbirrazzuoli, N.; Sangermano, M. Photopolymerization of furan-based monomers: Exploiting UV-light for a new age of green polymers. *React. Funct. Polym.* **2023**, *185*, 105540, doi:https://doi.org/10.1016/j.reactfunctpolym.2023.105540.

47. Liska, R.; Schuster, M.; Inführ, R.; Turecek, C.; Fritscher, C.; Seidl, B.; Schmidt, V.; Kuna, L.; Haase, A.; Varga, F.; et al. Photopolymers for rapid prototyping. *J. Coatings Technol. Res.* **2007**, *4*, 505–510, doi:10.1007/s11998-007-9059-3.

48. Mendes-Felipe, C.; Oliveira, J.; Etxebarria, I.; Vilas-Vilela, J.L.; Lanceros-Mendez, S. State-of-the-Art and Future Challenges of UV Curable Polymer-Based Smart Materials for Printing Technologies. *Adv. Mater. Technol.* **2019**, *4*, 1–16, doi:10.1002/admt.201800618.

49. Gandini, A. Monomers and Macromonomers from Renewable Resources. *Biocatal. Polym. Chem.* 2010, 1–33.

50. Zevallos Torres, L.A.; Lorenci Woiciechowski, A.; de Andrade Tanobe, V.O.; Karp, S.G.; Guimarães Lorenci, L.C.; Faulds, C.; Soccol, C.R. Lignin as a potential source of high-added value compounds: A review. *J. Clean. Prod.* **2020**, *263*, doi:10.1016/j.jclepro.2020.121499.

51. Ioannidou, S.M.; Pateraki, C.; Ladakis, D.; Papapostolou, H.; Tsakona, M.; Vlysidis, A.; Kookos, I.K.; Koutinas, A. Sustainable production of bio-based chemicals and polymers via integrated biomass refining and bioprocessing in a circular bioeconomy context. *Bioresour. Technol.* **2020**, *307*, 123093, doi:10.1016/j.biortech.2020.123093.

52. Chavan, P.; Singh, A.K.; Kaur, G. Recent progress in the utilization of industrial waste and by-products of citrus fruits: A review. *J. Food Process Eng.* **2018**, *41*, 1–10, doi:10.1111/jfpe.12895.

53. de la Torre, I.; Martin-Dominguez, V.; Acedos, M.G.; Esteban, J.; Santos, V.E.; Ladero, M. Utilisation/upgrading of orange peel waste from a biological biorefinery perspective. *Appl. Microbiol. Biotechnol.* **2019**, *103*, 5975–5991, doi:10.1007/s00253-019-09929-2.

54. Brännström, S.; Malmström, E.; Johansson, M. Biobased UV-curable coatings based on itaconic acid. *J. Coatings Technol. Res.* **2017**, *14*, 851–861, doi:10.1007/s11998-017-9949-y.

55. Wei, G.; Xu, H.; Chen, L.; Li, Z.; Liu, R. Isosorbide-based high performance UV-curable reactive diluents. *Prog. Org. Coatings* **2019**, *126*, 162–167, doi:10.1016/j.porgcoat.2018.10.028.

56. Malburet, S.; Di Mauro, C.; Noè, C.; Mija, A.; Sangermano, M.; Graillot, A. Sustainable access to fully biobased epoxidized vegetable oil thermoset materials prepared by thermal or UV-cationic processes. *RSC Adv.* **2020**, *10*, 41954–41966, doi:10.1039/D0RA07682A.

57. Claudino, M.; Mathevet, J.M.; Jonsson, M.; Johansson, M. Bringing d-limonene to the scene of bio-based thermoset coatings via free-radical thiol-ene chemistry: Macromonomer synthesis, UV-curing and thermo-mechanical characterization. *Polym. Chem.* **2014**, *5*, 3245–3260, doi:10.1039/c3py01302b.

58. Noè, C.; Hakkarainen, M.; Sangermano, M. Cationic uv-curing of epoxidized biobased resins. *Polymers (Basel).* **2021**, *13*, 1–16, doi:10.3390/polym13010089.

59. Fache, M.; Darroman, E.; Besse, V.; Auvergne, R.; Caillol, S.; Boutevin, B. Vanillin, a promising biobased building-block for monomer synthesis. *Green Chem.* **2014**, *16*, 1987–1998, doi:10.1039/c3gc42613k.

60. Bassett, A.W.; Honnig, A.E.; Breyta, C.M.; Dunn, I.C.; La Scala, J.J.; Stanzione, J.F. Vanillin-Based Resin for Additive Manufacturing. *ACS Sustain. Chem. Eng.* **2020**, *8*, 5626–5635, doi:10.1021/acssuschemeng.0c00159.

61. Navaruckiene, A.; Skliutas, E.; Kasetaite, S.; Rekštyte, S.; Raudoniene, V.; Bridziuviene, D.; Malinauskas, M.; Ostrauskaite, J. Vanillin acrylate-based resins for optical 3D printing. *Polymers (Basel).* **2020**, *12*, doi:10.3390/polym12020397.

62. Nameer, S.; Larsen, D.B.; Duus, J.O.; Daugaard, A.E.; Johansson, M. Biobased Cationically Polymerizable Epoxy Thermosets from Furan and Fatty Acid Derivatives. *ACS Sustain. Chem. Eng.* **2018**, *6*, 9442–9450, doi:10.1021/acssuschemeng.8b01817.

63. Fertier, L.; Ibert, M.; Buffe, C.; Saint-Loup, R.; Joly-Duhamel, C.; Robin, J.-J.; Giani, O. New biosourced UV curable coatings based on isosorbide. *Prog. Org. Coatings* **2016**, *99*, 393–399, doi:https://doi.org/10.1016/j.porgcoat.2016.07.001.

64. Çakmakçi, E.; Şen, F.; Kahraman, M.V. Isosorbide Diallyl Based Antibacterial Thiol-Ene Photocured Coatings Containing Polymerizable Fluorous Quaternary Phosphonium Salt. *ACS Sustain. Chem. Eng.* **2019**, *7*, 10605–10615, doi:10.1021/acssuschemeng.9b01161.

65. Noè, C.; Tonda-Turo, C.; Carmagnola, I.; Hakkarainen, M.; Sangermano, M. Uv-cured biodegradable methacrylated starch-based coatings. *Coatings* **2021**, *11*, 1–10, doi:10.3390/coatings11020127.

66. Yan, R.; Yang, D.; Zhang, N.; Zhao, Q.; Liu, B.; Xiang, W.; Sun, Z.; Xu, R.; Zhang, M.; Hu, W. Performance of UV curable lignin based epoxy acrylate coatings. *Prog. Org. Coatings* **2018**, *116*, 83–89, doi:10.1016/j.porgcoat.2017.11.011.

67. Rozman, H.D.; Koay, E.L.; Tay, G.S. Preliminary study on the utilization of lignin as filler in ultra-violet (UV) curable system. *J. Appl. Polym. Sci.* **2011**, *120*, 2527–2533, doi:10.1002/app.33205.

68. Ibrahim, F.; Mohan, D.; Sajab, M.S.; Bakarudin, S.B.; Kaco, H. Evaluation of the compatibility of organosolv lignin-graphene nanoplatelets with photo-curable polyurethane in stereolithography 3D printing. *Polymers (Basel).* **2019**, *11*, doi:10.3390/polym11101544.

69. Hajirahimkhan, S.; Xu, C.C.; Ragogna, P.J. Ultraviolet Curable Coatings of Modified Lignin. *ACS Sustain. Chem. Eng.* **2018**, *6*, 14685–14694, doi:10.1021/acssuschemeng.8b03252.

70. Hajirahimkhan, S.; Ragogna, P.J.; Xu, C. (Charles) Methacrylation of kraft lignin for UV-curable coatings: Process optimization using response surface methodology. *Biomass and Bioenergy* **2019**, *120*, 332–338, doi:10.1016/j.biombioe.2018.11.038.

71. Ding, R.; Du, Y.; Goncalves, R.B.; Francis, L.F.; Reineke, T.M. Sustainable near UV-curable acrylates based on natural phenolics for stereolithography 3D printing. *Polym. Chem.* **2019**, *10*, 1067–1077,

doi:10.1039/C8PY01652F.

72. Maturi, M.; Pulignani, C.; Locatelli, E.; Vetri Buratti, V.; Tortorella, S.; Sambri, L.; Comes Franchini, M. Phosphorescent bio-based resin for digital light processing (DLP) 3D-printing. *Green Chem.* **2020**, *22*, 6212–6224, doi:10.1039/d0gc01983f.

73. Wilbon, P.A.; Chu, F.; Tang, C. Progress in renewable polymers from natural terpenes, terpenoids, and rosin. *Macromol. Rapid Commun.* **2013**, *34*, 8–37, doi:10.1002/marc.201200513.

74. Chen, G.F. Developments in the field of rosin chemistry and its implications in coatings. *Prog. Org. Coatings* **1992**, *20*, 139–167, doi:10.1016/0033-0655(92)80002-E.

75. Do, H.S.; Park, J.H.; Kim, H.J. UV-curing behavior and adhesion performance of polymeric photoinitiators blended with hydrogenated rosin epoxy methacrylate for UV-crosslinkable acrylic pressure sensitive adhesives. *Eur. Polym. J.* **2008**, *44*, 3871–3882, doi:10.1016/j.eurpolymj.2008.07.046.

76. Ahn, B.K.; Sung, J.; Kim, N.; Kraft, S.; Sun, X.S. UV-curable pressure-sensitive adhesives derived from functionalized soybean oils and rosin ester. *Polym. Int.* **2013**, *62*, 1293–1301, doi:10.1002/pi.4420.

77. Silvestre, A.J.D.; Gandini, A. Terpenes: Major sources, properties and applications. *Monomers, Polym. Compos. from Renew. Resour.* **2008**, 17–38, doi:10.1016/B978-0-08-045316-3.00002-8.

78. Crivello, J. V; Yang, B. Studies of synthesis and cationic photopolymerization of three isomeric monoterpene diepoxides. *J. Polym. Sci. Part A Polym. Chem.* **1995**, *33*, 1881–1890, doi:https://doi.org/10.1002/pola.1995.080331116.

79. Crivello, J. V; Liu, S.S. Synthesis and cationic photopolymerization of monomers based on nopol. *J. Polym. Sci. Part A Polym. Chem.* **1999**, *37*, 1199–1209, doi:https://doi.org/10.1002/(SICI)1099-0518(19990415)37:8<1199::AID-POLA16>3.0.CO;2-L.

80. Crivello, J. V; Liu, S. Photoinitiated cationic polymerization of epoxy alcohol monomers. *J. Polym. Sci. Part A Polym. Chem.* **2000**, *38*, 389–401, doi:https://doi.org/10.1002/(SICI)1099-0518(20000201)38:3<389::AID-POLA1>3.0.CO;2-G.

81. Breloy, L.; Ouarabi, C.A.; Brosseau, A.; Dubot, P.; Brezova, V.; Abbad

Andaloussi, S.; Malval, J.P.; Versace, D.L. β-Carotene/Limonene Derivatives/Eugenol: Green Synthesis of Antibacterial Coatings under Visible-Light Exposure. *ACS Sustain. Chem. Eng.* **2019**, *7*, 19591–19604, doi:10.1021/acssuschemeng.9b04686.

82. Weems, A.C.; Delle Chiaie, K.R.; Worch, J.C.; Stubbs, C.J.; Dove, A.P. Terpene- and terpenoid-based polymeric resins for stereolithography 3D printing. *Polym. Chem.* **2019**, *10*, 5959–5966, doi:10.1039/c9py00950g.

83. Weems, A.C.; Delle Chiaie, K.R.; Yee, R.; Dove, A.P. Selective Reactivity of Myrcene for Vat Photopolymerization 3D Printing and Postfabrication Surface Modification. *Biomacromolecules* **2020**, *21*, 163–170, doi:10.1021/acs.biomac.9b01125.

84. Gandini, A.; Belgacem, M.N. Furans. *Handb. Thermoset Plast.* **2014**, 93–110, doi:10.1016/B978-1-4557-3107-7.00005-1.

85. Gandini, A.; Silvestre, A.J.D.; Neto, C.P.; Sousa, A.F.; Gomes, M. The furan counterpart of poly(ethylene terephthalate): An alternative material based on renewable resources. *J. Polym. Sci. Part A Polym. Chem.* **2009**, *47*, 295–298, doi:https://doi.org/10.1002/pola.23130.

86. Codou, A.; Guigo, N.; van Berkel, J.; de Jong, E.; Sbirrazzuoli, N. Non-isothermal Crystallization Kinetics of Biobased Poly(ethylene 2,5-furandicarboxylate) Synthesized via the Direct Esterification Process. *Macromol. Chem. Phys.* **2014**, *215*, 2065–2074, doi:https://doi.org/10.1002/macp.201400316.

87. Sousa, A.F.; Patrício, R.; Terzopoulou, Z.; Bikiaris, D.N.; Stern, T.; Wenger, J.; Loos, K.; Lotti, N.; Siracusa, V.; Szymczyk, A.; et al. Recommendations for replacing PET on packaging, fiber, and film materials with biobased counterparts. *Green Chem.* **2021**, *23*, 8795–8820, doi:10.1039/d1gc02082j.

88. de Jong, E.; Dam, M.A.; Sipos, L.; Gruter, G.-J.M. Furandicarboxylic Acid (FDCA), A Versatile Building Block for a Very Interesting Class of Polyesters. In *Biobased Monomers, Polymers, and Materials*; ACS Symposium Series; American Chemical Society, 2012; Vol. 1105, p. 1 ISBN 9780841227675.

89. Mordor Intelligence Research & Advisory Epoxy Resin Market Size & Share Analysis - Growth Trends & Forecasts (2023 - 2028) Available online: https://www.mordorintelligence.com/industry-reports/global-epoxy-resin-market-industry (accessed on Dec 14, 2023).

90. Chemanalyst Decode the future of Epoxy resin Available online:

https://www.chemanalyst.com/industry-report/epoxy-resin-market-597 (accessed on Dec 14, 2023).

91. Gandini, A.; Belgacem, M.N. Furans in polymer chemistry. *Prog. Polym. Sci.* **1997**, *22*, 1203–1379, doi:https://doi.org/10.1016/S0079-6700(97)00004-X.

92. Gandini, A.; M. Lacerda, T. Furan Polymers: State of the Art and Perspectives. *Macromol. Mater. Eng.* **2022**, *307*, 2100902, doi:https://doi.org/10.1002/mame.202100902.

93. Nakagawa, Y.; Tamura, M.; Tomishige, K. Catalytic Reduction of Biomass-Derived Furanic Compounds with Hydrogen. *ACS Catal.* **2013**, *3*, 2655–2668, doi:10.1021/cs400616p.

94. Richel, A.; Maireles-Torres, P.; Len, C. Recent advances in continuous reduction of furfural to added value chemicals. *Curr. Opin. Green Sustain. Chem.* **2022**, *37*, 100655, doi:https://doi.org/10.1016/j.cogsc.2022.100655.

95. Gandini, A. Furans as offspring of sugars and polysaccharides and progenitors of a family of remarkable polymers: A review of recent progress. *Polym. Chem.* **2010**, *1*, 245–251, doi:10.1039/b9py00233b.

96. Román-Leshkov, Y.; Chheda, J.N.; Dumesic, J.A. Phase modifiers promote efficient production of hydroxymethylfurfural from fructose. *Science (80-.).* **2006**, *312*, 1933–1937.

97. Zhao, H.; Holladay, J.E.; Brown, H.; Zhang, Z.C. Metal chlorides in ionic liquid solvents convert sugars to 5-hydroxymethylfurfural. *Science (80-.).* **2007**, *316*, 1597–1600.

98. Iroegbu, A.O.; Sadiku, E.R.; Ray, S.S.; Hamam, Y. Sustainable Chemicals: A Brief Survey of the Furans. *Chem. Africa* **2020**, *3*, 481–496, doi:10.1007/s42250-020-00123-w.

99. Cousin, E.; Namhaed, K.; Pérès, Y.; Cognet, P.; Delmas, M.; Hermansyah, H.; Gozan, M.; Alaba, P.A.; Aroua, M.K. Towards efficient and greener processes for furfural production from biomass: A review of the recent trends. *Sci. Total Environ.* **2022**, *847*, 157599, doi:https://doi.org/10.1016/j.scitotenv.2022.157599.

100. Corma, A.; Iborra, S.; Velty, A. Chemical Routes for the Transformation of Biomass into Chemicals. *Chem. Rev.* **2007**, *107*, 2411–2502, doi:10.1021/cr050989d.

101. Lems, E.M.; Winklehner, S.; Hansmann, C.; Gindl-Altmutter, W.; Veigel, S.

Reinforcing effect of poly(furfuryl alcohol) in cellulose-based porous materials. *Cellulose* **2019**, *6*, doi:10.1007/s10570-019-02348-6.

102. Mishra, D.K.; Kumar, S.; Shukla, R.S. Chapter 12 - Furfuryl alcohol—a promising platform chemical. In *Biomass, Biofuels, Biochemicals*; Saravanamurugan, S., Pandey, A., Li, H., Riisager Biofuels, Biochemicals, A.B.T.-B., Eds.; Elsevier, 2020; pp. 323–353 ISBN 978-0-444-64307-0.

103. Marefat Seyedlar, R.; Imani, M.; Mirabedini, S.M. Bio-based furan coatings: adhesion, mechanical and thermal properties. *Polym. Bull.* **2021**, *78*, 577–599, doi:10.1007/s00289-020-03124-4.

104. Guigo, N.; Mija, A.; Vincent, L.; Sbirrazzuoli, N. Eco-friendly composite resins based on renewable biomass resources: Polyfurfuryl alcohol/lignin thermosets. *Eur. Polym. J.* **2010**, *46*, 1016–1023, doi:https://doi.org/10.1016/j.eurpolymj.2010.02.010.

105. Iroegbu, A.O.; Hlangothi, S.P. Furfuryl Alcohol a Versatile, Eco-Sustainable Compound in Perspective. *Chem. Africa* **2019**, *2*, 223–239, doi:10.1007/s42250-018-00036-9.

106. Eerhart, A.; Faaij, A.P.C.; Patel, M.K. Replacing fossil based PET with biobased PEF; process analysis, energy and GHG balance. *Energy Environ. Sci.* **2012**, *5*, 6407–6422.

107. Haas, V.; Wenger, J.; Ranacher, L.; Guigo, N.; Sousa, A.F.; Stern, T. Developing future visions for bio-plastics substituting PET – A backcasting approach. *Sustain. Prod. Consum.* **2022**, *31*, 370–383, doi:https://doi.org/10.1016/j.spc.2022.02.019.

108. Marotta, A.; Faggio, N.; Ambrogi, V.; Cerruti, P.; Gentile, G.; Mija, A. Curing Behavior and Properties of Sustainable Furan-Based Epoxy/Anhydride Resins. *Biomacromolecules* **2019**, *20*, 3831–3841, doi:10.1021/acs.biomac.9b00919.

109. Marotta, A.; Faggio, N.; Ambrogi, V.; Mija, A.; Gentile, G.; Cerruti, P. Biobased furan-based epoxy/TiO2 nanocomposites for the preparation of coatings with improved chemical resistance. *Chem. Eng. J.* **2021**, *406*, 127107, doi:https://doi.org/10.1016/j.cej.2020.127107.

110. Liu, J.; Wang, S.; Peng, Y.; Zhu, J.; Zhao, W.; Liu, X. Advances in sustainable thermosetting resins: From renewable feedstock to high performance and recyclability. *Prog. Polym. Sci.* **2021**, *113*, 101353, doi:10.1016/j.progpolymsci.2020.101353.

111. Cho, J.K.; Lee, J.-S.; Jeong, J.; Kim, B.; Kim, B.; Kim, S.; Shin, S.; Kim, H.-J.; Lee, S.-H. Synthesis of carbohydrate biomass-based furanic compounds bearing epoxide end group(s) and evaluation of their feasibility as adhesives. *J. Adhes. Sci. Technol.* **2013**, *27*, 2127–2138, doi:10.1080/01694243.2012.697700.

112. Pezzana, L.; Melilli, G.; Nathanaël, G.; Sbirrazzuoli, N.; Sangermano, M. Cationic UV Curing of Bioderived Epoxy Furan-Based Coatings: Tailoring the Final Properties by In Situ Formation of Hybrid Network and Addition of Monofunctional Monomer. *ACS Sustain. Chem. Eng.* **2021**, doi:10.1021/acssuschemeng.1c06939.

113. Pezzana, L.; Melilli, G.; Guigo, N.; Sbirrazzuoli, N.; Sangermano, M. Cross-Linking of Biobased Monofunctional Furan Epoxy Monomer by Two Steps Process, UV Irradiation and Thermal Treatment. *Macromol. Chem. Phys.* **2022**, *n/a*, 2200012, doi:https://doi.org/10.1002/macp.202200012.

114. Pezzana, L.; Wolff, R.; Melilli, G.; Guigo, N.; Sbirrazzuoli, N.; Stampfl, J.; Liska, R.; Sangermano, M. Hot-lithography 3D printing of biobased epoxy resins. *Polymer (Guildf).* **2022**, *254*, 125097, doi:https://doi.org/10.1016/j.polymer.2022.125097.

115. Ye, J.; Ma, S.; Wang, B.; Chen, Q.; Huang, K.; Xu, X.; Li, Q.; Wang, S.; Lu, N.; Zhu, J. High-performance bio-based epoxies from ferulic acid and furfuryl alcohol: synthesis and properties. *Green Chem.* **2021**, *23*, 1772–1781, doi:10.1039/D0GC03946B.

116. Gorsche, C.; Harikrishna, R.; Baudis, S.; Knaack, P.; Husar, B.; Laeuger, J.; Hoffmann, H.; Liska, R. Real Time-NIR/MIR-Photorheology: A Versatile Tool for the in Situ Characterization of Photopolymerization Reactions. *Anal. Chem.* **2017**, *89*, 4958–4968, doi:10.1021/acs.analchem.7b00272.

117. Murayama, T.; Bell, J.P. Relation between the network structure and dynamic mechanical properties of a typical amine-cured epoxy polymer. *J. Polym. Sci. Part A-2 Polym. Phys.* **1970**, *8*, 437–445, doi:https://doi.org/10.1002/pol.1970.160080309.

118. Shimbo, M.; Nishitani, N.; Takahama, T. Mechanical properties of acid-cured epoxide resins with different network structures. *J. Appl. Polym. Sci.* **1984**, *29*, 1709–1721, doi:https://doi.org/10.1002/app.1984.070290524.

119. Çavuşoğlu, K.; Yalçin, E. Spectral shift supported epichlorohydrin toxicity and the protective role of sage. *Environ. Sci. Pollut. Res.* **2023**, *30*, 1374–1385.

120. Xin, J.; Li, M.; Li, R.; Wolcott, M.P.; Zhang, J. Green Epoxy Resin System Based on Lignin and Tung Oil and Its Application in Epoxy Asphalt. *ACS Sustain. Chem. Eng.* **2016**, *4*, 2754–2761, doi:10.1021/acssuschemeng.6b00256.

121. Eid, N.; Ameduri, B.; Boutevin, B. Synthesis and Properties of Furan Derivatives for Epoxy Resins. *ACS Sustain. Chem. Eng.* **2021**, *9*, 8018–8031, doi:10.1021/acssuschemeng.0c09313.

122. Caillol, S.; Boutevin, B.; Auvergne, R. Eugenol, a developing asset in biobased epoxy resins. *Polymer (Guildf).* **2021**, *223*, doi:10.1016/j.polymer.2021.123663.

123. Sternberg, J.; Sequerth, O.; Pilla, S. Green chemistry design in polymers derived from lignin: review and perspective. *Prog. Polym. Sci.* **2021**, *113*, 101344, doi:https://doi.org/10.1016/j.progpolymsci.2020.101344.

124. Chen, X.; Chen, S.; Xu, Z.; Zhang, J.; Miao, M.; Zhang, D. Degradable and recyclable bio-based thermoset epoxy resins. *Green Chem.* **2020**, *22*, 4187–4198, doi:10.1039/d0gc01250e.

125. Stamm, A.; Tengdelius, M.; Schmidt, B.; Engström, J.; Syrén, P.O.; Fogelström, L.; Malmström, E. Chemo-enzymatic pathways toward pinene-based renewable materials. *Green Chem.* **2019**, *21*, 2720–2731, doi:10.1039/C9GC00718K.

126. Grigoropoulou, G.; Clark, J.H.; Elings, J.A. Recent developments on the epoxidation of alkenes using hydrogen peroxide as an oxidant. *Green Chem.* **2003**, *5*, 1–7.

127. Noè, C.; Malburet, S.; Bouvet-Marchand, A.; Graillot, A.; Loubat, C.; Sangermano, M. Cationic photopolymerization of bio-renewable epoxidized monomers. *Prog. Org. Coatings* **2019**, *133*, 131–138, doi:https://doi.org/10.1016/j.porgcoat.2019.03.054.

128. Liu, F.; Liu, A.; Tao, W.; Yang, Y. Preparation of UV curable organic/inorganic hybrid coatings-a review. *Prog. Org. Coatings* **2020**, *145*, 105685, doi:https://doi.org/10.1016/j.porgcoat.2020.105685.

129. Malucelli, G.; Priola, A.; Sangermano, M.; Amerio, E.; Zini, E.; Fabbri, E. Hybrid nanocomposites containing silica and PEO segments: preparation through dual-curing process and characterization. *Polymer (Guildf).* **2005**, *46*, 2872–2879, doi:https://doi.org/10.1016/j.polymer.2005.02.045.

130. Amerio, E.; Malucelli, G.; Sangermano, M.; Priola, A. Nanostructured

hybrid materials obtained by UV curing and sol-gel processes involving alkoxysilane groups: *e-Polymers* **2009**, *9*, 59, doi:doi:10.1515/epoly.2009.9.1.727.

131. Sangermano, M.; Amerio, E.; Epicoco, P.; Priola, A.; Rizza, G.; Malucelli, G. Preparation and Characterization of Hybrid Nanocomposite Coatings by Cationic UV-Curing and the Sol-Gel Process of a Vinyl Ether Based System. *Macromol. Mater. Eng.* **2007**, *292*, 634–640, doi:10.1002/mame.200600507.

132. Sangermano, M.; Malucelli, G.; Amerio, E.; Priola, A.; Billi, E.; Rizza, G. Photopolymerization of epoxy coatings containing silica nanoparticles. *Prog. Org. Coatings* **2005**, *54*, 134–138, doi:https://doi.org/10.1016/j.porgcoat.2005.05.004.

133. Guigo, N.; Mija, A.; Vincent, L.; Sbirrazzuoli, N. Chemorheological analysis and model-free kinetics of acid catalysed furfuryl alcohol polymerization. *Phys. Chem. Chem. Phys.* **2007**, *9*, 5359–5366, doi:10.1039/b707950h.

134. Tondi, G.; Cefarin, N.; Sepperer, T.; D’Amico, F.; Berger, R.J.F.; Musso, M.; Birarda, G.; Reyer, A.; Schnabel, T.; Vaccari, L. Understanding the polymerization of polyfurfuryl alcohol: Ring opening and diels-alder reactions. *Polymers (Basel).* **2019**, *11*, 1–15, doi:10.3390/polym11122126.

135. D’Amico, F.; Musso, M.E.; Berger, R.J.F.; Cefarin, N.; Birarda, G.; Tondi, G.; Bertoldo Menezes, D.; Reyer, A.; Scarabattoli, L.; Sepperer, T.; et al. Chemical constitution of polyfurfuryl alcohol investigated by FTIR and Resonant Raman spectroscopy. *Spectrochim. Acta Part A Mol. Biomol. Spectrosc.* **2021**, *262*, 120090, doi:https://doi.org/10.1016/j.saa.2021.120090.

136. Falco, G.; Guigo, N.; Vincent, L.; Sbirrazzuoli, N. Opening Furan for Tailoring Properties of Bio-based Poly(Furfuryl Alcohol) Thermoset. *ChemSusChem* **2018**, *11*, 1805–1812, doi:https://doi.org/10.1002/cssc.201800620.

137. Brännström, S.; Johansson, M.; Malmström, E. Enzymatically Synthesized Vinyl Ether-Disulfide Monomer Enabling an Orthogonal Combination of Free Radical and Cationic Chemistry toward Sustainable Functional Networks. *Biomacromolecules* **2019**, *20*, 1308–1316, doi:10.1021/acs.biomac.8b01710.

138. Yagci, Y. Photoinitiated cationic polymerization of unconventional monomers. *Macromol. Symp.* **2006**, *240*, 93–101, doi:10.1002/masy.200650812.

139. Dutta, S.; Yu, I.K.M.; Tsang, D.C.W.; Ng, Y.H.; Ok, Y.S.; Sherwood, J.; Clark, J.H. Green synthesis of gamma-valerolactone (GVL) through hydrogenation of biomass-derived levulinic acid using non-noble metal catalysts: A critical review. *Chem. Eng. J.* **2019**, *372*, 992–1006, doi:https://doi.org/10.1016/j.cej.2019.04.199.

140. Zhu, R.; Chatzidimitriou, A.; Liu, B.; Kerwood, D.J.; Bond, J.Q. Understanding the Origin of Maleic Anhydride Selectivity during the Oxidative Scission of Levulinic Acid. *ACS Catal.* **2020**, *10*, 1555–1565, doi:10.1021/acscatal.9b04289.

141. Dell'Acqua, A.; Stadler, B.M.; Kirchhecker, S.; Tin, S.; de Vries, J.G. Scalable synthesis and polymerisation of a β-angelica lactone derived monomer. *Green Chem.* **2020**, *22*, 5267–5273, doi:10.1039/D0GC00338G.

142. Ligon, S.C.; Liska, R.; Stampfl, J.; Gurr, M.; Mülhaupt, R. Polymers for 3D Printing and Customized Additive Manufacturing. *Chem. Rev.* **2017**, *117*, 10212–10290, doi:10.1021/acs.chemrev.7b00074.

143. Wohlers, T.T.; (Firm), W.A.; Campbell, I.; Diegel, O.; Huff, R.; Kowen, J.; Mostow, N.; Staff, W.A. (Firm) *Wohlers Report 2021: 3D Printing and Additive Manufacturing Global State of the Industry*; Wohlers Associates, Incorporated, 2021; ISBN 9780991333271.

144. Shahbazi, M.; Jäger, H. Current Status in the Utilization of Biobased Polymers for 3D Printing Process: A Systematic Review of the Materials, Processes, and Challenges. *ACS Appl. Bio Mater.* **2021**, *4*, 325–369, doi:10.1021/acsabm.0c01379.

145. MacDonald, E.; Salas, R.; Espalin, D.; Perez, M.; Aguilera, E.; Muse, D.; Wicker, R.B. 3D printing for the rapid prototyping of structural electronics. *IEEE Access* **2014**, *2*, 234–242, doi:10.1109/ACCESS.2014.2311810.

146. Bagheri, A.; Jin, J. Photopolymerization in 3D printing. *ACS Appl. Polym. Mater.* **2019**, *1*, 593–611.

147. Sutton, J.T.; Rajan, K.; Harper, D.P.; Chmely, S.C. Lignin-Containing Photoactive Resins for 3D Printing by Stereolithography. *ACS Appl. Mater. Interfaces* **2018**, *10*, 36456–36463, doi:10.1021/acsami.8b13031.

148. Liu, Z.; Knetzer, D.A.; Wang, J.; Chu, F.; Lu, C.; Calvert, P.D. 3D printing acrylated epoxidized soybean oil reinforced with functionalized cellulose by UV curing. *J. Appl. Polym. Sci.* **2022**, *139*, doi:10.1002/app.51561.

149. Noè, C.; Cosola, A.; Tonda-Turo, C.; Sesana, R.; Delprete, C.; Chiappone,

A.; Hakkarainen, M.; Sangermano, M. DLP-printable fully biobased soybean oil composites. *Polymer (Guildf).* **2022**.

150. Stampfl, J.; Baudis, S.; Heller, C.; Liska, R.; Neumeister, A.; Kling, R.; Ostendorf, A.; Spitzbart, M. Photopolymers with tunable mechanical properties processed by laser-based high-resolution stereolithography. *J. Micromechanics Microengineering* **2008**, *18*, doi:10.1088/0960-1317/18/12/125014.

151. Dall'Argine, C.; Hochwallner, A.; Klikovits, N.; Liska, R.; Stampf, J.; Sangermano, M. Hot-Lithography SLA-3D Printing of Epoxy Resin. *Macromol. Mater. Eng.* **2020**, *305*, 1–6, doi:10.1002/mame.202000325.

152. Klikovits, N.; Sinawehl, L.; Knaack, P.; Koch, T.; Stampfl, J.; Gorsche, C.; Liska, R. UV-Induced Cationic Ring-Opening Polymerization of 2-Oxazolines for Hot Lithography. *ACS Macro Lett.* **2020**, *9*, 546–551, doi:10.1021/acsmacrolett.0c00055.

153. Isikgor, F.H.; Becer, C.R. Lignocellulosic biomass: a sustainable platform for the production of bio-based chemicals and polymers. *Polym. Chem.* **2015**, *6*, 4497–4559, doi:10.1039/c5py00263j.

154. Girdis, J.; Gaudion, L.; Proust, G.; Löschke, S.; Dong, A. Rethinking Timber: Investigation into the Use of Waste Macadamia Nut Shells for Additive Manufacturing. *JOM* **2016**, *69*, doi:10.1007/s11837-016-2213-6.

155. Crivello, J. V.; Falk, B.; Zonca, M.R. Photoinduced Cationic Ring-Opening Frontal Polymerizations of Oxetanes and Oxiranes. *J. Polym. Sci. Part A Polym. Chem.* **2004**, *42*, 1630–1646, doi:10.1002/pola.20012.

156. Falk, B.; Zonca, M.R.; Crivello, J. V. Photoactivated cationic frontal polymerization. *Macromol. Symp.* **2005**, *226*, 97–108, doi:10.1002/masy.200550810.

157. Petko, F.; Świeży, A.; Ortyl, J. Photoinitiating systems and kinetics of frontal photopolymerization processes-the prospects for efficient preparation of composites and thick 3D structures. *Polym. Chem.* **2021**, *12*, 4593–4612, doi:10.1039/d1py00596k.

158. Crivello, J. V; Liu, S. Free Radical Induced Acceleration of Cationic Photopolymerization. *Chem. Mater.* **1998**, *10*, 3724–3731, doi:10.1021/cm980494n.

159. Wolff, R.; Ehrmann, K.; Knaack, P.; Seidler, K.; Gorsche, C.; Koch, T.; Stampfl, J.; Liska, R. Photo-chemically induced polycondensation of a pure

phenolic resin for additive manufacturing. *Polym. Chem.* **2022**, doi:10.1039/d1py01665b.

160. Peer, G.; Dorfinger, P.; Koch, T.; Stampfl, J.; Gorsche, C.; Liska, R. Photopolymerization of Cyclopolymerizable Monomers and Their Application in Hot Lithography. *Macromolecules* **2018**, *51*, 9344–9353, doi:10.1021/acs.macromol.8b01991.

161. Ligon-Auer, S.C.; Schwentenwein, M.; Gorsche, C.; Stampfl, J.; Liska, R. Toughening of photo-curable polymer networks: A review. *Polym. Chem.* **2016**, *7*, 257–286, doi:10.1039/c5py01631b.

162. Sun, Z.; Fridrich, B.; De Santi, A.; Elangovan, S.; Barta, K. Bright Side of Lignin Depolymerization: Toward New Platform Chemicals. *Chem. Rev.* **2018**, *118*, 614–678, doi:10.1021/acs.chemrev.7b00588.

163. Gandini, A.; Lacerda, T.M. From monomers to polymers from renewable resources: Recent advances. *Prog. Polym. Sci.* **2015**, *48*, 1–39, doi:10.1016/j.progpolymsci.2014.11.002.

164. Haq, I.; Mazumder, P.; Kalamdhad, A.S. Recent advances in removal of lignin from paper industry wastewater and its industrial applications – A review. *Bioresour. Technol.* **2020**, *312*, 123636, doi:10.1016/j.biortech.2020.123636.

165. Belgacem, M.N.; Gandini, A. *Monomers, polymers and composites from renewable resources*; Elsevier, 2011; ISBN 0080560512.

166. Liao, J.J.; Latif, N.H.A.; Trache, D.; Brosse, N.; Hussin, M.H. Current advancement on the isolation, characterization and application of lignin. *Int. J. Biol. Macromol.* **2020**, *162*, 985–1024, doi:10.1016/j.ijbiomac.2020.06.168.

167. Fache, M.; Boutevin, B.; Caillol, S. Vanillin Production from Lignin and Its Use as a Renewable Chemical. *ACS Sustain. Chem. Eng.* **2016**, *4*, 35–46, doi:10.1021/acssuschemeng.5b01344.

168. Llevot, A.; Grau, E.; Carlotti, S.; Grelier, S.; Cramail, H. From Lignin-derived Aromatic Compounds to Novel Biobased Polymers. *Macromol. Rapid Commun.* **2016**, *37*, 9–28, doi:10.1002/marc.201500474.

169. Cao, L.; Yu, I.K.M.; Liu, Y.; Ruan, X.; Tsang, D.C.W.; Hunt, A.J.; Ok, Y.S.; Song, H.; Zhang, S. Lignin valorization for the production of renewable chemicals: State-of-the-art review and future prospects. *Bioresour. Technol.* **2018**, *269*, 465–475, doi:10.1016/j.biortech.2018.08.065.

170. de Oliveira, D.M.; Finger-Teixeira, A.; Rodrigues Mota, T.; Salvador, V.H.; Moreira-Vilar, F.C.; Correa Molinari, H.B.; Craig Mitchell, R.A.; Marchiosi, R.; Ferrarese-Filho, O.; dos Santos, W. Ferulic acid: a key component in grass lignocellulose recalcitrance to hydrolysis. *Plant Biotechnol. J.* **2015**, *13*, 1224–1232, doi:10.1111/pbi.12292.

171. Kumar, N.; Pruthi, V. Potential applications of ferulic acid from natural sources. *Biotechnol. Reports* **2014**, *4*, 86–93, doi:10.1016/j.btre.2014.09.002.

172. Mathew, S.; Abraham, T.E. Ferulic acid: An antioxidant found naturally in plant cell walls and feruloyl esterases involved in its release and their applications. *Crit. Rev. Biotechnol.* **2004**, *24*, 59–83, doi:10.1080/07388550490491467.

173. Bento-Silva, A.; Vaz Patto, M.C.; do Rosário Bronze, M. Relevance, structure and analysis of ferulic acid in maize cell walls. *Food Chem.* **2018**, *246*, 360–378, doi:10.1016/j.foodchem.2017.11.012.

174. Uraji, M.; Kimura, M.; Inoue, Y.; Kawakami, K.; Kumagai, Y.; Harazono, K.; Hatanaka, T. Enzymatic production of ferulic acid from defatted rice bran by using a combination of bacterial enzymes. *Appl. Biochem. Biotechnol.* **2013**, *171*, 1085–1093, doi:10.1007/s12010-013-0190-6.

175. da Silva Araujo, E.; da Silva Mota, G.; Lorenço, M.S.; Zidanes, U.L.; da Silva, L.R.; Silva, E.P.; Mori, F.A.; Ferreira, V.R.F.; das Graças Cardoso, M. Characterisation and valorisation of the bark of Myrcia eximia DC. Trees from the Amazon rainforest as a source of phenolic compounds. *Holzforschung* **2020**, *74*, 989–998, doi:10.1515/hf-2019-0294.

176. Williamson, J.J.; Bahrin, N.; Hardiman, E.M.; Bugg, T.D.H. Production of Substituted Styrene Bioproducts from Lignin and Lignocellulose Using Engineered Pseudomonas putida KT2440. *Biotechnol. J.* **2020**, *15*, 1–8, doi:10.1002/biot.201900571.

177. Fang, D.; Xue, D.; Liu, X.; Cao, L.; Zhang, J.; Gong, C. Concurrent production of ferulic acid and glucose from wheat bran by catalysis of a putative bifunctional enzyme. *Bioresour. Technol.* **2023**, *369*, 128393, doi:https://doi.org/10.1016/j.biortech.2022.128393.

178. Zhao, C.H.; Zhang, R.K.; Qiao, B.; Li, B.Z.; Yuan, Y.J. Engineering budding yeast for the production of coumarins from lignin. *Biochem. Eng. J.* **2020**, *160*, 107634, doi:10.1016/j.bej.2020.107634.

179. Sibhatu, H.K.; Anuradha Jabasingh, S.; Yimam, A.; Ahmed, S. Ferulic acid

production from brewery spent grains, an agro-industrial waste. *Lwt* **2021**, *135*, 110009, doi:10.1016/j.lwt.2020.110009.

180. Fonseca, A.C.; Lima, M.S.; Sousa, A.F.; Silvestre, A.J.; Coelho, J.F.J.; Serra, A.C. Cinnamic acid derivatives as promising building blocks for advanced polymers: Synthesis, properties and applications. *Polym. Chem.* **2019**, *10*, 1696–1723, doi:10.1039/c9py00121b.

181. Alexakis, A.E.; Ayyachi, T.; Mousa, M.; Olsén, P.; Malmström, E. 2-Methoxy-4-Vinylphenol as a Biobased Monomer Precursor for Thermoplastics and Thermoset Polymers. *Polymers (Basel).* 2023, *15*.

182. Rosazza, J.P.N.; Huang, Z.; Dostal, L.; Volm, T.; Rousseau, B. Biocatalytic transformations of ferulic acid: An abundant aromatic natural product. *J. Ind. Microbiol.* **1995**, *15*, 472–479, doi:10.1007/BF01570017.

183. Mialon, L.; Pemba, A.G.; Miller, S.A. Biorenewable polyethylene terephthalate mimics derived from lignin and acetic acid. *Green Chem.* **2010**, *12*, 1704–1706, doi:10.1039/c0gc00150c.

184. Pion, F.; Ducrot, P.H.; Allais, F. Renewable alternating aliphatic-aromatic copolyesters derived from biobased ferulic acid, diols, and diacids: Sustainable polymers with tunable thermal properties. *Macromol. Chem. Phys.* **2014**, *215*, 431–439, doi:10.1002/macp.201300702.

185. Kreye, O.; Tóth, T.; Meier, M.A.R. Copolymers derived from rapeseed derivatives via ADMET and thiol-ene addition. *Eur. Polym. J.* **2011**, *47*, 1804–1816, doi:10.1016/j.eurpolymj.2011.06.012.

186. Ménard, R.; Caillol, S.; Allais, F. Ferulic acid-based renewable esters and amides-containing epoxy thermosets from wheat bran and beetroot pulp: Chemo-enzymatic synthesis and thermo-mechanical properties characterization. *Ind. Crops Prod.* **2017**, *95*, 83–95, doi:10.1016/j.indcrop.2016.10.016.

187. Zhong, L.; Hao, Y.; Zhang, J.; Wei, F.; Li, T.; Miao, M.; Zhang, D. Closed-Loop Recyclable Fully Bio-Based Epoxy Vitrimers from Ferulic Acid-Derived Hyperbranched Epoxy Resin. *Macromolecules* **2022**, *55*, 595–607, doi:10.1021/acs.macromol.1c02247.

188. Stamm, A.; Biundo, A.; Schmidt, B.; Brücher, J.; Lundmark, S.; Olsén, P.; Fogelström, L.; Malmström, E.; Bornscheuer, U.T.; Syrén, P.-O. A Retrobiosynthesis-Based Route to Generate Pinene-Derived Polyesters. *ChemBioChem* **2019**, *20*, 1664–1671, doi:https://doi.org/10.1002/cbic.201900046.

189. Stamm, A.; Öhlin, J.; Mosbech, C.; Olsén, P.; Guo, B.; Söderberg, E.; Biundo, A.; Fogelström, L.; Bhattacharyya, S.; Bornscheuer, U.T.; et al. Pinene-Based Oxidative Synthetic Toolbox for Scalable Polyester Synthesis. *JACS Au* **2021**, *1*, 1949–1960, doi:10.1021/jacsau.1c00312.

190. Della Monica, F.; Kleij, A.W. From terpenes to sustainable and functional polymers. *Polym. Chem.* **2020**, *11*, 5109–5127, doi:10.1039/D0PY00817F.

191. Rose, M.; Palkovits, R. Isosorbide as a renewable platform chemical for versatile applications-quo vadis? *ChemSusChem* **2012**, *5*, 167–176, doi:10.1002/cssc.201100580.

192. Feng, X.; East, A.J.; Hammond, W.B.; Zhang, Y.; Jaffe, M. Overview of advances in sugar-based polymers. *Polym. Adv. Technol.* **2011**, *22*, 139–150, doi:10.1002/pat.1859.

193. Aricò, F. Isosorbide as biobased platform chemical: Recent advances. *Curr. Opin. Green Sustain. Chem.* **2020**, *21*, 82–88, doi:10.1016/j.cogsc.2020.02.002.

194. Hockett, R.C.; Fletcher, H.G.; Sheffield, E.L.; Goepp, R.M.; Soltzberg, S. Hexitol Anhydrides. The Structure of Isosorbide, a Crystalline Dianhydrosorbitol. *J. Am. Chem. Soc.* **1946**, *68*, 927–930, doi:10.1021/ja01210a003.

195. Fenouillot, F.; Rousseau, A.; Colomines, G.; Saint-Loup, R.; Pascault, J.P. Polymers from renewable 1,4:3,6-dianhydrohexitols (isosorbide, isomannide and isoidide): A review. *Prog. Polym. Sci.* **2010**, *35*, 578–622, doi:10.1016/j.progpolymsci.2009.10.001.

196. Flèche, G.; Huchette, M. Isosorbide. Preparation, Properties and Chemistry. *Starch - Stärke* **1986**, *38*, 26–30, doi:https://doi.org/10.1002/star.19860380107.

197. Li, C.; Dai, J.; Liu, X.; Jiang, Y.; Ma, S.; Zhu, J. Green Synthesis of a Bio-Based Epoxy Curing Agent from Isosorbide in Aqueous Condition and Shape Memory Properties Investigation of the Cured Resin. *Macromol. Chem. Phys.* **2016**, *217*, 1439–1447, doi:10.1002/macp.201600055.

198. Cho, J.-E.; Sim, D.-S.; Kim, Y.-W.; Lim, J.; Jeong, N.-H.; Kang, H.-C. Selective Syntheses and Properties of Anionic Surfactants Derived from Isosorbide. *J. Surfactants Deterg.* **2018**, *21*, 817–826, doi:https://doi.org/10.1002/jsde.12182.

199. Janvier, M.; Moebs-Sanchez, S.; Popowycz, F. Bio-Based Amides from

Renewable Isosorbide by a Direct and Atom-Economic Boric Acid Amidation Methodology. *European J. Org. Chem.* **2016**, *2016*, 2308–2318, doi:10.1002/ejoc.201600186.

200. Ma, S.; Webster, D.C.; Jabeen, F. Hard and Flexible, Degradable Thermosets from Renewable Bioresources with the Assistance of Water and Ethanol. *Macromolecules* **2016**, *49*, 3780–3788, doi:10.1021/acs.macromol.6b00594.

201. Lammel-Lindemann, J.; Dourado, I.A.; Shanklin, J.; Rodriguez, C.A.; Catalani, L.H.; Dean, D. Photocrosslinking-based 3D printing of unsaturated polyesters from isosorbide: A new material for resorbable medical devices. *Bioprinting* **2020**, *18*, e00062, doi:10.1016/j.bprint.2019.e00062.

202. Noordover, B.A.J.; Heise, A.; Malanowksi, P.; Senatore, D.; Mak, M.; Molhoek, L.; Duchateau, R.; Koning, C.E.; van Benthem, R.A.T.M. Biobased step-growth polymers in powder coating applications. *Prog. Org. Coatings* **2009**, *65*, 187–196, doi:10.1016/j.porgcoat.2008.11.001.

203. Gadgeel, A.A.; Mhaske, S.T. Synthesis and characterization of UV curable polyurethane acrylate derived from α-Ketoglutaric acid and isosorbide. *Prog. Org. Coatings* **2021**, *150*, 105983, doi:10.1016/j.porgcoat.2020.105983.

204. Gonçalves, F.A.M.M.; Santos, M.; Cernadas, T.; Ferreira, P.; Alves, P. Advances in the development of biobased epoxy resins: insight into more sustainable materials and future applications. *Int. Mater. Rev.* **2022**, *67*, 119–149.

205. Reddy, M.M.; Vivekanandhan, S.; Misra, M.; Bhatia, S.K.; Mohanty, A.K. Biobased plastics and bionanocomposites: Current status and future opportunities. *Prog. Polym. Sci.* **2013**, *38*, 1653–1689, doi:https://doi.org/10.1016/j.progpolymsci.2013.05.006.

206. Cortat, L.O.; Zanini, N.C.; Barbosa, R.F.S.; de Souza, A.G.; Rosa, D.S.; Mulinari, D.R. A sustainable perspective for macadamia nutshell residues revalorization by green composites development. *J. Polym. Environ.* **2021**, *29*, 3210–3226.

207. Lohar, D. V; Nikalje, A.M.; Damle, P.G. Development and testing of hybrid green polymer composite (HGPC) filaments of PLA reinforced with waste bio fillers. *Mater. Today Proc.* **2022**, *62*, 818–824.

208. Moodley, R.; Kindness, A.; Jonnalagadda, S.B. Chemical composition of edible Macadamia nuts (Macadamia integrifolia) and impact of soil quality. *J. Environ. Sci. Heal. Part A* **2007**, *42*, 2097–2104,

doi:10.1080/10934520701627074.

209. Wall, M.M.; Gentry, T.S. Carbohydrate composition and color development during drying and roasting of macadamia nuts (Macadamia integrifolia). *LWT - Food Sci. Technol.* **2007**, *40*, 587–593, doi:https://doi.org/10.1016/j.lwt.2006.03.015.

210. Pakade, V.E.; Ntuli, T.D.; Ofomaja, A.E. Biosorption of hexavalent chromium from aqueous solutions by Macadamia nutshell powder. *Appl. Water Sci.* **2017**, *7*, 3015–3030, doi:10.1007/s13201-016-0412-5.

211. Landucci, L.; Smith, R.A.; Liu, S.; Karlen, S.D.; Ralph, J. Eudicot nutshells: Cell-wall composition and biofuel feedstock potential. *Energy and Fuels* **2020**, *34*, 16274–16283, doi:10.1021/acs.energyfuels.0c03131.

212. Miao, S.; Wang, P.; Su, Z.; Zhang, S. Vegetable-oil-based polymers as future polymeric biomaterials. *Acta Biomater.* **2014**, *10*, 1692–1704, doi:https://doi.org/10.1016/j.actbio.2013.08.040.

213. Lligadas, G.; Ronda, J.C.; Galià, M.; Cádiz, V. Renewable polymeric materials from vegetable oils: a perspective. *Mater. Today* **2013**, *16*, 337–343, doi:https://doi.org/10.1016/j.mattod.2013.08.016.

214. Montero de Espinosa, L.; Meier, M.A.R. Plant oils: The perfect renewable resource for polymer science?! *Eur. Polym. J.* **2011**, *47*, 837–852, doi:https://doi.org/10.1016/j.eurpolymj.2010.11.020.

215. Marriam, F.; Irshad, A.; Umer, I.; Asghar, M.A.; Atif, M. Vegetable oils as bio-based precursors for epoxies. *Sustain. Chem. Pharm.* **2023**, *31*, 100935, doi:https://doi.org/10.1016/j.scp.2022.100935.

216. Crivello, J. V; Narayan, R. Epoxidized Triglycerides as Renewable Monomers in Photoinitiated Cationic Polymerization. **1992**, 692–699.

217. Crivello, J. V; Narayan, R.; Bratslavsky, S.A.; Yang, B. The synthesis and cationic polymerization of novel monomers from renewable sources. *Macromol. Symp.* **1996**, *107*, 75–83, doi:https://doi.org/10.1002/masy.19961070109.

218. Wan Rosli, W.D.; Kumar, R.N.; Mek Zah, S.; Hilmi, M.M. UV radiation curing of epoxidized palm oil–cycloaliphatic diepoxide system induced by cationic photoinitiators for surface coatings. *Eur. Polym. J.* **2003**, *39*, 593–600, doi:https://doi.org/10.1016/S0014-3057(02)00241-0.

219. Noè, C.; Iannucci, L.; Malburet, S.; Graillot, A.; Sangermano, M.; Grassini, S. New UV-Curable Anticorrosion Coatings from Vegetable Oils.

Macromol. Mater. Eng. **2021**, *306*, 1–11, doi:10.1002/mame.202100029.

220. Pezzana, L.; Malmström, E.; Johansson, M.; Casalegno, V.; Sangermano, M. Multiple approaches to exploit ferulic acid bio-based epoxy monomers for green thermosets.

221. Pezzana, L.; Emanuele, A.; Sesana, R.; Delprete, C.; Malmström, E.; Johansson, M.; Sangermano, M. Cationic UV-curing of isosorbide-based epoxy coating reinforced with macadamia nut shell powder. *Prog. Org. Coatings* **2023**, *185*, 107949, doi:https://doi.org/10.1016/j.porgcoat.2023.107949.

222. Pezzana, L.; Wolff, R.; Stampfl, J.; Liska, R.; Sangermano, M. Hot-lithography 3D printing of fully bio-based composites: green vegetable oil epoxy matrix & bio-derived filler powder. *Addit. Manuf.* **2024**.

223. Łukaszczyk, J.; Janicki, B.; Frick, A. Investigation on synthesis and properties of isosorbide based bis-GMA analogue. *J. Mater. Sci. Mater. Med.* **2012**, *23*, 1149–1155, doi:10.1007/s10856-012-4594-6.

224. Hong, J.; Radojčić, D.; Ionescu, M.; Petrović, Z.S.; Eastwood, E. Advanced materials from corn: isosorbide-based epoxy resins. *Polym. Chem.* **2014**, *5*, 5360–5368, doi:10.1039/C4PY00514G.

225. Speier, J.L. The preparation and properties of (hydroxyorgano)-silanes and related compounds. *J. Am. Chem. Soc.* **1952**, *74*, 1003–1010.

226. Członka, S.; Strąkowska, A.; Kairytė, A. Effect of walnut shells and silanized walnut shells on the mechanical and thermal properties of rigid polyurethane foams. *Polym. Test.* **2020**, *87*, 106534.

227. Coatings, R.; Society, C.; Convention, U.S.P. Standard Test Method for Epoxy Content of Epoxy Resins. *Acs* **6789**, *khuj*, 4–7, doi:10.1520/D1652-11R19.2.

228. Criado, J.M.; Málek, J.; Ortega, A. Applicability of the master plots in kinetic analysis of non-isothermal data. *Thermochim. Acta* **1989**, *147*, 377–385, doi:https://doi.org/10.1016/0040-6031(89)85192-5.

229. Kissinger, H.E. Reaction kinetics in differential thermal analysis. *Anal. Chem.* **1957**, *29*, 1702–1706.

230. Yoo, M.J.; Kim, S.H.; Park, S.D.; Lee, W.S.; Sun, J.-W.; Choi, J.-H.; Nahm, S. Investigation of curing kinetics of various cycloaliphatic epoxy resins using dynamic thermal analysis. *Eur. Polym. J.* **2010**, *46*, 1158–1162, doi:https://doi.org/10.1016/j.eurpolymj.2010.02.001.

231. Vyazovkin, S.; Sbirrazzuoli, N. Mechanism and Kinetics of Epoxy−Amine Cure Studied by Differential Scanning Calorimetry. *Macromolecules* **1996**, *29*, 1867–1873, doi:10.1021/ma951162w.

232. Kretzschmar, K.; Hoffmann, K.W. Reaction enthalpies during the curing oe epoxy resins with anhydrides. *Thermochim. Acta* **1985**, *94*, 105–112, doi:https://doi.org/10.1016/0040-6031(85)85250-3.

233. Calventus, Y.; Montserrat, S.; Hutchinson, J.M. Enthalpy relaxation of non-stoichiometric epoxy-amine resins. *Polymer (Guildf).* **2001**, *42*, 7081–7093, doi:https://doi.org/10.1016/S0032-3861(01)00133-1.

234. Lascano, D.; Lerma-Canto, A.; Fombuena, V.; Balart, R.; Montanes, N.; Quiles-Carrillo, L. Kinetic Analysis of the Curing Process of Biobased Epoxy Resin from Epoxidized Linseed Oil by Dynamic Differential Scanning Calorimetry. *Polymers (Basel).* 2021, *13*.

235. Mashouf Roudsari, G.; Mohanty, A.K.; Misra, M. Study of the curing kinetics of epoxy resins with biobased hardener and epoxidized soybean oil. *ACS Sustain. Chem. Eng.* **2014**, *2*, 2111–2116, doi:10.1021/sc500176z.

236. Romano, A.; Roppolo, I.; Giebler, M.; Dietliker, K.; Možina, Š.; Šket, P.; Mühlbacher, I.; Schlögl, S.; Sangermano, M. Stimuli-responsive thiol-epoxy networks with photo-switchable bulk and surface properties. *RSC Adv.* **2018**, *8*, 41904–41914, doi:10.1039/C8RA08937J.

237. Reisinger, D.; Dietliker, K.; Sangermano, M.; Schlögl, S. Streamlined concept towards spatially resolved photoactivation of dynamic transesterification in vitrimeric polymers by applying thermally stable photolatent bases. *Polym. Chem.* **2022**, *13*, 1169–1176, doi:10.1039/D1PY01722E.

238. Fernández-Francos, X.; Konuray, A.-O.; Belmonte, A.; De la Flor, S.; Serra, À.; Ramis, X. Sequential curing of off-stoichiometric thiol–epoxy thermosets with a custom-tailored structure. *Polym. Chem.* **2016**, *7*, 2280–2290, doi:10.1039/C6PY00099A.

239. Konuray, A.O.; Fernández-Francos, X.; Ramis, X. Analysis of the reaction mechanism of the thiol–epoxy addition initiated by nucleophilic tertiary amines. *Polym. Chem.* **2017**, *8*, 5934–5947, doi:10.1039/C7PY01263B.

240. Konuray, A.O.; Fernández-Francos, X.; Ramis, X. Latent curing of epoxy-thiol thermosets. *Polymer (Guildf).* **2017**, *116*, 191–203, doi:https://doi.org/10.1016/j.polymer.2017.03.064.

241. Konuray, O.; Fernández-Francos, X.; De la Flor, S.; Ramis, X.; Serra, À. The Use of Click-Type Reactions in the Preparation of Thermosets. *Polymers (Basel).* 2020, *12*.

242. Pezzana, L.; Mousa, M.; Malmström, E.; Johansson, M.; Sangermano, M. Bio-based monomers for UV-curable coatings: allylation of ferulic acid and investigation of photocured thiol-ene network. *Prog. Org. Coatings* **2021**, *150*, 105986, doi:https://doi.org/10.1016/j.porgcoat.2020.105986.

243. Chen, L.; Zheng, Y.; Meng, X.; Wei, G.; Dietliker, K.; Li, Z. Delayed Thiol-Epoxy Photopolymerization: A General and Effective Strategy to Prepare Thick Composites. *ACS Omega* **2020**, *5*, 15192–15201, doi:10.1021/acsomega.0c01170.

244. Pezzana, L.; Sangermano, M. Fully biobased UV-cured thiol-ene coatings. *Prog. Org. Coatings* **2021**, *157*, 106295.

245. Castell, P.; Galià, M.; Serra, A.; Salla, J.M.; Ramis, X. Study of lanthanide triflates as new curing initiators for DGEBA. *Polymer (Guildf).* **2000**, *41*, 8465–8474, doi:https://doi.org/10.1016/S0032-3861(00)00275-5.

246. Mas, C.; Serra, A.; Mantecón, A.; Salla, J.M.; Ramis, X. Study of Lanthanide Triflates as New Curing Initiators for Cycloaliphatic Epoxy Resins. *Macromol. Chem. Phys.* **2001**, *202*, 2554–2564, doi:https://doi.org/10.1002/1521-3935(20010801)202:12<2554::AID-MACP2554>3.0.CO;2-C.

247. Foix, D.; Ramis, X.; Sangermano, M.; Serra, A. Synthesis of a new hyperbranched-linear-hyperbranched triblock copolymer and its use as a chemical modifier for the cationic photo and thermal curing of epoxy resins. *J. Polym. Sci. Part A Polym. Chem.* **2012**, *50*, 1133–1142, doi:https://doi.org/10.1002/pola.25872.

248. Sbirrazzuoli, N.; Vyazovkin, S. Learning about epoxy cure mechanisms from isoconversional analysis of DSC data. *Thermochim. Acta* **2002**, *388*, 289–298, doi:https://doi.org/10.1016/S0040-6031(02)00053-9.

249. Lee, J.Y.; Choi, H.K.; Shim, M.J.; Kim, S.W. Kinetic studies of an epoxy cure reaction by isothermal DSC analysis. *Thermochim. Acta* **2000**, *343*, 111–117, doi:https://doi.org/10.1016/S0040-6031(99)00303-2.

250. Turani, M.; Baggio, A.; Casalegno, V.; Salvo, M.; Sangermano, M. An Epoxy Adhesive Crosslinked through Radical-Induced Cationic Frontal Polymerization. *Macromol. Mater. Eng.* **2021**, *306*, 2100495, doi:https://doi.org/10.1002/mame.202100495.

251. Crivello, J. V. Effect of temperature on the cationic photopolymerization of epoxides. *J. Macromol. Sci. Part A Pure Appl. Chem.* **2008**, *45*, 591–598, doi:10.1080/10601320802168710.

252. Sharif, M.; Pourabbas, B.; Sangermano, M.; Sadeghi Moghadam, F.; Mohammadi, M.; Roppolo, I.; Fazli, A. The effect of graphene oxide on UV curing kinetics and properties of SU8 nanocomposites. *Polym. Int.* **2017**, *66*, 405–417, doi:https://doi.org/10.1002/pi.5271.

253. Bongiovanni, R.; Turcato, E.A.; Di Gianni, A.; Ronchetti, S. Epoxy coatings containing clays and organoclays: Effect of the filler and its water content on the UV-curing process. *Prog. Org. Coatings* **2008**, *62*, 336–343, doi:10.1016/j.porgcoat.2008.01.014.

254. Esposito Corcione, C.; Malucelli, G.; Frigione, M.; Maffezzoli, A. UV-curable epoxy systems containing hyperbranched polymers: Kinetics investigation by photo-DSC and real-time FT-IR experiments. *Polym. Test.* **2009**, *28*, 157–164, doi:https://doi.org/10.1016/j.polymertesting.2008.11.002.

255. He, Q.; Ziegler-Devin, I.; Chrusciel, L.; Obame, S.N.; Hong, L.; Lu, X.; Brosse, N. Lignin-First Integrated Steam Explosion Process for Green Wood Adhesive Application. *ACS Sustain. Chem. Eng.* **2020**, *8*, 5380–5392, doi:10.1021/acssuschemeng.0c01065.

256. Wang, J.; Zhang, D.; Chu, F. Wood-Derived Functional Polymeric Materials. *Adv. Mater.* **2020**, *2001135*, 1–21, doi:10.1002/adma.202001135.

257. Luo, Y.; Li, Z.; Zuo, Y.; Su, Z.; Hu, C. A Simple Two-Step Method for the Selective Conversion of Hemicellulose in Pubescens to Furfural. *ACS Sustain. Chem. Eng.* **2017**, *5*, 8137–8147, doi:10.1021/acssuschemeng.7b01766.

258. Ding, N.; Song, X.; Jiang, Y.; Luo, B.; Zeng, X.; Sun, Y.; Tang, X.; Lei, T.; Lin, L. Cooking with active oxygen and solid alkali facilitates lignin degradation in bamboo pretreatment. *Sustain. Energy Fuels* **2018**, *2*, 2206–2214, doi:10.1039/C8SE00181B.

259. Ding, N.; Liu, H.; Sun, Y.; Tang, X.; Lei, T.; Xu, F.; Zeng, X.; Lin, L. Lignin degradation in cooking with active oxygen and solid Alkali process: A mechanism study. *J. Clean. Prod.* **2021**, *278*, 123984, doi:https://doi.org/10.1016/j.jclepro.2020.123984.

260. Yang, G.; Rohde, B.J.; Robertson, M.L. Hydrolytic degradation and thermal properties of epoxy resins derived from soybean oil. *Green Mater.* **2013**, *1*,

125–134, doi:10.1680/gmat.12.00023.

261. Geyer, R.; Jambeck, J.R.; Law, K.L. Production, use, and fate of all plastics ever made. *Sci. Adv.* **2017**, *3*, e1700782, doi:10.1126/sciadv.1700782.

262. Gandini, A. The irruption of polymers from renewable resources on the scene of macromolecular science and technology. *Green Chem.* **2011**, *13*, 1061–1083, doi:10.1039/C0GC00789G.

263. Auvergne, R.; Caillol, S.; David, G.; Boutevin, B.; Pascault, J.P. Biobased thermosetting epoxy: Present and future. *Chem. Rev.* **2014**, *114*, 1082–1115, doi:10.1021/cr3001274.

264. Boerjan, W.; Ralph, J.; Baucher, M. Lignin Biosynthesis. *Annu. Rev. Plant Biol.* **2003**, *54*, 519–546, doi:10.1146/annurev.arplant.54.031902.134938.

265. Jawerth, M.; Lawoko, M.; Lundmark, S.; Perez-Berumen, C.; Johansson, M. Allylation of a lignin model phenol: a highly selective reaction under benign conditions towards a new thermoset resin platform. *RSC Adv.* **2016**, *6*, 96281–96288, doi:10.1039/C6RA21447A.

266. Shibata, M.; Sugane, K.; Yanagisawa, Y. Biobased polymer networks by the thiol-ene photopolymerization of allylated p-coumaric and caffeic acids. *Polym. J.* **2019**, *51*, 461–470, doi:10.1038/s41428-018-0165-0.

267. Navari-Izzo, F.; Quartacci, M.F.; Sgherri, C. Lipoic acid: a unique antioxidant in the detoxification of activated oxygen species. *Plant Physiol. Biochem.* **2002**, *40*, 463–470, doi:https://doi.org/10.1016/S0981-9428(02)01407-9.

268. Sgherri, C.; Quartacci, M.F.; Izzo, R.; Navari-Izzo, F. Relation between lipoic acid and cell redox status in wheat grown in excess copper. *Plant Physiol. Biochem.* **2002**, *40*, 591–597, doi:https://doi.org/10.1016/S0981-9428(02)01421-3.

269. Chen, T.; Qiu, M.; Zhang, J.; Sun, H.; Deng, C.; Zhong, Z. Integrated Multifunctional Micelles Co-Self-Assembled from Polypeptides Conjugated with Natural Ferulic Acid and Lipoic Acid for Doxorubicin Delivery. *ChemPhysChem* **2018**, *19*, 2070–2077, doi:10.1002/cphc.201701367.

270. Barltrop, J.A.; Hayes, P.M.; Calvin, M. The Chemistry of 1,2-Dithiolane (Trimethylene Disulfide) as a Model for the Primary Quantum Conversion Act in Photosynthesis1a. *J. Am. Chem. Soc.* **1954**, *76*, 4348–4367, doi:10.1021/ja01646a029.

271. Nambu, Y.; Acar, M.H.; Suzuki, T.; Endo, T. Thermal and photoinitiated

copolymerization of the cyclic disulfide lipoamide with styrene. *Die Makromol. Chemie* **1988**, *189*, 495–500, doi:https://doi.org/10.1002/macp.1988.021890302.

272. Suzuki, T.; Yoko, N.; Takeshi, E. Radical Copolymerization of Lipoamide with Vinyl Monomers. *Macromolecules* **1990**, *23*, 1579–1582, doi:10.1021/ma00208a004.

273. Tang, H.; Tsarevsky, N. V. Lipoates as building blocks of sulfur-containing branched macromolecules. *Polym. Chem.* **2015**, *6*, 6936–6945, doi:10.1039/c5py01005e.

274. Finnveden, M.; Brännström, S.; Johansson, M.; Malmström, E.; Martinelle, M. Novel sustainable synthesis of vinyl ether ester building blocks, directly from carboxylic acids and the corresponding hydroxyl vinyl ether, and their photopolymerization. *RSC Adv.* **2018**, *8*, 24716–24723, doi:10.1039/c8ra04636k.

275. Larsen, D.B.; Sønderbæk-Jørgensen, R.; Duus, J.Ø.; Daugaard, A.E. Investigation of curing rates of bio-based thiol-ene films from diallyl 2,5-furandicaboxylate. *Eur. Polym. J.* **2018**, *102*, 1–8, doi:https://doi.org/10.1016/j.eurpolymj.2018.03.005.

276. Wang, Z.; Miller, B.; Mabin, M.; Shahni, R.; Wang, Z.D.; Ugrinov, A.; Chu, Q.R. Cyclobutane-1,3-Diacid (CBDA): A Semi-Rigid Building Block Prepared by [2+2] Photocyclization for Polymeric Materials. *Sci. Rep.* **2017**, *7*, 1–7, doi:10.1038/s41598-017-13983-z.

277. Wang, Z.; Scheuring, M.; Mabin, M.; Shahni, R.; Wang, Z.D.; Ugrinov, A.; Butz, J.; Chu, Q.R. Renewable Cyclobutane-1, 3-dicarboxylic Acid (CBDA) Building Block Synthesized from Furfural via Photocyclization. *ACS Sustain. Chem. Eng.* **2020**, *8*, 8909–8917.

278. Tellers, J.; Sbirrazzuoli, N.; Guigo, N. A rigid plant oil-based thermoset with a furfural-derived cyclobutane cross-linker. *Green Chem.* **2021**, *23*, 8053–8060, doi:10.1039/d0gc04323k.

279. Circa Group Furacell Process Available online: https://circa-group.com/.

280. Diot-Néant, F.; Rastoder, E.; Miller, S.A.; Allais, F. Chemo-Enzymatic Synthesis and Free Radical Polymerization of Renewable Acrylate Monomers from Cellulose-Based Lactones. *ACS Sustain. Chem. Eng.* **2018**, *6*, 17284–17293, doi:10.1021/acssuschemeng.8b04707.

281. Fadlallah, S.; Kayishaer, A.; Annatelli, M.; Mouterde, L.M.M.; Peru,

A.A.M.; Aricò, F.; Allais, F. Fully renewable photocrosslinkable polycarbonates from cellulose-derived monomers. *Green Chem.* **2022**, *24*, 2871–2881, doi:10.1039/D1GC04755H.

282. Fadlallah, S.; Peru, A.A.M.; Longé, L.; Allais, F. Chemo-enzymatic synthesis of a levoglucosenone-derived bi-functional monomer and its ring-opening metathesis polymerization in the green solvent Cyrene^{TM}. *Polym. Chem.* **2020**, *11*, 7471–7475, doi:10.1039/D0PY01471K.

283. Diot-Néant, F.; Mouterde, L.M.M.; Veith, C.; Couvreur, J.; Miller, S.A.; Allais, F. Sustainable One-Pot Synthesis and Polycondensation of a Levoglucosenone-Derived Cyclic Acetal Diol. *ACS Sustain. Chem. Eng.* **2022**, *10*, 10132–10143, doi:10.1021/acssuschemeng.2c01362.

284. Sanchez-Rexach, E.; Johnston, T.G.; Jehanno, C.; Sardon, H.; Nelson, A. Sustainable Materials and Chemical Processes for Additive Manufacturing. *Chem. Mater.* **2020**, *32*, 7105–7119, doi:10.1021/acs.chemmater.0c02008.

285. Voet, V.S.D.; Guit, J.; Loos, K. Sustainable Photopolymers in 3D Printing: A Review on Biobased, Biodegradable, and Recyclable Alternatives. *Macromol. Rapid Commun.* **2021**, *42*, 1–11, doi:10.1002/marc.202000475.

286. Werpy, T.; Petersen, G. Top Value Added Chemicals from Biomass Volume I. *Us Nrel* **2004**, Medium: ED; Size: 76 pp. pages, doi:10.2172/15008859.

287. Willke, T.; Vorlop, K.-D. Biotechnological production of itaconic acid. *Appl. Microbiol. Biotechnol.* **2001**, *56*, 289–295.

288. Teleky, B.-E.; Vodnar, D.C. Biomass-Derived Production of Itaconic Acid as a Building Block in Specialty Polymers. *Polymers (Basel).* 2019, *11*.

289. Papadopoulos, L.; Pezzana, L.; Malitowski, N.M.; Sangermano, M.; Bikiaris, D.N.; Robert, T. UV-Curing Additive Manufacturing of Bio-Based Thermosets: Effect of Diluent Concentration on Printing and Material Properties of Itaconic Acid-Based Materials. *ACS Omega* **2023**, *8*, 31009–31020, doi:10.1021/acsomega.3c02808.

290. Robert, T.; Friebel, S. Itaconic acid–a versatile building block for renewable polyesters with enhanced functionality. *Green Chem.* **2016**, *18*, 2922–2934.

291. Dong, X.; Ren, J.; Duan, Y.; Wu, D.; Lin, L.; Shi, J.; Jia, R.; Xu, X.; He, X. Preparation and properties of green UV-curable itaconic acid cross-linked modified waterborne polyurethane coating. *J. Appl. Polym. Sci.* **2022**, *139*, 52042, doi:https://doi.org/10.1002/app.52042.

292. Pezzana, L.; Melilli, G.; Delliere, P.; Moraru, D.; Guigo, N.; Sbirrazzuoli,

N.; Sangermano, M. Thiol-ene biobased networks: Furan allyl derivatives for green coating applications. *Prog. Org. Coatings* **2022**, *173*, 107203.

293. Flourat, A.L.; Pezzana, L.; Belgacem, S.; Dosso, A.; Sangermano, M.; Fadlallah, S.; Allais, F. Levoglucosenone to 3D-printed green materials: synthesizing sustainable and tunable monomers for eco-friendly photo-curing. *Green Chem.* **2023**, doi:10.1039/D3GC01833D.

294. Pezzana, L.; Melilli, G.; Sangermano, M.; Sbirrazzuoli, N.; Guigo, N. Sustainable approach for coating production: Room temperature curing of diglycidyl furfuryl amine and itaconic acid with UV-induced thiol-ene surface post-functionalization. *React. Funct. Polym.* **2023**, *182*, 105486, doi:https://doi.org/10.1016/j.reactfunctpolym.2022.105486.

295. Cottier, L.; Descotes, G.; Soro, Y. Heteromacrocycles from Ring-Closing Metathesis of Unsaturated Furanic Ethers. *Synth. Commun.* **2003**, *33*, 4285–4295, doi:10.1081/SCC-120026858.

296. Engel, T.; Kickelbick, G. Furan-Modified Spherosilicates as Building Blocks for Self-Healing Materials. *Eur. J. Inorg. Chem.* **2015**, *2015*, 1226–1232, doi:https://doi.org/10.1002/ejic.201402551.

297. Wang, Z.D.; Elliott, Q.; Wang, Z.; Setien, R.A.; Puttkammer, J.; Ugrinov, A.; Lee, J.; Webster, D.C.; Chu, Q.R. Furfural-Derived Diacid Prepared by Photoreaction for Sustainable Materials Synthesis. *ACS Sustain. Chem. Eng.* **2018**, *6*, 8136–8141, doi:10.1021/acssuschemeng.8b02415.

298. Yoshimura, T.; Shimasaki, T.; Teramoto, N.; Shibata, M. Bio-based polymer networks by thiol-ene photopolymerizations of allyl-etherified eugenol derivatives. *Eur. Polym. J.* **2015**, *67*, 397–408, doi:10.1016/j.eurpolymj.2014.11.013.

299. Rajaraman, S.K.; Mowers, W.A.; Crivello, J. V. Novel hybrid monomers bearing cycloaliphatic epoxy and 1-propenyl ether groups. *Macromolecules* **1999**, *32*, 36–47, doi:10.1021/ma981078r.

300. Davidson, R.S. *Exploring the science, technology and applications of UV and EB curing*; Sita Technology, 1999; ISBN 0947798412.

301. Northrop, B.H.; Coffey, R.N. Thiol-ene click chemistry: Computational and kinetic analysis of the influence of alkene functionality. *J. Am. Chem. Soc.* **2012**, *134*, 13804–13817, doi:10.1021/ja305441d.

302. ASTM D3363-05 Standard Test Method for Film Hardness by Pencil Test. *ASTM Int.* **2005**, doi:10.1520/D3363-05.

303. ASTM D3359-17 Standard Test Methods for Rating Adhesion by Tape Test. *ASTM Int.* **2017**, doi:10.1520/D3359-17.

304. BASF High lights! Radiation curing with resins and photoinitiators for industrial coatings and graphic arts: Laromer®, Irgacure®, Lucirin®, Darocur® Available online: https://www.dispersions-pigments.basf.com/portal/load/fid620253/low_EDC_2711_e_BR_Strahlung.pdf (accessed on Jun 26, 2020).

305. Mishra, D.; Wang, S.; Michel, S.; Palui, G.; Zhan, N.; Perng, W.; Jin, Z.; Mattoussi, H. Photochemical transformation of lipoic acid-based ligands: Probing the effects of solvent, ligand structure, oxygen and pH. *Phys. Chem. Chem. Phys.* **2018**, *20*, 3895–3902, doi:10.1039/c7cp06350d.

306. Lorenzini, C.; Haider, A.; Kang, I.K.; Sangermano, M.; Abbad-Andalloussi, S.; Mazeran, P.E.; Lalevée, J.; Renard, E.; Langlois, V.; Versace, D.L. Photoinduced Development of Antibacterial Materials Derived from Isosorbide Moiety. *Biomacromolecules* **2015**, *16*, 683–694, doi:10.1021/bm501755r.

307. Cramer, N.B.; Scott, J.P.; Bowman, C.N. Photopolymerizations of Thiol−Ene Polymers without Photoinitiators. *Macromolecules* **2002**, *35*, 5361–5365, doi:10.1021/ma0200672.

308. Ribca, I.; Jawerth, M.E.; Brett, C.J.; Lawoko, M.; Schwartzkopf, M.; Chumakov, A.; Roth, S. V; Johansson, M. Exploring the Effects of Different Cross-Linkers on Lignin-Based Thermoset Properties and Morphologies. *ACS Sustain. Chem. Eng.* **2021**, *9*, 1692–1702, doi:10.1021/acssuschemeng.0c07580.

309. Nameer, S.; Semlitsch, S.; Martinelle, M.; Johansson, M. One-pot enzyme-catalyzed synthesis of dual-functional polyester macromers towards surface-active hydrophobic films. *RSC Adv.* **2017**, *7*, 50294–50299, doi:10.1039/C7RA09828F.

310. Robinson, B.A.; Tester, J.W. Kinetics of alkaline hydrolysis of organic esters and amides in neutrally-buffered solution. *Int. J. Chem. Kinet.* **1990**, *22*, 431–448, doi:https://doi.org/10.1002/kin.550220502.

311. Leja, K.; Lewandowicz, G. Polymer biodegradation and biodegradable polymers-a review. *Polish J. Environ. Stud.* **2010**, *19*.

312. Quan, H.; Zhang, T.; Xu, H.; Luo, S.; Nie, J.; Zhu, X. Photo-curing 3D printing technique and its challenges. *Bioact. Mater.* **2020**, *5*, 110–115, doi:10.1016/j.bioactmat.2019.12.003.

313. Jonkheijm, P.; Weinrich, D.; Köhn, M.; Engelkamp, H.; Christianen, P.C.M.; Kuhlmann, J.; Maan, J.C.; Nüsse, D.; Schroeder, H.; Wacker, R.; et al. Photochemical Surface Patterning by the Thiol-Ene Reaction. *Angew. Chemie Int. Ed.* **2008**, *47*, 4421–4424, doi:https://doi.org/10.1002/anie.200800101.

314. Modjinou, T.; Versace, D.L.; Abbad-Andaloussi, S.; Langlois, V.; Renard, E. Enhancement of Biological Properties of Photoinduced Biobased Networks by Post-Functionalization with Antibacterial Molecule. *ACS Sustain. Chem. Eng.* **2019**, *7*, 2500–2507, doi:10.1021/acssuschemeng.8b05402.

315. Manhart, J.; Kramer, R.; Schaller, R.; Holzner, A.; Kern, W.; Schlögl, S. Surface Functionalization of Natural Rubber by UV-Induced Thiol-ene Chemistry. *Macromol. Symp.* **2016**, *365*, 32–39, doi:https://doi.org/10.1002/masy.201650016.

316. Tian, Q.; Yuan, Y.C.; Rong, M.Z.; Zhang, M.Q. A thermally remendable epoxy resin. *J. Mater. Chem.* **2009**, *19*, 1289–1296, doi:10.1039/B811938D.

317. Handique, J.; Dolui, S.K. A thermally remendable multiwalled carbon nanotube/epoxy composites via Diels-Alder bonding. *J. Polym. Res.* **2019**, *26*, 163, doi:10.1007/s10965-019-1804-7.

318. Baroncini, E.A.; Kumar Yadav, S.; Palmese, G.R.; Stanzione III, J.F. Recent advances in bio-based epoxy resins and bio-based epoxy curing agents. *J. Appl. Polym. Sci.* **2016**, *133*, doi:https://doi.org/10.1002/app.44103.

319. Ma, S.; Webster, D.C. Naturally Occurring Acids as Cross-Linkers To Yield VOC-Free, High-Performance, Fully Bio-Based, Degradable Thermosets. *Macromolecules* **2015**, *48*, 7127–7137, doi:10.1021/acs.macromol.5b01923.

320. Tellers, J.; Willems, P.; Tjeerdsma, B.; Guigo, N.; Sbirrazzuoli, N. Eutectic hardener from food-based chemicals to obtain fully bio-based and durable thermosets. *Green Chem.* **2020**, *22*, 3104–3110, doi:10.1039/D0GC00311E.

321. Feng, W.; Li, L.; Ueda, E.; Li, J.; Heißler, S.; Welle, A.; Trapp, O.; Levkin, P.A. Surface patterning via thiol-yne click chemistry: An extremely fast and versatile approach to superhydrophilic-superhydrophobic micropatterns. *Adv. Mater. Interfaces* **2014**, *1*, 1–6, doi:10.1002/admi.201400269.

322. Ma, W.; Zhao, J.; Oderinde, O.; Han, J.; Liu, Z.; Gao, B.; Xiong, R.; Zhang, Q.; Jiang, S.; Huang, C. Durable superhydrophobic and superoleophilic electrospun nanofibrous membrane for oil-water emulsion separation. *J. Colloid Interface Sci.* **2018**, *532*, 12–23, doi:10.1016/j.jcis.2018.06.067.

323. Schoon, I.; Kluge, M.; Eschig, S.; Robert, T. Catalyst influence on undesired side reactions in the polycondensation of fully bio-based polyester itaconates. *Polymers (Basel).* **2017**, *9*, 693.

324. Melilli, G.; Guigo, N.; Robert, T.; Sbirrazzuoli, N. Radical Oxidation of Itaconic Acid-Derived Unsaturated Polyesters under Thermal Curing Conditions. *Macromolecules* **2022**, *55*, 9011–9021, doi:10.1021/acs.macromol.2c01682.

325. Panic, V. V; Seslija, S.I.; Popovic, I.G.; Spasojevic, V.D.; Popovic, A.R.; Nikolic, V.B.; Spasojevic, P.M. Simple One-Pot Synthesis of Fully Biobased Unsaturated Polyester Resins Based on Itaconic Acid. *Biomacromolecules* **2017**, *18*, 3881–3891, doi:10.1021/acs.biomac.7b00840.

326. Dichiarante, V.; Martinez Espinoza, M.I.; Gazzera, L.; Vuckovac, M.; Latikka, M.; Cavallo, G.; Raffaini, G.; Oropesa-Nunez, R.; Canale, C.; Dante, S.; et al. A Short-Chain Multibranched Perfluoroalkyl Thiol for More Sustainable Hydrophobic Coatings. *ACS Sustain. Chem. Eng.* **2018**, *6*, 9734–9743, doi:10.1021/acssuschemeng.8b00777.

327. Kaminska, I.; Qi, W.; Barras, A.; Sobczak, J.; Niedziolka-Jonsson, J.; Woisel, P.; Lyskawa, J.; Laure, W.; Opallo, M.; Li, M.; et al. Thiol-yne click reactions on alkynyl-dopamine-modified reduced graphene oxide. *Chem. - A Eur. J.* **2013**, *19*, 8673–8678, doi:10.1002/chem.201300225.

328. Lesiak, B.; Kövér, L.; Tóth, J.; Zemek, J.; Jiricek, P.; Kromka, A.; Rangam, N. C sp 2 /sp 3 hybridisations in carbon nanomaterials – XPS and (X)AES study. *Appl. Surf. Sci.* **2018**, *452*, 223–231, doi:10.1016/j.apsusc.2018.04.269.

329. Guo, J.; Filpponen, I.; Johansson, L.S.; Heiβler, S.; Li, L.; Levkin, P.; Rojas, O.J. Micro-patterns on nanocellulose films and paper by photo-induced thiol–yne click coupling: a facile method toward wetting with spatial resolution. *Cellulose* **2018**, *25*, 367–375, doi:10.1007/s10570-017-1593-2.